Modelling of the Cross-Shore Mixed Sand Transport under Sheet Flow Conditions

Von der Fakultät für Bauingenieurwesen und Geodäsie
der Gottfried Wilhelm Leibniz Universität Hannover

zur Erlangung des Grades

DOKTOR-INGENIEUR
Dr.-Ing.

genehmigte Dissertation

von

M.Sc. Gholamreza Shiravani
aus Darab (Provinz Fars–Iran)

Hannover, 2022

Acknowledgments

your everlasting support and encouragement during my PhD program and generally my life in Germany. It is difficult to express my feeling in words and apologize you that I was not near you to be helpful.

Gholamreza Shiravani

Norderney, 2023

Abstract

Cross-shore sediment transport during extreme climate events (e.g. storm surges) may lead to significant morphological evolution and shoreline recession with drastic irreversible consequences. To protect sandy beaches against storm induced erosion issues, coastal engineering practices could be classified into hard/gray protecting coastal structures versus soft or environmentally friendly engineering measurements. Hard structures (e.g. seawalls) have usually been posed many problems during storm surges, which can be summarized as expensive reparation costs of structures after storm and damages of protected infrastructures as well as restriction of human access to beach for leisure activities, and consequently reduction the tourist attraction. In contrast, the soft measurements for beach protection like beach nourishment can protect the sandy beaches against storms and preserves the beautiful beach scenes for tourists, and therefore provide financial support for people living along the coastline. The productivity as well as favorability of soft measurements for both nature and human parties lead to calling these activities in literature as building with nature in contrast to hard structures, which are known as building against nature.

The high rate of beach erosion during storms and corresponding high costs for beach (re)nourishment to compensate the lost sand is one of the major issues in coastal zone management. To understand the erosion of sandy beaches under storm conditions, the associated erosion mode in literature is known as sheet flow, where the near bed current velocity is such great that sands are basically transported within highly concentrated sheets near the bed and therefore the bed forms are disappeared.

The practical experiences on beach nourishment show that the new applied material (borrow material) have usually different properties, particularly grain size distribution, than the native sand. Moreover, this discrepancy between the grain size distribution of incorporated and native sand has an important role in increment/reduction of the erosion rate of (re)nourished beaches under future storms. To understand the erosion mechanisms of (re)nourished beaches, coastal engineers were interested to study the transport mechanisms of mixed sand versus uniform sand. Performed experiments in the Großer Wellenkanal (GWK) on mixed sands (well graded sand) with the same median grain size to a uniform sand (well sorted sand) in small scale experiments under storm induced transport mode (i.e. sheet flow) revealed that the erosion rate of the mixed sand is smaller than the uniform. This importance can approve the practical experiences, where the final sand mixture grain size distribution after (re)nourishment is a deciding parameter to reduce the erosion rate at future storms.

Due to the natural heterogeneity of sand grains, coastal engineers tried to modify the effective shear stress or critical shear stress on grains using empirical/theoretical modification factors to include this in prediction formulas. These modification approaches are known in sediment transport as hiding/exposure factors. However, these are not able to include the detailed mechanisms of mixed sand transport in prediction formulas, and therefore depending on the applied formula for predicting the transport rate. The accuracy of transport formulas generally differs with respect to the applied modification factor. Moreover, the hiding/exposure factors are not able to provide detailed information about the concentration flux of constituting fractions in a mixed sand. Therefore, with regard to the positive economical property of mixed sand based on the performed experiments, detailed investigations like this thesis could be worthful to improve the protection performance of beach (re)nourishment as a sustainable environmentally friendly measurement in coastal engineering.

In this study, the available experiments on mixed sand transport under sheet flow conditions are systematically compared. Then the capability of available (semi-) empirical formulas in coastal engineering for sheet flow induced sand transport in combination with available empirical equations for hiding/exposure coefficients are evaluated. Moreover, due to the importance of non-uniformity of mixed sand in reduction of the erosion rate after (re)nourishment under storm condition, a detailed RANS (Reynolds Averaged Navier Stokes) Eulerian two-phase numerical solver, mixedSedFoam, within the open-source CFD-toolbox framework OpenFOAM is developed, and with available experimental data calibrated and validated. This is the first time that accompanied with the sand concentration and velocity, the concentration of constituting fractions as well as their corresponding velocities are computed. This importance could improve the understanding of the transport mechanisms of mixed sand under sheet flow conditions and be implemented in the practice of coastal engineering, by deciding on the available borrow material with different grain size distribution for beach (re)nourishment.

Moreover, due to the importance of inter-particle interactions within the sheet flow layer, in this thesis a new intergranular drag force coefficient based on the collision of particles (here sand grains) and the kinetic energy of granular system is developed. The developed new drag force coefficient can better than the previous describe the dynamics of different granular systems. Finally, a new formula for prediction of sheet flow layer thickness is presented, which improves the accuracy of available (semi-) empirical transport formula for mixed sand transport prediction.

Keywords: Mixed sand transport, sheet flow, numerical modeling, (semi-) empirical sand transport formulas

Kurzfassung

Küstennaher Sedimenttransport in Richtung des Strandes könnte bei z. B. Sturmfluten zu erheblichen morphologischen Veränderungen und massiver Küstenerosion mit drastischen, teils irreversiblen Folgen führen. Um Strände vor sturmbedingten Erosionen zu schützen, werden Küstenschutzmaßnahmen in harte/graue oder weiche/umweltfreundliche Ingenieurmaßnahmen klassifiziert. Schäden an harten Schutzmaßnahmen (z. B. Ufermauern) haben meist sowohl hohe Reparaturkosten zur Folge, als auch Einschränkungen des Zugangs und folglich eine Verringerung der touristischen Attraktivität. Um diese Probleme zu umgehen, werden häufig weiche Unterhaltungsmaßnahmen, wie z.B. die Strandaufspülung, angewendet. Diese können den Strand ebenfalls vor möglichen schweren Sturmschäden schützen. Die Produktivität sowie die Beliebtheit der weichen Maßnahmen, sowohl für die Natur als auch für den Menschen, führen dazu, dass diese in der Literatur als Bauen mit der Natur bezeichnet werden, im Gegensatz zu grauen Strukturen, die als Bauen in der Natur bekannt sind.

Die große Menge an Stranderosionen aufgrund von Sturmereignissen und den damit verbundenen hohen Unterhaltungskosten der Strandaufspülungen sind eines der Hauptfragestellungen in der Strandunterhaltung. Um das Erosionsverhalten von sandigen Stränden und Sturmflutbedingungen zu verstehen, wird hauptsächlich die Erosions-Methode im „Sheet Flow" verwendet. Beim „Sheet Flow" wird die Sohlschubgeschwindigkeit so groß, dass Sand hauptsächlich in sogenannten hochkonzentrierten Schichten nahe der Sohle transportiert wird. Die Sohlenformen werden dadurch erodiert, sodass die Sohle flach bleibt.

Die praktischen Erfahrungen bei der Strandaufspülung zeigen, dass das neu aufgebrachte Material in der Regel andere Eigenschaften, insbesondere in der Korngrößenverteilung, aufweist als der ursprüngliche Sand. Darüber hinaus spielt diese Diskrepanz zwischen der Korngrößenverteilung von eingelagertem und bereits vorhandenem Sand eine wichtige Rolle bei der Erhöhung/Verringerung der Erosionsrate bei zukünftigen Sturmereignissen. Um die Erosionsmechanismen von aufgespülten Stränden zu verstehen, ist es entscheidend, die Transportmechanismen von gemischtem Sand im Gegensatz zu homogen verteiltem Sand zu untersuchen. Experimente im Großer Wellenkanal (GWK) mit gemischtem Sand mit der gleichen mittleren Korngröße wie bei homogenem Sand zeigten in speziellen Untersuchungen, dass die Erosionsrate von gemischtem Sand kleiner ist verglichen zum homogenen Sandgemisch. Diese Erkenntnis bestätigt die praktischen Erfahrungen, bei denen die Kornzusammensetzung nach der Strandaufspülung ein entscheidender Parameter ist, um die Erosionsrate bei zukünftigen Stürmen zu steuern bzw. zu reduzieren.

Aufgrund der natürlichen ungleichförmigen Zusammensetzung von Sedimenten wurde in Küsteningenieurwesen versucht, die effektive Schubspannung oder kritische Schubspannung von Sandkörnern mit empirischen Faktoren zu modifizieren, die im Sedimenttransport als Hiding/Exposure-Formeln bekannt sind. Diese empirischen Faktoren sind jedoch nicht in der Lage, die im Detail vorkommenden Prozesse des gemischten Sedimenttransports in Transportformeln miteinzubeziehen und daher ergeben sich je nach verwendeter Gleichung unterschiedliche Transportraten. Somit ist die Genauigkeit von Transportformeln abhängig von den angewendeten Modifikationsfaktoren. Darüber hinaus können die Hiding/Exposure-Faktoren keine detaillierten Informationen über den Konzentrationsfluss der einzelnen Fraktionen in einem gemischten Sand liefern. Daher ist es von großer Wichtigkeit, diese Prozesse zu verstehen und die Strandaufspülungen umwelttechnisch und -schonend zu verbessern, um auch langfristig für eine nachhaltige umweltfreundliche Sicherung der Küstenlinie zu sorgen.

In der vorliegenden Studie werden die vorhandenen Experimente zum gemischten Sedimenttransport unter „Sheet Flow"-Bedingungen systematisch verglichen und die Leistungsfähigkeit der entsprechenden Gleichungen aus dem Küsteningenieurwesen in Kombination mit verfügbaren empirischen Gleichungen für Hiding/Exposure-Formeln bewertet. Aufgrund der Bedeutung von gemischtem Sand, zur Reduzierung der Erosionsrate nach einer Sandaufspülung bei Sturmfluten, wird hier ein detaillierter RANS (Reynolds Averaged Navier Stokes) eulerscher zweiphasiger numerischer Löser (solver), mixedSedFoam, innerhalb des Open-Source-CFD-Toolbox-Frameworks OpenFOAM entwickelt. Der hier entwickelte Ansatz ist anhand von verfügbaren experimentellen Daten aus der Literatur kalibriert und validiert worden. Dies ist der erste Ansatz seiner Art, bei der die Sandkonzentration und die Transportgeschwindigkeit der konstituierenden Fraktionen, sowie ihre entsprechenden Geschwindigkeiten zusammen berechnet werden. Aufgrund der Bedeutung von interpartikulären Wechselwirkungen innerhalb des „Sheet Flow"-Zustands wurde in dieser Arbeit außerdem ein neuer interkristalliner Widerstandsbeiwert basierend auf der Kollision von Partikeln (hier Sandkörnern) und der kinetischen Energie des granularen Systems entwickelt. Der entwickelte neue Widerstandsbeiwert kann die Dynamik verschiedener granularer Systeme wesentlich besser beschreiben als die bisherigen Beiwerte. Eine neue Formel zur Vorhersage der Schichtdicke der Schichtströmung wird vorgestellt, die in der Lage ist, die Genauigkeit der verfügbaren (semi-) empirischen Transportformeln für die Vorhersage des gemischten Sandtransports zu verbessern.

Der hier entwickelte Modellansatz verbessert das Verständnis der Transportmechanismen von gemischten Sandfraktionen unter Schichtströmungsbedingungen und ist in der Lage zukünftig bei der Entscheidung über die Korngrößenverteilung von Sandaufspülungen zu unterstützen. Ebenfalls kann dieser Ansatz verwendet werden, um das neue aufzubringende Material hinsichtlich der Stabilitätskriterien zu untersuchen, um so den zukünftigen Unterhaltungsaufwand zu reduzieren bzw. zu optimieren.

Schlüsselwörter: gemischter Sedimenttransport, „Sheet Flow", numerischer Modellversuch, (semi-) empirische Sedimenttransportformeln

Contents

List of Figures

List of Tables

Nomenclature

Abbreviations

ABS	Acoustic Backscattering System
AOFT	Aberdeen Oscillatory Flow Tunnel
BBLT	Bed Boundary Layer Thickness
BSS	Brier Skill Score
CCM	Conductivity Concentration Meter
CCP	Conductivity Concentration Profiler
CFD	Computational Fluid Dynamics
COR	Coefficient Of Restitution
DGFR	Dense Granular Flow Rheology
FSK	Forschungsstelle Küste
FZK	Forschungszentrum Küste
GI	Graded Index
GWK	Grosser Wellenkanal
IDC	Interparticle drag force coefficient
KTGF	Kinetic Theory of Granular Flow
LOWT	Large Oscillating Water Tunnel
OFT	Oscillatory Flow Tunnel
PF	Percentage of Fine
SFLT	Sheet Flow Layer Thickness
SFLTC	Sheet Flow Layer Thickness Crest
SFLTT	Sheet Flow Layer Thickness Trough
SWL	Still Water Level

TSS	Transverse Suction System
$TUOFT$	Tokyo University Oscillatory Flow Tunnel
VDF	Velocity Distribution Function

Greek Symbols

α	volume concentration of sand
α_1	volume concentration of the first fraction
α_2	volume concentration of the second fraction
α_3	volume concentration of the third fraction
α_C	volume concentration of the coarse fraction
α_c	maximum allowable value of volumetric sand concentration
α_F	volume concentration of the fine fraction
α_i	volume concentration of the ith fraction
α_j	volume concentration of jth fraction
α_k	volume concentration of kth fraction
α_M	volume concentration of the medium fraction
α_m	volume concentration of mth sand fraction
α_n	volume concentration of nth fraction
α_p	calibration factor
α_s	sand-phase volume concentration
α_w	volume fraction of water
β	asymmetry value
χ_m	deviator of the strain rate tensor for mth sand fraction
Δm	momentum exchange due to the collision between two particles
Δt_{max}	maximum time-step

δ	bed boundary layer thickness
δ_f	delta function
Δ_t	turbulence suspension
δ_w	Stokes boundary layer thickness
δ_{em}	maximum erosion depth
δ_{ij}	Kronecker delta function
δ_{si}	sheet flow layer thickness in crest/trough
δ_{sm}	maximum SFLT
ϵ_b	bed load efficiency factor
ϵ_s	suspended load efficiency factor
ϵ_w	dissipation of the turbulence kinetic energy of water
η	hiding/exposure parameter
η_m	calibration factor
η_r	ripple length
$\forall$	volume
γ	calibration factor
Γ_j	total exchange rate of the j-fraction sand
γ_m	dissipation rate of T_m due to the inelastic collisions
κ	von Kármán constant
λ_1	modification factor
λ_2	modification factor
λ_d	calibration factor
λ_m^c	bulk viscosity of mth granular fraction for collision
λ_m^f	bulk viscosity of mth granular fraction for friction

λ_r	ripple length
λ_w	bulk viscosity of water
μ_m^c	dynamic viscosity of the mth granular fraction for collision
μ_m^f	dynamic viscosity of the mth granular fraction for friction
μ_N	friction coefficient
μ_w	dynamic viscosity of water
μ_w^t	turbulent dynamic viscosity
ν	kinematic visosity
ν^t	turbulent kinematic viscosity
ω	angular velocity
$\Omega'_{i,j}$	exchange rate from crest/trought to trough/crest for the j-fraction sand
$\Omega_{cc,j}$	in crest part transported rate of the j-fraction sand
$\Omega_{ct,j}$	from crest to trough part transported rate of the j-fraction sand
$\Omega_{i,j}$	crest/trough exchange rate of the j-fraction sand
$\Omega_{tc,j}$	from trough to crest part transported rate of the j-fraction sand
$\Omega_{tt,j}$	in trough part transported rate of the j-fraction sand
ϕ_f	destabilizing factor
ψ	mobility number
ψ_m	maximum mobility number
ρ_g	density of glass beads
ρ_m	density of mth sand fraction
ρ_n	density of nth sand fraction
ρ_s	sand density
ρ_w	water density

σ	average of particle diameters
σ_c	Schmidt number
σ_k	calibration coefficient
τ	bed-shear stress
τ_{cr}	critical bed-shear stress
θ_{cr}	critical Shields parameter
$\theta_j(t)$	instantaneous effective Shields parameter of the j-fraction sand
$\theta_{c,j}$	Shields parameter in crest for the j-sand fraction
$\theta_{cr(corrected),j}$	corrected Shields parameters for the j-fraction
$\theta_{cr,j}$	critical Shields parameter of the j-fraction sand
$\theta_{i,j}$	Shields parameter in creat/trough part of the j-fraction sand
θ_{max}	maximum Shields parameter
$\theta_{t,j}$	Shields parameter in trough for the j-sand fraction
φ	internal friction angle of sand
$\xi_{Day,j}$	the Day (1980) modification factor
$\xi_{Egi.,j}$	the Egiazaroff (1965) modification factor
$\xi_{V,j}$	the Van Rijn (2007) modification factor
ζ_i	time-scale of the phase-lag for the j-fraction sand
$\zeta_{cr,j}$	critical time-scale parameter for j-fraction sand
$\zeta_{i,j}$	time-scale of the crest/trough part for the j-sand fraction
∇	gradient operator
ϕ	angle with i-vector
θ	angle with h-vector
$\hat{\theta}_i$	Shields parameter with $\hat{u}_i$

$\tilde{\tau}_m^c$	collisional shear stress tensor of mth sand fraction
$\tilde{\tau}_m^f$	frictional shear stress tensor of mth sand fraction
$\tilde{\tau}_m$	shear stress tensor of mth sand fraction
$\tilde{\tau}_w$	shear stress tensor of water
$\tilde{\tau_{Ds}}$	diffusive shear stress tensor of sand-phase
$\tilde{\tau}_s$	shear stress tensor of sand-phase

Roman Symbols

A	free stream oscillatory amplitude
a	skewness value
a_b	near bed amplitude of oscillatory orbitals
a_c	crest acceleration
a_l	longest length of a non-spherical grain
A_m	flow following capability of the mth sand fraction
a_m	maximum amplitude of the oscillatory orbital in free stream
A_p	projected area
A_s	area of sand grain
a_t	trough acceleration
B	calibration coefficient
b	unit vector in the direction of collision
b_l	intermediate length of a non-spherical grain
c	sand concentration
$c\prime_k$	velocity of k particle after collision
$c\prime_{kj}$	relative velocity of k and j particles after collision
C_D	drag coefficient

C_j	difference between the time dependent velocity and ensemble averaged velocity of j-fraction
c_j	velocity of particle j
C_k	difference between the time dependent velocity and ensemble averaged velocity of k-fraction
c_k	velocity of particle k
C_L	lift coefficient
c_l	shortest length of a non-spherical grain
$C_{1\epsilon}$	calibration coefficient
$C_{2\epsilon}$	calibration coefficient
$C_{3\epsilon}$	calibration coefficient
$C_{4\epsilon}$	calibration coefficient
C_μ	calibration coefficient
C_{ch}	Chézy friction coefficient
$C_{f,(m,n)}$	friction coefficient between m^{th} sand n^{th} sand fraction
C_{kj}	relative velocity of velocity differences with ensemble averaged velocity of two particles k and j
c_{kj}	relative velocity of particle k to particle j
$C_{x,m}$	velocity fluctuations of the mth sand fraction in x-direction
$C_{y,m}$	velocity fluctuations of the mth sand fraction in y-direction
$C_{z,m}$	velocity fluctuations of the mth sand fraction in z-direction
COG	center of gravity
D	diameter of sand grain
D_*	non-dimensional grain size
D_A	ineffective grain size of mixed sand

D_j	size of j-fraction sand
d_j	particle size of jth fraction
d_k	particle size of kth fraction
D_m	mean grain size of mixed sand
d_m	grain size of mth sand fraction
d_n	grain size of nth fraction
$D_{1,2}$	drag force coefficient of first and second sand fraction
$D_{1,3}$	drag force coefficient of first and third sand fraction
D_{10}	sand size of 10% finer
D_{16}	sand size of 16% finer
D_{50}	median grain size
D_{84}	sand size of 84% finer
D_{90}	sand size of 90% finer
$D_{C,w}$	drag force coefficient of the coarse fraction and water
$D_{F,C}$	drag force coefficient of the fine and coarse fractions
$D_{F,M}$	drag force coefficient of the fine and medium fractions
$D_{F,w}$	drag force coefficient of the fine fraction and water
D_{kj}	interparticle drag force coefficient between particles system of j and k
$D_{M,C}$	drag force coefficient of the medium and coarse fractions
$D_{m,n}$	drag force coefficient of mth and n^{th} sand fraction
$D_{M,w}$	drag force coefficient of the medium fraction and water
$D_{m,w}$	drag force coefficient of mth sand fraction and water
e	coefficient of restitution
e_1	calibration factor

xx

e_2	calibration factor
$e_{(m,n)}$	coefficient of restitution for the collision between m^{th} sand n^{th} sand fraction
F	force
f_1	calibration factor
f_2	calibration factor
f_3	calibration factor
f_b	friction factor near the bed
F_D	drag force
F_G	gravitational force
F_I	inertial force
f_j	probability velocity distribution function for particle j
f_k	probability velocity distribution function for particle k
F_L	lift force
f_w	bed friction factor under waves
g	gravitational acceleration
$g_{0,(m,m)}$	radial distribution function for m^{th} sand fraction
$g_{0,(m,n)}$	radial distribution function for m^{th} and n^{th} sand fraction
$g_{0,(s,s)}$	radial distribution function for a well-sorted sand
g_{kj}	radial distribution function for particle k with partilces j
H	wave height
h	water depth
$h_{(m,m)}$	calibration factor
I	identity tensor

I_{kj} collisional momentum transfer rate per unit volume between particle k and j

J exchanged momentum between two particles

J_t momentum exchange in the tangent direction

$J_{m,n}$ granular energy exchange between m^{th} and n^{th} sand fractions

J_{mw} granular energy exchange between water and m^{th} sand fraction

k_m diffusion parameter of granular temperature for mth sand fraction

k_s bed roughness height

k_w turbulence kinetic energy of water

$k_{(m,m)}$ calibration factor

k_{γ_m} factor of dissipation of flactuation energy for the mth sand fraction

k_{sw} bed-roughness height under wave induced sheet flow

L wave length

$l_{(m,m)}$ calibration factor

m mass of particle

m_j mass of particle j

m_k mass of particle k

M_m momentum exchange between m^{th} sand fraction and water as well as other sand fractions

m_r calibration factor

m_s constant value

$M_{1,n}$ momentum exchange between first sand fraction with other n-sand fractions

$M_{m,n}$ momentum exchange between m^{th} and n^{th} sand fraction and water

xxii

$M_{w,m}$	momentum exchange between m^{th} sand fraction and water
N	total number of composing fractions of a mixed sand
n	particle density
n_r	calibration factor
n_s	constant value
P_c	phase-lag number for crest
p_j	percentage of j-fraction sand
P_m	pressure of mth sand fraction
P_m^c	collisional pressure for m^{th} sand fraction
P_m^f	frictional pressure for m^{th} sand fraction
P_t	phase-lag number for trough
P_w	pressure of water
$P_{i,j}$	phase-lag number for crest/trough of the j-fraction sand
Q_c	total transport rate in crest
q_g	transport rate of graded sand
q_N	net transport rate
Q_t	total transport rate in trough
$q_{b,j}$	bed load transport rate of j-fraction sand
$q_{s,j}$	suspended load transport rate of j-fraction sand
$q_{t,j}$	total transport rate of the j-fraction sand
r	position vector
r_w	velocity asymmetry
Re	Reynolds number
Re_m	Reynolds number of mth sand fraction

s	specific density of sand
s_f	shape factor
St_m	Stokes number of mth sand fraction
T	wave period
t	time
T_c	crest period
T_j	fluctuating energy of j-fraction
T_k	fluctuating energy of k-fraction
t_m	sand particle response time for the mth sand fraction
t_n	unit vector in the tangent direction
T_t	trough period
t_w	time-scale of water-phase eddies
T_{cu}	first part of crest-period
T_{fall}	required time for resettling a picked-up sand
T_i	crest/trough part of the wave period
T_{tu}	first part of trough-period
U	time averaged flow velocity
$u(t)$	time dependent flow velocity
U_1	time-averaged velocity of the first sand fraction
u_1	first-order amplitudes of velocity
U_2	time-averaged velocity of the second sand fraction
u_2	second-order amplitudes of velocity
U_3	time-averaged velocity of the third sand fraction
U_a	time-averaged velocity of phase-a

U_b	time-averaged velocity of phase-b
u_b	flow velocity near the bed
U_C	time-averaged velocity of the coarse fraction
u_c	crest velocity
U_F	time-averaged velocity of the fine fraction
U_i	time-averaged velocity of the ith fraction
U_M	time-averaged velocity of the medium fraction
U_m	time-averaged velocity of mth sand fraction
U_m^T	transpose of the time-averaged m^{th} fraction velocity
U_s	time-averaged sand velocity
u_t	trough period
U_w	time-averaged velocity of water
U_w^T	transpose of the time-averaged water velocity
$u_{1/10}$	average of the heighest 10% of velocities
$U_{m,a}$	time-averaged velocity of mth sand fraction after collision
$U_{m,b}$	time-averaged velocity of mth sand fraction before collision
u_{max}	maximum velocity
u_{min}	minimum velocity
U_{ms}	time-averaged relative velocity of the mth sand fraction with mixture of all fractions
u_{rms}	root mean saquare velocity
$U_{w,crsf}$	critical wave velocity for sheet flow inception
$u_{w,max}$	maximum onshore wave velocity
$u_{w,min}$	minimum onffshore wave velocity
v_j	ensemble averaged velocity of jth fraction

v_k	ensemble averaged velocity of kth fraction
v_{kj}	relative velocity of ensembel averaged velocity of particles k and j
$w_{s,j}$	settling velocity of j-fraction sand
z_0	bed level for reference concentration
$\hat{a}$	excursion amplitude for the whole flow period
$\hat{u}_i$	orbital velocity amplitude in crest/trough
$\hat{u}_{off}$	offshore velocity
$\hat{u}_{on}$	onshore velocity
$\overline{U_1}'$	complement phase-averaged velocity for the first fraction
$\overline{U_2}'$	complement phase-averaged velocity for the second fraction
$\overline{U_3}'$	complement phase-averaged velocity for the third fraction
$\overline{U_i}'$	complement phase-averaged velocity for the ith fraction
$\overline{U}$	phase-averaged of time-averaged velocity
$\tilde{u}_{i,r}$	root mean square velocity of a sinusoidal flow with amplitude of $\hat{u}_i$

1 Introduction

Sandy beaches are the main human access to coastal waters, where the land areas are protected against sea climate and storm surges. This natural advantage in addition to the economical importance and recreational significance have made the sandy beaches as the most important areas in countries with coastal cities. However, the beach erosion as a result of sea and land interaction is one of the most significant threatening issues for sandy beaches. Moreover, intensified climate change effects in recent years have increased the frequency of storm surges, which pronounce the erosion problem and increase the coastal flooding risks (Muis et al., 2016).

To protect the public and assets along the beach against storms, at a first glance the hard constructions made of reinforced concrete were suggested and build like seawalls (Fig. 1.1) to manage the coastal zones and reduce the risks of storm impacts. However, these types of sea defense measurements could not fulfill the planned objectives for a sustainable coastal management. As an example, the scouring at the toe of these structures due to the strong vertical currents after breaking of water waves on structures, has reduced their stability and consequently resulted in significant impairments to the defense structures as well as infrastructures behind these structures. Moreover, expensive reparation costs after storms to return them to the conditions before the damage might not always be successful. In cases of not affected and stable parts of these structures, the water-waves induced up-rushing jets on these structures could increase the financial as well as life damages behind of these structures, which is a research field to improve the efficiency of these hard/gray measurements (Shiravani et al., 2014).

On the other hand, construction of hard sea defense structures have been lead to the restriction of human access to the beach as one of the most important economical resource for the population living along the shoreline. This importance could be a high economical loss, when for example \$3.1 billion were spent annually by 11 million tourists and visitors along the Gold Coast beaches in Australia (Jackson et al., 2017). This importance for the coastal areas can be enhanced, when the Staatsbad Norderney on the Island Norderney (with population around 6000) reported the number of overnight tourists as 3.8 million stayed and 260,000 as daily visitors in year 2019 (Norderney Jahresbericht, 2019).

Therefore, beach (re)nourishment is introduced as the sediment-based protection also referred to as soft structures (Pörtner et al., 2019) to solve the beach erosion and remedy the hard engineering impacts for a sustainable coastal management (Fig. 1.1).

Figure 1.1: Shoreline protection against erosion. Left: Mega beach nourishment (sand motor), the Delfland Coast, the Netherlands (https://dezandmotor.nl/fotos-en-videos/). Right: Seawall at La Crabiere, St. Ouen's bay, Jersey, Photo: Oliver Dixon.

Due to the many advantages of beach (re)nourishment, such as a favorable place for tourist activities and leisure facilities as well as ecological consistency with nature, it has been accepted as a popular coastal zone management measurement for beach protection against erosion. Available studies on the frequency of the beach (re)nourishment worldwide from different point of views (e. g. Staudt et al. (2021)) depicts the popularity of beach (re) nourishment, which is also classified among practices recognized as *building with nature* solutions.

Cross-shore erosion under storm conditions is one of the most important problems for intact sandy beaches as well as (re)nourishment sand transported to the beach to compensate the sand in eroded locations of shorelines. It is supposed that under storm conditions the near bed velocity is increased enough to mobilize the sands in highly concentrated thin layers (in a few centimeters based on the experiments of O'Donoghue and Wright (2004a)) near the bed, which are known as sands in sheet layers or sheet flow sand transport. To overcome this problem and retrofit the sandy beaches in a sustainable and environmentally friendly way, a comprehensive knowledge on the eroding components (e.g. random sea waves) as well as sediment parameters (e.g. grain size distribution) is required.

One of the sustainable solution to reduce the erosion volume of sands under storm condition is to retrofit the erosion-prone zones with appropriate sand mixtures within beach (re)nourishment. However, to the best knowledge of the author, a detailed guideline/manual, which can recommend the optimum sand mixture based upon the hydrodynamic as well as morhphodynamic conditions is yet not available. To understand the physics behind the sand transport mechanisms under sheet flow conditions, an extensive experimentally (e.g. O'Donoghue and Wright (2004a) and Schretlen (2012)) as well as numerically (e.g. Kranenburg et al. (2013) and Cheng et al. (2017)) research has already been performed, but due the complexity of mixed sand dynamics, the available studies on the mixed sand transport are rare. Moreover, because of this theoretical complexity, available studies on the mixed sands transport under sheet flow conditions are limited to small- or large-scale experiments (e.g. Hassan and Ribberink (2005) or Van der Werf et al. (2019)).

Available modification coefficients (e.g. Egiazaroff (1965) or Day (1980)) to adapt the (semi-) empirical transport rate equations for uniform sand transport prediction to mixed sands are such investigations on the mixed sands, where could not accurately represent the mechanisms of mixed sand transport under sheet flow conditions (e.g. interparticle interactions), and therefore the knowledge gaps on understanding the mixed sand transport mechanisms under sheet flow conditions are still open and require further investigations (Van Rijn, 2007). The worth and importance of the research on this subject is the capability of mixed sand property on the erosion mitigation under storm conditions. This erosion mitigation capability was observed in experimental studies of Hassan and Ribberink (2005) up to ten times compared to uniform sand (Fig. 1.3).

The extensive experimental and numerical studies on nearshore hydrodynamics and exposed morphodynamics show the complexity of water waves interaction with sandy beaches. These investigations have contributed to improve the available knowledge on influencing parameters. However, due to the complexity of problem and required simplifying assumptions, proposed methodologies lead to over-/under-estimated predictions. Moreover, a significant part of recommended formulas for sediment transport in coastal engineering tools emanates from the river induced transport formulas, and hence neglect the determining parameters in both hydrodynamics (e. g. wave periodicity) and morphodynamics (e. g. bed forms).

1.1   Motivations

While long-shore sediment transport and its effect on the evolution of the shoreline are relatively well-understood, several knowledge gaps related to cross-shore sediment transport, especially under sheet flow conditions, still remain despite the considerable number of research studies in the last decades.

Cross-shore sediment transport may occur under three basically different regimes (Karambas, 2003):

- transport under sheet flow, i.e. flow with high velocity near the bed (Shields parameter$(\theta) >$ 0.8-1 (Dohmen-Janssen et al., 2002)) that washes out all bedforms and results in a plane bed flow with large volumes of erosion,

- transport under rippled-bed flow, i.e. a moderate flow velocity regime where bed ripples can appear, and

- bed load transport, i.e. the flow is large enough to move the bed sediment, but too weak for a ripple-bed to form, so that a plane-bed flow results.

Particularly for a sheet flow regime more investigations are required due to its following properties: (i) sheet flow essentially occurs in relatively shallow waters within the nearshore zones, especially in the outer surf zone and the swash zone (Fig. 1.2) (Fromant et al., 2019), (ii) large shear stresses are associated with the sheet flow transport regime which result in high volume sediment transport (Dohmen-Janssen et al., 2001), (iii) presence of coastal structures in sheet flow dominated transport regions like breakwaters, groins and sea walls, and (iv) sheet flow represents the major cross-shore sediment transport mode within tsunamis and severe storms like hurricane-induced storm surges (Yeh and Wenwen, 2008).

Due to complex interactions among near-bed transporting sediment grains in strong velocities (sheet flow) as well as their interactions with carrier flow, most of available experimental and numerical studies simplify or neglect some significantly important mechanisms in sheet flow transport regime. For instance, a significant number of systematically conducted experiments to study the sheet flow transport have been performed in small-scale Oscillatory Flow Tunnels (OFTs). OFTs are not able to simulate the vertical transport mechanisms under real surface waves. Moreover, after performing significantly rare experiments in large wave flumes like Grosser Wellenkanal (GWK)(Schretlen, 2012), it was understood that another determining transport mechanism which is referred as boundary layer streaming, a wave boundary layer current produced by means of vertical momentum transport in the direction of the progressive waves, is also neglected in available small-scale OFT experiments (Kranenburg et al., 2013). Therefore, resulted practical formulas to predict the sediment transport rate under natural sheet flow transport conditions are strongly over- or underestimated. Sediment non-uniformity in aforementioned mechanisms could increase the complexity of problem and hence it was not considered in detailed during past decades. Restriction of this property in sediment transport to empirical hiding/exposure coefficients by critical shear stress is a simple way to include it in transport formulas. On the other hand, one of the most significantly influencing parameters on reducing the sandy beach erosion is the stability performance of sand fractions during storm surges.

Fig. 1.3 shows the results of the OFT experiments of Hassan and Ribberink (2005) using mixed/graded as well as uniform sands under the same hydrodynamic condition, which represents storm surges (sheet flow transport regime). As can be seen, the erosion rate of graded sands under strong near-bed velocities is around ten times smaller than erosion rate
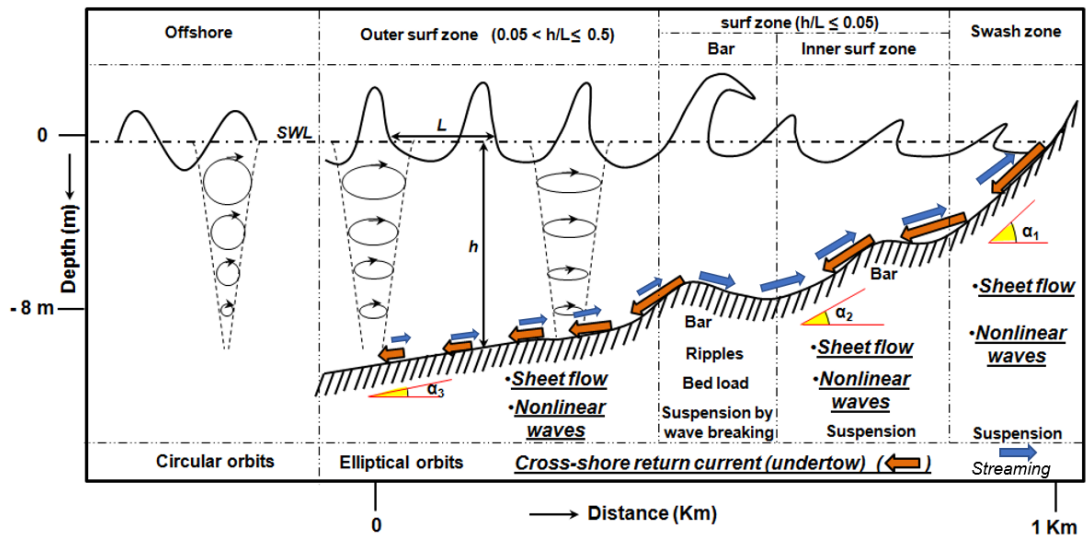
Figure 1.2: Sheet flow sediment transport and wave nonlinearity along a cross-shore profile (modified from Hassan (2003) and Peters (2003)).

of uniform sands under same wave conditions. However, due to the weaknesses of small scale OFT experiments, which are more intensified under storm-surge conditions (Wong, 2010) large scale experiments in large wave flumes like the GWK (e. g. experiments of Van der Werf et al. (2019)) could help to understand the role of different graded sands in reducing the erosion rate. Moreover, to the knowledge of the author, there are no recommendation in coastal handbooks about characteristics of appropriate sand for nourishment of eroded areas to reduce the sand lost under next storm surges. Therefore, this study will try to improve the available knowledge on transport of graded sands under storm surges and help to understand the contributing transport mechanisms of mixed sand transport under sheet flow conditions.

Furthermore, most available coastal structures have been constructed in areas before or after the breaking line, where the dominant transport mode due to the nonlinearity of approaching waves is sheet flow. Sedimentation and erosion are main problems of these structures during the storm surges. Therefore, a better understanding of the sheet flow transport mechanisms will improve the accuracy of predicting practical formulas for cross-shore sediment transport rate, and consequently the optimum position for construction of coastal structures. Moreover, due to the dominance of sheet flow transport regime under extreme wave climates such as tsunamis or hurricanes and weaknesses of available predicting numerical tools (e.g. XBeach, Roelvink et al. (2015)), a detailed study on the structure of sheet flow layer is necessary to provide more accurate formulas and hence improve the results of available numerical predictions.

The main objective of this research is to study the interparticle interactions within sand grains in mixed sands and develop a new formula based on the available experimental results, prediction formulas and new developed and applied approach for mixed sands. Therefore, the analysis of available data on mixed sands and examination of proposed predicting formulas play an important role for new developments. Moreover, the fine scale numerical tool to follow the transport mechanisms will provide the possibility of extending the experimental dataset to a wide numerically new generated dataset.

The development of a new CFD-numerical tool for mixed sands is performed by means of
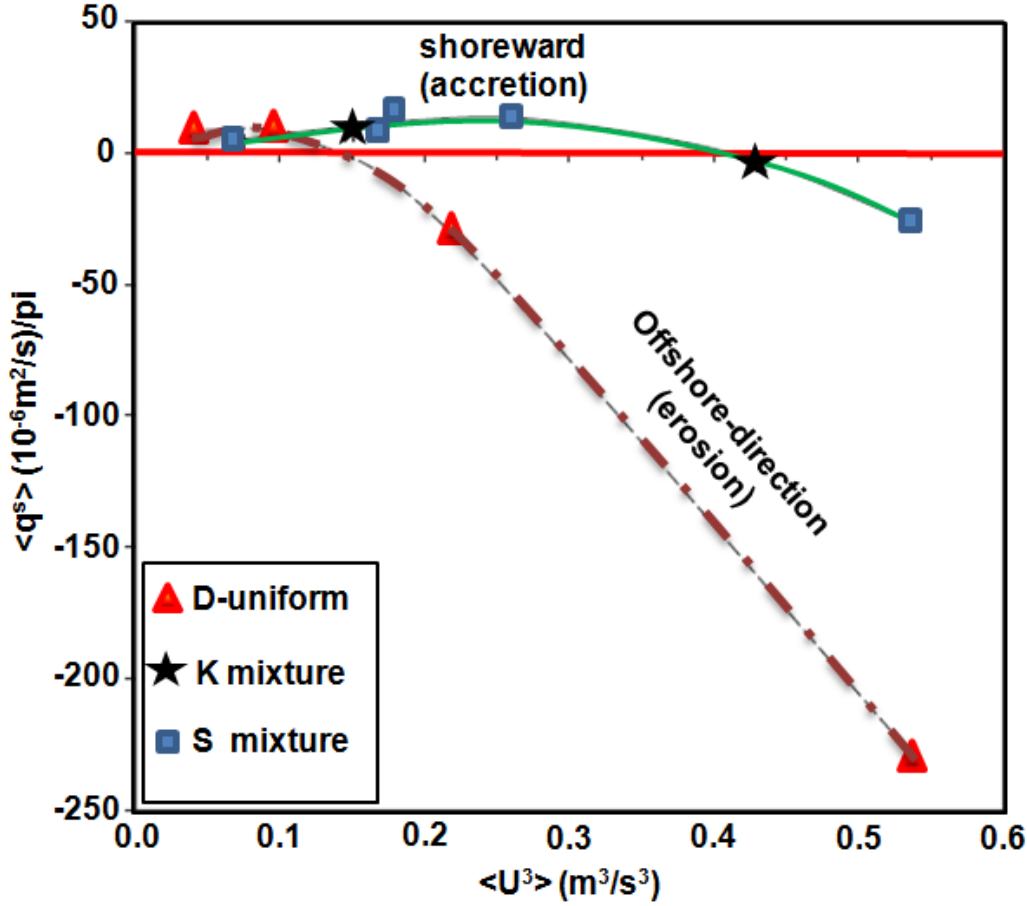
Figure 1.3: Comparison between net transport rates of fine sands (D_{50}=0.13 mm) being part of a sand mixture ("S-mixture": 60% of D_{50}=0.13 mm, 20% of D_{50}=0.34 mm and 20% of D_{50}=0.97 mm, "K-mixture": 50% of D_{50}=0.21mm and 50% of D_{50}=0.32mm) and in a uniform fine sand ("D-uniform") under velocity skewed waves ($a = u_{max}/(u_{max} + |u_{min}|)$=0.65) of wave period $T = 6.5$ s (modified from Hassan and Ribberink (2005)).

an available OpenFOAM solver for uniform sand under sheet flow condition sedFoam of Cheng et al. (2017).

The newly developed solver (mixedSedFoam) is different than the available(sedFoam) in following quantitative points:

- computation of the sand concentration is found after finding the fractional concentrations for each constituting sand fraction by means of the modified mixture approach of Manninen et al. (1996).

- the new developed iteration loop to find the velocity of each sand fraction using interparticle interactions is called in each time step of the available solver.

- the results of the available solver for sediment concentration and consequently velocities are computed based on the new results for volume fractions of both sand and water phases, and hence the new developments are coupled with the available solver.

To understand the sheet flow transport mode and role of the sediment non-uniformity in

these mechanisms current study is conducted to cover the following objectives:

1.2 Objectives and Methodology

The primary objective of this thesis is to provide a well validated numerical tool for mixed sand transport modeling and therefor improve the knowledge of the mixed sand transport mechanisms under sheet flow conditions. Moreover, due to the requirement of the available measurement results for calibration and validation of the developed model, a unique knowledge base from available measurements on the mixed sand transport under sheet flow will be provided. To evaluate the available formulas, an intercomparison of their results with the gathered dataset will also be performed, where the incapability/capability of available formulas will be illustrated. This overall goal can be broken down into the following described objectives as also is illustrated in Fig. 1.4.

- extension of a systematic state-of-the-art review based on the analysis of available knowledge from experimental and numerical studies on sheet flow sediment transport

- reanalyzing the available OFT data for sheet flow sediment transport

- calibration and validation of an extended two-phase numerical model which takes the grading effect into account

- conduct a systematic parameter study using the validated numerical model to extend the range of tested conditions.

These objectives comprise the structure of this thesis and each chapter discusses and researches to find and solve the corresponding knowledge-gaps in sheet flow sediment transport.

1.3 Outline

Chapter 2 investigates the principals of sand transport in general and finally reviews the available aspects and formulas for sheet flow transport inception. Chapter 3 gathers the available experimental data from different OFTs and compares the predicted transport rates using various (semi-)empirical equations with the measurements as well as intercomparision of predictions by means of available formulas. Finally, it is tried to understand the behavior of formulas based on the gathered datasets, and develop the most accurate predicting formula in such a way to consider and describe better the mixed sand transport mechanisms. Chapter 4 investigates the fine scale two-phase flow model equations and provides a new equation, which estimates the interparticle drag force better than the available formula of Syamlal (1987). Finally, the model results are compared with the detailed measurements of O'Donoghue and Wright (2004a) for bi-and tri-modal mixed sands and illustrates the limitation as well as capabilities of the developed model. In chapter 5, the calibrated and validated model in chapter 4 is run for different mixtures of a mixed sand to parameterize the role of non-uniformity in the mixed sand transport mechanisms and control the developed formula based on the intercompered formulas and experimental data in chapter 4. Chapter 6 summarizes the achievements in this research and suggests the new research possibilities for further investigations.

Ch.2: *Literature review and state-of-the-art:*

Main tasks:
- ➢ Detailed review and comparison of published studies from small scale, large scale and field experiments on sheet-flow sediment transport.
- ➢ Comparative review of available numerical models and experimental data on sheet-flow sediment transport.

Main outcomes:
- ✓ Underlined knowledge-gaps in available experimental data and weaknesses in numerical approaches for sheet-flow sediment transport.
- ✓ Identified available experimental data and practical formulas for Ch.3 as well as numerical equations/solvers for Ch.4.

Ch.3: *Selection and re-Analysis of OFT data:*

Main tasks:
- ➢ Re-analysis of available experiments performed on graded-sands under nonlinear waves induced sheet-flow conditions.
- ➢ Comparison of predicted results using reviewed practical formulas in Ch.2 with re-analyzed experiments for graded-sands.

Main outcomes:
- ✓ Well-organized experiment data base of graded sands under nonlinear wave induced sheet-flow for calibration/ validation of numerical model in Ch.4.
- ✓ Detailed measurements data of concentrations and velocities for sand fractions in sheet-flow layer.

Ch.4: *Development and validation of an extended 3D two-phase Eulerian numerical model:*

Main tasks:
- ➢ Development of abovementioned model by OpenFOAM® based on modified equations and proposed solvers in Ch.2.
- ➢ Model calibration and validation by means of organized data in Ch.3.

Main outcomes:
- ✓ A robust 3D validated model which accounts for: (i) the multi interaction of sands and fluid, (ii) reproduction of the hydrodynamics and morphodynamics characteristics of graded sands transport under sheet-flow conditions; ready for parameter study in Ch.5.

Ch.5: *Systematic parameter study*

Main tasks:
- ➢ Extend the range of numerical experiments for sediment non-uniformity by means of developed model in Ch.4 for different mixtures of sand fractions.
- ➢ Reproducing the corresponding hydro- /morpho- dynamics characteristics for different graded sands under the same wave nonlinearity.
- ➢ Comparative analysis of net transport rate of different graded sands under the same wave nonlinearity to understand the effect of sediment non-uniformity.

Main outcomes:
- ✓ Understanding the role of sediments non-uniformity on the transport rate by intercomparison of calculated parameters for different graded sands.
- ✓ An enriched numerical database for graded sands parameters under nonlinear waves within sheet-flow condition.
- ✓ A new practical formula to improve the prediction of graded sands transport rate.

Figure 1.4: Structure of this thesis.

2   State-of-the-art review

A large number of formulas have been proposed for sediment transport rate prediction accounting for the nearshore characteristics (e.g. Van Rijn (1993)). However, most of them emanate from the particular experimental and field data, and hence they are not capable of covering a wide range of applications. Moreover, a significant number of applied experimental data in calibration and validation of these formulas comes from experiments, which simplify the characteristics of nearshore hydrodynamics (e.g. 1D oscillatory flow for progressive waves modeling) and morphodynamics (e.g. uniform sands for non-uniform sandy beaches).

Fig. 2.1 compares schematically the U-tube Oscillatory Flow Tunnel (OFT), where many of available data cited by Van der Werf et al. (2009) originate from, with field conditions of sandy beaches. As can be seen, the 3D flow velocities are simplified to a 1D flow velocity and hence the vertical and cross-sectional components of sediment transport are neglected. Moreover, due to the absence of the wave propagation in OFTs, streaming, which is an onshore directed current induced by non-orthogonality of vertical and horizontal orbital velocities under real surface waves is not reproduced in OFT experiments. This cannot only contribute into the amount of transported sands, but also might change the transport direction (Dohmen-Janssen and Hanes (2002), Naqshband (2009), Wong (2010), Schretlen (2012), and Kranenburg et al. (2013)).
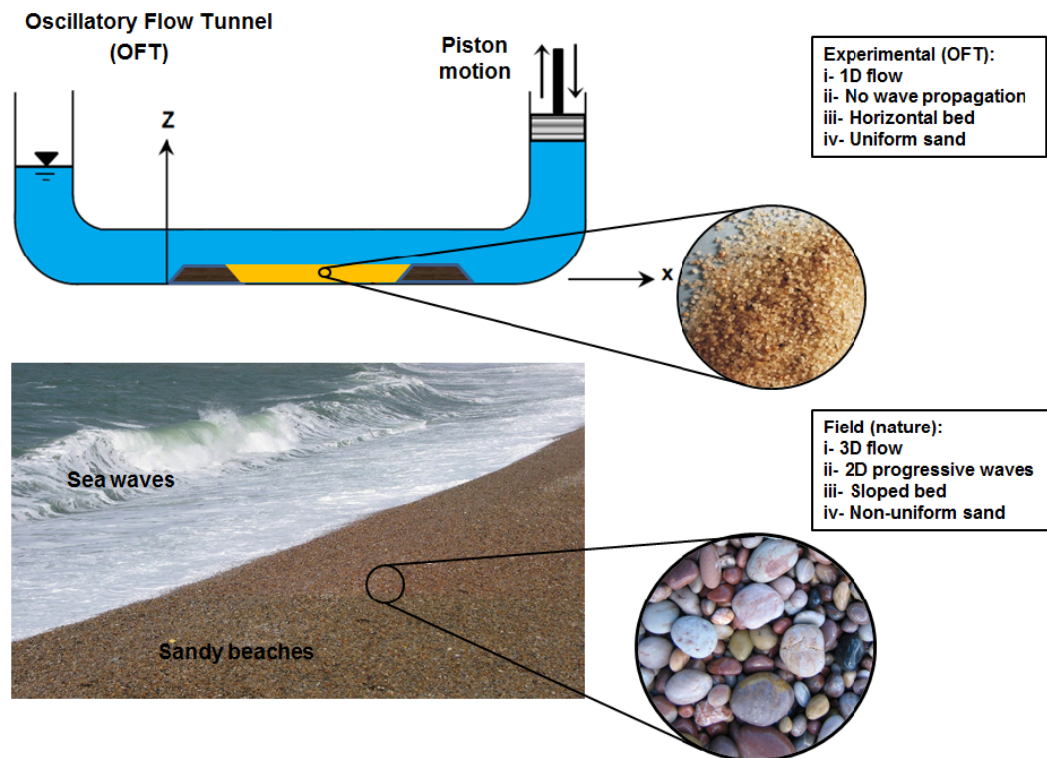
Figure 2.1: Comparison of hydrodynamic and morphodynamic properties of the simulated experiments by OFTs with natural filed conditions.

The effects of the beach slope and bathymetry are also omitted in OFT experiments and therefore leads to excluding the undertow effect. Undertow is an offshore oriented return

flow, which is induced by hydrodynamic balance forces between water bodies before and after wave braking (Hansen and Svendsen, 1985). It is known as the main eroding component at the surf-zone under field conditions. As a result, researchers tried to mimic the undertow in OFTs by superimposing the currents in opposite direction of oscillatory motion, but they were not able to reproduce its behavior similar to filed/naturally conditions (Van der Werf et al., 2009). Furthermore, most of sediments applied in OFTs have been uniform sands, whereas the natural sands of beaches are non-uniform; comprised of various fractions of uniform fine, medium and coarse sand. Uniform fine sand due to their low weights in comparison with medium and coarse sand can be resuspended to higher levels of the water column and therefore require longer time to settle back. This property of fine sand, which is referred as the phase-lag effect, causes a substantially different behavior of fine sand compared to coarse and medium sand (Dohmen-Janssen, 1999). Moreover, present fine sands in a non-uniform sand mixture are usually hidden among other fractions and hence experience a lower force to transport (Hassan, 2003). In contrast, coarser fractions in non-uniform sand are exposed to higher hydrodynamic forces and hence are transported easier than the time that they are uniform. Fig. 2.2 illustrates this mechanism for non-uniform sands schematically. It can be seen, hidden fine sand not only are protected with coarser fractions, but also serve as a lubricating factor in reducing the internal frictional forces among coarser sand (Schendel, 2018).
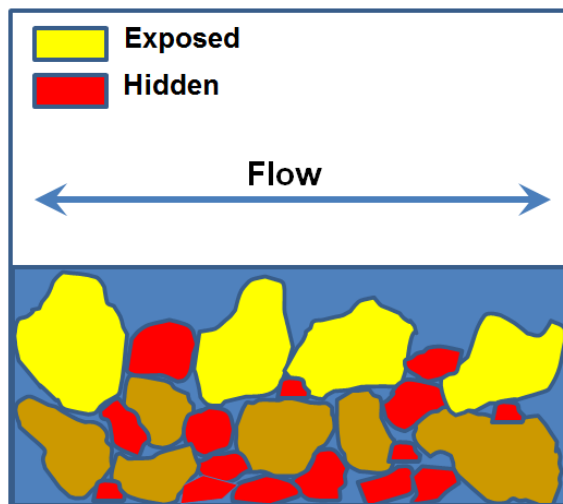
Figure 2.2: Principle sketch of hiding/exposure effect within graded sands (illustrated using yellow, red, and brown colors. The blue color is the void space of the sand mixture, which is filled with water).

The importance of aforementioned influencing parameters, which are simplified and neglected in OFT experiments, is pronounced by increasing the flow energy under storm surges (Naqshband, 2009). However, experimental and numerical studies on non-uniform sands are significantly rare (Van der Werf et al., 2009). In addition, available studies on non-uniform sands have been performed through OFT experiments, which are incapable of including real surface wave characteristics (e.g. streaming).

To address the weaknesses of OFTs and understand the effects of vertical velocity under progressive waves, Ribberink et al. (2001) and Dohmen-Janssen and Hanes (2002) performed the first large flume scale experiments in the Grosser Wellenkanal (the GWK) of

the Forschungszentrum Küste (FZK). Large wave flumes like the GWK, are able to reproduce 2D orbital motions and 1D wave propagation. Therefore, they can overcome the fundamental weaknesses of OFTs, particularly streaming effect and undertow current. These experiments were performed over a horizontal bed composed of medium sand (D_{50}=0.24 mm) and revealed that the transport rate is about 2.5 times larger than measured ones in OFT. To approve this importance and understand its effect on fine sands, Schretlen (2012) conducted the experiments for both fine (D_{50}=0.138 mm) and medium (D_{50}=0.245 mm) sand in the GWK and compared the measured results with OFT experiments under same wave conditions. It was observed that for medium sand like experiments of Ribberink et al. (2001) the transport rate is larger than that of OFT experiments and for the fine sand, not only the transport rate, but also the transport direction is different (onshore in the GWK compared to offshore in OFT). These differences were mainly arisen from the presence of streaming within the GWK experiments under progressive surface waves, which is absent in OFT experiments.

2.1 Inception of sediment movement

Before to discuss the different sediment transport modes, it might be important to know when sediments under oscillatory flows become unstable, entrained to the water column and finally are transported. To answer this fundamental question, it is reasonable to consider a system of affecting forces on a spherical assumed sediment particle as depicted in Fig. 2.3. Following the approach of Fredsøe and Deigaard (1992), the forces balance equation in horizontal direction is written as:

$$\sum_{i=0}^{n} \boldsymbol{F}_i = 0$$

$$\frac{1}{2}\, \rho_w C_D A_P (\alpha U_*)^2 = \mu_N (\rho_s - \rho_w) \forall g \qquad (2.1)$$

$$\frac{1}{2}\, \rho_w C_D (\frac{\pi D^2}{4})(\alpha U_*)^2 = \mu_N (\rho_s - \rho_w) \frac{\pi D^3}{6} g$$

where ρ_w and ρ_s are water and sand density respectively, C_D the drag force coefficient,
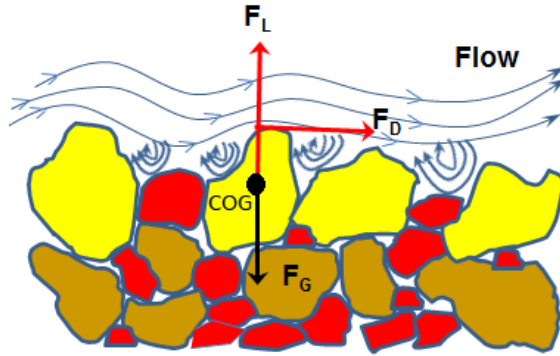
Figure 2.3: Drag (F_D), lift (F_L) and gravitational (F_G) forces on a sediment particle among a mixed sand with yellow, red, and brown fractions exposed to carrier flow.

A_P the projected area in front of the flow direction, U_* is the friction velocity near the bed, α the dimensionless factor to describe the friction velocity above the bed, μ_N the friction

coefficient, $\forall$ the volume of sediment particle and g is gravitational acceleration.

If we neglect the shape of sediment particles and simplify them as spherical grains, D is the diameter of sand grains and considered as median grain size(D_{50}) of sand. Using algebraic simplification, Eq. 2.1 is expressed as:

$$\frac{U_*^2}{(s-1)gD_{50}} = \frac{4\mu_N}{3C_D\alpha^2} \tag{2.2}$$

where s is the specific density of sediments($s = \rho_s/\rho_w$).

The left hand side of Eq. 2.2 is referred as the Shields parameter. C_D in the right hand side of Eq. 2.2 is drag coefficient and obtained by means of experimental graphs (Fig. 2.9). It is a function of grain shape and the Reynolds number. The Reynolds number is defined as:

$$Re = \frac{U_* D_{50}}{\nu} \tag{2.3}$$

where ν is kinematic viscosity of water. Therefore, the Shields parameter can be evaluated for different sand using the Reynolds number. Shields (1936) performed the first systematical experiments using different sands under various river flow conditions and proposed a graph (Fig. 2.4). The hatched area in this graph shows the area of initiation of motion, where below of this area the sediment grains are stable and above of that the sediments start to suspend and are transported using forcing flow as showed by Van Rijn (1993) in Fig. 2.5.

The threshold for sediment motion is also referred as critical Shields parameter (θ_{cr}) and using the relationship between friction velocity and critical bed-shear stress $\tau_{\mathrm{cr}} = \rho_w U_*^2$, it can be expressed as:

$$\theta_{\mathrm{cr}} = \frac{\tau_{\mathrm{cr}}}{(\rho_s - \rho_w)gD_{50}} \tag{2.4}$$

Van Rijn (1993) represented the θ_{cr} as a function of non-dimensional grain size (D_*), which is defined as:

$$D_* = d_{50}\sqrt[3]{(s-1)g/\nu^2} \tag{2.5}$$

and

$$\theta_{cr} = \begin{cases} 0.24\ D_*^{-1} & \text{if } 1 < D_* \leq 4 \\ 0.14\ D_*^{-0.64} & \text{if } 4 < D_* \leq 10 \\ 0.04\ D_*^{-0.1} & \text{if } 10 < D_* \leq 20 \\ 0.013\ D_*^{0.29} & \text{if } 20 < D_* \leq 150 \\ 0.055 & \text{if } D_* > 150 \end{cases} \tag{2.6}$$

Fig. 2.6 shows the critical bed-shear stress using D_* represented by Van Rijn (1993). To define the Shields parameter as a function of flow velocity (U) instead of the frictional velocity (U_*), the bed-shear stress on the sediments could be defined through drag force as:

$$\tau = \frac{F_D}{A_s} = \frac{\frac{1}{2}\rho_w C_D A_P(\beta U)^2}{A_s} = \frac{1}{2}\rho_w(C_D\frac{A_P}{A_s}\beta^2)U^2 = \frac{1}{2}\rho_w f_b U^2 \tag{2.7}$$

where β is the velocity coefficient to define velocity near the bed using depth averaged velocity and f_b is referred to as friction factor near the bed.
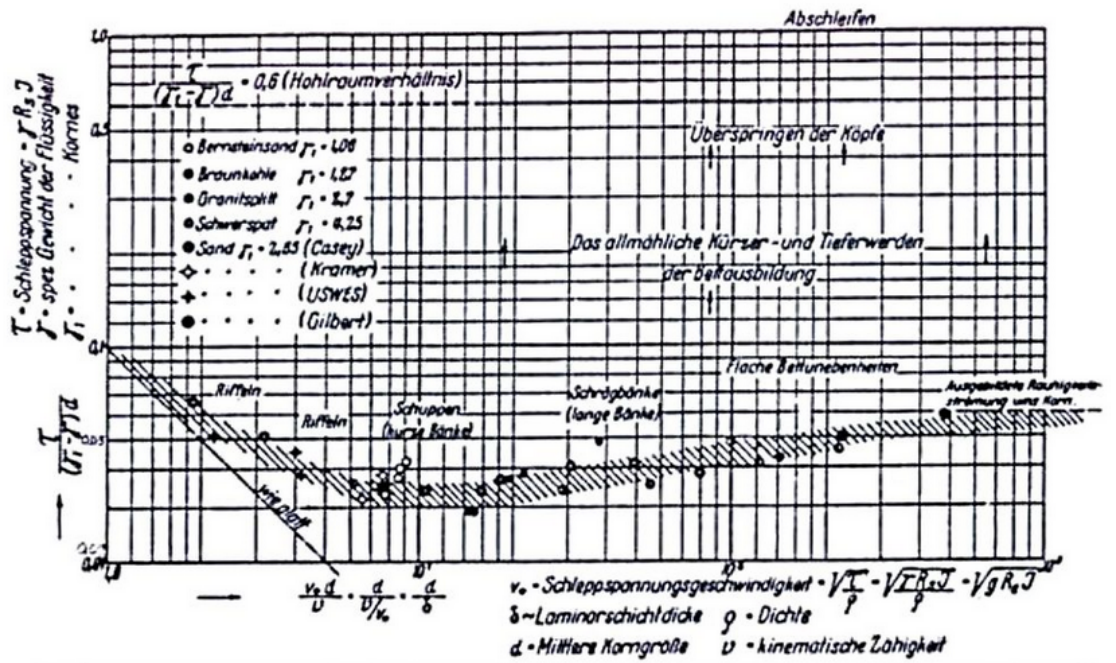
Figure 2.4: Original Shields (1936) diagram.
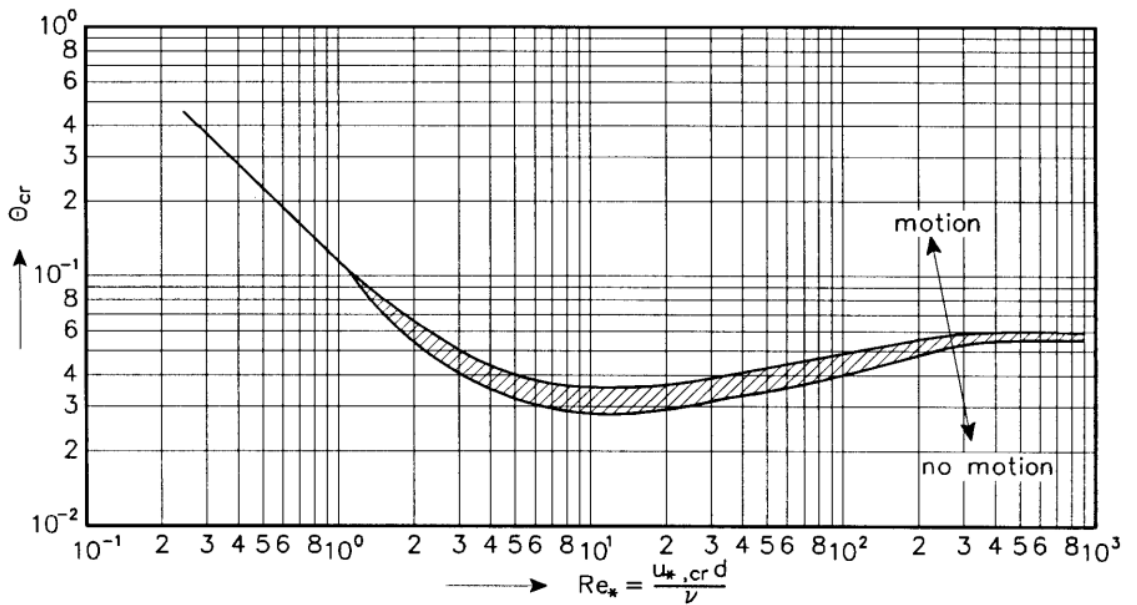
Figure 2.5: Re-drawn Shields diagram by Van Rijn (1993) .
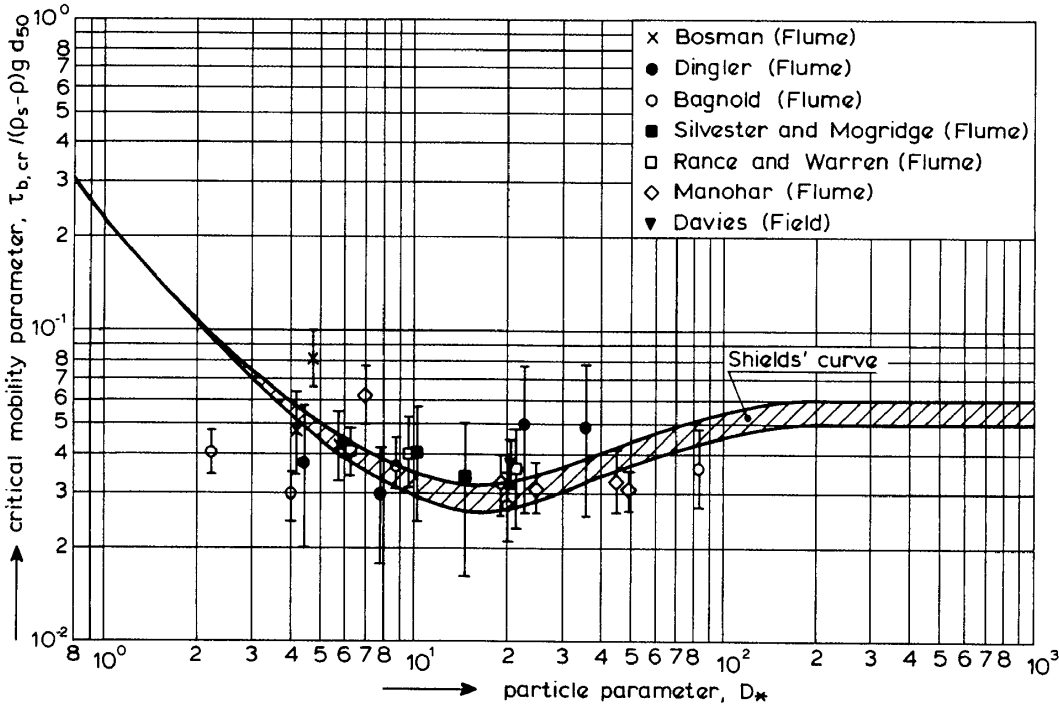
Figure 2.6: Re-drawn Shields diagram by Van Rijn (1993) based on D_* (Eq. 2.6).

The friction factor can be defined using the Chézy friction coefficient for open channel and river flows as:

$$f_b = \frac{2g}{C_{ch}^2} \tag{2.8}$$

where C_{ch} is the Chézy friction coefficient and is given as:

$$C_{ch} = 18 \; log(\frac{12h}{k_s}) \tag{2.9}$$

where h is the water depth and k_s is the bed roughness height. However, instead of applying the depth-averaged velocity and the Chézy friction coefficient, which assumes a logarithmic profile for velocity within the whole water column, it is recommended to define a bed boundary layer with arbitrary thickness of δ in such a way that the velocity only in this near bed layer is logarithmic (Ribberink, 1998). This 'near-bed' approach has a more general validity than the 'depth-averaged' approach, since non-uniform and/or non-steady flows are not necessarily excluded. Therefore, the bed-shear stress is written as:

$$\tau = \frac{1}{2}\rho_w f_b u_b^2 \tag{2.10}$$

where

$$f_b = 2\left(\frac{\kappa}{ln\frac{\delta}{z_0}}\right) \tag{2.11}$$

and κ is the von Kármán constant, which is around 0.4, and z_0 is the bed level, where the velocity is close to friction velocity and was recommended by Nikuradse (1933) as:

$$z_0 = \left(\frac{k_s}{30}\right) \tag{2.12}$$

13
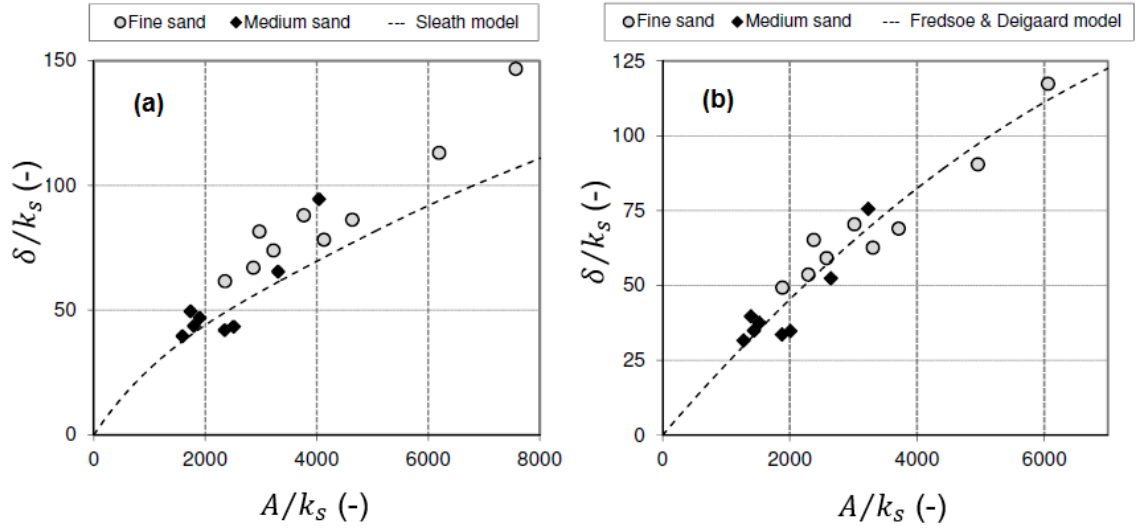
Figure 2.7: Comparison of BBLT of the GWK experiments with (a) Sleath (1987) and (b) Fredsøe and Deigaard (1992) formula (Schretlen, 2012).

where k_s is the bed roughness height and depends on the dominant transport regime. δ is the bed boundary layer thickness (BBLT), which is most often defined as the distance from the instantaneous undisturbed bed to the level of maximum overshoot velocity and u_b is the velocity in the edge of the bed boundary layer.

Sleath (1987) suggested the following empirical formula for BBLT based on their OFT experiments for medium ($D_{50} = 0.2\ mm$) and coarse ($D_{50} = 1.63\ mm$) sands as well as gravel ($D_{50} = 8.12\ mm$) and pebbles ($D_{50} = 30\ mm$) under oscillatory flows with period of 4.5 s and maximum velocities of 0.05-0.7 m/s:

$$\left(\frac{\delta}{k_s}\right) = 0.27 \left(\frac{A}{k_s}\right)^{0.67} \tag{2.13}$$

where $k_s = 2D_{50}$ and A is the amplitude of the oscillatory motion in the free stream and is defined for a sinusoidal wave as:

$$A = \frac{Tu_{max}}{2\pi} \tag{2.14}$$

Using a theoretical approach and suggestion of bed roughness as $k_s = 2.5D_{50}$, Fredsøe and Deigaard (1992) calculated the BBLT for a sinusoidal wave as:

$$\left(\frac{\delta}{k_s}\right) = 0.09 \left(\frac{A}{k_s}\right)^{0.82} \tag{2.15}$$

Schretlen (2012) compared the BBLT of performed experiments in the GWK for two medium ($D_{50} = 0.245\ mm$) and fine ($D_{50} = 0.138\ mm$) sands under regular waves with periods of T=5.0, 6.5 and 7.5 s with A=0.94-2.03 m. It was concluded that the Fredsøe and Deigaard (1992) formula for BBLT shows a good agreement for both fine and medium sands as illustrated in Fig. 2.7.

Swart (1974) represented a formula for bed friction factor under waves (f_w) based on the
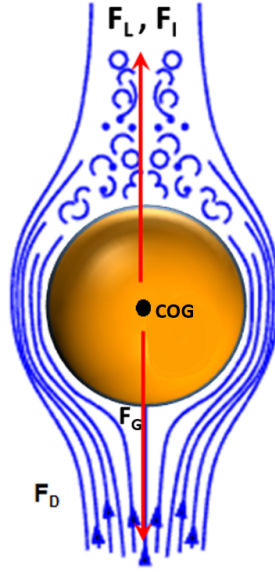
Figure 2.8: Drag (F_D), Lift (F_L) and gravitational forces on a sediment particle.

implicit formula of Jonsson (1967). The Swart (1974) formula is expressed as:

$$f_w = \begin{cases} exp\left(5.213\left(\frac{k_s}{A}\right)^{0.194} - 5.977\right) & \text{if } \left(\frac{k_s}{A}\right) < 0.63 \\ 0.3 & \text{if } \left(\frac{k_s}{A}\right) > 0.63 \end{cases} \tag{2.16}$$

where, k_s is a function of sediment grain size as well as bedform.

2.2 Modes of sediment transport

After sediments have been destabilized and entrained to the water column, the effective forces on a settling sediment particle in vertical direction could be described by drag (F_D), lift (F_L), inertial (F_I) and stabilizing gravitational (F_G) forces as is illustrated in Fig 2.8. Therefore, the degree of instability for a sediment particle exposed to an arbitrary flow condition can be expressed as the ratio between destabilizing and stabilizing forces:

$$\phi_f = \frac{F_D + F_L + F_I}{F_G} \tag{2.17}$$

Assuming that at the stage of instability drag and lift forces dominate the inertia force and consider the sediment grains as spherical particles, Eq. 2.17 can be rewritten as:

$$\phi_f = \frac{\frac{1}{2}\rho_w C_D \left(\frac{\pi D^2}{4}\right) u_{max}^2 + \frac{1}{2}\rho_w C_L \left(\frac{\pi D^2}{4}\right) u_{max}^2}{(\rho_s - \rho_w)\left(\frac{\pi D^3}{6}\right) g} \tag{2.18}$$

where u_{max} represents the velocity amplitude for sinusoidal waves and for second-order Stokes waves is represented as:

$$u_{max} = \sqrt{0.5\ \hat{u}_{on}^2 + 0.5\ \hat{u}_{off}^2} \tag{2.19}$$

where $\hat{u}_{on}$, $\hat{u}_{off}$ represent the onshore (positive) and offshore (negative) velocity components (Schretlen (2012)).

Using algebraic simplifications, Eq. 2.18 can be written as:

$$\phi_f = \frac{3\left(C_D + C_L\right)}{4} \frac{u_{max}^2}{(s-1)gD_{50}} \tag{2.20}$$

where C_D and C_L are functions of the shape and Reynolds number (Fig. 2.9). Shape effects are usually included using a shape factor coefficient in C_D and C_L, which is defined as:

$$s_f = \frac{c_l}{\sqrt{a_l b_l}} \tag{2.21}$$

where s_f is the shape factor and a_l, b_l, and c_l in Eq. (2.21) are lengths of the longest, intermediate and shortest axes of the sediment particle. This shape factor is also known in literature as Corey shape factor (Wu and Wang, 2006).

Therefore, assuming a spherical shape for sediment particles and a turbulent hydrodynamic regime, the first part of Eq. 2.20 is constant and the second part could describe the degree of sediment destabilization, which is written as:

$$\psi = \frac{u_{max}^2}{(s-1)gD_{50}} \tag{2.22}$$

where ψ is referred as mobility number and can be applied to distinguish between sediment transport regimes.

Bagnold (1946) performed the first systematic experiments using an oscillating tray filled with sands, located in a still water tank to understand the bedforms under different transport modes. These experiments revealed that sediments after passing the threshold of movement, roll over the bed and travel for a special distance corresponding to the angular speed ω of tray and finally rest at parallel transverse zones on the bed. Therefore, the bed changes to a wavy bedform with heights of a few grains referred to as ripples. Based on these observations, Bagnold (1946) divided the ripples into two classes:

- rolling-grain ripples

- vortex ripples

Rolling-grain ripples are produced only through rolling of grains without leaving the bed under gentle flow conditions, while within vortex ripples the shedding vortices eject a significant volume of sediments into the water column. Fig. 2.10 shows the mechanism of flow separation and vortex generation leading to sediments ejection into the water column within a vortex-ripple condition.

It is seen that, when onshore-velocity is close to the maximum (point a) a vortex in lee-wake of ripple starts to grow (V1). During the deceleration part of velocity (point b), the generated vortex travels as well as grabs the sediments toward the ripple crest. When it reaches the crest, where corresponds to the flow reversal instant (point c), V1 is a fully developed vortex, ready to leave the ripple, whereas contains sediment to eject them as the suspended load in the water column. Between $t/T = 0.5 - 0.7$, V2 grows, grabs the sand grains and transports them to the ripple crest. However, due to the weaker velocity in trough (corresponding to nonlinear waves) V2 is not as strong as V1. Finally, at the end of the wave period V2 is a fully developed vortex and is ready to leave the ripple and eject the grabbed sediments into water column. Due to significant transport rate
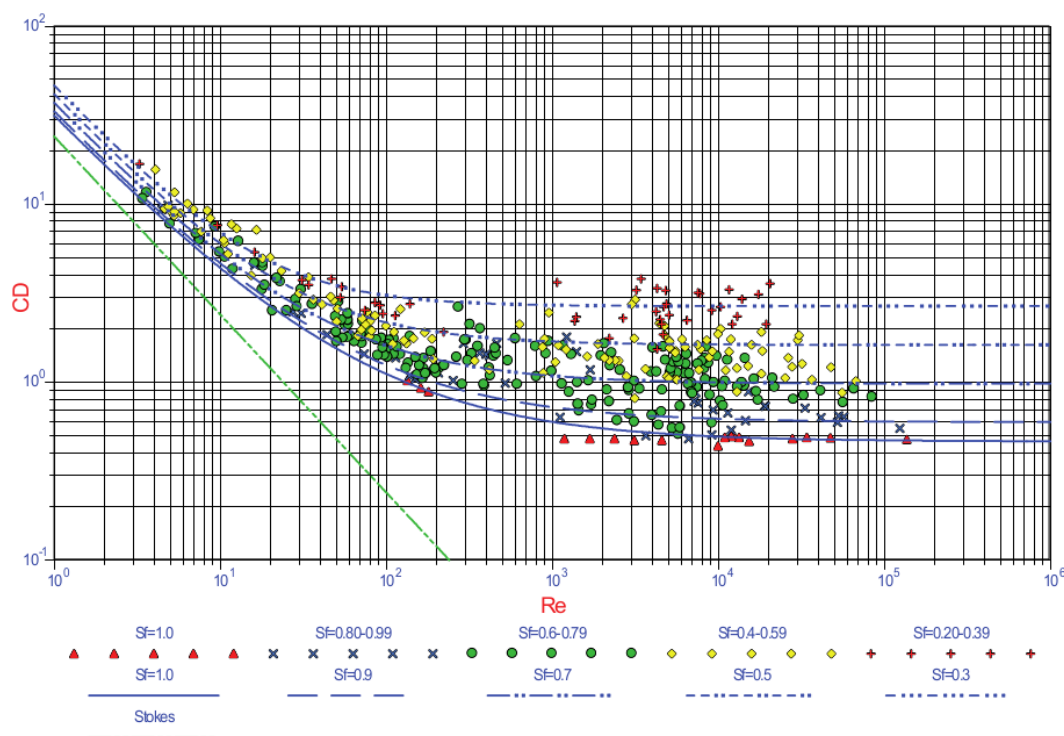
Figure 2.9: C_D for sand with different shapes against the Reynolds number, (Ramsdell and Miedema, 2011).

through vortex-induced ripples compared to rolling-grain ripples, most studies on sediment transport through ripples, are vortex-induced ripples and within this thesis the rippled-bed transport regime means also vortex-induced ripple-bed regime.

O'Donoghue and Clubb (2001) proposed the lower limit of $\psi < 10$ as inception of rippled-bed transport regime. Moreover, O'Donoghue et al. (2006) conducted a wide range of experiments to characterize the bedforms under regular and irregular waves over medium and coarse sands. It was observed that for $10 \leq \psi \leq 190$ the dominant transport mode is rippled-bed flow and for $\psi \geq 300$, the ripples are completely disappeared. This transport mode is referred to as sheet flow, where the bedforms are washed out and bed becomes completely flat. However, for $190 \leq \psi \leq 300$ the transport mode is transient. It was also observed that for regular waves, u_{max} and for irregular waves $u_{1/10}$ reproduce the most accurate prediction of bedform characteristics. These characteristics are important for rippled-bed flows, where the ripple height (η_r) and ripple length (λ_r) play an important role in transport rate predictions. In this sense, sediment grain size (D_{50}) in corresponding mobility number plays an important role in evolution of shape and dimensions of appeared ripples. Fig. 2.11 shows exemplary the bedform evolution during mobility number increasing. As can be seen in Fig 2.11, for coarse sands in rippled-bed flow condition stable 2D ripple bedforms are observed (a, b), whereas for medium sands in rippled-bed as well as transient flow conditions, unstable 3D ripples are appeared (c, d). However, by increasing the flow velocity to reach the sheet flow condition (e) ripple bedforms are disappeared and sheet flow conditions with a flat-bed will be the dominant transport regime.

However, Nielsen (1992) suggested $\psi = 156$ as the upper limit for rippled-bed flow transport mode and, like O'Donoghue and Clubb (2001), $\psi = 10$ as the lower limit for vortex-ripple inception. Due to wider range of reported experiments by O'Donoghue et al. (2006) com-
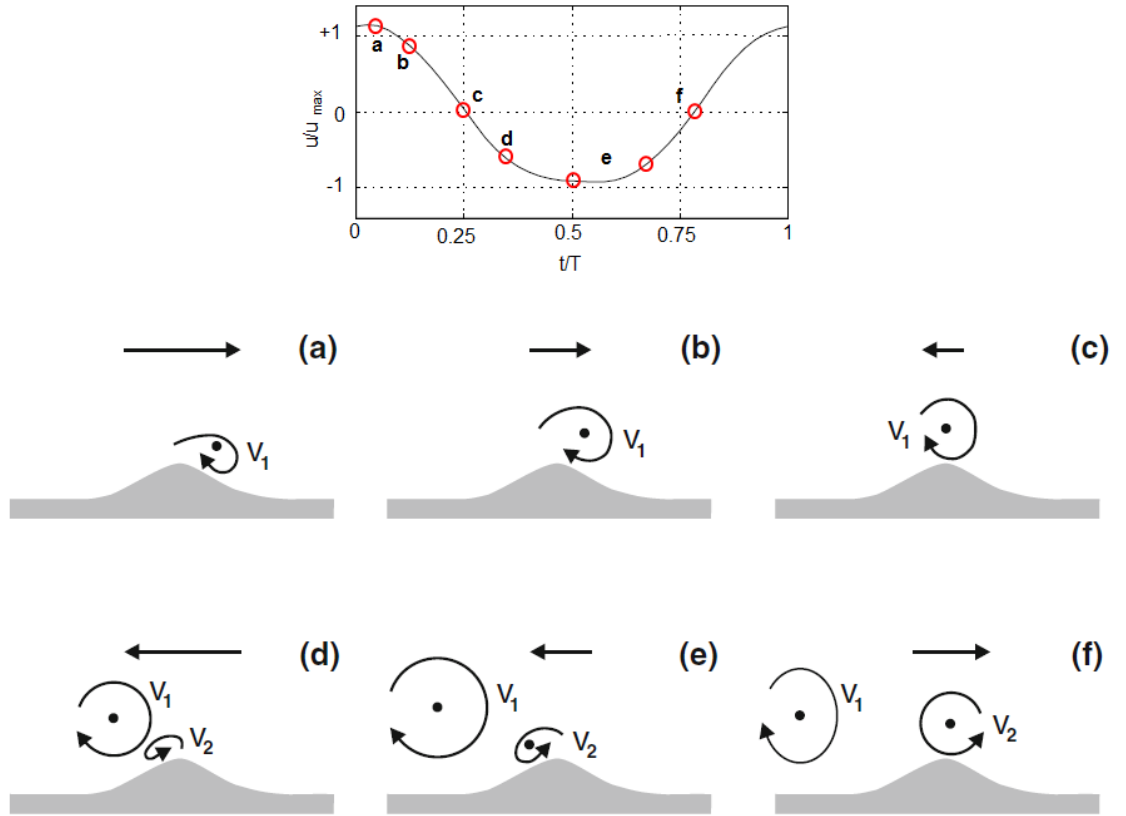
Figure 2.10: Vortex ripples and sediment suspending through vortex shedding (after Thorne et al. (2003) and Ahmari (2012)).

pared to Nielsen (1992) dataset, and including the irregular waves as well as regular waves in O'Donoghue et al. (2006), Schretlen (2012) referred to O'Donoghue et al. (2006) criteria for distinguishing between different sediment transport modes in the GWK. However, Ahmari (2012) proposed a criteria more similar to Nielsen (1992) based on his observation in the GWK (Fig. 2.12). It is seen, that observed bedforms in the GWK by Ahmari (2012) were divided into four classes:

- 2D steep ripples, $\psi \leq 80$

- 2D to 3D ripples, $80 < \psi \leq 120$

- low ripples, $120 < \psi \leq 150$

- plane bed, $\psi \geq 150$.

Therefore, $\psi = 150$ was suggested by Ahmari (2012) as the upper limit for rippled-bed flow condition. This difference with O'Donoghue et al. (2006) could be explained through applied velocity in mobility number equation. The maximum velocity for irregular waves by O'Donoghue et al. (2006) approach is $u_{1/10}$, while Ahmari (2012) used the calculated maximum velocity ($a_b \omega$), where a_b is the near bed amplitude of water particle displacement and ω is the angular velocity ($\omega = 2\pi/T$), where T is the peak-period for irregular waves. It should be noticed that apart from entrained sediments by means of vortex shedding in rippled-bed flow or lifted highly concentrated sand sheets in the sheet flow, rolling and
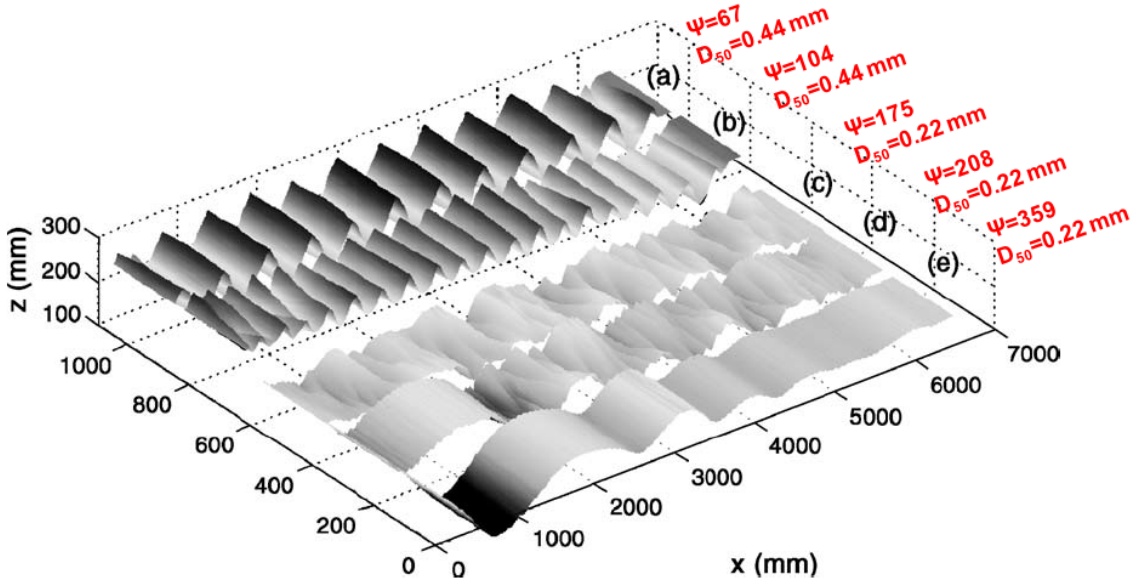
Figure 2.11:   Different bedforms under increasing mobility number (Modified from O'Donoghue et al. (2006).

sliding of sediment particles on the bed-surface are present within both of transport modes. The third mode of transport, which is common between rippled-bed flow and sheet flow, is referred to as bed-load transport mode.

Wilson (1989) suggested that for unidirectional flow, sheet flow occurs when the Shields parameter exceeds about 0.8 and Dohmen-Janssen (1999) suggested the Shields parameter as 0.8-1 for sheet flow inception in oscillatory flow condition. Within sheet flow, sands are transported in vicinity to the bed through highly concentrated sheets with thickness of a few sand grain sizes. Camenen and Larson (2006) compared the available criteria for sheet flow inception with around 300 oscillatory flow experimental dataset and proposed the inception of sheet flow transport mode as:

$$U_{w,crsf} = 8.35\sqrt{(s-1)g\sqrt{D_{50}\delta_w}}(1+r_w) \tag{2.23}$$

where $U_{w,crsf}$ is critical wave velocity in sheet flow inception at the edge of wave boundary layer, δ_w is the Stokes boundary layer thickness ($\delta_w = \sqrt{\nu T/\pi}$) and r_w represents the velocity asymmetry as:

$$r_w = u_{w,max}/(U_w - 1) \tag{2.24}$$

where $u_{w,max}$ is maximum onshore wave velocity and U_w is defined as ($u_{w,max} - u_{w,min}$).

2.3   Bedforms, velocity and concentration

Intercomparison of time-dependent velocity profiles as well as sand concentration and bedforms is important for better understanding the sand transport mechanisms. Fig. 2.13 shows the velocity time series over resulted rippled-bed flow and sheet flow transport regimes recorded by ABS (Acoustic Backscatter System) sensor within the rippled-bed flow (from ripple crest) and the sheet flow conditions at the GWK (Ahmari, 2012). As can be seen, the velocity in rippled-bed flow mode has a weakly asymmetric form in comparison
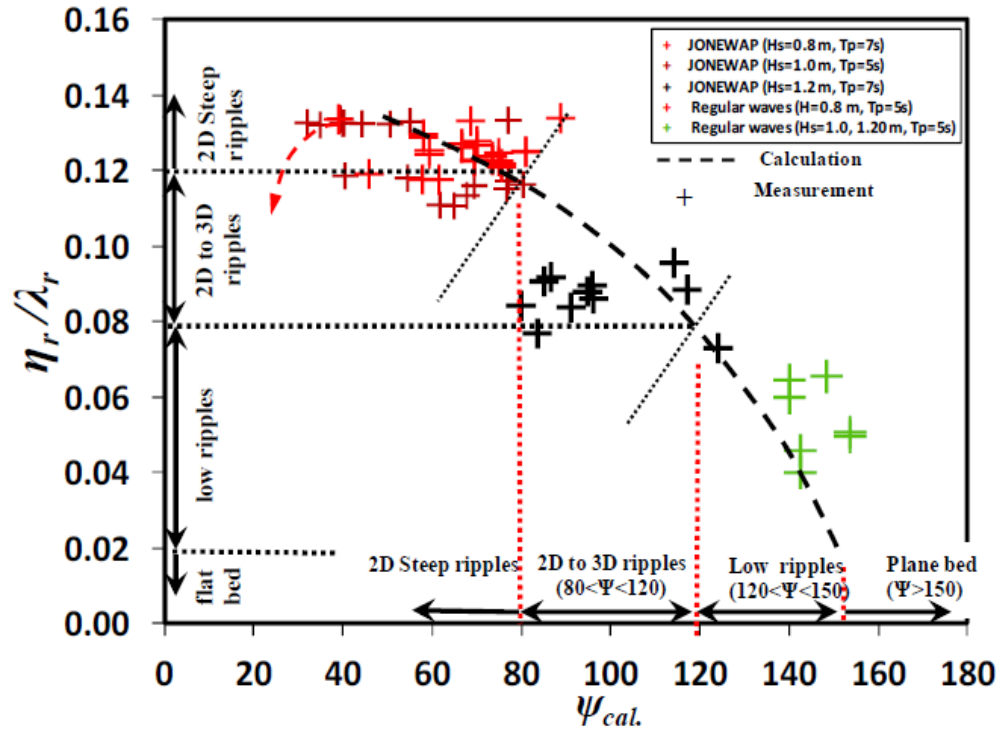
Figure 2.12: Bedform classification versus mobility number (Ahmari, 2012).

to strongly asymmetric velocity in sheet flow condition.

Moreover, the suspended area above the bed level in rippled-bed flow regime is significantly larger than sheet flow condition. However, the highly concentrated layer just close to the bed is thicker within the sheet flow condition. Furthermore, it is seen that the bedform under rippled-bed flow has a 2D ripple form, whereas it is dynamically plane under sheet flow transport mode. This evidence shows that the main transport load within rippled-bed flow conditions is suspended load, while the near bed transporting layers are the main transport mode within the sheet flow condition. Therefore, the transport direction in rippled-bed flow, due to onshore velocity half-cycle contribution in vortex generation and offshore part in shedding and convection is offshore, while in sheet flow transport mode is onshore.

Fig. 2.14 shows the sediment concentration profiles recorded with ABS in the rippled-bed flow and sheet flow conditions by Ahmari (2012) and with CCM (Conductivity Concentration Meter) by Schretlen (2012) in the GWK. Both profiles are related to regular waves with the same wave-period ($T = 5\ s$). However, rippled-bed flow corresponds to wave height of $H = 1.2\ m$ and $h = 3.20\ m$ compared to $H = 1\ m$ and $h = 1.26\ m$ in sheet flow. As can be seen, in rippled-bed condition the concentration continues to higher elevations above the initial bed level compared to sheet flow concentration profile. In contrast, sheet flow concentration profile extends in significantly large values close to the bed-level and has a significant high concentration gradient at a small distance from the initial bed level. Due to the limitations of ABS in measuring the sediment concentration under sheet flow conditions within the strongly-concentrated sheet layers, Ribberink et al. (2001), Dohmen-Janssen and Hanes (2002), and Schretlen (2012) applied the CCM to measure the concentration in moving layers close to the immobile bed (Fig. 2.14 (c)). The concentration
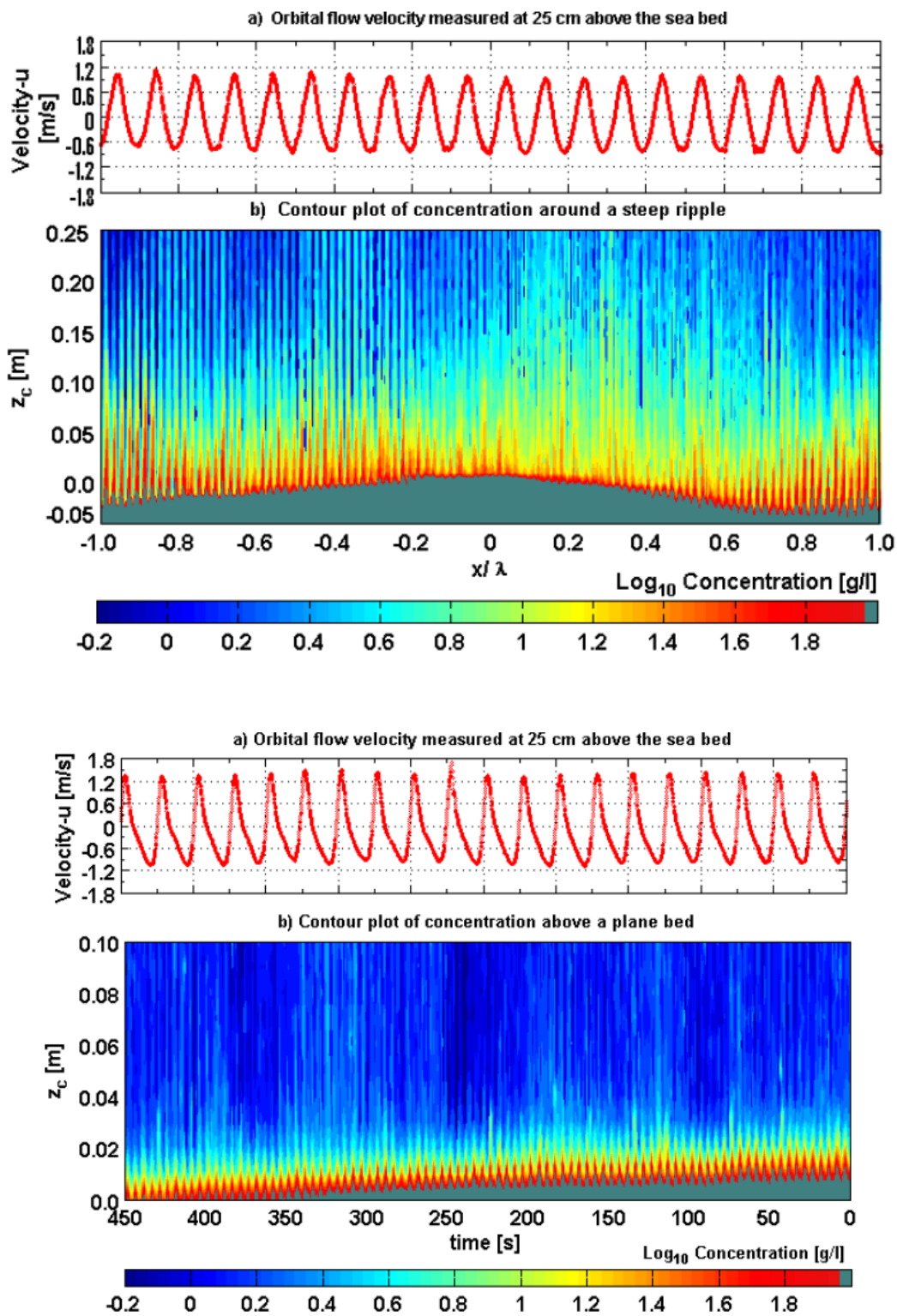
Figure 2.13: Velocity time series, time-dependent sediment concentration and bedforms, two upper panels are rippled-bed $H = 1\ m$, $T = 5\ s$, $h/L = 0.125$) and lower sheet flow regime ($H = 1\ m$, $T = 5\ s$, $h/L = 0.075$) (Ahmari, 2012).

(a)

(b)

(c)
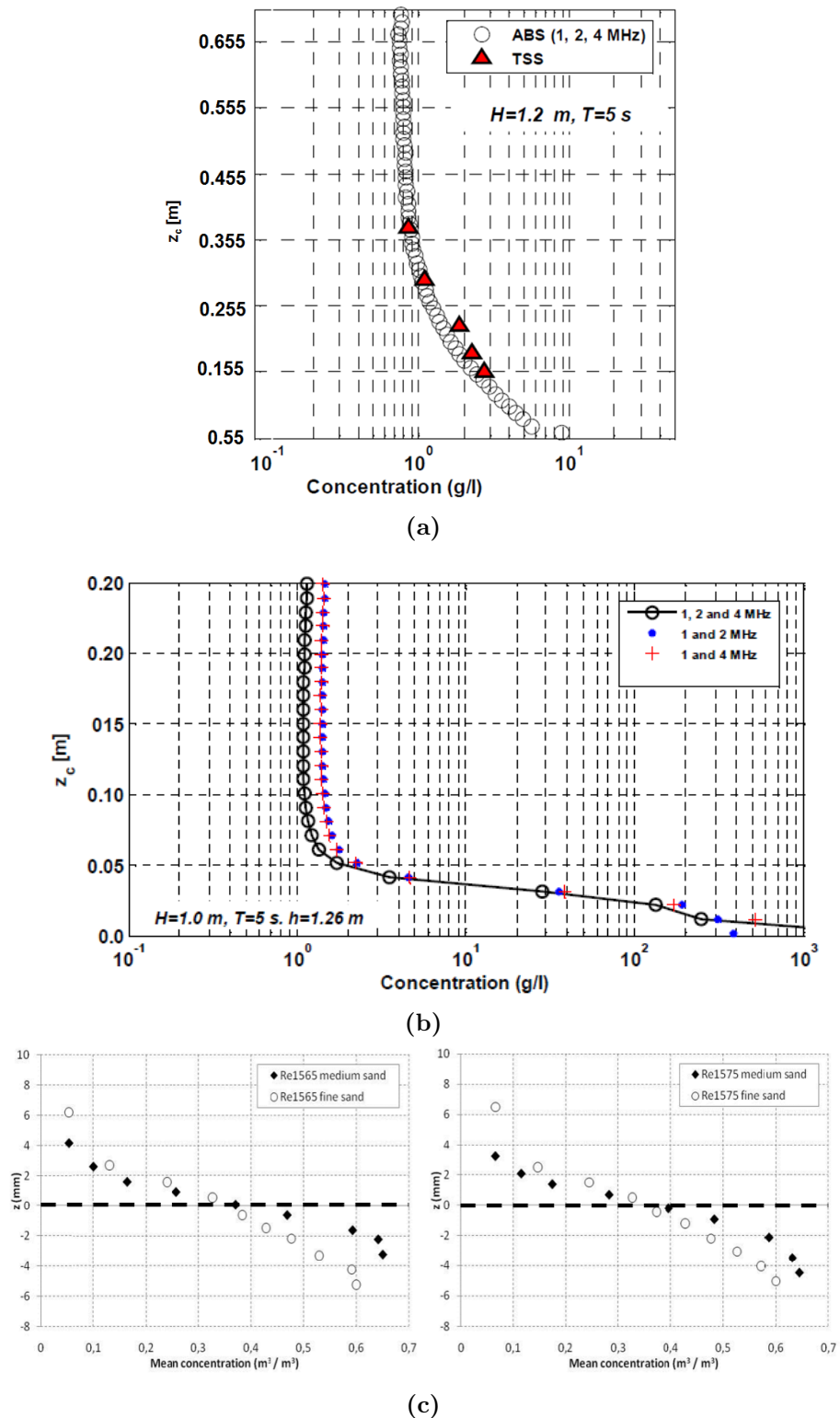
Figure 2.14: Concentration profile in (a) rippled-bed flow and (b) sheet flow, measured by ABS (Ahmari, 2012) and (c) concentration profile in sheet flow, measured by CCM (Schretlen, 2012) in the GWK.

profiles by CCM corresponds to the regular waves with $H = 1.5\ m$, $h = 3.5\ m$ and wave periods of T=6.5 and 7.5 s over fine ($D_{50} = 0.138\ mm$) and medium ($D_{50} = 0.245\ mm$) sands. As can be seen, the recorded profiles by CCM continue to elevations under the initial bed-level, where ABS is not capable of measuring the concentration.

2.4   OFT-experiments with sheet flow conditions and graded sands

In contrast to the rare large wave flume experiments on sheet flow, there are several OFT experiments for graded sands under sheet flow conditions. Van der Werf et al. (2009) presented a database, which includes these OFT-experiments. The main advantage of OFTs is their simple structure to conduct desired waves and sediment experiments. They are comprised of a U-tube with a piston at one end to generate oscillatory water motions (Fig. 2.1). Therefore, OFT experiments are more economic and controllable than large scale flume experiments. However, OFTs are not capable of representing the all real surface wave characteristics near the bed layer. Fig. 2.15 outlines the available OFT experiments on graded sands under sheet flow conditions, performed in Aberdeen-OFT (AOFT), Tokyo University-OFT (TUOFT) and Large Oscillating Water Tunnel (LOWT) of the Delft Hydraulics. To have a comparative review of these 52 available test-cases, some characteristics for applied graded sands as well as generated oscillatory motions are defined. In terms of grading degree, the grading Index (GI), which is defined as D_{90}/D_{10}, identifies the non-uniformity value of graded sands (Sistermans, 2002). Sands with GI=2-3 are referred to as well-sorted sands, whereas sands with larger GI are classified as well-graded sands.

The waves in the natural fields are nonlinear and sediment are non-uniform. Increasing the wave nonlinearity in storms could result in washing out the ripples (appeared in calm hydrodynamic conditions) and transporting a significant volume of sediments in the form of highly concentrated sheets near the bed. This mode of sediment transport is known as sheet flow. In terms of generated oscillatory motions, wave nonlinearity was considered in OFTs during sheet flow experiments. This experimental attempt was due to the depth reduction from deep to shallow water, where approaching waves in the surf-zone become usually nonlinear. Wave nonlinearity plays a significant role in the inception of sheet flow conditions (Dibajnia and Watanabe, 1992). This nonlinearity might be briefly classified into two different modes:

- **skewness mode**, which describes nonlinear waves with higher crest than trough and shorter crest-period than trough-period as is exemplarly demonstrated in Fig. 2.16.

- **asymmetry mode**, which describes the nonlinear waves with a forward-leaning/sawtooth shape (Gonzalez-Rodriguez, 2009) as is exemplarly demonstrated in Fig. 2.17.

Progressive real surface waves in the shoaling zone before breaking are dominantly skewed waves (Gonzalez-Rodriguez and Madsen, 2007). A good representative wave-shape to investigate the skewed waves is the Stokes wave, therefore, most of available experiments on skewed waves have been conducted under Stokes waves. The skewness degree is defined as:

$$R = u_c/(u_c + |u_t|) \tag{2.25}$$

where R is the skewness degree and u_c, u_t are the crest and trough- velocities, respectively (cf. Fig. 2.16). It should be noted that skewness in this thesis refers to the velocity-skewness/velocity-asymmetry already presented in literature (e.g. Abreu et al.

References	Fractions	Graded sands mixtures				Nonlinearity, Wave period			Facility	Number of exp.
						R	β	T(s)		
Innui et al. (1995)	D50=0.20 mm Medium; D50=0.87 mm Coarse2	GI=- (25/75)	GI=- (50/50)	GI=- (25/75)		0.7	0.5	3, 5	TUOFT	10
Hamm et al. (1998)	D50=0.128 mm Fine; D50=0.317 mm Coarse1	GI=4.19 (50/50)				0.66	0.55	6.5, 6.4, 7.2	LOWT	13
Ahmed and Sato (2003)	D50=0.21 mm Medium; D50=0.49 mm Coarse1; D50=0.74 mm Coarse2	GI=3.12 (10/20/70)	GI=3.61 (20/50/30)	GI=3.84 (40/30/30)	GI=3.50 (40/20/40)	0.60	0.5	3	TUOFT	14
O'Donoghue and Wright (2004)	D50=0.15 mm Fine; D50=0.28 mm Medium; D50=0.51 mm Coarse1	GI=4.10 (10/60/30)	GI=3.79 (20/60/20)	GI=3.67 (5/60/35)	GI=5.55 (50/50)	0.63	0.5	5, 7.5	AOFT	6
Hassan and Ribberink (2005)	D50=0.13 mm Fine; D50=0.21 mm Medium; D50=0.34 mm Coarse1; D50=0.97 mm Coarse2	GI=6.19 (30/70)	GI=9.82 (20/20/60)	GI=4.19 (50/50)		0.65	0.5	6.5, 12	LOWT	9
Total										52

Figure 2.15: Selected graded sands with corresponding fractions and wave conditions.

(2010), Van der A et al. (2013), for velocity-skewness and Dong et al. (2013) for velocity-asymmetry).

Asymmetry mode of nonlinearity is mainly dominant in the inner surf-zone, where broken waves are present (Gonzalez-Rodriguez and Madsen, 2007) and is also referred to as acceleration-skewness in literature (e.g. Abreu et al. (2010), Van der A et al. (2010), and Van der A et al. (2013)).

The asymmetry degree is defined as:

$$\beta = a_c/(a_c + |a_t|) \tag{2.26}$$

in which β represents the degree of asymmetry and a_c, a_t are crest and trough accelerations, respectively. The GI varies from highly-graded sands in Hassan and Ribberink (2005) experiments (GI=9.82) to well-sorted sands of Ahmed and Sato (2003) experiments. For the case of Inui et al. (1995) experiments, the grain size-distribution results of the graded sands were not reported.

To classify the fraction sizes, those with $D_{50} \leq 0.15$ mm are termed as fine sands, $0.15 < D_{50} \leq 0.30$ mm as medium sands, $0.30 < D_{50} \leq 0.70$ as 'coarse1' and $D_{50} > 0.70$ mm as 'coarse2'. AOFT and LOWT include variable fractions of fine sand to comprise the graded sand, while the experiments in the TUOFT were only carried out for graded sands composed of medium and coarse sands. The data related to the Hamm et al. (1998) experiments are acquired from the Cloin (1998) investigations. Graded sand fractions in the Hamm et al. (1998) experiments are similar to one of the Hassan and Ribberink (2005) experiments (GI=4.19), but the wave conditions are different.

The experiments performed by O'Donoghue and Wright (2004a) at the AOFT were second-
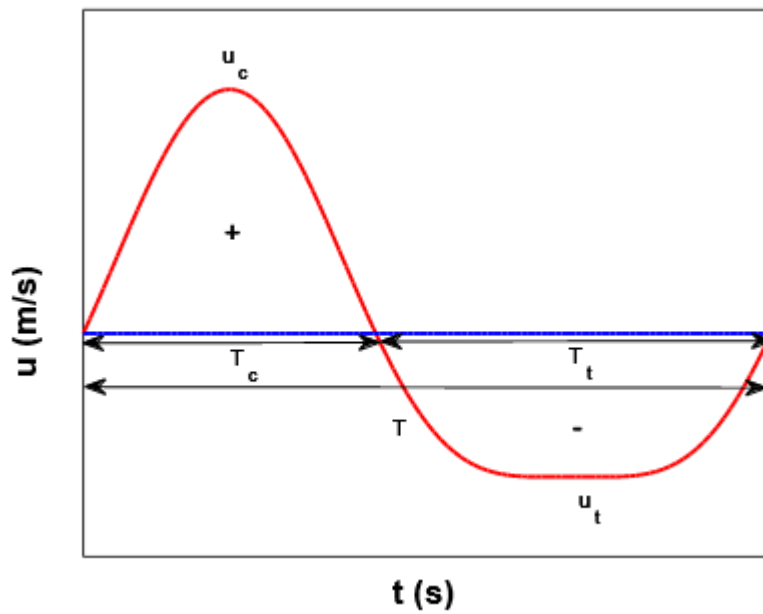
Figure 2.16: General scheme of a skewed wave, u_c: crest-velocity, u_t: trough-velocity, T_c: crest-period, T_t: trough-period .
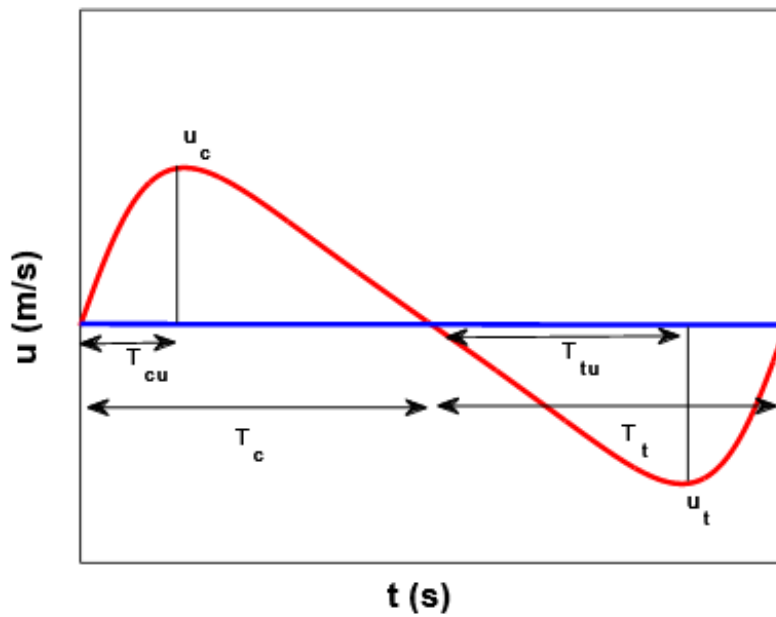
Figure 2.17: Asymmetric wave: u_c: crest-velocity, u_t: trough-velocity, T_{cu}: first part of crest-period, T_{tu}: first part of trough-period, T_c: crest-period, T_t: trough-period.

order Stokes waves. The near-bed velocity equation within these experiments was defined as:

$$u(t) = u_1 sin(\omega t) - u_2 cos(2\omega t) \tag{2.27}$$

where u_1 and u_2 are first- and second-order amplitudes of instantaneous near-bed velocity $u(t)$, and ω is the angular velocity of the wave $(= 2\pi/T$, T is wave period). The wave nonlinearity was considered in LOWT using second-order Stokes waves, but it was slightly different from the velocity time-series in AOFT as following (Hassan and Ribberink, 2005):

$$u(t) = u_1 cos(\omega t) + u_2 cos(2\omega t) \tag{2.28}$$

TUOFT used the firs order cnoidal wave theory to simulate the velocity asymmetry (Ahmed and Sato, 2003). However, the nonlinearity of generated oscillatory motions in all OFTs are classified using R and β as depicted in Fig. 2.15. All performed experiments have a velocity asymmetry of $0.6 < R < 0.7$. However, performed experiments with the acceleration asymmetry over graded sands are only the experiments performed in the LOWT by Hamm et al. (1998).

The periods of the generated oscillatory motions in OFTs cover a wide range of wave periods from 3-12 (s). The sheet flow experiments at the TUOFT were conducted mostly under short wave periods (i.e. 3-5 (s)). In contrast, the experiments at the LOWT and AOFT for sheet flow were performed under nonlinear oscillatory motions with perios from 5-12 (s).

2.5 Field campaigns under sheet flow conditions

Due to the high variation of the mobile bed under sheet flow, high costs of instrument deployment as well as instability of meteorological condition, field measurements under sheet flow conditions are rare. Bakker et al. (1988) and Lanckriet et al. (2013) campaigns are known examples of field experiments.

Bakker et al. (1988) in cooperation with the Forschungsstelle Küste (FSK) performed the first in-situ experiments for the sheet flow concentration and transport rate on the Norderney island, Germany. In these experiments two innovative measuring devices called "Harp" and "Swan" developed by Delft Hydraulics were installed in the swash zone of the Norderney beach in front of the Kaiserwiese coastline. Fig. 2.18 shows the position of the field campaign of Bakker et al. (1988) on Norderney. The field measurements on Norderney
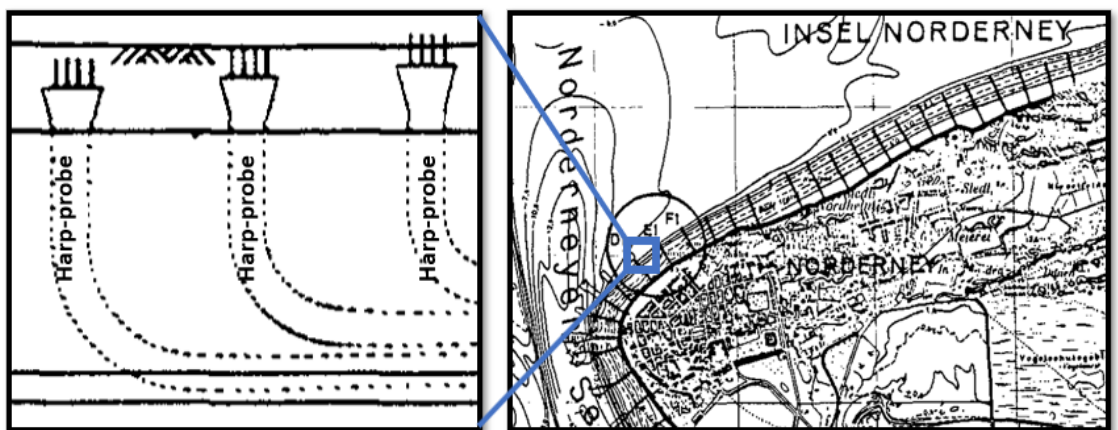
Figure 2.18: Harp probes in three different elevations in the swash zone of sheet flow measurement campaign on Norderney applied by Bakker et al. (1988).

showed a sheet flow layer thickness of around 6 mm. Fig. 2.19 shows the recorded sand

concentrations on 11 December 1987 by Bakker et al. (1988) in this field campaign. As explained by Bakker et al. (1988), A, B and C moments in Fig. 2.19 are the lifting of Harp probe for each 2 mm after covering with sand, respectively. Before A, the probe is covered with sands and after lifting for 2 mm (moment A), a fall is seen in the measurement signal for sand concentration, which is recovered by moving sheet flow layers quickly in about 15 (s). Therefore, these measurements reveals the high volume of sand transport in a time-scale smaller than one minutes under sheet flow condition. Moreover, it could be concluded that the main erosion under storm conditions is occurred in a transport regime with predominant sheet flow.

Lanckriet et al. (2013) applied CCP (Conductivity Concentration Profiler) in the swash zone of the Parenporth Beach, Cornwall, United Kingdom from 9-15 October in 2011 to measure the sheet flow sand concentration. Their measurement analysis for backwash induced sheet flow conditions revealed that the ensemble-averaged sheet flow concentration profile has a linear form in lower elevations (where high sand concentration is present) and a power-law form at higher elevations and between these two parts (volume concentration of 0.2-0.3) is the shape of concentration profile transient from line to power-law shape.
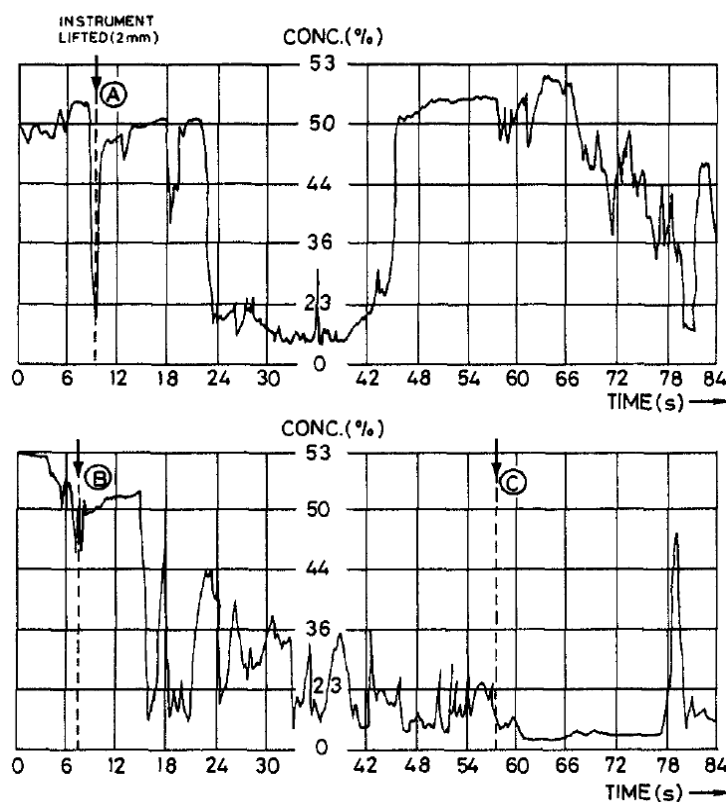
Figure 2.19: Sheet flow sand concentrations measured in the swash zone of field campaign on Norderney at 11 of December 1987 (Bakker et al., 1988).

2.6   Economical importance of the sheet flow transport regime

In outer surf-zones and swash zones, where near-bed wave orbital velocities are sufficiently high, sheet flow becomes the dominant transport mode. Sheet flow dominant areas are shoaling-zone, where waves are near-breaking and strongly skewed (velocity asymmetry),

and swash-zones, where the undertow produces offshore sheet flow transport and broken waves are strongly asymmetric (acceleration asymmetry). Due to the fact that the wave nonlinearity plays a substantial roll in inception of the sheet flow transport (Dibajnia and Watanabe, 1992), it could be concluded that the dominant transport mode before breaking and after breaking is sheet flow. In addition, under storm conditions the sheet flow dominant area extends to a larger zone of outer surf-zones and whole swash-zones, hence high volumes of sediments due to the high shear-stresses will be transported (Dohmen-Janssen and Hanes, 2002). This leads to a large sand lost of sandy beaches and can result in extreme costs to repair/(re-)nourish the affected beaches. Fig. 2.20 shows exemplary the affected beaches of Wangerooge, Germany at the Xaver storm surge in December, 2013. The municipality of the island estimated 400.000€ to renourish the eroded beach (`http://www.haz.de/Nachrichten/Wirtschaft/Niedersachsen/Flut-spuelt-Strand-weg`).

2.7 Sheet flow layer structure

To understand the sediment transport mechanisms under sheet flow, it is necessary to study its constituting sub-layers. Due to the substantially different sediment behavior at different concentrations, the sheet flow layer is divided into several sub-layers based on the sediment concentration. Amoudry et al. (2008) divided the sheet flow layer into four sublayers as illustrated in Fig. 2.21. Concentration is decreased from the immobile bed layer to the upper dilute layer.

The first sub-layer above the immobile bed layer is referred to as enduring contact layer, which is distinguished from lower and upper sub-layers through volume concentration (c=volume of sand/total volume of sand and water) limits of c=0.635(= 1683 kgm^{-3}) and c=0.57(= 1511 kgm^{-3}), respectively. In this sublayer sand grains are close-packing and transported as layers, where the grains are in contact with their neighbors frictionally. The second sub-layer is collisional layer, where the dominant intergranular interactions is representative with collisions among particles. The frictional forces among grains in this sub-layer are neglected. Moreover, the behavior of sand transport is usually described as the behavior of particles within dense gases (Jenkins and Hanes, 1998). Kinetic Theory of Granular Flow (KTGF), which considers the binary collisions of grains, could be modified to describe the behavior of granular interactions in this sub-layer. Hsu et al. (2004) modified KTGF in such a way to include the multi-collisional intergranular interactions in collisional sub-layer. For enduring contact layer, KTGF is not valid and usually a different frictional approach for pressure and particle shear stresses like the approach of Jonsson (1967) is applied (see Eq. A.10). The lower interface with immobile bed layer is referred to as failure interface, where the shear stress just exceeds the Coulomb criterion.

2.8 Numerical models for sheet flow transport regime

Importance of net transport rate predictions for sandy beaches has motivated many researchers and scientists to try to develop the numerical models, which can serve as a tool to better understand the transport mechanisms, particularly under sheet flow conditions. In this sense, available numerical models for sheet flow sediment transport could be divided into two general groups:

- numerical models for uniform sands transport
- numerical models for mixed sands transport

In contrast to extensive research on numerical modeling of uniform sands, available models
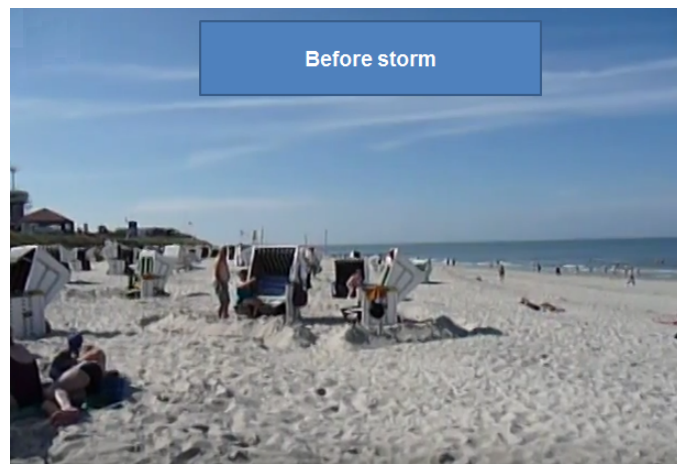
(a)
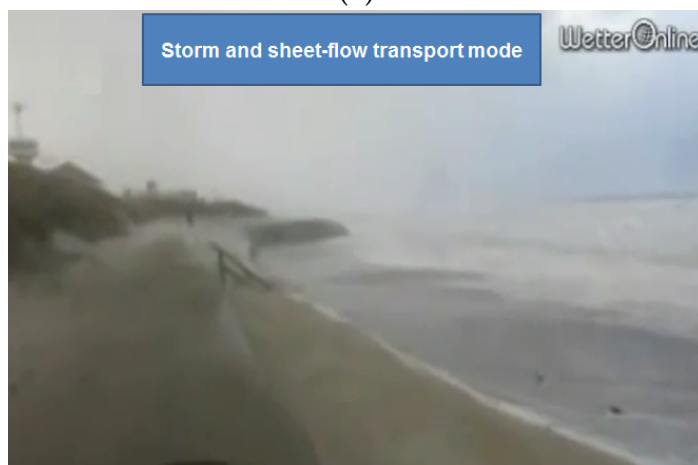
(b)
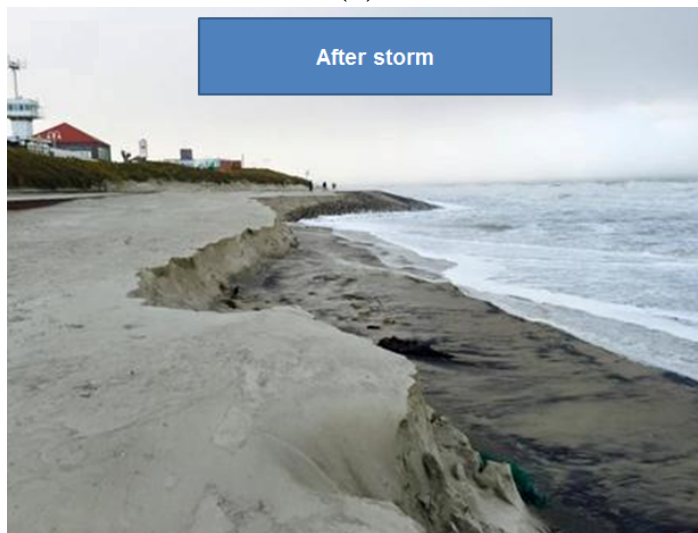
(c)

Figure 2.20: Wangerooge island beach in storm surge Xaver, December 2013, (a) before and (b) during and(c) after erosion induced by storminess condition (sheet flow transport regime), (http://www.nwzonline.de/ and http://www.wetteronline.de/).
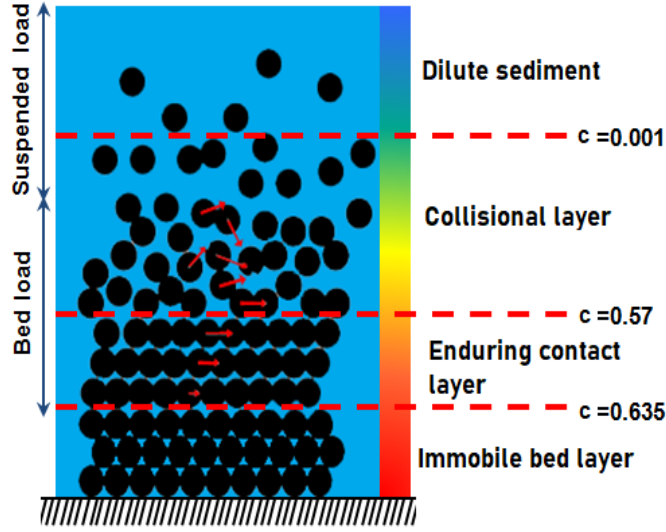
Figure 2.21: Constituting sub-layers of sheet flow layer modified from Amoudry et al. (2008).

for mixed sands are rare. Available models for uniform sands could be divided into two main groups:

- single-phase models
- two-phase models

Single-phase models assume an equal behavior for both sediment particles and carrier flow. They define a mixture density for simulated fluid as:

$$\rho = \rho_s c + (1 - c)\rho_w \tag{2.29}$$

where ρ, ρ_s and ρ_w are mixture, sediment and water density, respectively and c is volumetric sediment concentration. Single-phase models solve the conservation and momentum equations without including the multi interactions among sediments and fluid and try to include these interactions through empirical equations like empirical formula for including the hindered settling effect on the settling velocity of sediment in high concentrations or reference concentration as a proxy of bed concentration (e.g. RANS-based models of Hassan and Ribberink (2010) or Fuhrman et al. (2013)). Therefore, they are not able to reproduce the highly concentrated regions near and below the initial bed level (e.g. sheet flow layer) precisely. To approximate the sediment concentration in the elevations close to the bed, the single phase models apply an empirical concentration which is known in literature as reference concentration (c_0) or pick-up function. Using c_0 is one of the most uncertain part of single-phase models formulation (Davies and Li, 1997). Most well-known pick-up functions or reference concentrations in single phase models are defined for $z = 2D_{50}$ and known as:

- pick-up function of Engelund and Fredsøe (1976)
- pick-up function of Van Rijn (1984)
- pick-up function of Zyserman and Fredsøe (1994) and

- pick-up function of Einstein (1950)

where the Engelund and Fredsøe (1976) pick-up function is defined as:

$$c_0 = 0.65/(1 + 1/\lambda)^3 \tag{2.30}$$

and

$$\lambda = \begin{cases} \left(\frac{|\theta| - \theta_c - \pi p^*/6}{0.027|\theta|s}\right)^{1/2} & \text{for } |\theta| > \theta_c + \pi p^*/6 \\ 0 & \text{for} |\theta| \leq \theta_c + \pi p^*/6 \end{cases} \tag{2.31}$$

where

$$p^* = \left[1 + (\frac{\pi/6}{|\theta| - \theta_c})^4\right]^{-1/4} \tag{2.32}$$

the Van Rijn (1984) pick-up function was defined as:

$$c_0 = 0.00033 D_*^{0.3} T^{1.5} \quad \text{for } |\theta| > \theta_c \tag{2.33}$$

where

$$T = \frac{(u_*)^2 - (u_{*,cr})^2}{(u_{*,cr})^2} \tag{2.34}$$

Davies and Li (1997) defined the Van Rijn (1984) pick-up function based on the Shields parameter as:

$$c_0 = 0.00033 \left[\frac{(s-1)^{0.6} g^{0.6} D_{50}^0.8}{\nu^0.2}\right] \left[\frac{|\theta|}{\theta_c} - 1\right]^{3/2} \quad \text{for } |\theta| > \theta_c \tag{2.35}$$

The proposed pick-up function by Zyserman and Fredsøe (1994) is given as:

$$c_0 = \frac{0.331(\theta - 0.045)^{1.75}}{1 + \frac{0.331}{0.46}(\theta - 0.045)^{1.75}} \tag{2.36}$$

The Einstein (1950)'s pick-up function was applied by Fuhrman et al. (2013) as:

$$c_0 = \pi p/12 \tag{2.37}$$

where p is defined as:

$$p = \left[1 + (\frac{\pi \mu_d}{6(\theta - \theta_c)^4})\right]^{-1/4} \tag{2.38}$$

where μ_d is the dynamic friction factor and serves as a calibration factor, which proposed in the single-phase model of Fuhrman et al. (2013) as μ_d =1.6.

To understand the performance of these reference concentrations, Fig. 2.22 compares the Eq. 2.30 to Eq. 2.37 for $\theta_c = 0.048$ of a uniform sand with $D_{50} = 0.21\ mm$. As can be seen, the Van Rijn (1984) suggestion for c_0 has no upper limit compared with its three counterparts. Moreover, for $\theta < 1$ the values of c_0 are different from each other, where the Van Rijn (1984) equation takes the lower limit and Einstein (1950) the upper limit for these four pick-up functions. The pick-up functions of Zyserman and Fredsøe (1994) and Engelund and Fredsøe (1976) are converged for high values of the Shields parameter ($\theta > 3.5$) to around 0.3. The Einstein (1950) pick-up function shows slightly smaller value for c_0 and the Van Rijn (1984) equation results in a c_0-value at ($\theta = 3.5$), which is almost two times larger than other pick-up functions. Moreover, the Einstein (1950) pick-up function reaches the $c_0 = 0.23$ around $\theta = 1$ and does not vary for $\theta > 1$.
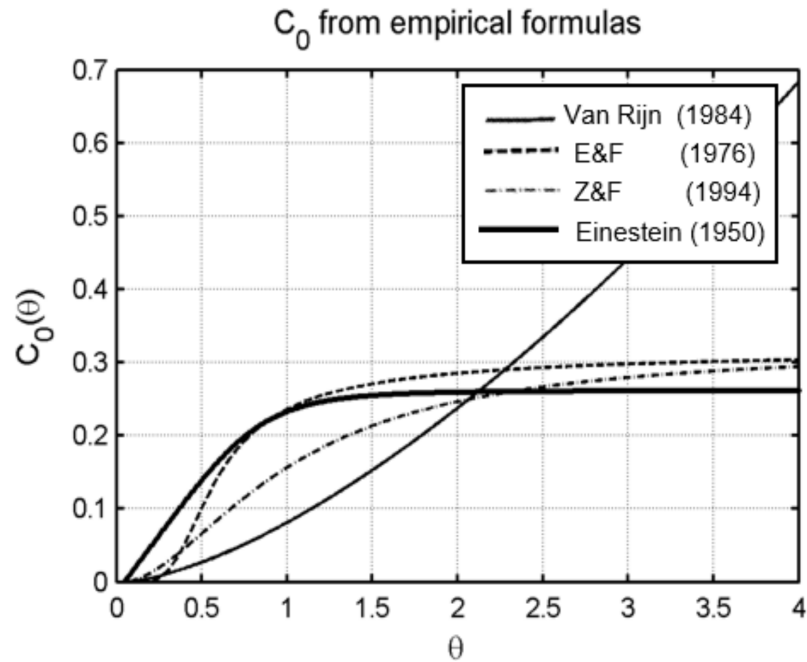
Figure 2.22: Comparison of different reference concentrations by increasing the Shields parameter: Van Rijn (1984)(thin solid line), Zyserman and Fredsøe (1994)(Z&F)(dash-dotted line), Engelund and Fredsøe (1976)(E&F)(dashed line) and Einstein (1950)(thick solid line).

O'Donoghue and Wright (2004a) compared the measured sheet flow induced concentration time series close to the bed ($z = 2D_{50}$) with the predicted results by the pick-up functions of Engelund and Fredsøe (1976) and Zyserman and Fredsøe (1994) for symmetric as well as asymmetric wave velocities. Fig. 2.23 and Fig. 2.24 show the results from O'Donoghue and Wright (2004a) studies. As can be seen these pick-up functions are not capable of describing the sand concentrations close to the bed within the sheet flow conditions, particularly in the crest-part. Furthermore, the high concentrations at the flow reversal in measurements is estimated as zero using these pick-up functions. In addition, unclear sediment diffusivity and turbulent eddy viscosity parameters in different levels and applied clear water turbulence equations make these model results questionable to apply for natural conditions.

2.9   Two-phase flow models

In contrast to conventional single-phase flow models, two-phase flow models are capable of including the sediment-flow interaction, and therefore can provide a better accuracy than single-phase models, where the sediment concentration is high (Asano, 1990). Two-phase flow models apply conservation equations separately for the sediment phase and fluid phase and consider the interaction between different phases through mutual hydrodynamic forces (e.g. drag and lift) in corresponding momentum equations. Also, internal interactions of sediment grains are simulated through (semi-)empirical shear and normal stress formulas. Asano (1990) applied the constitutive equation of Savage and McKeown (1983) to include the intergranular stresses for sand grains.

Likewise, Dong and Zhang (1999) applied the intergranular shear stress formulation of
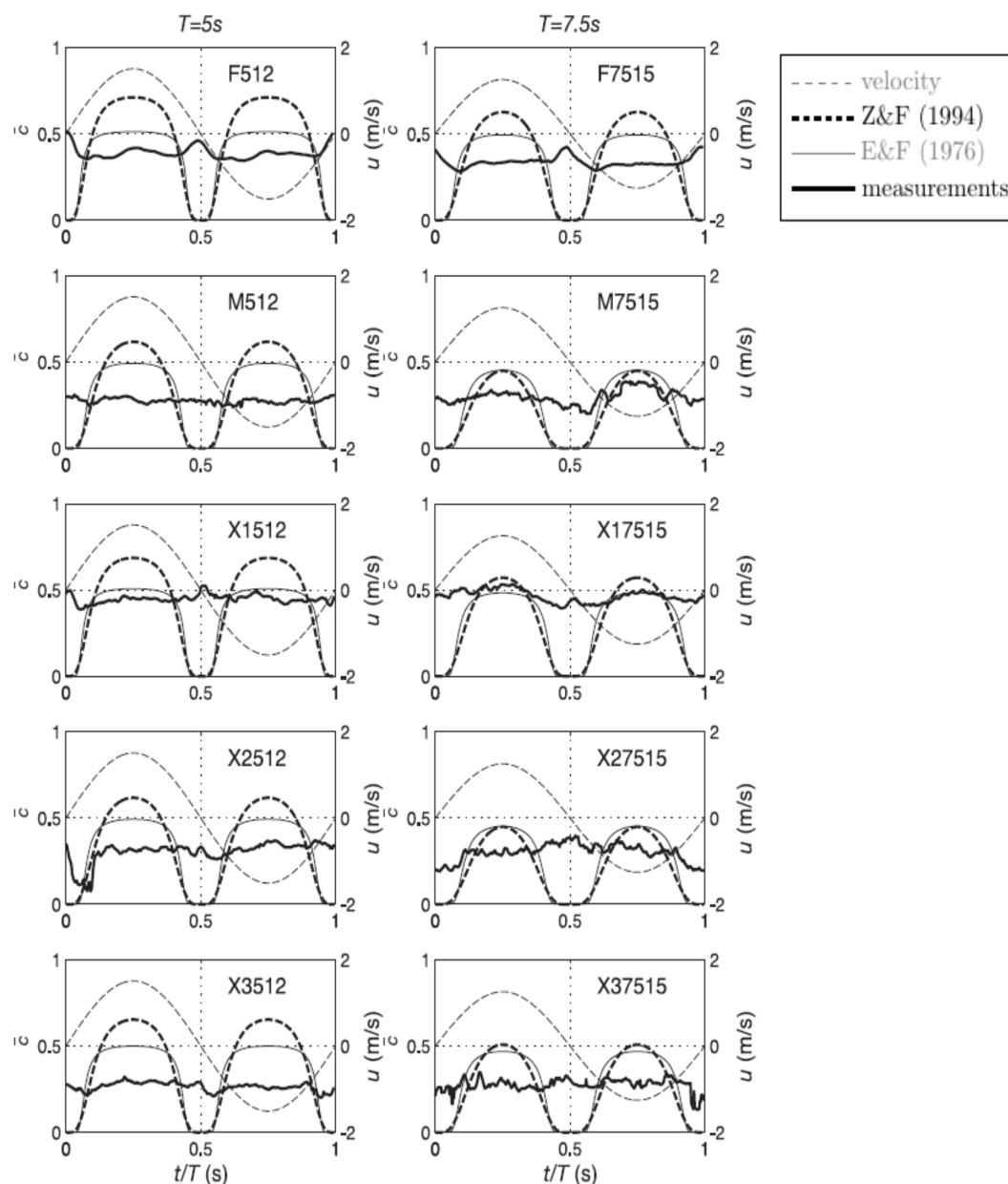
Figure 2.23: Comparison of c_0 formulas with measurements in the Aberdeen Oscillatory Flow Tunnel (AOFT) for symmetric velocity signal: X is the notation for mixed sand, F Fine, and M medium uniform sand,$--$:velocity, $--$:Zyserman and Fredsøe (1994)(Z&F, 1994),$—$:Engelund and Fredsøe (1976)(E&F, 1976), $\rule{12pt}{2pt}$: concentration measurements, after O'Donoghue and Wright (2004a).

Savage and McKeown (1983) but calculated the normal intergranular stresses using a simplified formulation including the frictional angle of sediment. Hsu et al. (2003) developed a two-phase flow model for dilute sediment suspension (the intergranular stresses were therefore neglected) to investigate the momentum exchange between water and sand phases. In contrast to applied models using the emperical formulation of Savage and McKeown (1983), Hsu et al. (2004) applied the Kinetic Theory of Granular Flow (KTGF) of Jenkins

33
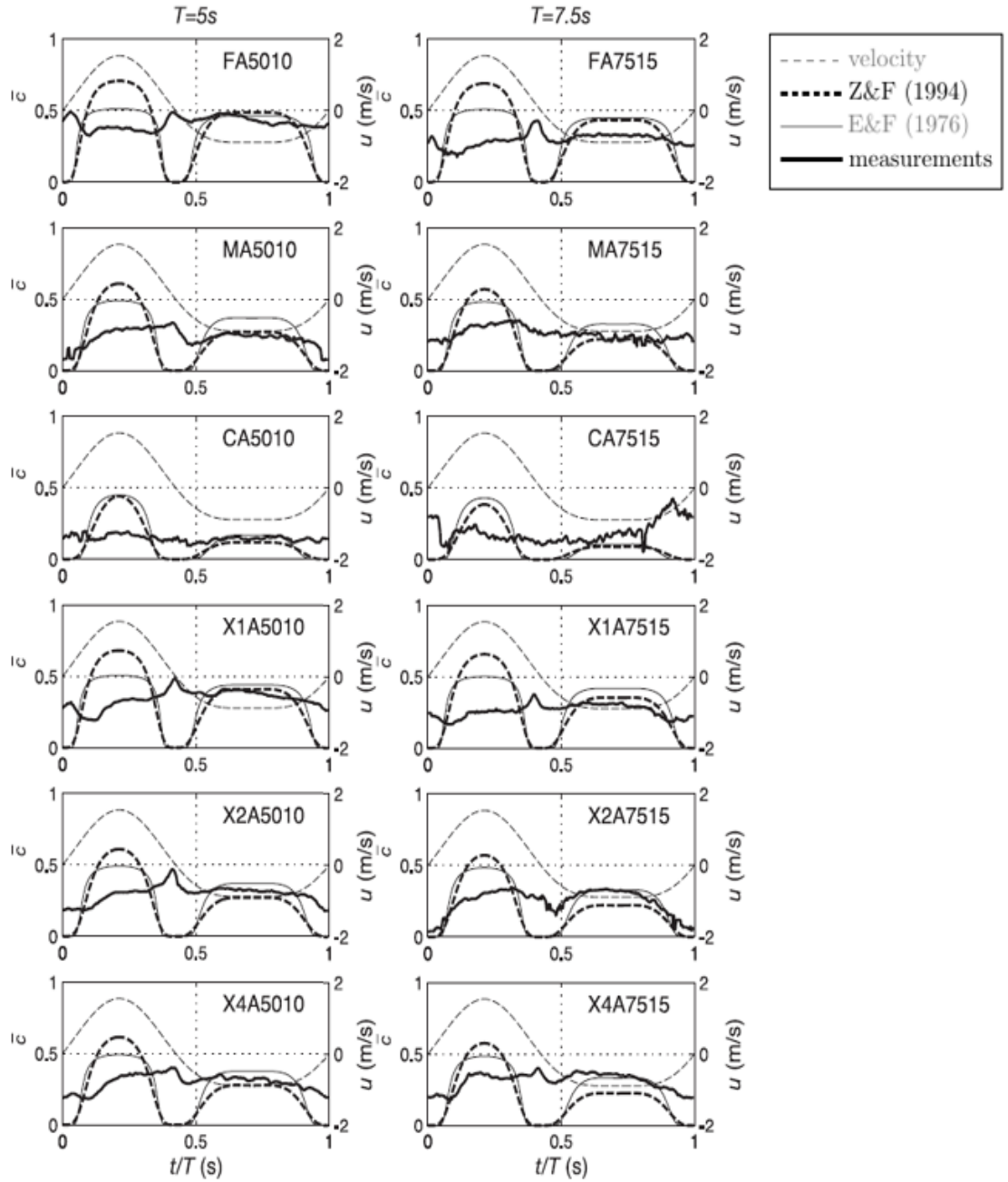
Figure 2.24: Comparison of different reference concentrations with measurements in the Aberdeen Oscillatory Flow Tunnel (AOFT) for asymmetric velocity signal: X is the notation for mixed sand sign, F Fine, M medium, and C coarse uniform sand, A stands for asymmetric velocity,−−:velocity, --:Zyserman and Fredsøe (1994)(Z&F, 1994),—-:Engelund and Fredsøe (1976)(E&F, 1976), ▬: concentration measurements, after O'Donoghue and Wright (2004a).

and Savage (1983) for intergranular shear stresses and the proposed equation by Cundall et al. (1989) for normal intergranular stresses to model the dilute as well as the enduring contact layer of sheet flow.

The Capability of two-phase flow models to simulate the highly concentrated regions near
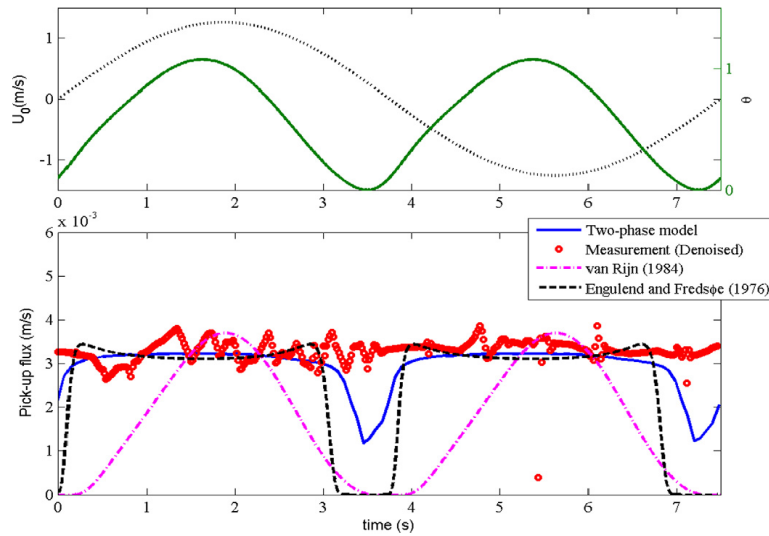
Figure 2.25: Lower plot: comparison of the two-phase flow model results for pick-up flux: (▬) with those predicted by application of the Van Rijn (1984) equation: (▪▪▪) and the Engelund and Fredsøe (1976) equation: (▪▪▪) vs. the measurements of O'Donoghue and Wright (2004a): (○) for upper plot: a symmetric velocity (T=7.5 s, sinusoidal wave) (····) with the corresponding Shields parameter (▬), after Yu et al. (2012).
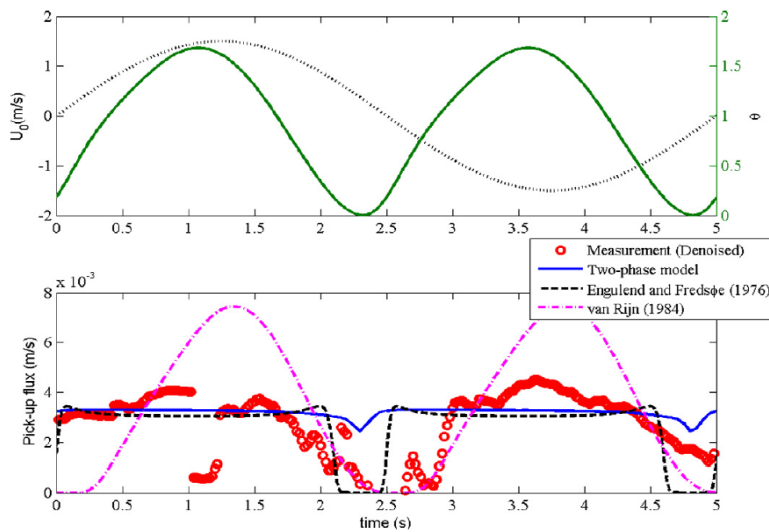
Figure 2.26: Lower plot: comparison of the two-phase flow model results for pick-up flux: (▬) with those predicted by application of the Van Rijn (1984) equation: (▪▪▪) and the Engelund and Fredsøe (1976) equation: (▪▪▪) vs. the measurements of O'Donoghue and Wright (2004a): (○) for upper plot: a symmetric velocity (T=5.0 s, sinusoidal wave) (····) with the corresponding Shields parameter (▬), after Yu et al. (2012).

the bed can be clearly seen in Fig. 2.25 and Fig. 2.26 , where Yu et al. (2012) applied a second order stocks velocity as the pressure gradient in the momentum equation of fluid phase ($U(t) = U_1 cos(\omega t) + U_2 cos(2\omega t)$, where $\omega = 2\pi/T$). The reason that the two-phase flow models can more accurately reproduce the sediment concentration is hidden in the separately applied momentum equations for sediment and flow phases. In these momentum

equations, no empirical equation to reproduce the high sediment concentration is applied and in contrast to the single-phase models, the sediment concentration is resolved from the momentum and continuity equation of sediment. The momentum transport between flow-phase and sediment-phase are added as a source to the momentum equations, whereas these are not explicitly considered in single-phase models. Moreover, in two-phase flow models, the effect of sediment concentration on the flow turbulence is coupled to the momentum equations, where the turbulence drag is considered. Yu et al. (2012) compared their two-phase flow model results for the test-case A7515 (period T=7.5 s, u_{max}=1.5 m/s, skewness degree (R=$max/(u_{max} + |u_{min}|$=0.63), uniform sand with D_{50}=0.28 mm) with the measurements of O'Donoghue and Wright (2004a) as well as the empirical pick-up functions of Van Rijn (1984) and Engelund and Fredsøe (1976), which are usually applied in single-phase sediment transport models as the bottom boundary condition of sediment concentration (c_0) (Fig. 2.25 and Fig. 2.26). As can be seen, the two-phase flow model results have better consistency and agreement with the measurements close to the bed. Therefore, this capability of two-phase flow models makes them ideal to study the complex sediment $\longleftrightarrow$ fluid and sediment $\longleftrightarrow$ sediment interactions inside the sheet flow layer, where the sediment concentration is high. However, the fluid turbulence models and sediment interaction closures to consider the 3D multi interactions have not been fully understood and require further investigations. Although the numerical study of mixed sands using an Eulerian two-phase flow model is yet not available, the capability of two-phase flow models in reproducing the uniform sand concentration (Cheng et al., 2017) and mixed sand by means of a coupled Eulerian-Lagrangian model (Rafati et al., 2022) were approved in literature.

Tab. 2.1 compares the available two-phase flow models for uniform sands in terms of the turbulence closure, interparticle sediment stress closure, velocity asymmetry, current superposition, D_{50} of uniform sand transport simulations. As can be seen, despite the wide range of available two-phase numerical models, they have been run for uniform sands with KTGF (Jenkins and Hanes, 1998), the Dense Granular Flow Rheology (DGFR) (Revil-Baudard and Chauchat, 2013) or empirical formulations. KTGF and DGFR approaches have been developed to overcome the uncertainty of available empirical equations for shear and normal stresses resulting in particles-particle interactions. KTGF postulates that sediment particles interaction is similar to the binary granular materials in dense gaseous fields and does not consider the multiple-interactions of particles in enduring contact sub-layer of the sheet flow layer (Fig. 2.21). DGFR lacks a systematic formulation which connects the friction and dilatancy functions to the particle properties (e.g. coefficient of restitution COR and particle shape) (Revil-Baudard and Chauchat, 2013).

2.10   Modeling framework

In recent years, OpenFOAM (Open Field Operation And Manipulation) as a free and open-source CFD toolbox, which is able to model the complex physical problems in 3D cases attracted the coastal engineers interest. Higuera et al. (2013) mentioned the advantages of OpenFOAM as an efficient numerical toolbox for two-phase studies in coastal engineering. Jacobsen et al. (2012) developed a new CFD toolbox (waves2Foam) for OpenFOAM to regenerate the free surface waves and artificial shore using relaxation zone technique. Cheng et al. (2017) developed a two-phase numerical model by implementation of KTGF in already developed solver by Rusche (2003) (twoPhaseEulerFoam) in OpenFOAM to study the sheet flow sediment transport mechanisms for uniform sands (sedFoam). Chauchat et al. (2017) improved sedFoam and developed sedFoam-2.0 to include the DGFR as well as

$k - \omega$ turbulence model. SettlingFoam (Carrillo-Serrano and Pacheco-Tobar, 2018) solver is another example, which depicts the ability of OpenFOAM in multiphase interactions modelling.

Recently, Kim et al. (2019) developed a new solver based on sedFoam and waves2Foam, which is referred to as SedWaveFoam to study the sheet flow sediment transport for uniform sand under progressive surface waves. The development of a new solver in this thesis which is called mixedSedFoam can profit the capabilities of two-phase flow model of the available sedFoam of Cheng et al. (2017) for uniform sands and open-source property of OpenFOAM. Moreover, it can be integratedinto the sedWaveFoam to develop a newer solver to study the mixed sand transport under progressive surface waves. However, development of a two-phase flow model to a multi-phase due to the presence of different sand fractions has been a challenge for researchers. The expensive computations to solve the transport equations for each fraction make the complexity more challenging. This requires more investigation as will be discussed in detail in chapter 4.

Conclusion

- The available literature proposes the inception of the sheet flow transport mode for uniform sand by exceeding the Shields parameter of about 0.8, or when the mobility number is larger than 300. Moreover, the mobility number is usually applied to describe and follow the bedforms evolution from ripples to sheet flow plane bed. However, the considered threshold of the mobility number in OFTs is different than large wave flumes ($\psi \geq 150$ in the GWK compared with $\psi \geq 300$ in AOFT). The reason for this could be described through the incapability of OFT to reproduce the streaming under progressive surface waves, which is present in the performed experiments in large wave flumes like the GWK.

- OFT experiments for mixed sand transport under sheet flow are available. These experiments provide a sufficient range of the mixed sand non-uniformity and oscillatory flow periodicity. However, the frequently applied experiments in the literature for the calibration and validation of the developed numerical models for sheet flow are the experimental data of O'Donoghue and Wright (2004a) in the AOFT. Therefore, for the validation and calibration of the developed model in this thesis also these measurement data are recommended, as will be discussed in chapter 4.

- Despite the high importance of sheet flow transport mode under storm surges (due to the fact that sheet flow is the predominant sediment transport mode under storm surges), the field campaigns are too rare. Only two field measurements (on Norderney, Germany and Perranport Beach, UK) are available. The main reason for this is the instability of meteorological conditions as well as expensive costs of field measurements under stormy conditions.

- A well-validated and detailed Eulerian-Eulerian numerical model for mixed sand transport did not find in literature. Therefore, this thesis will be the first attempt to model the mixed sand transport under sheet flow using an Eulerian-Eulerian model formulation. The results will provide the understanding of the interparticle interactions and will improve the practical application of mixed sands in coastal engineering such as beach (re)nourishment.

- The available measurement results for the uniform sand concentration under sheet flow show that the applied reference concentration formulations in single-phase models are not capable of reproducing the sand concentration close to the bed and based on the experiments this threshold is defined using bed roughness as $k_s = 2D_{50}$ (Davies et al., 2002) and $z_0 = k_s/30$. In contrast, the model results of a two-phase flow formulation in literature (e.g. Yu et al. (2012) and Cheng et al. (2017)) show a better agreement with measurements. Moreover, the single-phase models are not capable of providing information about the concentration under the reference level. Therefore, due to the pronounced dynamics of sands in a mixture compared to uniform and capabilities of two-phase flow models to reproduce these processes better than single-phase models, the formulation of a two-phase flow model is recommended for the development of a new numerical model in this thesis.

- The available two-phase flow model of Cheng et al. (2017) is the best choice for the developments on the mixed sands, because it was calibrated and validated for uniform sands. Moreover, it was developed under OpenFOAM framework, therefore it is open-source and developments are possible. However, this model was not developed for mixed sands, therefore the development, calibration and validation for mixed sands could extend the knowledge on the sheet flow transport regime in nature, because the available sands on the beach as well as the (re)nourished sands are mixed sands (due to the differences between the grain size distribution of transported sands with the native sands).

Table 2.1: Studied two phase-flow models characteristics for sheet flow conditions under linear and non-linear waves.

Author (s)	Turbulence closure	Sediment stress closure	Studied waves					Sediment grains size (s) (D_{50}) (mm)	Mixed sands	Dim.	Slop effect	Streaming effect
			Sym.	Sk.	Asym.	Sk. plus Asym.	Waves plus Current					
Asano (1990)	Zero-equation	Savage and McKeown (1983)	Yes	No	No	No	No	2-4-4.3-5	No	1DV	No	No
Dong and Zhang (1999)	Zero-equation	Ahilan and Sleath (1987)	Yes	No	No	No	No	2-5	No	1DV	No	No
Dong and Zhang (2002)	Zero-equation	Ahilan and Sleath (1987)	Yes	No	No	No	Yes	0.13-0.2-0.21	No	1DV	No	No
Hsu et al. (2003)	Two-equations ($k - \epsilon$)	Neglected	No	No	No	No	Yes	0.13-0.15-0.19-0.24-2.6-3	No	1DV	No	No
Hsu et al. (2004)	Two-equations ($k - \epsilon$)	KTGF	Yes	No	No	No	No	0.13-0.15-0.19	No	1DV	No	No
Amoudry et al. (2005)	Two-equations ($k - \epsilon$)	Neglected	Yes	No	No	No	Yes	0.13-0.20-0.21	No	1DV	No	No
Liu and Sato (2006)	Zero-equation	Ahilan and Sleath (1987)	Yes	Yes (R =0.63)	No	No	No	0.15-0.28-0.51	No	1DV	No	No
Li et al. (2008)	One-equation (k)	Ahilan and Sleath (1987)	Yes	Yes (R =0.63)	No	No	No	0.13	No	1DV	No	No
Amoudry et al. (2008)	Two-equations ($k - \epsilon$)	KTGF	Yes	No	No	No	Yes	2-5	No	1DV	No	No
Bakhtyar et al. (2009)	Two-equations ($k - \epsilon$)	Savage and McKeown (1983)	Yes	Yes (R =0.63)	No	No	No	0.13-0.15-0.2-0.28	No	2DHV	No	No
Bakhtyar et al. (2010)	Two-equations ($k - \epsilon$)	Ahilan and Sleath (1987)	Yes	Yes (R =0.63)	Yes	Yes	Yes	0.5-0.8-1	No	2DHV	Yes	Yes
Yu et al. (2010)	Two-equations ($k - \epsilon$)	KTGF	Yes	Yes (R =0.63)	Yes	Yes	Yes	0.24	No	2DHV	Yes	Yes

Continuation of Table 2.1

Author (s)	Turbulence closure	Sediment stress closure	Studied waves				Waves plus Current	Sediment grains size (s) (D_{50}) (mm)	Mixed sands	Dim.	Bed slope	Streaming effect
			Sym.	Sk.	Asym.	Sk. plus Asym.						
Chen et al. (2011)	Two-equations ($k-\epsilon$)	Ahilan and Sleath (1987)	Yes	Yes (R =0.63)	No	No	No	0.13-0.2-0.27-0.46	No	2DHV	No	No
Yu et al. (2012)	Two-equations ($k-\epsilon$)	KTGF	Yes	Yes (R =0.63)	No	No	Yes	0.24-0.28	No	2DHV	No	Yes
Kranenburg et al. (2013)	Two-equations ($k-\epsilon$)	KTGF	Yes	Yes (R =0.63)	No	No	No	0.138-0.15-0.245-0.27-0.46	No	1DV	No	Yes
Revil-Baudard and Chauchat (2013)	Zero-equation	DGFR	No	No	No	No	No	0.25-2.60	No	1DV	No	No
Cheng et al. (2017)	Two-equations ($k-\epsilon$)	KTGF	Yes	Yes (R =0.63)	No	No	No	0.28-0.20	No	3D	No	No
Kim et al. (2019)	Two-equations ($k-\epsilon$)	KTGF	Yes	Yes (R =0.61)	Yes	Yes	No	0.17	No	3D	Yes	Yes
Rafati et al. (2022)	Two-equations ($k-\epsilon$)	KTGF	Yes	Yes (R =0.61)	Yes	Yes	No	0.21, 0.34, 0.97	Yes	3D	Yes	Yes

3 Intercomparison of transport formulas

Although extensive research on uniform sediment transport under sheet flow has been carried out, the studies on graded sands are rare. To fill this knowledge-gap, this chapter compares the predicted net transport rate for five groups of graded sands experiments (52 test cases) as described in section 2.4. These experiments were performed in various Oscillatory Flow Tunnels (OFTs) (Fig. 2.15) under nonlinear wave induced sheet flow conditions. Consequently, using statistical parameters the accuracy of formulas is systematically evaluated and using their intercomparison the guidelines for modelers on selecting the most accurate one within corresponding conditions is presented. The considered experiments in this chapter cover a suitable range of sediment non-uniformity indices (D_{90}/D_{10}=3.12-9.82) and wave nonlinearity periods (T=3-12 s). Moreover, the studied formulas are recommended/mostly-applied for cross-shore sheet flow induced transport rate predictions.

3.1 Wave nonlinearity and sediment non-uniformity

Wave nonlinearity (section 2.4, Fig. 2.16 and Fig. 2.17) and sediment non-uniformity (section 2.4 and Fig. 2.15) are two influencing parameters in sediment transport. Although there is a comprehensive literature on both subjects, sediment non-uniformity integrated with wave nonlinearity in sediment transport, as observed in nature, needs further investigation. Wave nonlinearity is the natural property of water waves in shoaling and surf zone and based on experiments of Hassan and Ribberink (2005), sediment non-uniformity can significantly change the sediment transport rate for mixed sand compared to uniform sand with the same median grain size.

3.1.1 Wave nonlinearity

The importance of the wave nonlinearity and its classification into the velocity skewness and acceleration asymmetry (section 2.4, Fig. 2.16 and Fig. 2.17) were introduced in chapter 2. However, a real surface wave as illustrated schematically in Fig. 3.1 seems to be neither entirely skewed nor purely asymmetric, but it could be represented as a combination of both skewness and asymmetry.

3.1.2 Sediment non-uniformity

To study the influence of sediment non-uniformity, it is useful to consider a principal sketch as illustrated in Fig. 2.2. As can be seen, finer grains are hidden among the coarser ones and consequently the exposure of coarser sands to the carrier flow is increased. In order to include these hiding/exposure processes in practical formulas for uniform sand transport predictions, proposed modification factors are implemented.

Hiding/exposure modification factors represented by Egiazaroff (1965) and Day (1980) are two known approaches, which take into account the multi-fractional interactions in different ways. The Egiazaroff (1965) modification factor tries to modify the uniform sand equations by increasing the threshold of critical shear stress for finer and reducing it for coarser sand. Therefore, the coarser sands in a multi-fractional mixture will be entrained easier compared to uniform condition (single fraction). In contrast, the finer fractions entrainment will require higher shear stresses compared to uniform conditions.
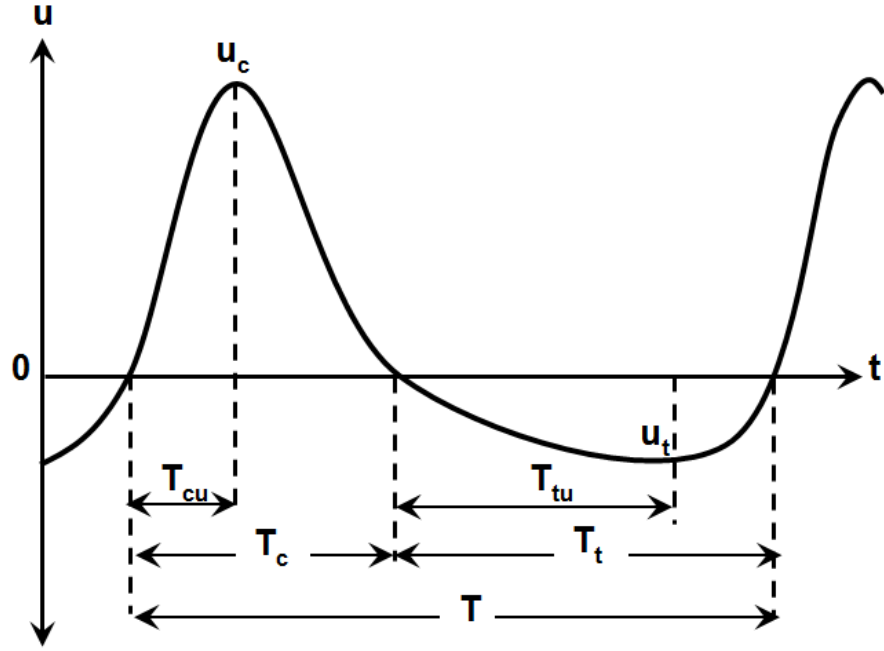
Figure 3.1: Definition of parameters for a field-observed nonlinear (skewed and asymmetric) wave.

The Egiazaroff (1965) modification factor for each fraction in a mixture is defined as:

$$\xi_{Egi.,j} = \frac{\theta_{cr(corrected),j}}{\theta_{cr,j}} = (\frac{log19}{log(19D_j/D_m)})^2 \tag{3.1}$$

where $\theta_{cr(corrected),j}$, and $\theta_{cr,j}$ are the corrected and original critical Shields parameters for the jth fraction, respectively. The D_j and D_m are the grain size of the jth fraction and the mean grain size of the mixture. The $\theta_{cr,j}$ can be computed following the proposed approach by Van Rijn (1993) as a function of non-dimensional grain size D_j^* (Eq. 2.6).
Contrary to the Egiazaroff (1965) approach, the Day (1980) approach tries to modify the effective shear stress applied on the sediment fractions. This approach is formulated on the basis of a large number of experiments, whereas the Egiazaroff (1965) approach has a theoretical basis. It is defined as:

$$\xi_{Day,j} = (\frac{0.4}{(D_j/D_A)^{0.5}} + 0.6) \tag{3.2}$$

where D_A is the ineffective grain size of mixture (grain size in the mixture that needs no correction (Cloin, 1998)), which is not necessarily equal to D_{50} but nearly depends on the gradation level. It is defined as:

$$\frac{D_A}{D_{50}} = 1.6(\frac{D_{84}}{D_{16}})^{-0.28} \tag{3.3}$$

where D_{50}, D_{84} and D_{16} are respectively the diameters through which 50%, 84% and 16% of the total graded sand mass is passing.
To investigate the performance of these hiding/exposure modification strategies, Cloin (1998) conducted a series of bimodal graded sand experiments under skewed waves and

slightly asymmetric waves within sheet flow conditions at the LOWT. It was concluded that the Day (1980) approach reproduces more promising results than the Egiazaroff (1965) approach. Moreover, Hassan et al. (2001) compared their experimental dataset with predicted transport rates by means of integrated Egiazaroff (1965) as well as the Day (1980) approaches in practical formulas. It was suggested that the Day (1980) approach is significantly more efficient in improving the accuracy of predicted results than the Egiazaroff (1965) approach.

Van Rijn (2007) introduced a dimensionless bed shear stress parameter using Egiazaroff (1965) modification factor within four scenarios that for the sake of brevity are not presented here. A simplified modification factor following the Van Rijn (2007) scenarios was applied by Van der A et al. (2013) in the SANTOSS (2013) formula to modify the effective shear stress on each fraction as:

$$\xi_{V,j} = (\frac{D_j}{D_{50}})^{0.25} \tag{3.4}$$

in which $\xi_{V,j}$ is the simplified modification factor and D_{50} is the medium grain size of graded sand.

3.2   Sediment transport approaches

The available practical formulas to predict sediment transport rate can generally be classified in three main groups (Van der A et al., 2013). The first group is known as time–averaged formulas, which follow the approach of Bijker (1971) based on the bed shear stress approximation. They apply separate formulas for bed- and suspended-load prediction by means of time-averaged wave induced shear stresses. Moreover, they usually assume that the wave velocity component is collinear with the current velocity.

The second group is termed as quasi-steady formulas which include the temporal components. In this group, the instantaneous velocity is directly applied in transport formulas. Therefore, they are not capable of including the unsteady mechanisms induced by phase-lag between wave velocity and sediment concentration (Dohmen-Janssen et al., 2002). The Bailard (1981) and the Ribberink (1998) formulas are two known examples of this group. However, in the same way like the Bijker (1971) formula in the first group, the Bailard (1981) formula predicts the transport rate through suspended- and bed-loads, whereas the Ribberink (1998) formula is a bed-load transport formula.

The third group is referred to as semi-unsteady formulas which have been developed to take the unsteady behavior of velocity and concentration (phase-lag effect) into account. On the basis of these formulas, entrained sediments in the crest-/trough-parts of a wave period are not resettled in the same part of the wave period. Therefore, there is usually a sediment interchange between two parts of a wave period, particularly for fine sands and short wave periods, where the sediments are suspended for a longer time relative to the wave period. Dibajnia and Watanabe (1992) were the first, who developed a systematic methodology to take the phase-lag effect into account and other available semi-unsteady formulas have a close relationship with this formula. The more recently published SANTOSS (2013) formula (Van der A et al., 2013) is the newest modified version of this group. To apply the aforementioned groups of formulas to graded sands, the simplest approach is a direct proportional contribution of each fraction in graded sands transport rate as:

$$q_g = \sum_{j=1}^{N} p_j q_j \tag{3.5}$$

where q_g is the transport rate of graded sand, q_j is the individual fractional transport rate (in such a way that each fraction is considered as a single fraction), p_j represents the contribution percentage of corresponding fraction and N is the number of contributing fractions. When $N=1$, Eq. 3.5 estimates the net transport rate for a single fraction (uniform) sand. However, as can be seen, this equation is only a linear-weighted average of constituting fractions and therefore it cannot take the interaction among different fractions (e.g. hiding/exposure processes) into account. These modifications are included by means of hiding/exposure modification factors.

3.2.1   Quasi-steady formulas

Quasi-steady formulas assume an instantaneous reaction of exposed sediments to oscillatory flows. They are more useful for conditions where sediments pick-up and resettling occur in a much shorter time-scale than the wave period, like coarse sands.

3.2.1.1   Bailard formula

Bailard (1981) developed a general formula for sediment transport rate prediction based on the wave energy concept represented already by Bagnold (1963). He defined the sediment transport load through two major classical loads, (i.e., bed- and suspended-load) as:

$$q_{t,j}(t) = q_{b,j}(t) + q_{s,j}(t) \tag{3.6}$$

in which $q_{t,j}(t)$, $q_{b,j}(t)$ and $q_{s,j}(t)$ are respectively the time-dependent total-, bed- and suspended-load transport rates per unit width $(m^3 m^{-1} s^{-1})$ corresponding to the jth fraction. The bed-load for a horizontal bed is given by:

$$q_{b,j}(t) = \frac{0.5 f_w \epsilon_b}{(s-1)g\ tan(\varphi)} |u^2(t)| u(t) \tag{3.7}$$

and suspended-load:

$$q_{s,j} = \frac{0.5 f_w \epsilon_s}{(s-1)g\ w_{s,j}} |u^3(t)| u(t) \tag{3.8}$$

where f_w is the wave friction factor computed according to Swart (1974) as Eq. 2.16. ϵ_b and ϵ_s are the bed- and suspended-load efficiency factors proposed from a calibration with field data as 0.1 and 0.02, respectively. φ is the friction angle of sediments (herein $tan(\varphi)$ =0.63) and $w_{s,j}$ (ms^{-1}) is the settling velocity of jth fraction in still-water, computed by means of the Soulsby (1997) formula as:

$$w_{s,j} = \frac{\nu}{D_j} (\sqrt{(m_s{}^2 + n_s D_j^{*3})} - m_s) \tag{3.9}$$

where m_s=10.36 and n_s=1.049. As can be seen, the Bailard (1981) formula is independent of effective and critical Shields parameters due to the direct application of instantaneous velocity. Therefore, the previously discussed hiding/exposure modification factors in section 3.1.2 are not applicable to the Bailard (1981) formula. In addition, the bed- and suspended-loads are directly related to the third and fourth powers of instantaneous wave velocity, respectively. As a result, it would be expected that under high velocities (such as sheet flow conditions) the suspended-load will be higher than the bed-load. Fig. 3.2b illustrates the time dependent transport rate estimated by the Bailard (1981) formula for
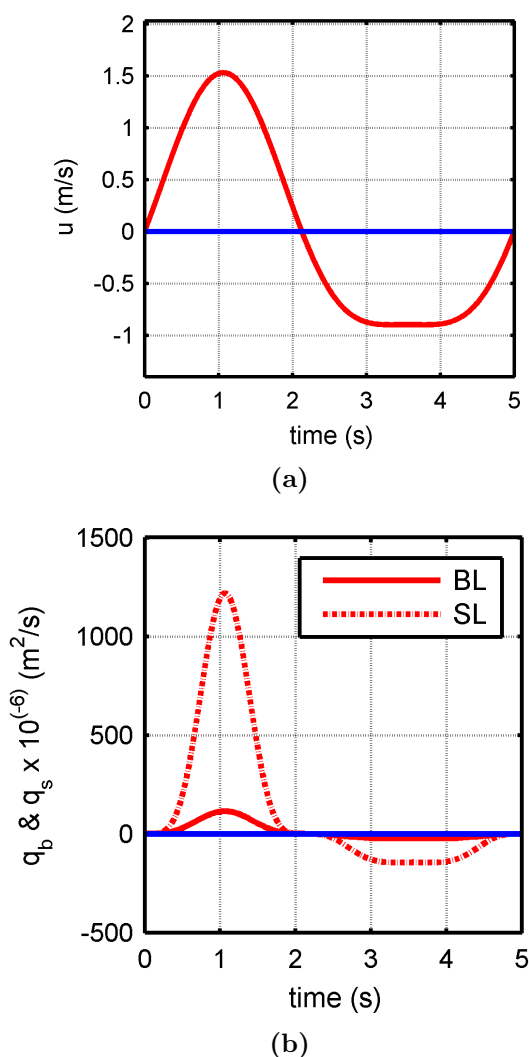
Figure 3.2: (a) Time series of the near-bed skewed velocity of O'Donoghue and Wright (2004a) for test-case Mix1 (X1)-A5010, (b) corresponding Bailard (1981) formula transport rate prediction, BL: Bed-load, SL: Suspended load.

test case Mix1(X1) of O'Donoghue and Wright (2004a). The graded sand in this experiment consists of 60% fine (D_{50}=0.15 mm), 30% medium (D_{50}=0.28 mm) and 10% coarse (D_{50}=0.51 mm) sand under skewed waves with T=5 (sec) and R=0.63 as shown in Fig. 3.2 a.

It is apparent that instantaneous velocity shape (Fig. 3.2 a) has simultaneously appeared in both bed- and suspended loads (Fig. 3.2 b) which is the main characteristic of the quasi-steady formulas group.

Moreover, the onshore transport load is by far larger than offshore one which, as will be evaluated in section 3.6, confirms that the Bailard (1981) formula is an onshore oriented transport formula. Furthermore, the predicted suspended load is by far larger than the bed load. It can be explained by forth power of velocity in suspension-load (Eq. 3.8) compared with third power for bed-load (Eq. 3.9). The time-averaged predicted loads for this test case are outlined in Tab. 3.1. As can be seen, the predicted suspended-loads for sand frac-

Table 3.1: Predicted sediment transport rate for the test case Mix1(X1)-A5010 of O'Donoghue and Wright (2004a) by means of the Bailard (1981) formula.

Test case	D_{50} (mm)	Percen. (%)	Sus.-load $\times 10^{-6}$ $(m^2 s^{-1})$	Bed-load $\times 10^{-6}$ $(m^2 s^{-1})$	Predicted total transport rate $\times 10^{-6}$ $(m^2 s^{-1})$	Meas. total transport rate $\times 10^{-6}$ $(m^2 s^{-1})$
Mix1	0.15	60	183.23	11.17	0.60×194.40+	
(X1)-	0.28	30	67.30	11.17	0.30×78.47+	15
A5010	0.51	10	34.40	11.20	0.10×45.60=144.74	

tions vary significantly, whereas the bed-loads are interestingly similar. It can be explained by the fact that the bed-load formulation of Bailard (1981) is a function of relative sand density (s), instantaneous wave velocity $(u(t))$, internal friction angle $(tan(\varphi))$, and wave friction factor (f_w). However, all of these parameters apart from the f_w remain constant. The f_w for each fraction is a function of D_{50} which influences the roughness coefficient (k_s) through a small exponent (0.194). Furthermore, the predicted net transport rate for this test case is over-predicted more than nine times.

3.2.1.2   Ribberink formula

The weak performance of the Bailard (1981) formula is due to the misrepresentation of the suspended-load as the dominant load (cf. Fig. 3.2b), which in turn renders this formula incapable of representing the transport load in sheet flow, where the main transport load is defined as bed-load. Therefore, Ribberink (1998) proposed a transport formula predominantly constituting of bed-load, applying the Shields parameter threshold instead of directly implementing the velocity like in the Bailard (1981) formula. The modified form with incorporation of the Day (1980) modification factor for j^{th} fraction is represented as:

$$q_j = \begin{cases} \sqrt{(s-1)gD_j^3} \ m_r \ (\xi_{Day,j}|\theta_j(t) - \theta_{cr,j}|^{n_r} \ \frac{\theta_j(t)}{|\theta_j(t)|}) & \text{if } |\theta_j(t)| > \theta_{cr,j} \\ 0 & \text{if } |\theta_j(t)| < \theta_{cr,j} \end{cases} \quad (3.10)$$

in which m_r and n_r are calibration coefficients proposed based on a large number of flume and field datasets as 11 and 1.65, respectively. The $\theta_j(t)$ is the instantaneous effective Shields parameter for j^{th} fraction and is given as:

$$\theta_j(t) = \frac{0.5 f_w u(t)|u(t)|}{(s-1)gD_j} \quad (3.11)$$

As can be seen, the Ribberink (1998) formula strongly depends on the sediment grain size in $\sqrt{(s-1)gD_j^3}$ term as well as critical and effective Shields parameters. This leads to high sensitivity of the Ribberink (1998) formula to grain size (Camenen and Larroudé, 2003). Moreover, the Ribberink (1998) formula is based on the Shields parameter, and consequently the modification factors of graded sands are applicable in the Ribberink (1998) formula.

Fig. 3.3 exemplarly represents the net transport rate for test case Mix1(X1) (which was already discussed by application the Bailard (1981) formula in the previous section) by means of Ribberink (1998) formula. As it would be expected from quasi-steady formulas, the skewed instantaneous velocity shape (Fig. 3.3a) is apparent in the corresponding transport rate of Ribberink (1998) formula (Fig. 3.3b).

(a)

(b)
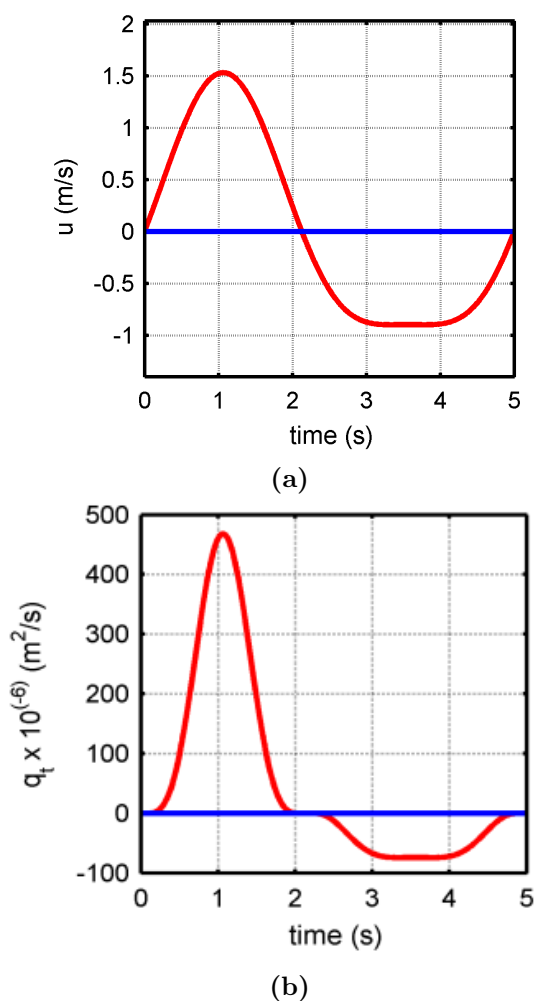
Figure 3.3: (a) Time series of the near-bed skewed velocity of O'Donoghue and Wright (2004a) for test-case Mix1 (X1)-A5010, (b) corresponding Ribberink (1998) formula transport rates.

Tab. 3.2 outlines the net transport rate of each fraction and also the total graded sand

Table 3.2:   Predicted sediment transport rate for the test case Mix1(X1)-A5010 of O'Donoghue and Wright (2004a) by means of the Ribberink (1998) formula.

Test case	D_{50} (mm)	Percen. (%)	Net transport rate $\times 10^{-6}$ (m^2s^{-1})	Predicted total transport rate $\times 10^{-6}$ (m^2s^{-1})	Meas. total transport rate $\times 10^{-6}$ (m^2s^{-1})
Mix1	0.15	60	56.16	0.60×56.16+	
(X1)-	0.28	30	41.80	0.30×41.80+	15
A5010	0.51	10	32.11	0.10×32.11=49.45	

transport for the Mix1 (X1) test case using Ribberink (1998) formula incorporated with Day (1980) modification factor. According to the Tab. 3.2, the predicted transport rate for each fraction varies due to the hiding/exposure factor application, and consequently

the net transport rate of coarse sand (D_{50}=0.51 mm) is around half of the net transport rate of fine sand (D_{50}=0.15 mm). However, its fractional volume in graded sand is only one sixth of fine sand (10% compared to 60%). Likewise, the net transport rate of medium sand (D_{50}=0.28 mm) is by 74% of fine sands, while its volume contribution in graded sand is half times that of fine sands. Moreover, the Ribberink (1998) formula seems to present a more reasonable prediction transport rate than the Bailard (1981) formula for this graded sand under sheet flow conditions. The total transport rate predicted by the Ribberink (1998) formula is slightly more than three times over-predicted, whereas the Bailard (1981) is nine times over-predicted.

3.2.2   Semi-unsteady formulas

Due to the phase-lag between wave propagation velocity and sediment concentration, as well as the hindered settling in high sediment concentration, sediments do not follow the wave hydrodynamics simultaneously. Therefore, the entrained sediments do not settle back to the bed within the corresponding part of the wave period and consequently interchanged with the successive part. Among discussed groups of empirical formulas, only semi-unsteady formulas are capable of describing this unsteady behavior.

3.2.2.1   Dibajnia and Watanabe formula

Dibajnia and Watanabe (1992) proposed a general formula for sediment transport to take the unsteady mechanism of the phase-lag effect into account. They defined a time-scale based on a simplified energy balance principle as:

$$\zeta_i = \frac{T_{fall}}{T_i} = \frac{u_i^2}{2g(s-1)W_{s,j}T_i} \tag{3.12}$$

where the subscript "i" is for the crest-part of the wave period "c", and for the trough-part "t" (Fig. 3.1). T_{fall} is the required time for resettling a picked-up sediment particle from the bed in its corresponding part of the wave period. u_i^2 is representative of the kinetic wave energy for each part of the wave period and is given for crest and trough as:

$$u_c^2 = \frac{2}{T_c}\int_0^{T_c} u^2 dt \tag{3.13}$$

and

$$u_t^2 = \frac{2}{T_t}\int_{T_c}^{T} u^2 dt \tag{3.14}$$

The net transport rate for j^{th} fraction was proposed as:

$$q_j = \lambda_d W_{s,j}D_j\Gamma_j|\Gamma_j|^{-0.5} \tag{3.15}$$

where λ_d is a calibration factor and proposed by Dibajnia and Watanabe (1996), based on their experiments in the TUOFT, as 0.0015, and Γ_j is defined by:

$$\Gamma_j = \frac{u_c T_c(\Omega_{c,j}^3 + \Omega_{t,j}^{'3}) - u_t T_t(\Omega_{t,j}^3 + \Omega_{c,j}^{'3})}{(u_c + u_t)T} \tag{3.16}$$

where Ω determines the rate of sediment interchange between successive parts of a wave period and is defined through a time-scale conditional formula as:

$$
\begin{cases}
\text{if} \quad \zeta_{i,j} \leq \zeta_{cr,j} & \begin{cases} \Omega_{i,j} = \zeta_{i,j} T_i \sqrt{\frac{sg}{D_j}} \\ \Omega'_{i,j} = 0 \end{cases} \\[4ex]
\text{if} \quad \zeta_{i,j} > \zeta_{cr,j} & \begin{cases} \Omega_{i,j} = \zeta_{cr,j} T_i \sqrt{\frac{sg}{D_j}} \\ \Omega'_{i,j} = (\zeta_{i,j} - \zeta_{cr,j}) T_i \sqrt{\frac{sg}{D_j}} \end{cases}
\end{cases}
\tag{3.17}
$$

where $\zeta_{cr,j}$ is the critical time-scale parameter for j^{th} fraction and distinguishes an oscillatory flow with dominantly sheet flow condition from ripple-bed condition. According to Dibajnia and Watanabe (1996), $\zeta_{cr,j}$ is suggested to be considered equal to one.

3.2.2.2   Tanaka formula

Tanaka (2000) adjusted the Dibajnia and Watanabe (1996) formula to take into account the hiding and exposure effect through the time-scale ($\zeta_{i,j}$) modifications and interchange rate Ω. According to TUOFT experiments for graded sands, interchange rate Ω is modified as:

$$
\begin{cases}
\text{if} \quad (\zeta_{i,j}\lambda_2) \leq \zeta_{cr,j} & \begin{cases} \Omega_{i,j} = \zeta_{i,j} T_i \sqrt{\frac{sg}{D_j}} \lambda_1 \\ \Omega'_{i,j} = 0 \end{cases} \\[4ex]
\text{if} \quad (\zeta_{i,j}\lambda_2) > \zeta_{cr,j} & \begin{cases} \Omega_{i,j} = \frac{\zeta_{cr,j}}{\lambda_2} T_i \sqrt{\frac{sg}{D_j}} \lambda_1 \\ \Omega'_{i,j} = (\zeta_{i,j} - \frac{\zeta_{cr,j}}{\lambda_2}) T_i \sqrt{\frac{sg}{D_j}} \lambda_1 \end{cases}
\end{cases}
\tag{3.18}
$$

where λ_1 and λ_2 are modification factors and defined by: $\lambda_1 = (D_j/D_m)^{0.5}$ and $\lambda_2 = (D_j/D_m)^{0.7}$ wherein D_m is the arithmetic mean size of the graded sand and is computed by:

$$
D_m = \sum_{j=1}^{N} p_j D_j
\tag{3.19}
$$

The net transport rate for j^{th} fraction was calculates like the Dibajnia and Watanabe (1996) formula as:

$$
q_j = 0.0015 W_{s,j} D_j \Gamma_j |\Gamma_j|^{-0.5}
\tag{3.20}
$$

3.2.2.3   Ahmed and Sato formula

Ahmed and Sato (2003) performed a remarkable number of experiments for bi and trimodal graded sands under sheet flow conditions induced by skewed waves (first-order cnoidal) in the TUOFT. Analyzing the experiments and comparing them with Dibajnia and Watanabe (1996) predictions yield in a new modified Dibajnia and Watanabe (1996) formula as:

$$
q_j = \gamma W_{s,j} D_j \left(\frac{1}{D_j^*}\right) \frac{u_c T_c (\Omega_{c,j}^2 + \Omega'^2_{t,j}) - u_t T_t (\Omega_{t,j}^2 + \Omega'^2_{c,j})}{(u_c + u_t)(T_c + T_t)}
\tag{3.21}
$$

where γ is a calibration factor and proposed to 300 based on the TUOFT experiments and interchange rate Ω is defined as:

$$
\begin{cases}
\text{if} \quad (\zeta_{i,j}\eta) \leq \zeta_{cr,j} & \begin{cases} \Omega_{i,j} = \zeta_{i,j}(\frac{2W_{s,j}T_i}{D_j})^{0.4}\,\eta \\ \Omega'_{i,j} = 0 \end{cases} \\
\text{if} \quad (\zeta_{i,j}\eta) > \zeta_{cr,j} & \begin{cases} \Omega_{i,j} = \zeta_{cr,j}(\frac{2W_{s,j}T_i}{D_j})^{0.4}\,\eta \\ \Omega'_{i,j} = (\zeta_{i,j} - \zeta_{cr,j})(\frac{2W_{s,j}T_i}{D_j})^{0.4}\,\eta \end{cases}
\end{cases}
\tag{3.22}
$$

where

$$
\zeta_{i,j} = \theta_{i,j}(\frac{a_m}{D_j})^{0.29}\frac{D_j}{W_{s,j}T_i}
\tag{3.23}
$$

and η is the hiding/exposure parameter which is defined by:

$$
\eta = \begin{cases}
0.25 + 0.276\,exp(D_j/D_m) & \text{if } \frac{D_j}{D_m} \leq 1 \\
1 + 2(\frac{D_j}{D_m} - 1)\,exp(1 - D_j/D_m) & \text{if } \frac{D_j}{D_m} > 1
\end{cases}
\tag{3.24}
$$

3.2.2.4   SANTOSS (2013) formula

Van der A et al. (2013) developed a formula based on the unsteady approach of Dibajnia and Watanabe (1992) which is known as SANTOSS (2013) formula. However, contrary to the Dibajnia and Watanabe (1992) formula and its previous adjustments, the SANTOSS (2013) formula implements the effective shear stress instead of velocity (in the same way as Ribberink (1998) formula. In addition, it applies the phase-lag parameter as the condition instead of the already applied time-scale parameter. Moreover, the asymmetric waves, progressive waves, and steady flows as well as graded sands are included in this formula. The SANTOSS (2013) formula with incorporated modification factor for graded sands is written as follows:

$$
q_i = \sqrt{(s-1)gD_j^3}\frac{(Q_c + Q_t)}{T}
\tag{3.25}
$$

Where:

$$
Q_c = \sqrt{|\xi_{V,j}\theta_{c,j}|}T_c(\Omega_{cc,j} + \frac{T_c}{2T_{cu}}\Omega_{tc,j})\frac{\theta_{c,j}}{|\theta_{c,j}|}
\tag{3.26}
$$

and

$$
Q_t = \sqrt{|\xi_{V,j}\theta_{t,j}|}T_t(\Omega_{tt,j} + \frac{T_t}{2T_{tu}}\Omega_{ct,j})\frac{\theta_{t,j}}{|\theta_{t,j}|}
\tag{3.27}
$$

where $\theta_{i,j}$ stands for the effective shear stress in the crest/trough cycle on j^{th} fraction and for oscillatory flows without current as:

$$
\theta_{i,j} = \frac{0.5f_w|\tilde{u}_{i,r}|\tilde{u}_{i,r}}{(s-1)gD_j}
\tag{3.28}
$$

in which $\tilde{u}_{i,r}$ is the root mean square velocity of a sinusoidal flow with amplitude of $\hat{u}_i$ and is acquired as:

$$
\tilde{u}_{i,r} = \frac{\hat{u}_i}{\sqrt{2}}
\tag{3.29}
$$

in which $\hat{u}_i$ is the representative orbital velocity amplitude in crest or trough. The velocity for the whole flow cycle is obtained as:

$$\hat{u} = \sqrt{\frac{2}{T} \int_0^T u^2(t)dt} \tag{3.30}$$

The f_w is computed using the modified Swart (1974) formula by the Da Silva et al. (2006) approach as:

$$f_w = \begin{cases} exp\left(5.213\left(\frac{k_{sw}}{\gamma\hat{a}}\right)^{0.194} - 5.977\right) & \text{if } \left(\frac{k_{sw}}{\hat{a}}\right) < 0.635 \\ 0.3 & \text{if } \left(\frac{k_{sw}}{\hat{a}}\right) \geq 0.63 \end{cases} \tag{3.31}$$

where k_{sw} is the bed-roughness height under wave induced sheet flow and γ is a dimensionless parameter given by:

$$\gamma = \left(\frac{2T_{iu}}{T_i}\right)^{c_1} \tag{3.32}$$

where c_1 is a constant and was suggested by Da Silva et al. (2006) as c_1=2.6. Ribberink (1998) proposed the k_{sw} formula as:

$$k_{sw} = max\{D_{50}, D_{50}(1 + 6(\langle|\theta|\rangle - 1))\} \tag{3.33}$$

where $\langle|\theta|\rangle$ is the time-averaged of the Shields parameter absolute value within a wave period and represented as:

$$\langle|\theta|\rangle = \frac{0.5f_w\langle u(t)^2\rangle}{(s-1)gD_{50}} \tag{3.34}$$

$\hat{a}$ is the orbital excursion amplitude for the whole flow period and is given as:

$$\hat{a} = \frac{T\hat{u}}{2\pi} \tag{3.35}$$

The Ω value, which is the non-dimensional sediment entrainment potential, is defined by:

$$\Omega_{cc} = \begin{cases} \Omega_c & \text{if } P_c \leq 1 \\ \frac{1}{P_c}\Omega_c & \text{if } P_c > 1 \end{cases} \tag{3.36}$$

$$\Omega_{ct} = \begin{cases} 0 & \text{if } P_c \leq 1 \\ (1 - \frac{1}{P_c})\Omega_c & \text{if } P_c > 1 \end{cases} \tag{3.37}$$

$$\Omega_{tt} = \begin{cases} \Omega_t & \text{if } P_t \leq 1 \\ \frac{1}{P_t}\Omega_t & \text{if } P_t > 1 \end{cases} \tag{3.38}$$

$$\Omega_{tc} = \begin{cases} 0 & \text{if } P_t \leq 1 \\ (1 - \frac{1}{P_t})\Omega_t & \text{if } P_t > 1 \end{cases} \tag{3.39}$$

where Ω_i is computed by means of the Ribberink (1998) formula as:

$$\Omega_i = \begin{cases} m_r(|\xi_i\theta_i| - \theta_{cr,j})^{n_r} & \text{if } |\xi_i\theta_i| > \theta_{cr,j} \\ 0 & \text{if } |\xi_i\theta_i| \leq \theta_{cr,j} \end{cases} \tag{3.40}$$

where m_r and n_r are empirical coefficients proposed as: m_r=11 and n_r=1.2. The T_c, T_t, T_{cu} and T_{tu} are defined as illustrated in Fig. 3.1. The $P_{i,j}$ is the phase-lag number of the corresponding part of the wave period for j^{th} fraction and is represented as:

$$P_{i,j} = \frac{\alpha_p \delta_{si}}{2(T_i - T_{iu})W_{s,j}} \tag{3.41}$$

in which α_p is the calibration coefficient proposed as $\alpha_p = 8.2$, and δ_{si} stands for the sheet flow layer thickness (SFLT) in the corresponding part of the wave period. It is computed by means of the Dohmen-Janssen (1999) formula as:

$$\frac{\delta_{si}}{D_{50}} = \begin{cases} 25\hat{\theta}_i & \text{if} \quad D_{50} \leq 0.15 \; mm \\ [25 - \frac{12(D_{50}-0.15)}{(0.20-0.15)}] & \text{if} \quad 0.15 \; mm < D_{50} < 0.20 \; mm \\ 13\hat{\theta}_i & \text{if} \quad D_{50} \geq 0.20 \; mm \end{cases} \tag{3.42}$$

In this thesis a new modification on the SANTOSS (2013) formula in section 3.3.7 is developed, that parameterizes the SFLT based on the degree of the sand heterogeneity and the fine fraction percentage. Moreover, the performance of the newly modified SFLT equation in the net sand transport prediction accuracy is evaluated.

3.3 Intercomparison and evaluation of transport formulas

To compare the accuracy and assess the suitability of the aforementioned formulas, the predicted transport rates for five groups of available experiments with graded sands under sheet flow conditions, as were introduced in chapter 2, are discussed. To this end, the accuracy of formulas is evaluated based on the Brier Skill Score (BSS)(Van Rijn et al. (2003) and Van der A et al. (2010)), which is defined as $BSS = 1 - \langle|q_{s,pre.} - q_{s,meas.}|^2\rangle/\langle q^2_{meas.}\rangle$. The accuracy levels of BSS is defined as: BSS=1 : prefect agreement; BSS=1-0.8 : good; BSS=0.8-0.6 : fair; BSS=0.6-0.3 : poor; BSS=0.3-0 : bad; $BSS < 0$: do-nothing scenario. The next evaluation parameter is bias. Bias is defined as $bias = \langle(q_{s,pre.} - q_{s,meas.})/q_{s,meas.}\rangle$ and indicates the over-prediction trend, when it is positive and under-prediction, when it is negative. The Pearson correlation coefficient ($Corr.$) is also applied to evaluate the linear dependency of the predicted results to the measurements. All of these experiments have been performed under skewed waves. Moreover, the asymmetric waves were also additionally generated among LOWT experiments by Hamm et al. (1998). Owing to the various sediment fractions, wave conditions, as well as the degree of wave nonlinearity, the number of experiments in each group differs. The sediment grain sizes cover a wide range of fine sands (D_{50}=0.128, 0.13, 0.15 mm) to coarse sands (0.74 and 0.97 mm). The wave periods also vary from short waves (T=3, 5 s) to long waves (T=7.5, 12 s). Lastly, the 52 experiments (Appendix A-Tab. A1) are analyzed and compared as follows:

3.3.1 Bailard formula predictions

Using the Bailard (1981) formula (Eq. 3.7 and 3.8), the time-averaged transport rate of each fraction is computed. Then using equation 3.5 , the net transport rate for graded sands is determined. Fig. 3.4 shows the comparison between time-averaged predicted net transport rates by means of the Bailard (1981) formula and measured ones. As can be seen, the Bailard (1981) formula over-predicts the measured results, particularly for experiments containing fractions of fine sands. None of the predicted transport rates for AOFT

experiments of O'Donoghue and Wright (2004a) as well as LOWT experiments of Hamm et al. (1998), which include different percentages of fine sands, are placed within the borders with factor of two of the measurements.

Moreover, the Bailard (1981) formula is an onshore-oriented prediction formula, and hence

Figure 3.4: Comparison of the measured net transport rates with the predicted results by means of the Bailard (1981) formula. The solid diagonal line depicts the perfect agreement and dashed lines the differences with factor 2.

is incapable of predicting the offshore transport rates (negative transport rates). Furthermore, the Bailard (1981) formula is incapable of predicting the transport rate for pure asymmetric tests of Hamm et al. (1998), where they are predicted as zero. The statistics parameters for evaluating the predicted results are outlined in Tab. 3.3. It is apparent that the Bailard (1981) formula due to the phase-lag effect, particularly for fine sands, cannot estimate the transport rate accurately. The highest positive bias for predicted results ($bias$=1.52) illustrates that the Bailard (1981) formula is the most over-predictive formula among other formulas. Moreover, the predicted transport rates have the lowest correlation with measured rates (29.85%). Therefore, it can be concluded that the Bailard (1981) formula is not suitable to predict the transport rate for graded sands under sheet

Table 3.3: Statistics parameters to evaluate the formulas performance (the total number of experiments is 52 (Tab. A1)).

Prediction formula	BSS	$Bias$	$Corr.(\%)$
Bailard (1981)	-4.37	1.52	29.85
Ribberink (1998)	0.20	0.29	66.69
Dibajnia and Watanabe (1996)	0.33	-0.36	35.69
Tanaka (2000)	0.71	0.19	59.79
Ahmed and Sato (2003)	0.44	-0.33	57.57
SANTOSS (2013)	0.84	0.13	79.13
This thesis (section 3.3.7)	0.92	-0.09	90.22

flow conditions.

3.3.2 Ribberink formula predictions

In contrast to the Bailard (1981) formula, due to depending of the Ribberink (1998) formula on the bed-shear stress, the proposed hiding/exposure modification factors are applicable. The applied hiding/exposure modification factor in the Ribberink (1998) formula is the Day (1980) formula. Moreover, due to the application of sheet flow experiment results in calibration of the Ribberink (1998), as would be expected, the Ribberink (1998) formula predicts the transport rates more accurately than the Bailard (1981) formula. Fig. 3.5 shows the comparison of time-averaged predicted transport rates using the Ribberink (1998) formula with measured datasets. As it is apparent, the Ribberink (1998) formula also over-predicts the transport rates and, like the Bailard (1981) formula, cannot predict the negative transport rate for offshore transported sediments.

Moreover, it is also incapable of predicting the transport rate for asymmetric nonlinear waves. However, as outlined in Tab. 3.3, the bias is reduced to around six times that of the Bailard (1981) formula and the correlation is increased to more than two times that of the Bailard (1981) formula, to 66.69%. But BSS is 0.20, which does not classifies the accuracy level of Ribberink (1998) formula based on the proposed groups by Van Rijn et al. (2003) in the good group (Tab. 3.3).

3.3.3 Dibajnia and Watanabe formula predictions

The unsteady mechanism of sediment interchange between two parts of a wave period for nonlinear waves was included in the Dibajnia and Watanabe (1996) formula. The predicted results by means of the Dibajnia and Watanabe (1996) formula are not like the Bailard (1981) or the Ribberink (1998) time-averaged, but they are computed under the same wave conditions using proposed formula as were represented in section 3.2.2. Fig. 3.6 shows the comparison between predicted transport rates by means of the Dibajnia and Watanabe (1996) formula and measured ones. As can be seen, in contrast to the Bailard (1981) and the Ribberink (1998) formula, the Dibajnia and Watanabe (1996) is capable of predicting the offshore transport rate, due to including the unsteadiness of the fine fractions. This leads to the longer entrainment of fine fractions after the maximum concentration, and consequently transport of these fractions by successive offshore oriented flow during the second half-cycle of the wave period. As a result, due to the strongly pronounced unsteady characteristics, the transport rate for graded sands with predominantly fine sand fractions (e.g. O'Donoghue and Wright (2004a)) are predicted within the factor of two.
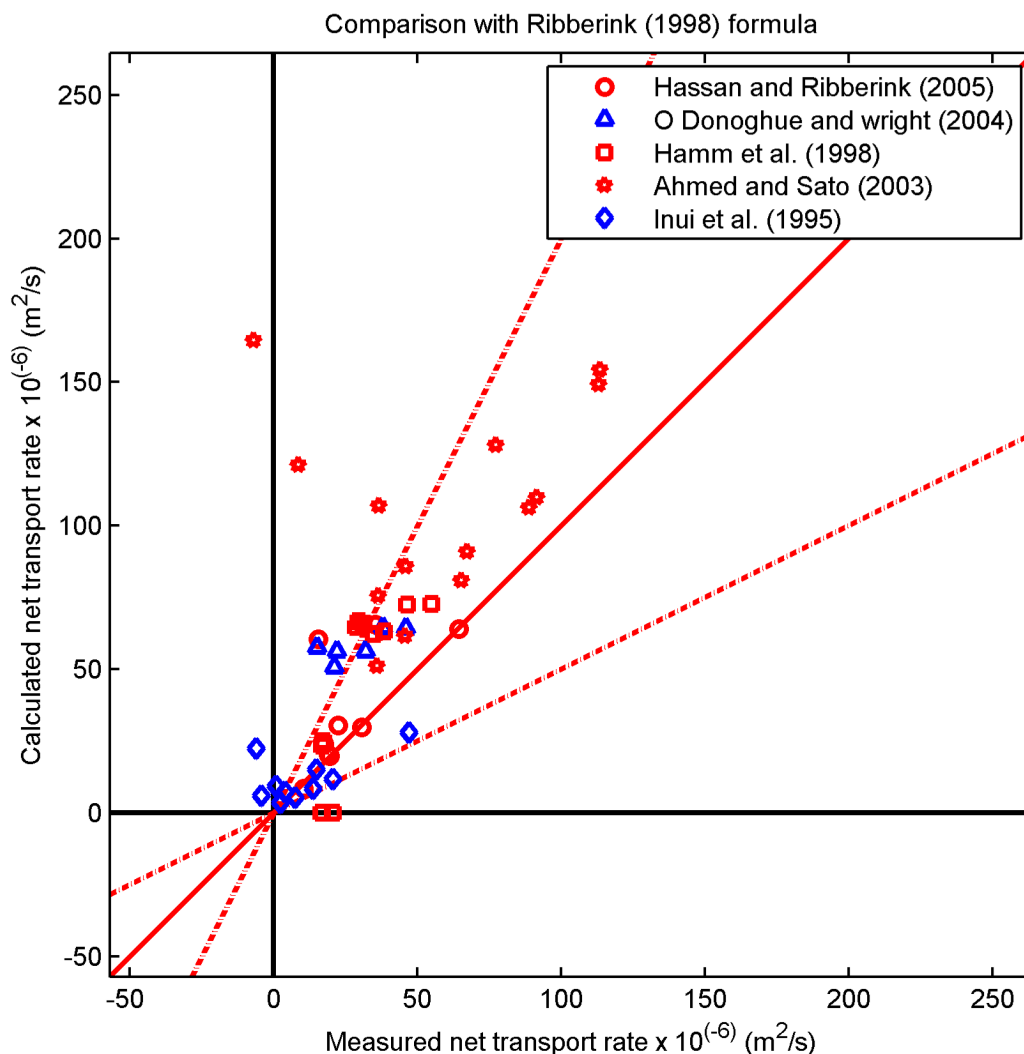
Figure 3.5: Comparison of the measured net transport rates with the predicted results by means of the Ribberink (1998) formula. The solid diagonal line depicts the perfect agreement and dashed lines the differences with factor 2.

However, due to the definition of the Dibajnia and Watanabe (1996) formula based on the near-bed velocity instead of the bed-shear stress, it is incapable of applying the hiding/-exposure modification factors. It tends to reproduce under-predicted results for graded sands composed of only medium and coarse sands. For example, all of the Ahmed and Sato (2003) experiments are under-predicted, while they were also carried out at the same flume (TUOFT), where Dibajnia and Watanabe (1996) performed their experiments. Moreover, like previous formulas, the Dibajnia and Watanabe (1996) formula is also incapable of predicting the transport rate for asymmetric waves. The under-prediction characteristics of the Dibajnia and Watanabe (1996) is also apparent in the statistics parameter of bias as outlined in Tab. 3.3. The bias value is negative (-0.36), which represents the formula as an under-predictive formula. The BSS value is 0.33, which classifies this formula in the poor group of estimation, as its correlation with measured data is about 35.69%.
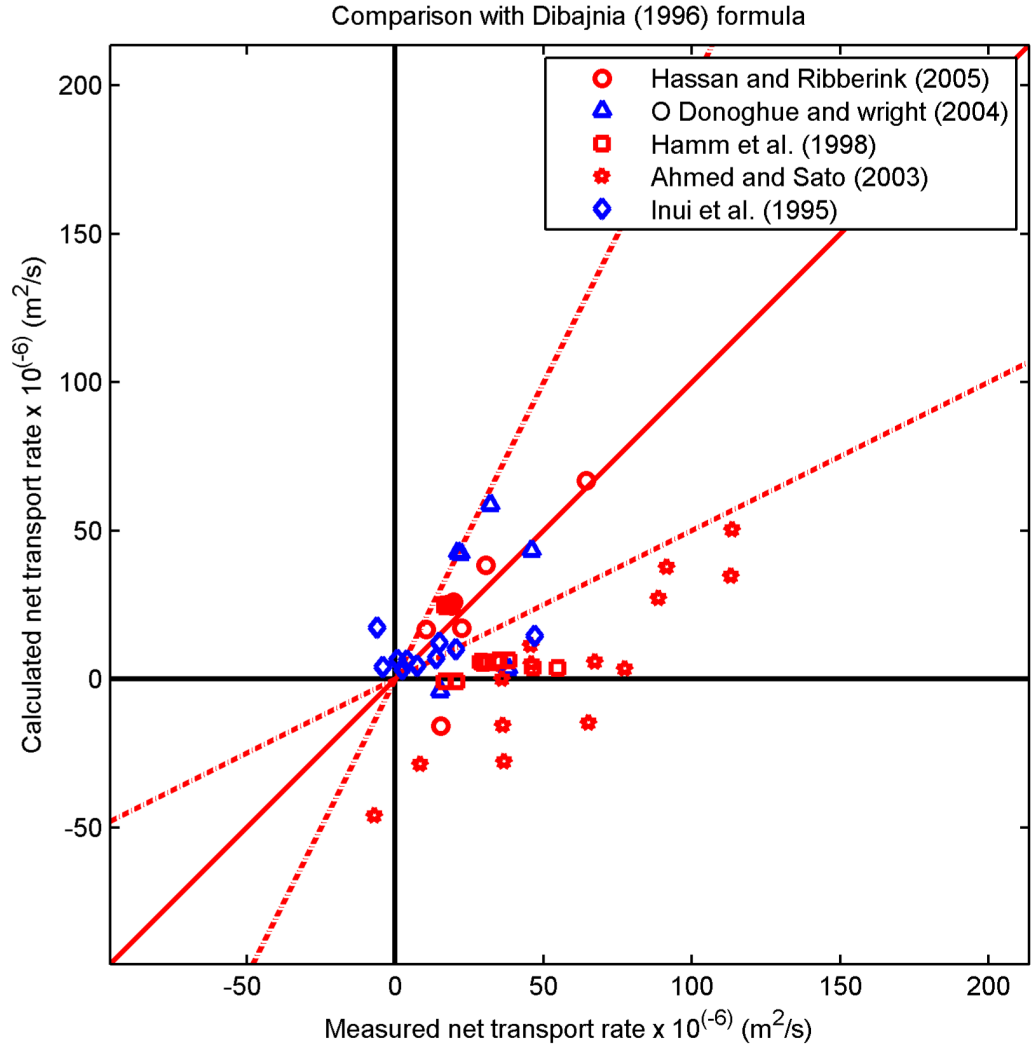
Figure 3.6: Comparison of the measured net transport rates with the predicted results by means of the Dibajnia and Watanabe (1996) formula. The solid diagonal line depicts the perfect agreement and dashed lines the differences with factor 2.

3.3.4   Tanaka formula predictions

Tanaka (2000) modified the sediment interchange rate between two parts of a wave period in the Dibajnia and Watanabe (1996) by means of his new hiding/exposure parameters (λ_1, λ_2) as presented in section 3.2.2.2. These modifications not only reduce the time-scale parameter in the Dibajnia and Watanabe (1996) formula proportionally to the size of fractions, but also diminish the interchange rate between crest- and trough-periods. As a consequence, the under-prediction of the Dibajnia and Watanabe (1996) formula is compensated in the Tanaka (2000) formula. Fig. 3.7 shows the predicted transport rates using Tanaka (2000) formula in comparison with measured datasets. As can be seen, the modification of time-scale in the Dibajnia and Watanabe (1996) formula, improves the prediction accuracy. The BSS value is increased from 0.33 in the Dibajnia and Watanabe (1996) formula to 0.71 and hence classifies the Tanaka (2000) formula in the fair group (compared to poor group of the Dibajnia and Watanabe (1996) formula. The bias and
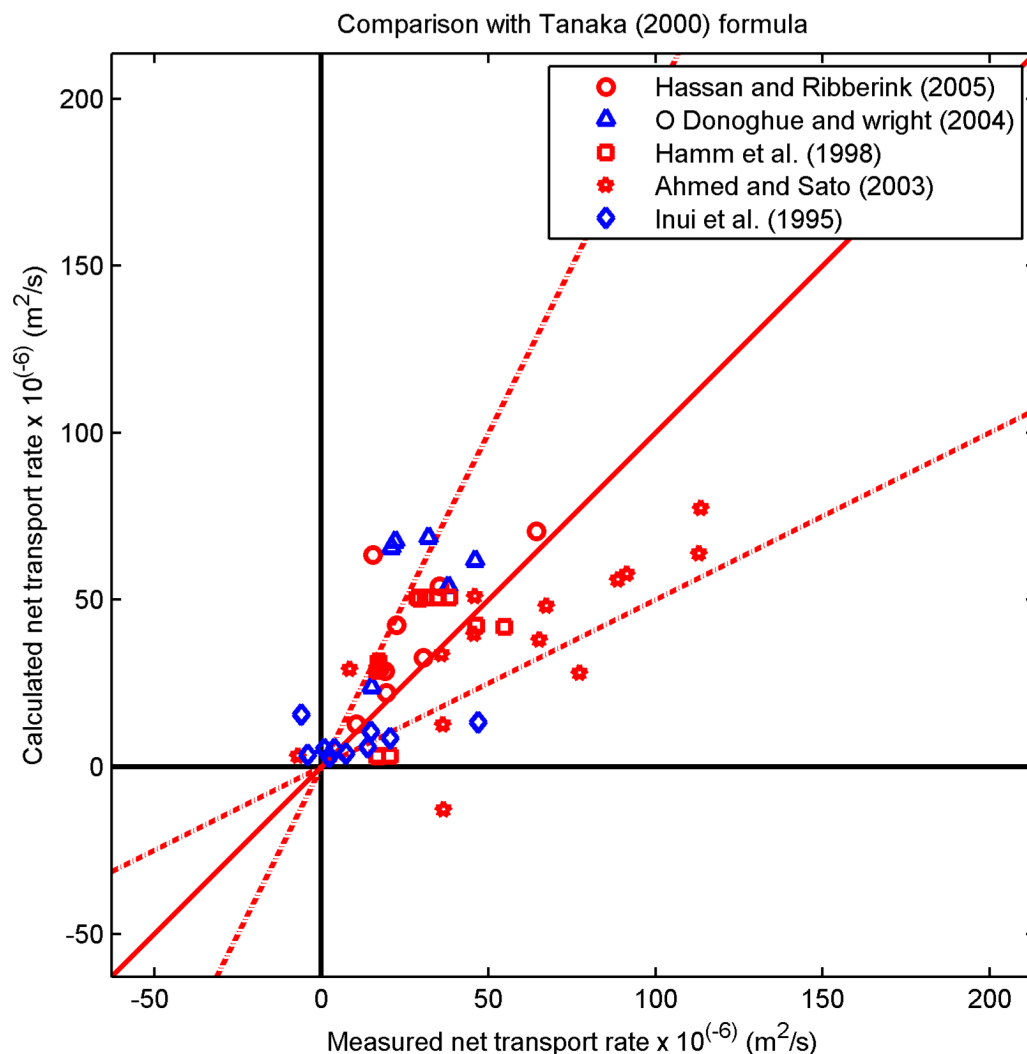
Figure 3.7: Comparison of the measured net transport rates with the predicted results by means of the Tanaka (2000) formula. The solid diagonal line depicts the perfect agreement and dashed lines the differences with factor 2.

correlation are also improved respectively to 0.19 and 59.79% from -0.36 and 35.69% in the Dibajnia and Watanabe (1996) formula.

3.3.5   Ahmed and Sato formula predictions

The new time-scale (ζ_i) defined by Ahmed and Sato (2003) in section 3.2.2.3 relates the sand interchange rate (Ω_i) to the Shields parameter instead of only the velocity square formula of the Dibajnia and Watanabe (1996) as well as Tanaka (2000) formulas. They presented a new hiding/exposure parameter based on the calibration with the experimental data of Dibajnia and Watanabe (2000), Hassan et al. (2001) and their experiments in the TUOFT(see please section 2.4).

Fig. 3.8 represents the predicted results for net transport rates based on the Ahmed and Sato (2003) formula. According to Fig. 3.8, the net transport rate for the O'Donoghue and Wright (2004a) as well as Hamm et al. (1998) experiments, which include fractions of fine

sands, are predicted more accurately than the Tanaka (2000) and Dibajnia and Watanabe (1996) formulas. However, the measurements of Ahmed and Sato (2003) do not support their predictions, as they also expressed in their paper. This can be explained by the fact that, compared to fine fractions in other datasets, the graded sands of Ahmed and Sato (2003) are mainly composed of fractions of medium and coarse sand.

Moreover, it is like previous formulas incapable of predicting the transport rate under asymmetric waves for the case of Hamm et al. (1998). The negative bias value (-0.33) of the Ahmed and Sato (2003) formula represents it as an under-predictive formula. Also, the smaller BSS value (0.44) than that of Tanaka (2000) formula (0.71) classifies the Ahmed and Sato (2003) formula in the poor group. In addition, the correlation (57.57%) is also smaller than the Tanaka (2000) formula (59.79%).
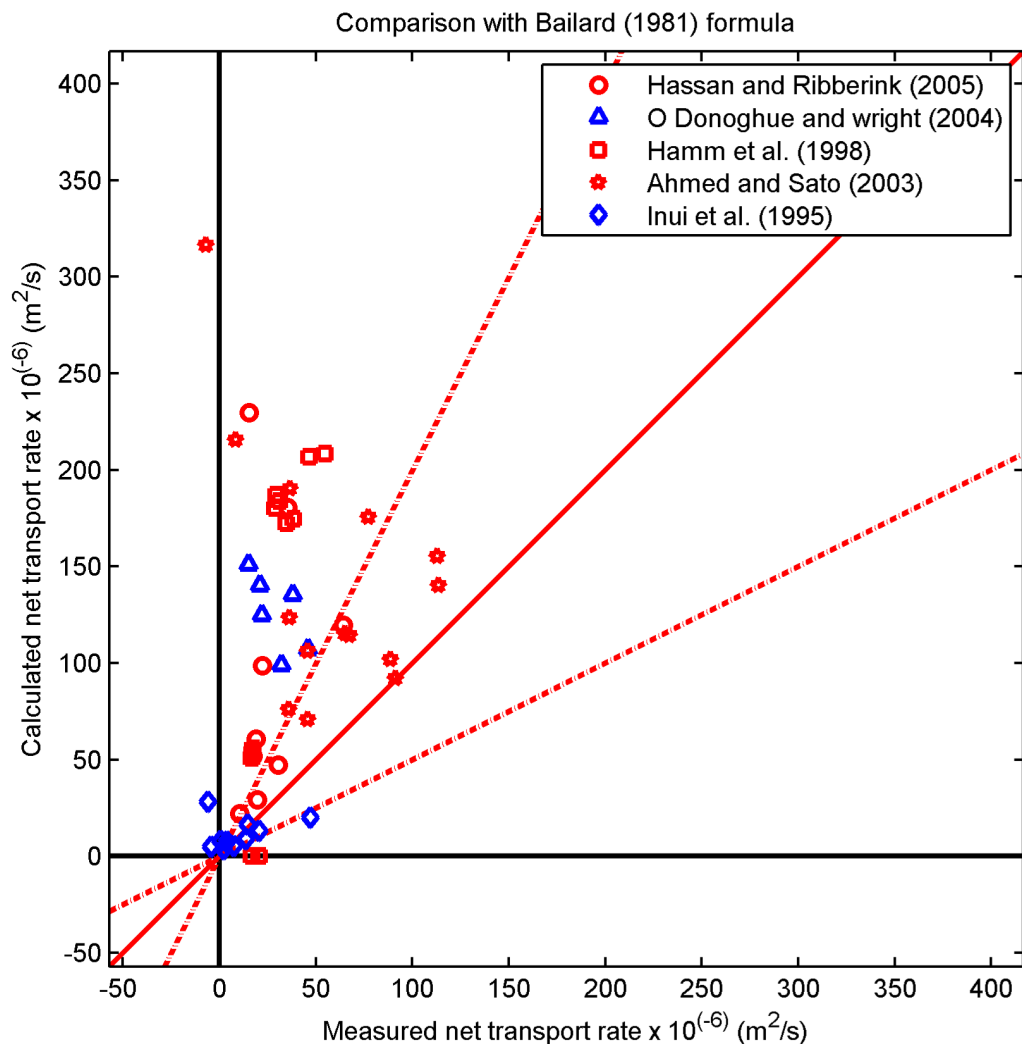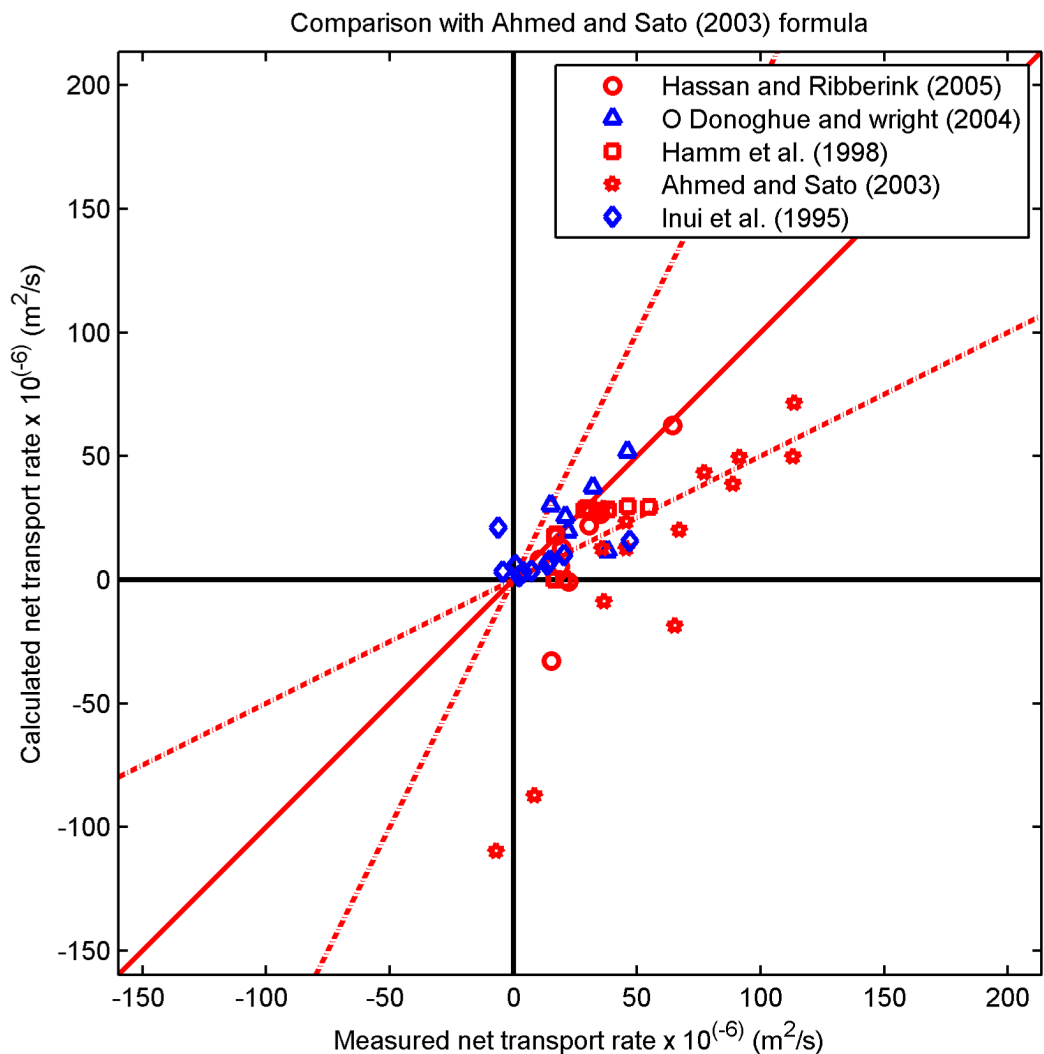

Figure 3.8: Comparison of the measured net transport rates with the predicted results by means of the Ahmed and Sato (2003) formula. The solid diagonal line depicts the perfect agreement and dashed lines the differences with factor 2.

3.3.6   SANTOSS (2013) formula prediction

SANTOSS (2013) formula is the recently improved formula based on the Dibajnia and Watanabe (1992) methodology, which can take wave nonlinearity (skewness as well as asymmetry), real surface waves effect (streaming), current as well as grading into consideration. It has been calibrated with an extended database constituted of not only sheet flow experiments but also ripple-bed experiments, which is known as the SANTOSS database (Van der Werf et al., 2009).

It depends on the bed-shear stress as opposed to the near-bed velocity in previously mentioned formulas. Also, the sediment interchange between crest- and trough-periods is defined as a conditional function of the phase-lag parameter instead of the time-scale in previous semi-unsteady formulas. Moreover, it does not intensify the sediment interchange rate between crest- and trough-periods as previous formulas with power of three (Dibajnia and Watanabe, 1996) or two (Ahmed and Sato, 2003) of the interchange rate.

The main part of the interchange rate is defined based on the improved Ribberink (1998) formula using new calibration factors derived from the SANTOSS database (m=11, n=1.2 instead of m=11, n=1.65 in the Ribberink (1998), please see section 3.2.1.2). The hiding/-exposure modification factor in the SANTOSS (2013) formula emanates from the Van Rijn (2007) modification factor, which considers the proportion of the fraction grain size to the D_{50} of the mixture in contrast to previous formulas, which applied the arithmetic size (D_m) or ineffective grain size (D_A) (Day, 1980).

Fig. 3.9 shows the predicted net transport rates by means of the SANTOSS (2013) formula. As can be seen, predicted results by means of the SANTOSS (2013) formula are more accurate than the previous formulas. Further, it includes the phase-lag effect of fine fractions in graded sands (e.g. Hamm et al. (1998), O'Donoghue and Wright (2004a) experiments) as well as short wave periods of the TUOFT experiments (Ahmed and Sato (2003) and Inui et al. (1995) experiments) better than previous semi-unsteady formulas. These are also apparent in statistics parameters outlined in Tab. 3.3. The BSS value of the SANTOSS (2013) formula is 0.84 which classifies it in the good group. Also, its Pearson correlation coefficient is 79.13% which is higher than its previous counterparts. However, the bias value is 0.13 which describes the slightly over-prediction behavior of the SANTOSS (2013) formula for net transport of these graded sands.

In addition to the skewed waves induced transport rate prediction, the SANTOSS (2013) formula predicts the net transport rate under asymmetric waves (test cases of Hamm et al. (1998)). To this end, the wave friction factor in the SANTOSS (2013) formula is modified using the proposed formula by Da Silva et al. (2006) for crest- and trough-periods. However, the SANTOSS (2013) formula applies the same sheet flow layer thickness for uniform and graded sands which reduces its accuracy to predict the well-graded sands ($GI >$ 4.0) transport rate. Therein the sheet flow layer thickness is larger than uniform sands (O'Donoghue and Wright, 2004a), and therefore the net transport rate of test cases with well-graded sands such as test cases of Hassan and Ribberink (2005) with GI=9.82 are not predicted as accurately as other test cases.

3.3.7   This thesis formula

Predicted transport rates by means of SANTOSS (2013) formula considerably depends on the sheet flow layer thickness (SFLT) due to its direct relation with phase-lag number. However, it applies the similar rule to estimate the SFLT for graded and uniform sands. Experiments of O'Donoghue and Wright (2004a) revealed that grading as well as the fine
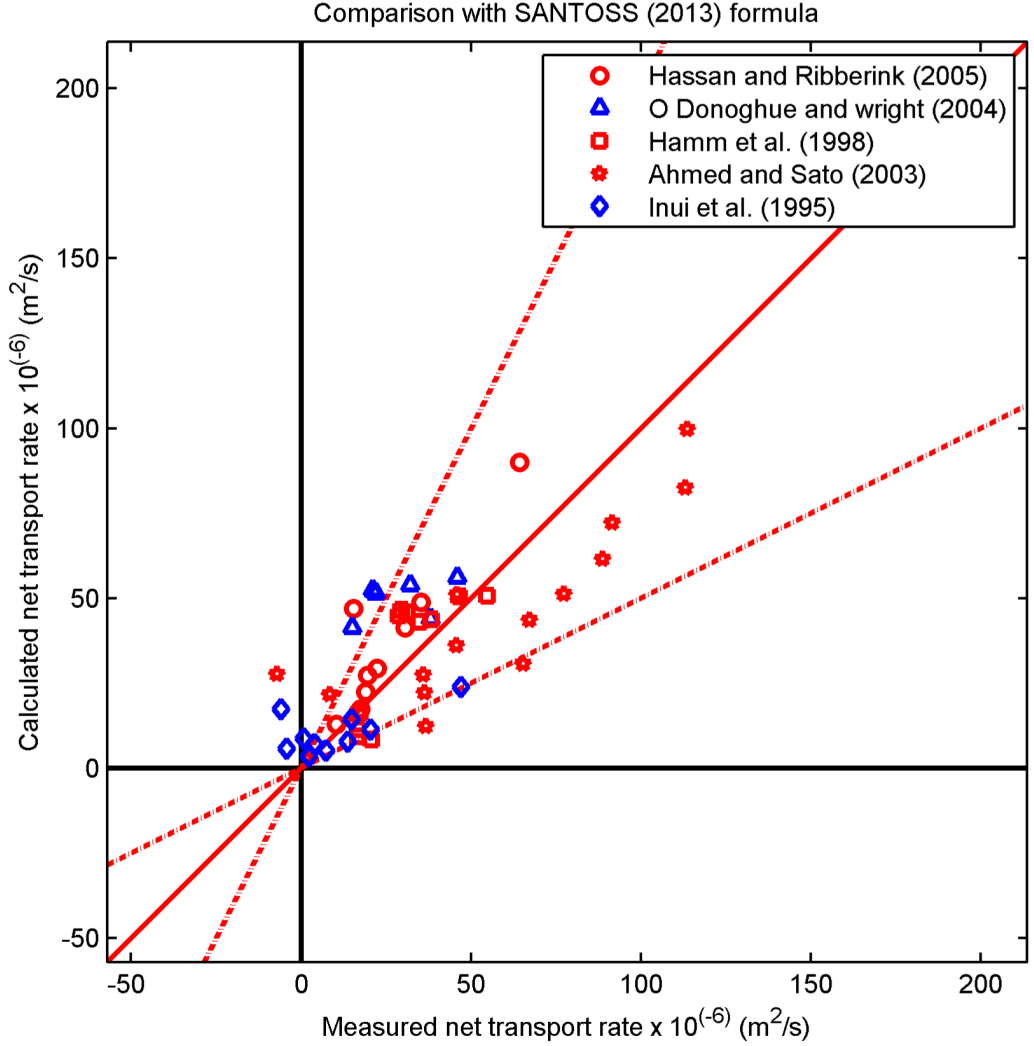
Figure 3.9: Comparison of the measured net transport rates with the predicted results by means of the SANTOSS (2013) formula (Van der A et al., 2013) formula. The solid diagonal line depicts the perfect agreement and dashed lines the differences with factor 2.

fraction play substantial roles in SFLT. They observed that within uniform and graded sands with the same D_{50}, the graded sands with higher percentage of fine fraction have a thicker SFLT than that of uniform sands. Based upon these observations, a MATLAB® script in this thesis was developed to optimize the SFLT prediction (Appendix ?? and A.5). To this end, the general form of modified SFLT for graded sand is proposed as:

$$\frac{\delta_{si}}{D_{50}} = \begin{cases} 25 f_1 \hat{\theta}_i & \text{if} \quad D_{50} \leq 0.15 \ mm \\ f_2 [25 - \frac{12(D_{50}-0.15)}{(0.20-0.15)}] & \text{if} \quad 0.15 \ mm < D_{50} < 0.20 \ mm \\ 13 f_3 \hat{\theta}_i & \text{if} \quad D_{50} \geq 0.20 \ mm \end{cases} \qquad (3.43)$$

where f_1, f_2 and f_3 are calibration factors and defined as functions of grading and fine fraction ($D_{50} \leq 0.15 \ mm$) percentage. Like a classical physics formulation, where a parameter is a function of different variables, it can be defined as the multiplication of these variables (also like the approach of separation of variables in mathematics to solve a partial

60

differential equation), f_1, f_2, and f_3 are written in a general form as:

$$f_1, f_2, f_3 = GI^{e_1}(1 + PF)^{e_2} \tag{3.44}$$

where PF is the Percentage of Fine fraction and e_1, e_2 are obtained after running the optimization script. Fig. 3.10 shows the variation of proposed SFLT-coefficients ($f_{1,2,3}$) in this thesis by changing the e_1 value for positive numbers. As can be seen, by increasing the sediment non-uniformity (increment of GI) the SFLT-coefficients are increasing for positive values of e_1. Moreover, by increasing the e_1 values, the SFLT-coefficient are increased, and consequently the SFLT in Eq. 3.43 is increased.

Fig. 3.11 shows the behavior of proposed SFLT-coefficients ($f_{1,2,3}$) by means of negative
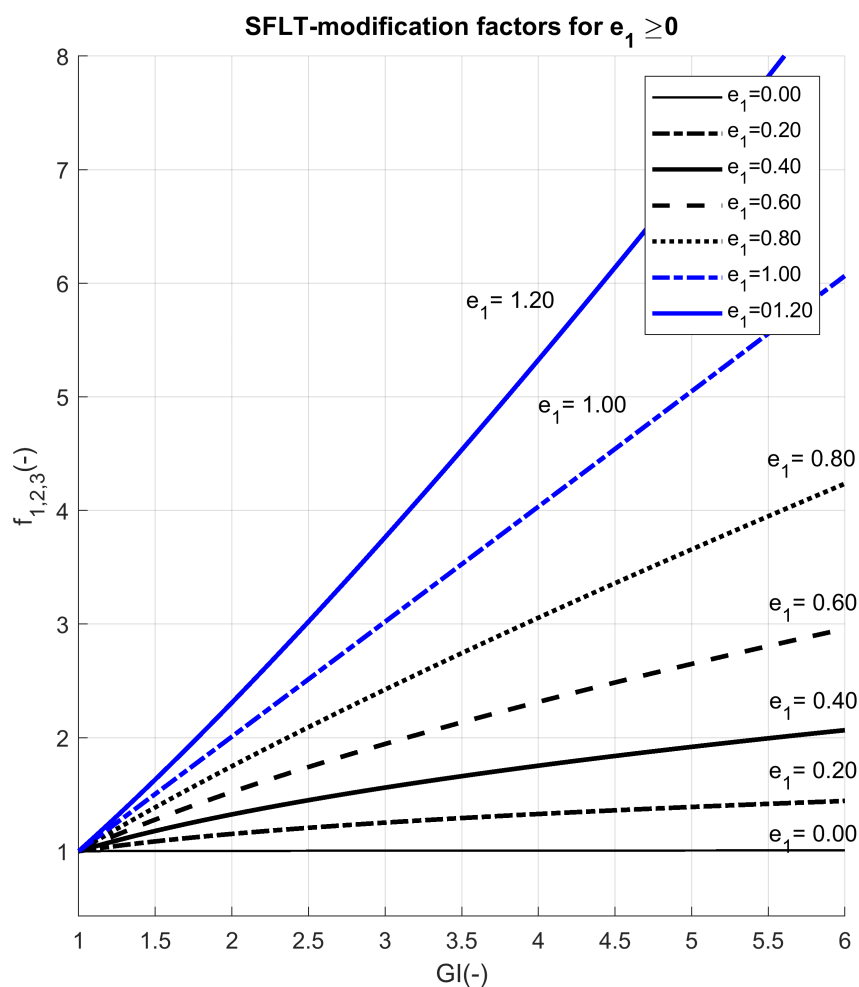
Figure 3.10: SFLT-coefficients for different GI using positive modification factor of e_1.

values for modification factor of e_1. As is shown, in contrast to positive values of e_1, SFLT-coefficients are decreasing by increasing the sediment non-uniformity. This means, that the negative power of GI cause the reduction of SFLT in new modification for SFLT. Fig. 3.12 shows the variation of the proposed SFLT-coefficients by changing the fine fraction proportion for positive values of e_2. The SFLT-coefficients show an increasing trend by increasing the fine fraction percentage in a mixed sand. Moreover, by increasing the e_2
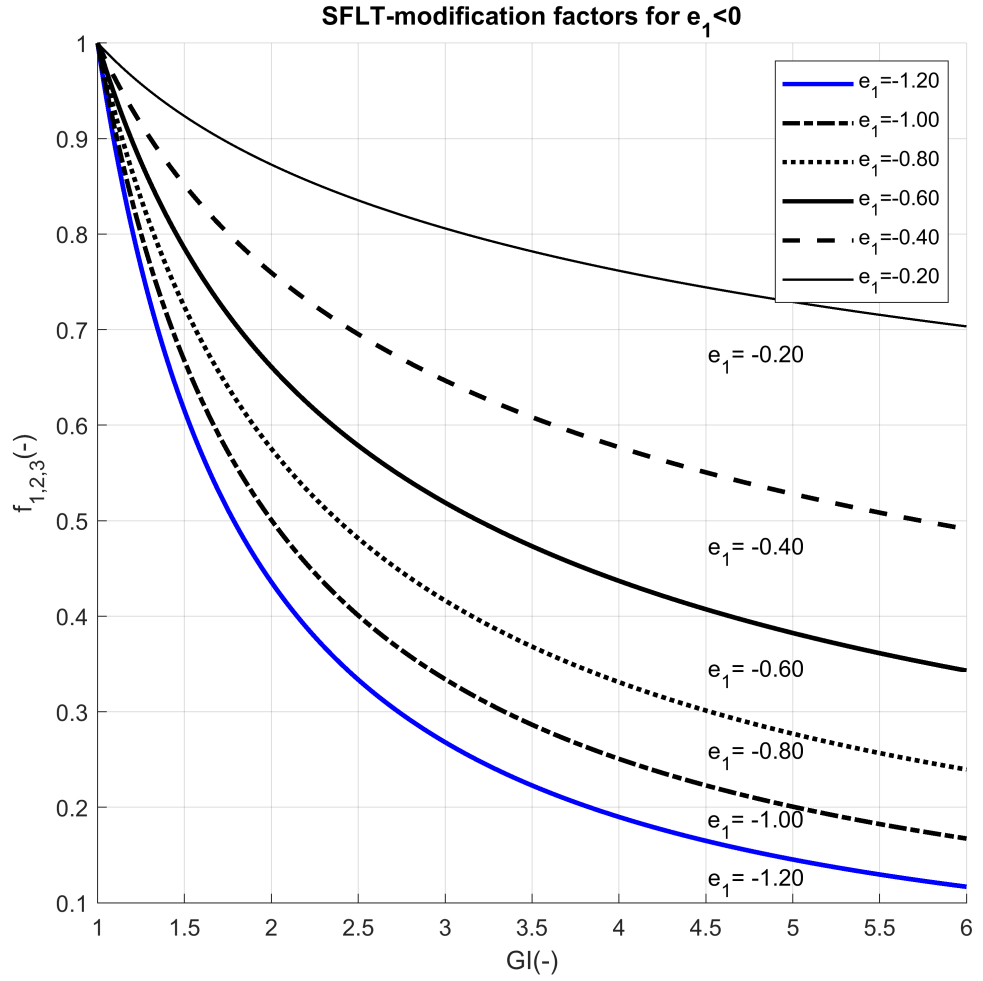
Figure 3.11: SFLT-coefficients for different GI using negative modification factor of e_1.

value, the SFLT is also increased. Conversely, the negative values for e_2 show in Fig. 3.13 the reducing of SFLT by increasing the fine fraction proportion and by reducing the e_2 values, the reduction of SFLT is followed steeply.

The conditional value of 4.0 was selected based on the proposed value of 4.1 by Van Rijn (2007). Following values are the optimum values for e_1, e_2 to have the best performance of SFLT in the prediction of net sediment transport rate for the mixed sand dataset (Tab. A1)). However, in section 4.9 after running the two-phase flow model and comparison the SFLT through different approaches, the performance of this formula will be discussed.

$$\begin{cases} \text{if} \quad GI \geq 4.0 & \begin{cases} e_1 = 0.40 \\ e_2 = 0.60 \end{cases} \\ \\ \text{if} \quad GI < 4.0 & \begin{cases} f_1 = & \begin{cases} e_1 = -0.20 \\ e_2 = 1.50 \end{cases} \\ f_2, f_3 = & \begin{cases} e_1 = -0.20 \\ e_2 = 1.0 \end{cases} \end{cases} \end{cases} \quad (3.45)$$

62
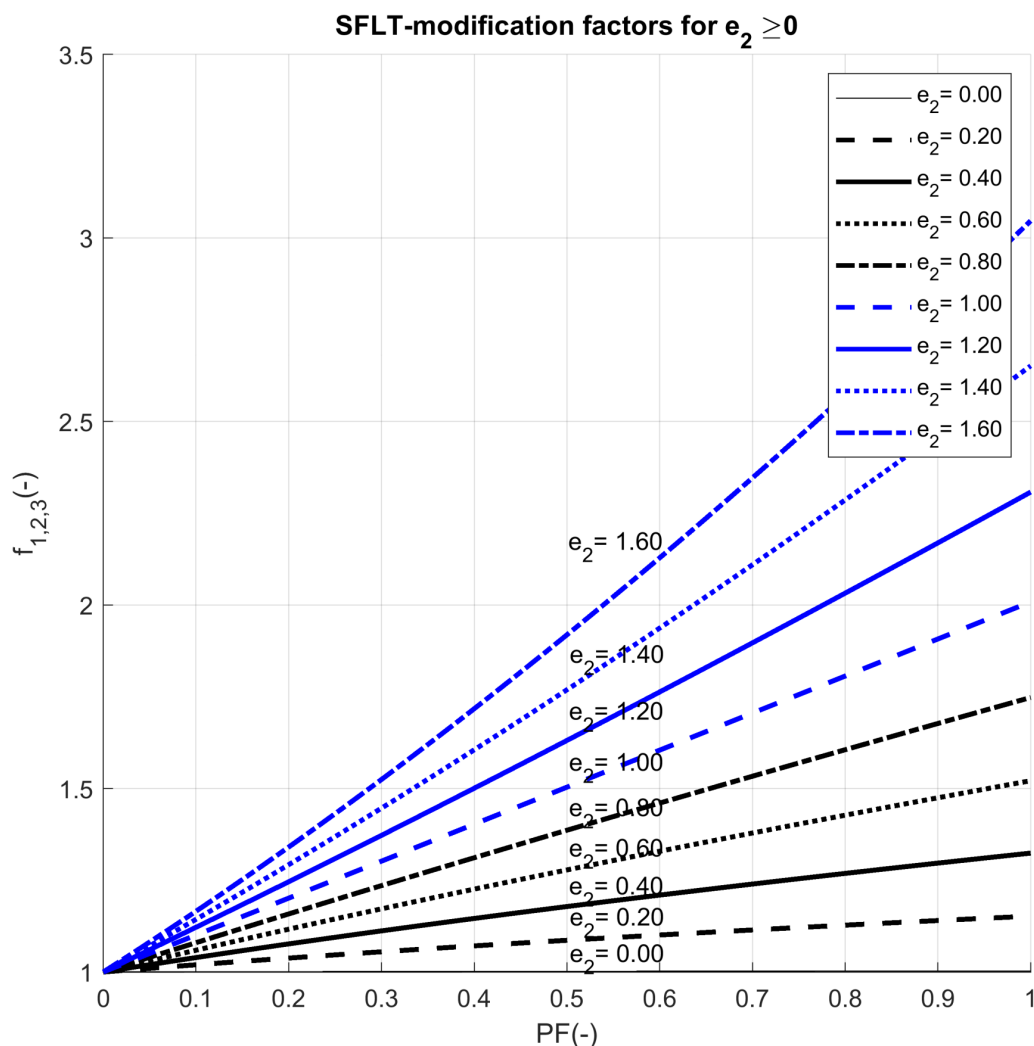
Figure 3.12: SFLT-coefficients for different PF using positive modification factor of e_2.

Eq. 3.45 illustrates that the SFLT in well-graded sands ($GI > 4.0$) as well as well-sorted sands ($GI < 4.0$) is significantly dependent on the GI value. Moreover, it depends inversely on the GI for well-sorted (poorly-graded) sands. It means that in contrast to the well-graded sands, the SFLT of poorly-graded sands decreases by increasing the GI up to the threshold value of GI (i.e. GI=4.0). More research is required to examine this behavior of poorly-graded sands in field and large scale flume experiments, because the proposed formula in this thesis is based upon the available experiments in OFTs. Fig. 3.14 depicts the measured and predicted results by means of the modified SANTOSS (2013) formula in this thesis. As can be seen, the modified formula predicts the measured net transport rates better than the former. The BSS is improved to 0.92 compared to 0.84. The Pearson correlation factor is also enhanced from 79.13% in original to 90.22% in modified formula. Moreover, the $bias$ is also improved from 0.13 to -0.09.

However, the predicted results for the experiments of Ahmed and Sato (2003) and Inui et al. (1995) in the TUOFT, are not in a good agreement with the corresponding measurements. An explanation for these, is that as noted by Van der A et al. (2013) the applied method in the TUOFT to measure the net transport rate is on the basis of difference
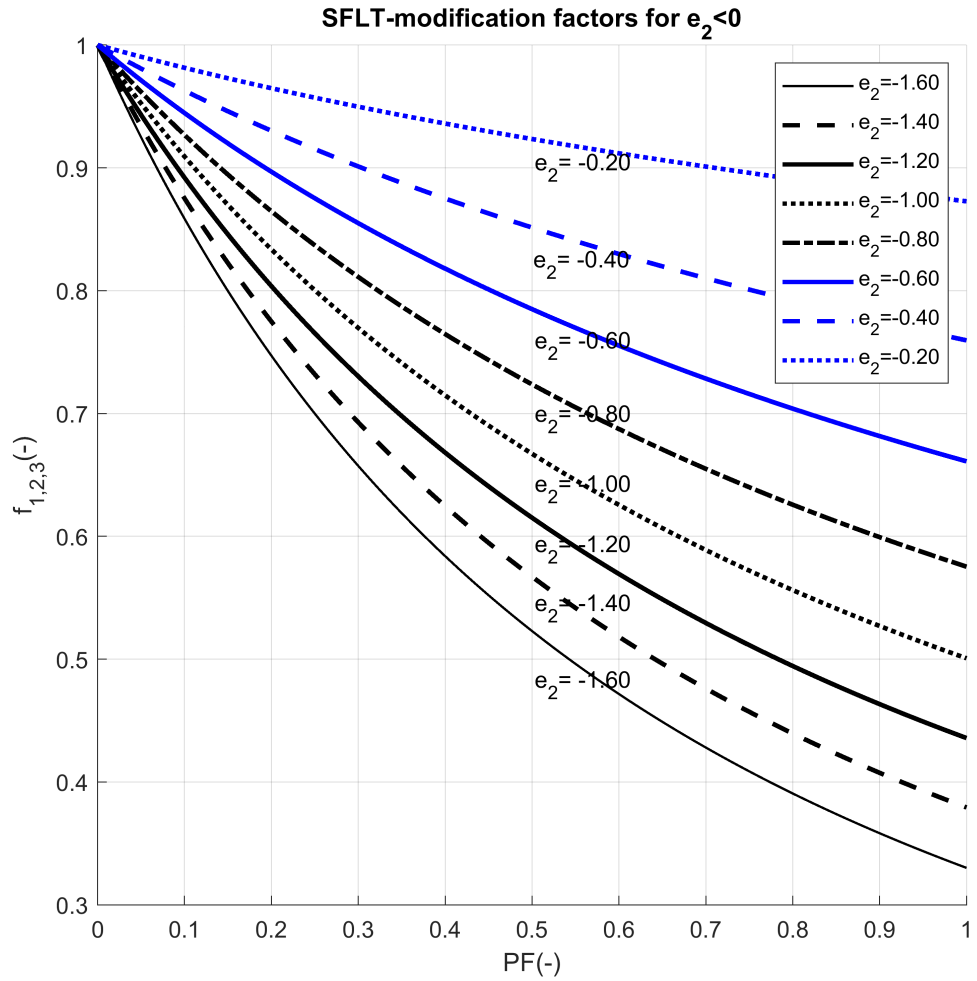
Figure 3.13: SFLT-coefficients for different PF using negative modification factor of e_2.

between the masses of sand collected at the end of the test section. This method is more prone to measurement error than the method based on the mass conservation applied to the whole test sections as used in other test cases.

Fig. 3.15 compares the SFLT predicted by former and modified SANTOSS (2013) formula in crest (C is added at the end of SFLT)(SFLTC) and trough (T is added at the end of SFLT)(SFLTT) half-cycles, respectively. It is clear that both SFLTC and SFLTT of strongly graded sands ($GI \geq 4.0$) are around two to three times larger than previous predictions. In contrast, those of poorly graded sands are slightly decreased. For the data, which GI is not reported both of formulas show the same values. Also, it is apparent that GI=4.0 is capable of classifying the sands into well graded and poorly graded.

As a result, SANTOSS (2013) formula under-predicts the SFLT for graded and over-predicts for well-sorted sands. However, the under-prediction for graded sands is larger than over-prediction for well-sorted sands. Fig. 3.16 depicts the phase-lag number (P) for predicted by the SANTOSS (2013) formula and the modified one. Due to the direct relation of phase-lag with SFLT (Eq. 3.41), differences of SFLT are reflected in phase-lag number. Also, the phase-lag number for crest half-cycle (P_c) is always larger than trough
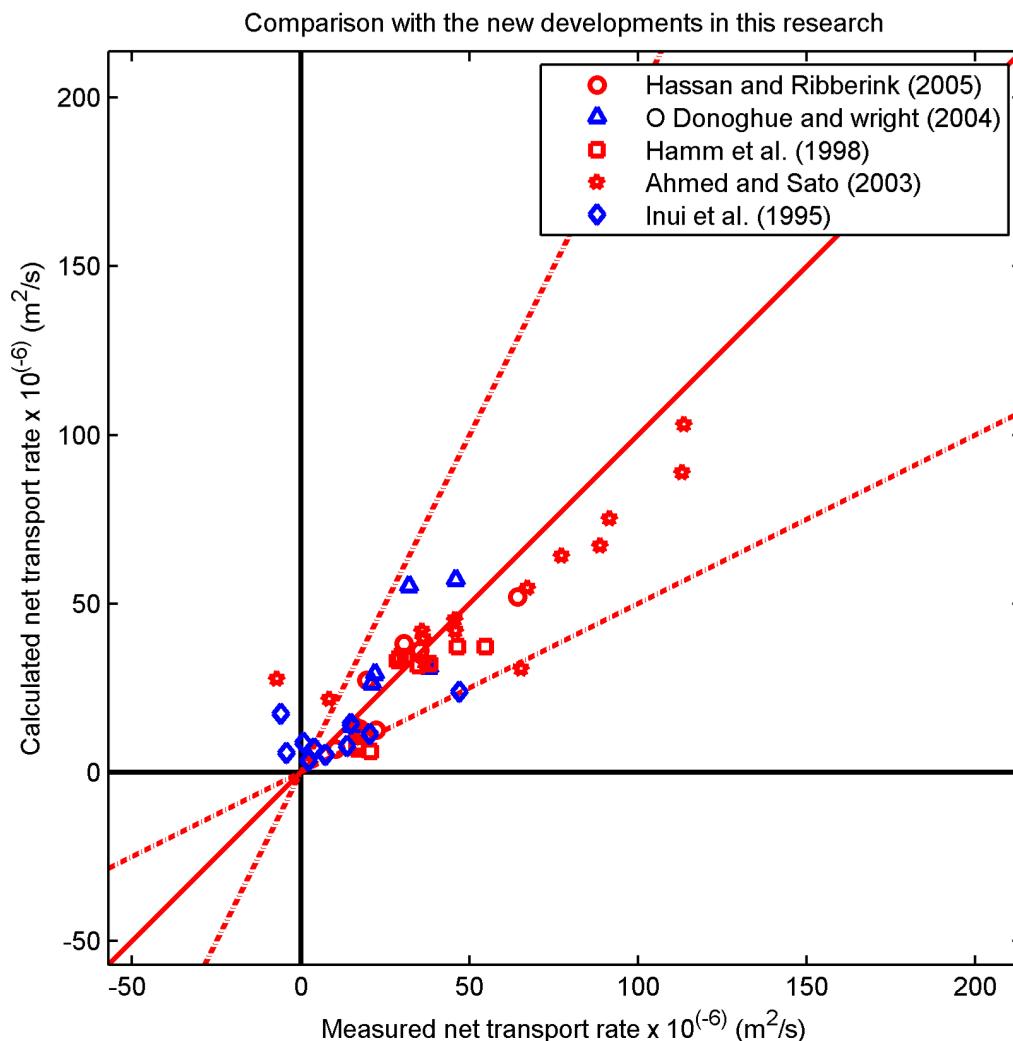
Figure 3.14: Comparison of the measured net transport rates with the predicted results by means of the new developments in this research for the SANTOSS (2013) formula (Van der A et al., 2013) formula. The solid diagonal line depicts the perfect agreement and dashed lines the differences with factor 2.

(P_t). The influences of the new formula for SFLT on the potential of sand exchange from crest to trough (Ω_{ct}) and from trough to crest (Ω_{tc}) are represented in Fig. 3.17. As can be seen, both of them are increased using new formula for SFLT in graded sands, but the increment in Ω_{tc} is more significant than Ω_{ct}. However, the Ω_{ct} values are larger than its corresponding Ω_{tc}. The exchanged sands between crest and trough half-cycles are increased for graded sands, while decreased for slightly graded by means of the modified formula. However, the larger values of Ω_{ct} make the lower net transport rate for graded sands based on the proposed modification in this thesis.

Fig. 3.18 represents the predicted values for the entrainment potential only in the crest without exchange from trough to crest (Ω_{cc}) and entrainment potential in trough without exchange from crest to trough (Ω_{tt}) by means of the SANTOSS (2013) formula and proposed modification formula for fractions of graded sands. Unchanged values are corresponding to the $P_c \leq 1$ and $P_t \leq 1$ where phase-lag effect is negligible. It is seen that

the proposed modification predicts smaller values than the SANTOSS (2013) formula for graded sands. In contrast, it predicts larger values for both of Ω_{ct} and Ω_{tc}. It means that grading effect reduces the transport in both half-cycles, while it increases the sand exchange between them owing to the larger SFLT.

Fig. 3.19 compares the predicted net transport rate for graded sands by means of the SANTOSS (2013) formula and the proposed modification in this thesis. It shows that the modification presented in Eq. 3.45 for graded sands reduces the net transport rate for graded sands, while the proposed modification results in larger values than the original SANTOSS (2013) formula for poorly-graded sands. It is explained through enhancement of the SFLT for graded sands by the proposed formula in this thesis. A greater SFLT will result in higher phase-lag (Fig. 3.16) and consequently higher sand interchange between half-cycles, which in turn reduces the net transport rate for well-graded sands.

3.3.8   New experiments to understand the mixed sand dynamics

More recently, the mixed sand dynamics has attracted the interest of the researchers which leads to research projects of the Hydralab+ (COMPLEX) as well as the STENCIL. The experiments under progressive surface waves induced sheet flow conditions in the GWK at the Forschungszentrum Küste (FZK) within STENCIL were conducted for bimodal graded sands (Van der Werf et al., 2019). The fine fraction used in these experiments was uniform sand with the median grain size (D_{50}) of 0.21 mm, which is slightly coarser than the fine fraction with $D_{50} = 0.15\ mm$ used in AOFT by O'Donoghue and Wright (2004b). However, this fine fraction could be comparable with the fine fraction ($D_{50} = 0.21\ mm$) of the performed experiments at the TUOFT by Ahmed and Sato (2003) for a tri-modal graded sand as well as the medium sand of $D_{50} = 0.21\ mm$ in the cases of Hassan and Ribberink (2005) at LOWT. The coarse fraction used in the GWK-experiments was a uniform sand with $D_{50} = 0.58\ mm$, which is comparable with the coarse fraction of the O'Donoghue and Wright (2004b) experiment, where the coarse fraction was slightly finer ($D_{50} = 0.51\ mm$). Parallel with the experiments at the GWK, other bimodal mixed sand experiments were performed at the AOFT within the research project Hydralab+(Boscia et al., 2019). The fine sand fraction in the AOFT was a uniform sand with $D_{50} = 0.17\ mm$ and the coarse fraction of $D_{50} = 0.61\ mm$. This mixture was not already used for graded sands and hence the results cannot be compared with the previously performed experiments for graded sands. Moreover, the produced mixtures were different from the GWK experiments which weakens the comparability of the experiments for graded sands under progressive surface waves (large scale, the GWK) and the OFT results (small scale, the AOFT).

The GWK experiments were conducted under skewed waves ($R = 0.61 - 0.64$) with two wave heights of 1.0 m and 1.5 m but the same wave period of T = 7 s. Unfortunately, to the knowledge of the author, there is no publication about the measured velocity in and out of the wave boundary layer for the experiments at the GWK for graded sands, which is for the sheet flow experiments significantly important, particularly for comparison the net transport rate with the predicted by means of empirical formulas, because the velocity time series is the inseparable part of these formulas. Based on the comparison performed by Van der Werf et al. (2019), the agreement between the predicted net transport rates by the SANTOSS (2013) formula and the measured at the GWK is not good and the SANTOSS (2013) formula is for these cases under-predictive. However, at the time of doing this research, no information was published about the velocity time series generated at the GWK over the graded sands, and therefore the inclusion of the corresponding experiments into the prediction formulas was not possible.
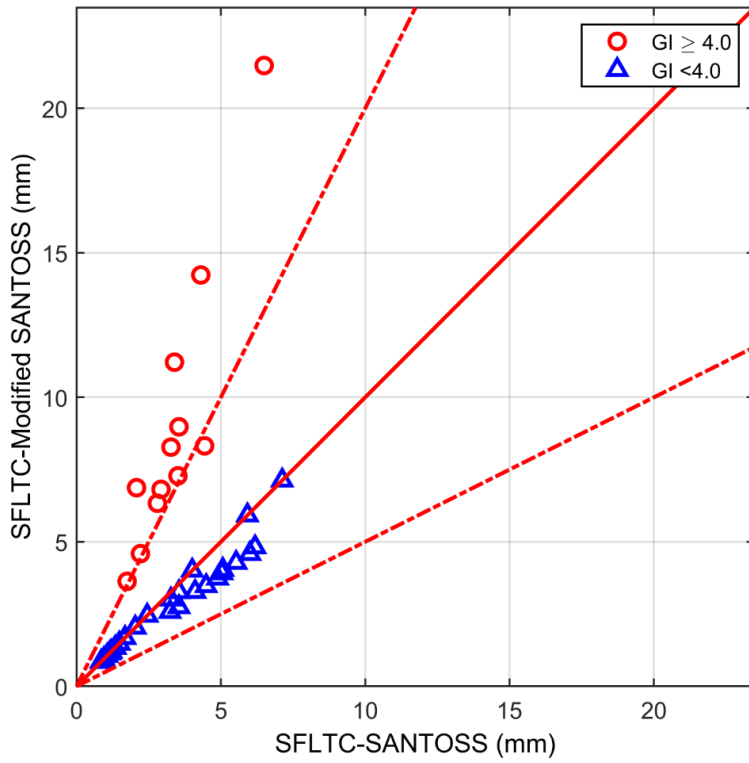
(a)
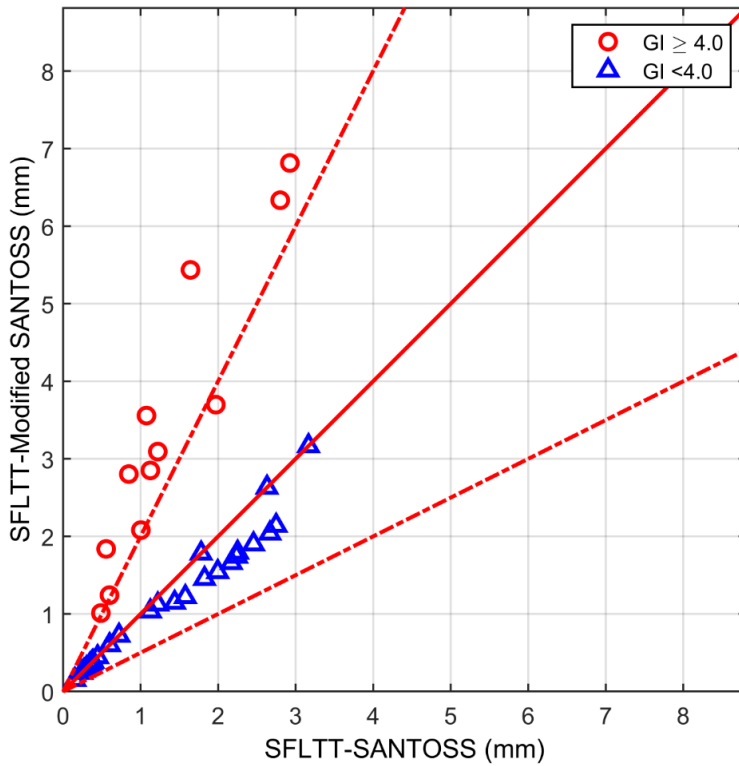
(b)

Figure 3.15: (a) Sheet Flow Layer Thickness at Crest (SFLTC), (b) Sheet Flow Layer Thickness at Trough (SFLTT) for well-graded (GI≥4.0) and well-sorted (GI<4.0) using the SANTOSS (2013) formula in comparison with the proposed modification.
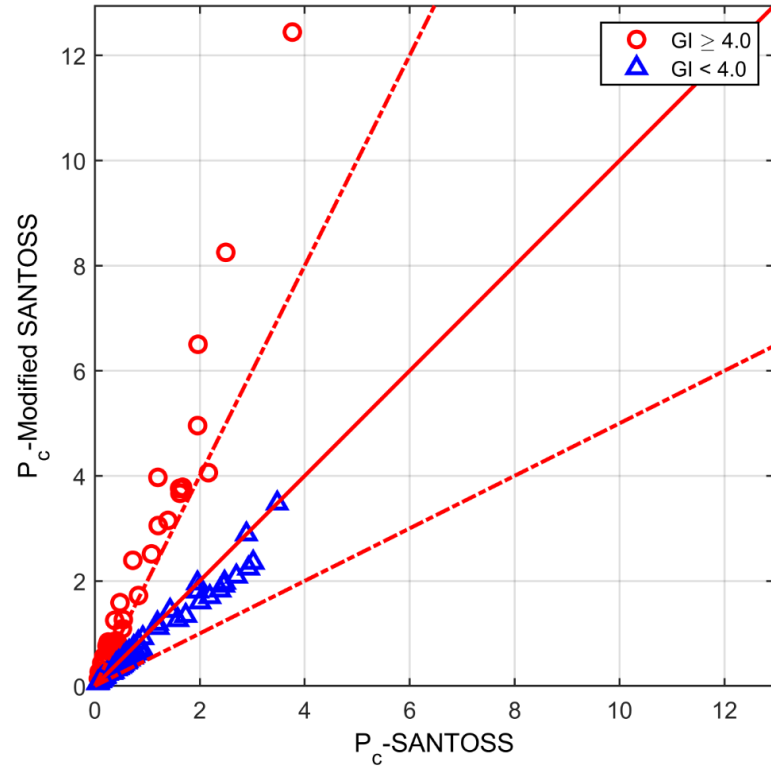
(a)
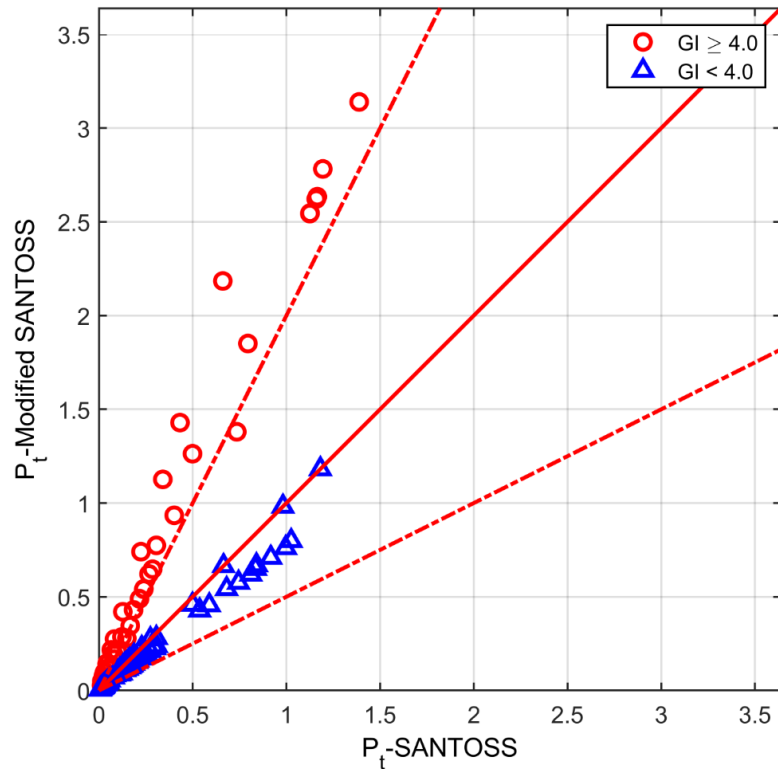
(b)

Figure 3.16: (a) Phase-lag number at crest (P_c), (b) Phase-lag number at trough (P_t) for well-graded (GI≥4.0) and well-sorted (GI<4.0) using the SANTOSS (2013) formula in comparison with the proposed modification.
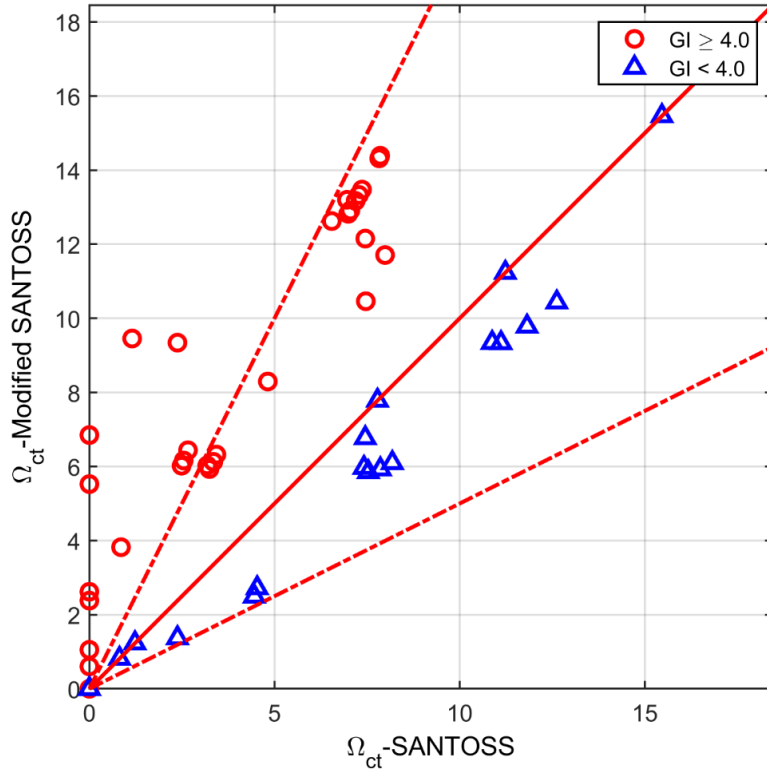
(a)
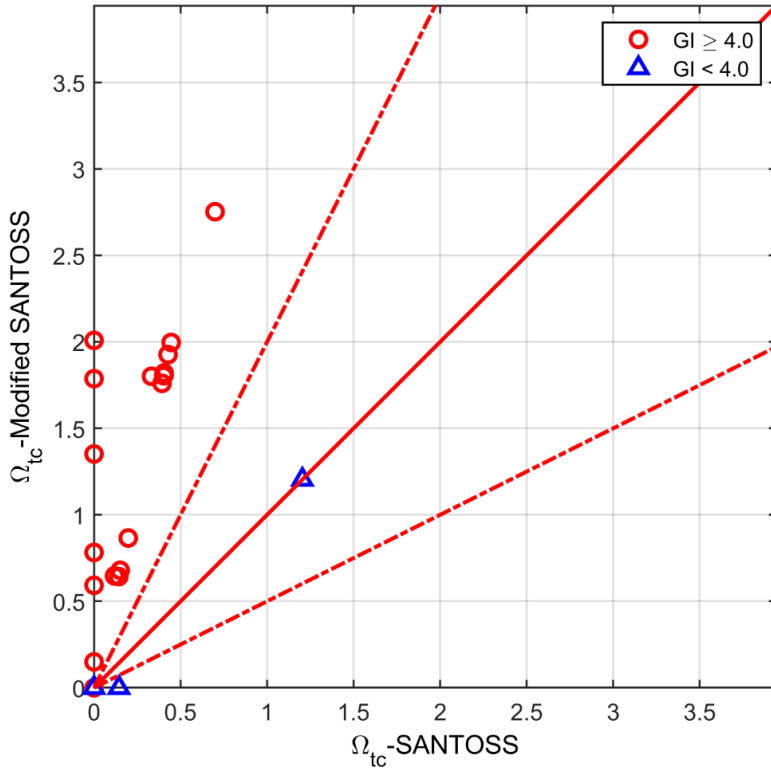
(b)

Figure 3.17: (a) Potential exchange from crest to trough (Ω_{ct}), (b) Potential exchange from trough to crest (Ω_{tc}) for well-graded (GI≥4.0) and well-sorted (GI<4.0) using the SANTOSS (2013) formula in comparison with the proposed modification.
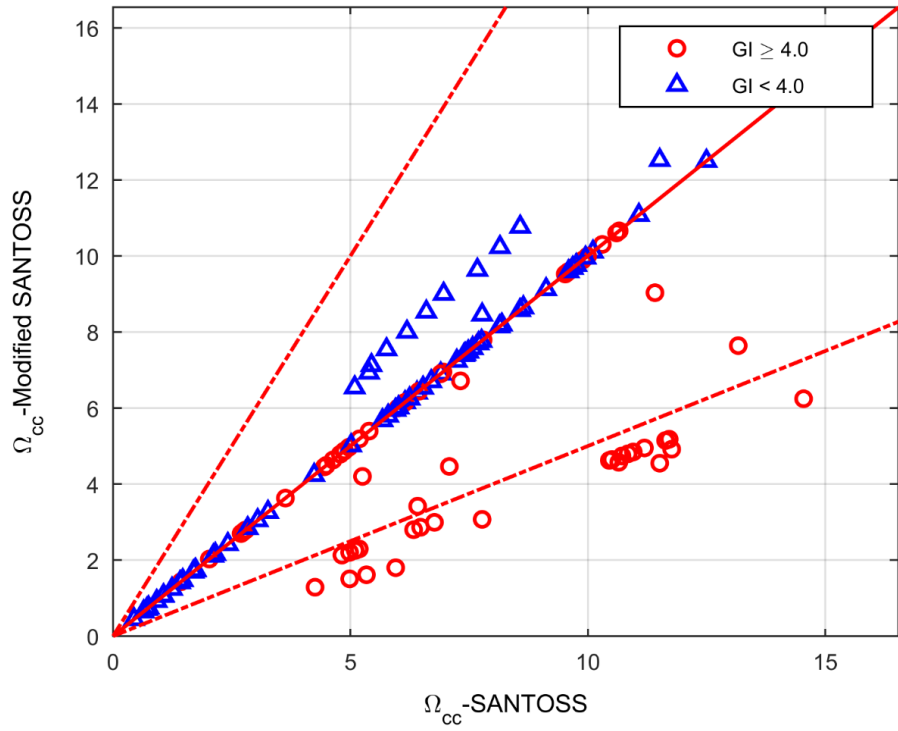
(a)
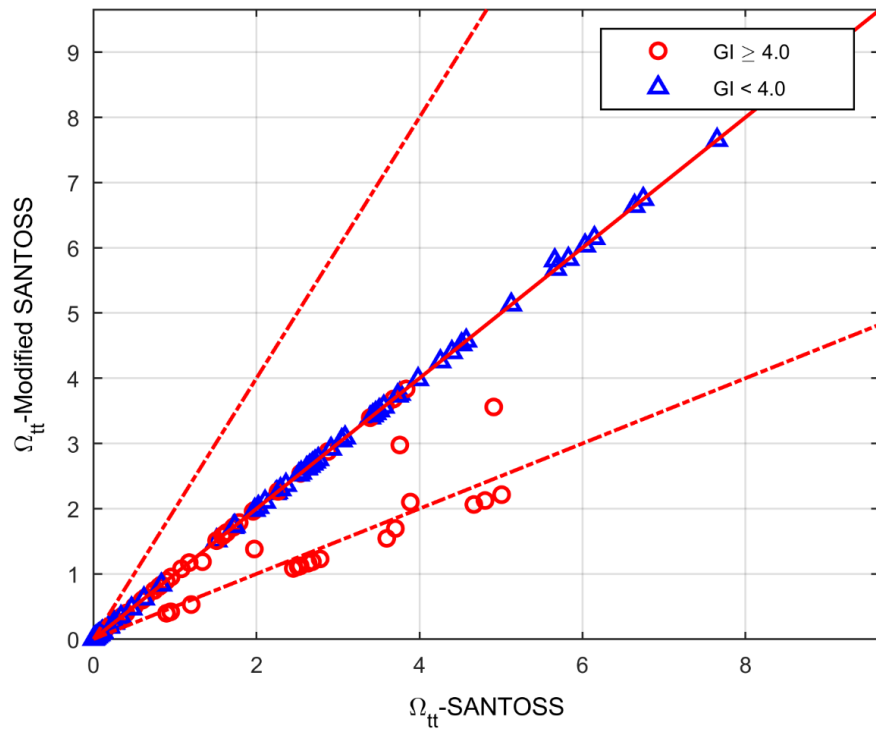
(b)

Figure 3.18: (a) Potential entrainment at crest (Ω_{cc}), (b) Potential entrainment at trough (Ω_{tt}) for well-graded (GI≥4.0) and well-sorted (GI<4.0) using the SANTOSS (2013) formula in comparison with the proposed modification.
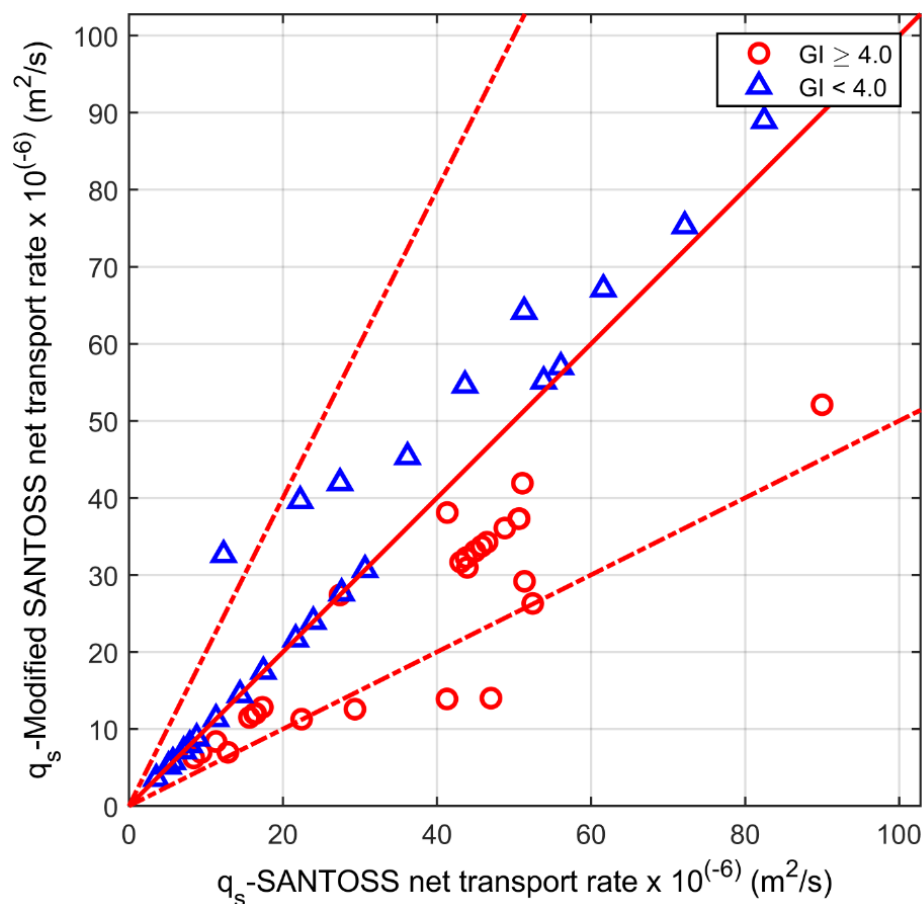
Figure 3.19: Comparison of net transport rate from the SANTOSS (2013) with the proposed modification.

Four bimodal graded sands with the fine fraction percentages of 100 %, 68 %, 46% and 26% were paved for a length of 30 m and thickness of 30 cm at the GWK. These were in the AOFT seven mixtures with the fine fraction proportions of 100%, 90%, 75%, 50%, 25%, 10% and 0 under the wave period of T=6 s and peak velocities of 1.5, 1 and 0.5 m/s. Based on both experiments, it was observed that the graded sands bedforms evolved from 2D ripples in the case of only coarse sands to the flat bed in the case of only fine sands. For the performed experiments in the GWK, the total net transport rate is onshore and increased by increasing the fine fraction percentage for both wave heights up to the fine fraction percentage of 68%. Interestingly, from 68% of fine fraction the onshore transport rate is not increased continuously by increasing the fine fraction percentage and for higher velocity corresponding to the higher wave height, the total net transport is decreased, whether for the case of smaller velocity increased. It can be explained by the enhanced unsteadiness behavior of fine sands under higher velocities, where the entrained fine sands within the onshore half-cycle are more transported offshore compared to the smaller velocity.

Due to the importance of the sand transport under the progressive waves as well as rare experiments for the graded sands under this condition, it is necessary to perform a systematic data analysis and produce an organized dataset for the conducted experiments within the STENCIL at the GWK. To this end, the structure of the dataset produced at

the AOFT by O'Donoghue and Wright (2004b) could be applied.

Conclusion

Five groups of graded sand datasets (Appendix A-Tab. A1) exposed to second order Stokes and first order cnoidal skewed waves as well as asymmetric waves under sheet flow conditions were discussed. Moreover, their net transport rates were predicted by means of six different empirical transport formulas. Their comparison shows that the SANTOSS (2013) formula estimates more accurately the net transport rate for graded sands in comparison with other sediment transport formulas.

However, the SANTOSS (2013) formula cannot distinguish the phase-lag and hence interchange rate of the entrained sands between half-cycles of the well graded with the poorly graded sands. The proposed approach in this chapter (section 3.3.7) for modification the sheet flow layer thickness with regard to the grading index and the fine fraction percentage in mixed sands, improves the prediction results of the SANTOSS (2013) transport formula for mixed sands.

Consequently, application of proposed approach in this thesis leads to smaller net transport rate for graded sands and slightly larger for poorly-graded sands, and hence enhances the accuracy of predicted results. Phase-lag effect is increased for graded sands, particularly the graded sands with higher proportion of the fine fraction, while decreased for poorly graded sands. As a result, unsteady effect for well-graded sands was more intensive which led to larger sands exchange between half-cycles. However, more detailed experiments are required for better understanding the grading effect in multi-way interactions of graded sands within the sheet flow layer under nonlinear waves. In chapter 4 a new intergranular drag term is developed, which could improve the numerical modeling of interparticle interactions between sand grains from different fractions in the sheet flow layer.

4 Development of a two-phase numerical model for mixed sands transport (mixedSedFoam)

4.1 Governing equations

For each sand fraction as well as water the continuity equation is written as:

$$\frac{\partial \alpha_m}{\partial t} + \boldsymbol{\nabla}.\left(\alpha_m \boldsymbol{U_m}\right) = 0 \tag{4.1}$$

where α_m is the volumetric concentration of sand fractions or water in a computational cell, m is representative of sand fractions as well as water in a numerical cell (i.e. $m = s_1, s_2, s_3, ..., s_N$ as well as w). To use the benefits of indices characteristics, the $m = s_1, s_2, s_3, ..., s_N$ will be abbreviated as $m = 1, 2, 3, ..., N$. Bold symbols refer to vectorial parameters. $\boldsymbol{\nabla}$ is gradient vector and $\boldsymbol{U_m}$ is the velocity of sand fractions and water. $\boldsymbol{U_m}$ for each sand fraction and water is different and each sand fraction as well as water are transported/flowed with their corresponding velocities. It is clear that:

$$\sum_{m=1}^{N} \alpha_m + \alpha_w = 1 \tag{4.2}$$

where m is the number of sand fractions, which is limited to N and α_w is volume fraction of water. $\boldsymbol{U_1}$ is the velocity vector of the first sand fraction and should not be erred with the first component of velocity. For example $\boldsymbol{U_1}$ is:

$$\boldsymbol{U_1} = (u_{1x}, u_{1y}, u_{1z}) \tag{4.3}$$

where u_{1x}, u_{1y} and u_{1z} are x-, y- and z-velocity components of the first sand fraction, respectively and $\boldsymbol{U_w}$ is the velocity vector of water, which is:

$$\boldsymbol{U_w} = (u_{wx}, u_{wy}, u_{wz}) \tag{4.4}$$

and u_{wx}, u_{wy} and u_{wz} are x-, y- and z-velocity components of water-phase.
The momentum equation based on the second low of Newton is written as:

$$\frac{\partial(\alpha_m \rho_m \boldsymbol{U_m})}{\partial t} + \boldsymbol{\nabla}.\left(\alpha_m \rho_m \boldsymbol{U_m} \boldsymbol{U_m}\right) = -\alpha_m \boldsymbol{\nabla} P_w - \boldsymbol{\nabla} P_m + \boldsymbol{\nabla}.\tilde{\boldsymbol{\tau_m}} + \boldsymbol{M_m} + \alpha_m \rho_m \boldsymbol{g} \tag{4.5}$$

where $\boldsymbol{g}$ is gravitational acceleration vector ($\boldsymbol{g} = (0, 0, 9.81) ms^{-2}$), $\tilde{\boldsymbol{\tau_m}}$ shear stresses tensor and $\boldsymbol{M_m}$ is the interaction of each sand fraction with water as well as other fractions. To make Eq. 4.5 more clear, we expand it later for an example of a sand mixture composed of three fractions within water-phase.
For water-phase, the momentum equation is written as:

$$\frac{\partial(\alpha_w \rho_w \boldsymbol{U_w})}{\partial t} + \left(\alpha_w \rho_w \boldsymbol{U_w} \boldsymbol{U_w}\right) = -\alpha_w \boldsymbol{\nabla} P_w + \boldsymbol{\nabla}.\tilde{\boldsymbol{\tau_w}} + \boldsymbol{M_{w,m}} + \alpha_w \rho_w \boldsymbol{g} \tag{4.6}$$

where $\boldsymbol{M_{w,m}}$ is:
$$\boldsymbol{M_{w,m}} = -\alpha_m D_{m,w}\left(\boldsymbol{U_w} - \boldsymbol{U_m}\right) - D_{m,w}(\boldsymbol{\Delta_t}) \tag{4.7}$$

here $D_{m,w}$ is the drag force coefficient of mth sand fraction. Based on the drag force coefficient of Ding and Gidaspow (1990), applied in two-phase model of Cheng et al. (2017) for uniform sands, it is defined as Eq. A.1. In the developed model in this thesis d_m in Eq.

A.1 is considered as the D_{50} of the sand fractions, which is applied in available empirical formulas. α is the sum of volumetric concentrations of different fractions:

$$\alpha = \sum_{m=1}^{N} \alpha_m \tag{4.8}$$

and therefore:

$$\alpha + \alpha_w = 1 \tag{4.9}$$

For three sand fractions in this example, the momentum equation is written as:

$$\frac{\partial(\alpha_m \rho_m \boldsymbol{U_m})}{\partial t} + (\alpha_m \rho_m \boldsymbol{U_m U_m}) = -\alpha_m \boldsymbol{\nabla} P_w - \boldsymbol{\nabla} P_m$$
$$+ \boldsymbol{\nabla}.\tilde{\boldsymbol{\tau_m}} + \boldsymbol{M_{m,w}} + \boldsymbol{M_{m,n}} + \alpha_m \rho_m \boldsymbol{g} \tag{4.10}$$

where $\boldsymbol{M_{w,m}}$ is the interaction between water-phase and sand fraction, which is given as:

$$\boldsymbol{M_{m,w}} = -\boldsymbol{M_{w,m}} = \alpha_m D_{m,w} \left(\boldsymbol{U_w} - \boldsymbol{U_m}\right) + D_{m,w}(\boldsymbol{\Delta_t}) \tag{4.11}$$

Δ_t is representative for turbulence suspension and after Reynolds averaging was proposed by McTigue (1981) as Eq. A.4. $\boldsymbol{M_{m,n}}$ is the interaction of each sand fraction with other fractions and defined as:

$$\boldsymbol{M_{m,n}} = \sum_{m=1,m\neq n}^{N} D_{m,n}(\boldsymbol{U_m} - \boldsymbol{U_n}) \tag{4.12}$$

for the first fraction of a mixed sand composed of three fractions, it could be written as:

$$\boldsymbol{M_{1,n}} = D_{1,2}(\boldsymbol{U_1} - \boldsymbol{U_2}) + D_{1,3}(\boldsymbol{U_1} - \boldsymbol{U_3}) \tag{4.13}$$

$D_{m,n}$ is the drag force coefficient between sand fractions. Syamlal (1987) proposed the Eq. A.5, which is also used in MFiX (Syamlal et al., 1993) toolbox for granular flow simulation in chemical engineering.

4.2 Development of a new formula for interparticle drag force coefficient

Because of the importance of the interparticle momentum transfer between particles of different size classes, the drag force coefficient plays an important role in the sheet flow layer, where the collisional or enduring contact between sand grains is dominant (Fig. 2.21). The proposed formula by Syamlal (1987) (Eq. A.5) is a practical as well as simple approach which can describe the interparticle interactions. However, he used a simplifying assumption, which considers the same velocity for all particles of each fraction. It means all particles of different fractions have the same velocity before collision. In this thesis this assumption is not applied and therefore a new approach is developed. Due to the importance of this section, the principal physics of particles collision is described in section A.3 and the achievement of a more realistic equation for the drag force coefficient is presented here.

Fig. 4.1 shows exemplary the Velocity Distribution Function (VDF) for a fraction with the same velocity for all grains of 2 m/s for all particles in the Syamlal (1987) approach. In contrast, in this thesis a VDF, describing the variable velocities of a particle system is considered. The VDF of Maxwell (1860)-Boltzmann (1872) is applied to find the interparticle drag force coefficient for a particle system with variable velocities. Therefore, instead
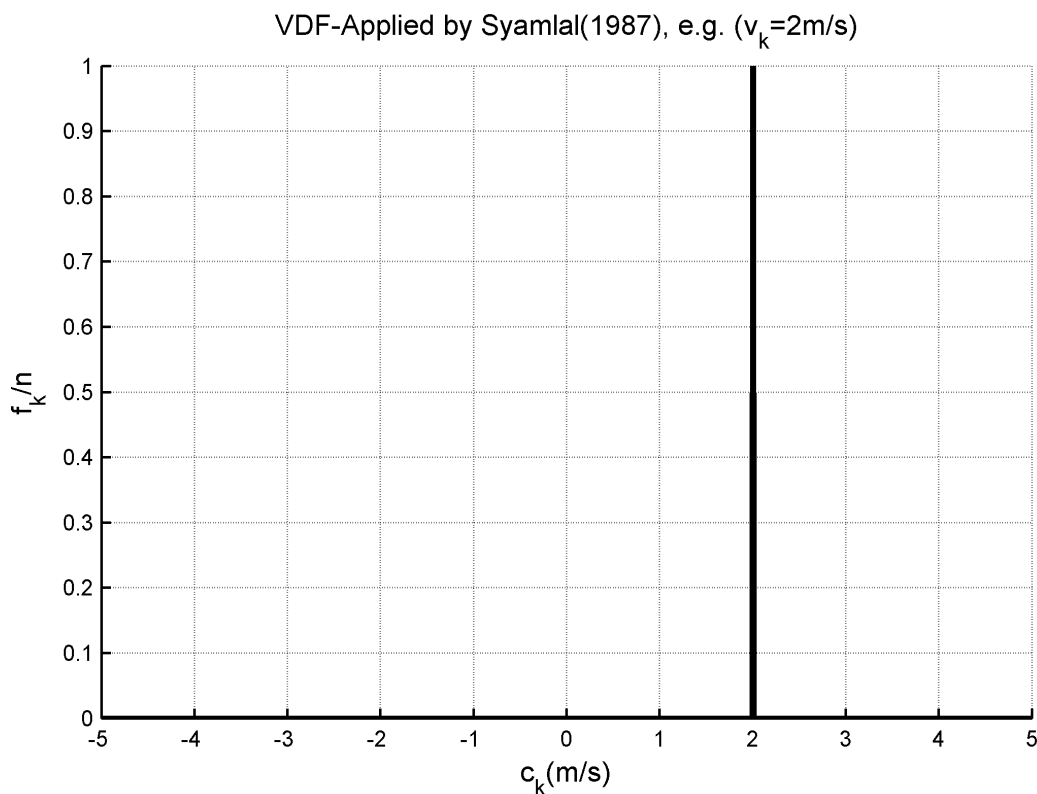
Figure 4.1: Velocity Distribution Function (VDF) applied by Syamlal (1987) to find the interparticle drag force coefficient.

of Dirac delta function applied by Syamlal (1987) in Eq. A.5, the 3D-VDF of Maxwell (1860)-Boltzmann (1872) (Eq. A.43) is applied. Due to inclusion of the kinetic energy of a particulate system (T parameter) in the Maxwell (1860)-Boltzmann (1872) VDF, it has been frequently applied in literature to describe the VDF of particulate systems composed of different grains. T for k^{th} granular system in a mixture of different fractions is defined as:

$$T_k = (1/3) < {C_k}^2 > \tag{4.14}$$

which could describe the magnitude of kinetic energy for a system of particles. Fig. 4.2 shows exemplary the Maxwell (1860)-Boltzmann (1872) VDF for four different T. As can be seen in Fig. 4.2 compared with Fig. 4.1 for the same ensemble averaged velocity (i.e. $v_k = 2\,m/s$), the particle velocity in the Maxwell (1860)-Boltzmann (1872) could better describe the single particle velocities compared with the applied same velocity for all particles of a granular system in the proposed interparticle drag by Syamlal (1987). The Syamlal (1987) solution for interparticle drag force coefficient is found in section A.3. Due to the deficient assumption in the approach of Syamlal (1987), where all particles of a system have the same velocity equal to their average velocity, this thesis develops a new approach using a VDF of Maxwell (1860)-Boltzmann (1872) instead of a single value applied by Syamlal (1987) in the Dirac delta function. Therefore, the Eq. A.40 is written
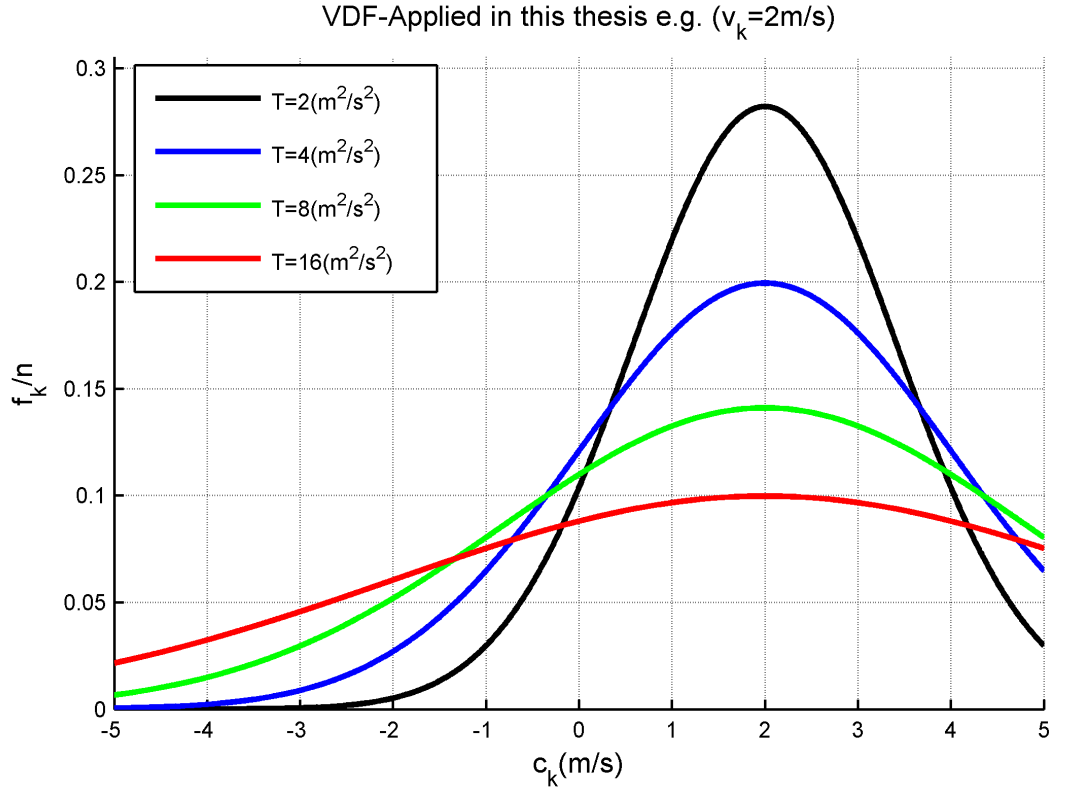
Figure 4.2: Velocity Distribution Function (VDF) of Maxwell (1860)-Boltzmann (1872) applied in this thesis to find the interparticle drag force coefficient.

as:

$$\boldsymbol{I_{kj}} = -m_k m_j/(m_k + m_j)(1 + e)(\sigma^2 g_{kj})$$

$$\int_{\boldsymbol{c_{kj}.b}>0} (\boldsymbol{c_{kj}.b})^2(\boldsymbol{b} + \mu_N \boldsymbol{t_n})\,(n_k/(2\pi T_k)^{(3/2)})(n_j/(2\pi T_j)^{(3/2)}) \tag{4.15}$$

$$exp(-((\boldsymbol{c_k} - \boldsymbol{v_k})^2/(2T_k) + (\boldsymbol{c_j} - \boldsymbol{v_j})^2/(2T_j)))\,\boldsymbol{db\,dc_k\,dc_j}$$

Now the parameters $\boldsymbol{c_k} - \boldsymbol{v_k}$ and $\boldsymbol{c_j} - \boldsymbol{v_j}$ are considered as new parameters:

$$\begin{cases} \boldsymbol{c_k} - \boldsymbol{v_k} = \boldsymbol{C_k} \\ \boldsymbol{c_j} - \boldsymbol{v_j} = \boldsymbol{C_j} \end{cases} \tag{4.16}$$

therefore:

$$\begin{cases} \boldsymbol{dc_k} = \boldsymbol{dC_k} \\ \boldsymbol{dc_j} = \boldsymbol{dC_j} \end{cases} \tag{4.17}$$

$$\boldsymbol{C_{kj}} = \boldsymbol{c_{kj}} + \boldsymbol{v_{jk}} \quad , \quad \boldsymbol{c_{kj}} = \boldsymbol{C_{kj}} + \boldsymbol{v_{kj}} \tag{4.18}$$

$$m_k n_k = \alpha_k \rho_k \ , \ m_j n_j = \alpha_j \rho_j \tag{4.19}$$

Using Eq. 4.16 to Eq. 4.19, Eq. 4.15 is written as:

$$I_{kj} = -\alpha_k \alpha_j \rho_k \rho_j / ((m_k + m_j)(2\pi)^3 (T_k T j)^{(3/2)})(1 + e)(\sigma^2 g_{kj})$$

$$\int_{c_{kj}.b>0} ((C_{kj} + v_{kj}).b)^2 (b + \mu_N t_n) \ exp(-((C_k)^2/(2T_k) + (C_j)^2/(2T_j))) \ db \ dC_k \ dC_j$$

(4.20)

Using Eq. A.44, Eq. 4.20 is written as:

$$I_{kj} = -\alpha_k \alpha_j \rho_k \rho_j / ((m_k + m_j)(2\pi)^3 (T_k T j)^{(3/2)})(1 + e)(\sigma^2 g_{kj})$$

$$\left(\int_{c_{kj}.b>0} ((C_{kj} + v_{kj})cos\theta)^2 (b) \ exp(-((C_k)^2/(2T_k) + (C_j)^2/(2T_j))) \ db \ dC_k \ dC_j \right.$$

$$\left. + \int_{c_{kj}.b>0} ((C_{kj} + v_{kj})cos\theta)^2 (\mu_N t_n) \ exp(-((C_k)^2/(2T_k) + (C_j)^2/(2T_j))) \ db \ dC_k \ dC_j \right)$$

(4.21)

Solution of the integral in Eq. 4.21 is found in A.3.1 to A.3.2. Using Eq. A.57, Eq. A.60 and Eq. A.70, this integral is written as:

$$I_{kj} = -\alpha_k \alpha_j \rho_k \rho_j / ((m_k + m_j)(2\pi)^3 (T_k T j)^{(3/2)})(1 + e)(\sigma^2 g_{kj})$$

$$2\pi \sqrt{T_k T_j}(T_k + T_j + v_{kj}^2)(\pi/2 + \mu_N \pi^2/8)h$$

(4.22)

if we consider the direction of c_{kj} as v_{kj} then:

$$I_{kj} = -\alpha_k \alpha_j \rho_k \rho_j / ((m_k + m_j)(2\pi)^3 (T_k T j)^{(3/2)})(1 + e)(\sigma^2 g_{kj})$$

$$2\pi \sqrt{T_k T_j}(T_k + T_j + v_{kj}^2)(\pi/2 + \mu_N \pi^2/8)(v_{kj}/|v_{kj}|)$$

(4.23)

therefore:

$$I_{kj} = -\alpha_k \alpha_j \rho_k \rho_j / ((m_k + m_j)(2\pi)^3 (T_k T j)^{(3/2)})(1 + e)(\sigma^2 g_{kj})$$

$$2\pi \sqrt{T_k T_j}(T_k/|v_{kj}| + T_j/|v_{kj}| + |v_{kj}|)(\pi/2 + \mu_N \pi^2/8)v_{kj}$$

(4.24)

Using one-dimensional Maxwell (1860)-Boltzmann (1872) VDF the Eq. 4.24 is written as:

$$I_{kj} = -\alpha_k \alpha_j \rho_k \rho_j / ((m_k + m_j)(2\pi)(T_k T j)^{(1/2)})(1 + e)(\sigma^2 g_{kj})$$

$$2\pi \sqrt{T_k T_j}(T_k/|v_{kj}| + T_j/|v_{kj}| + |v_{kj}|)(\pi/2 + \mu_N \pi^2/8)v_{kj}$$

(4.25)

or:

$$I_{kj} = -\alpha_k \alpha_j \rho_k \rho_j (1 + e)(\sigma^2 g_{kj})(T_k/|v_{kj}| + T_j/|v_{kj}| + |v_{kj}|)(\pi/2 + \mu_N \pi^2/8)v_{kj}/(m_k + m_j)$$

(4.26)

and using the assumption of spherical particles, $m_k = \rho_k(\pi d_k^3)/6$, $m_j = \rho_j(\pi d_j^3)/6$ and $\sigma = (d_k + d_j)/2$, then Eq. 4.26 is written in such a way to be comparable with Syamlal (1987) relationship:

$$I_{kj} = -3\alpha_k \alpha_j \rho_k \rho_j (1 + e)(d_k + d_j)^2 g_{kj}(T_k/|v_{kj}| + T_j/|v_{kj}| + |v_{kj}|)(\pi/2 + \mu_N \pi^2/8)v_{kj}/$$

$$(2\pi(\rho_k d_k^3 + \rho_j d_j^3))$$

(4.27)

The new equation (Eq. 4.27) for the interparticle drag force coefficient (IDC) of this research is:

$$D_{kj} = 3\alpha_k \alpha_j \rho_k \rho_j (1 + e)(\pi/2 + \mu_N \pi^2/8)(d_k + d_j)^2 g_{kj}(T_k/|v_{kj}| + T_j/|v_{kj}| + |v_{kj}|)$$

$$/(2\pi(\rho_k d_k^3 + \rho_j d_j^3))$$

(4.28)

Comparison between the new relationship for IDC in this research (Eq. 4.28) and the
Syamlal (1987)'s equation (Eq. A.5) shows, that two new terms of $T_k/|\boldsymbol{v_{kj}}|$ and $T_j/|\boldsymbol{v_{kj}}|$
are in the newly developed formula. Because of the new terms of T_k and T_j in the new
particle-particle drag force coefficient formula, it can better explain the dynamic intensity
of particles, where $T_k = (1/3) < C_k{}^2 >$ and $T_j = (1/3) < C_j{}^2 >$.

Dividing the developed formula for interparticle drag force coefficient to the proposed by
Syamlal (1987), results in:

$$\frac{D_{kj}(of\ this\ thesis)}{D_{kj}(of\ Syamlal(1987))} = (\frac{T_k}{|\boldsymbol{v_{kj}}|^2} + \frac{T_j}{|\boldsymbol{v_{kj}}|^2} + 1) \tag{4.29}$$

Fig. 4.3 illustrates the increasing of the developed interparticle drag force coefficient com-
pared with the proposed by Syamlal (1987)'s equation (Eq. A.5). As can bee seen, for
a $(T_k + Tj)$ of unit, the proposed interparticle drag force coefficient for a $|v_{kj}| = 0.5$ is
five times higher than its counterpart. Because of the term $|v_{kj}|$ in denominator, for its
smaller values, the difference between the proposed IDC- with the Syamlal (1987) increased
significantly.
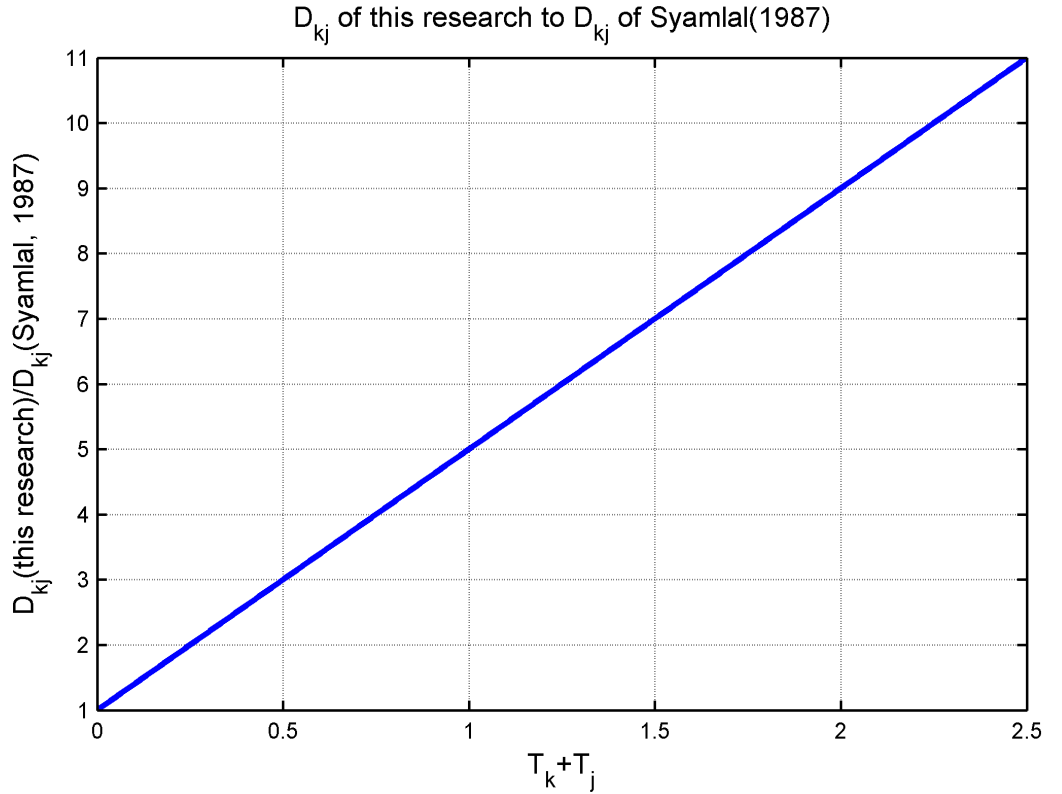
Figure 4.3: Developed drag force coefficient in comparison with the proposed by Syamlal
(1987) for fluctuating energy of particle systems.

If T depicts the $T_k + T_j$, Fig. 4.4 shows the behavior of the developed IDC in comparison
with that of proposed by Syamlal (1987). As can be seen, when the averaged velocity
difference between two particle systems decreased, the developed IDC gives higher value
compared with the Syamlal (1987) formula. This ICD is increased by increasing the gran-
ular fluctuating energy. This can be explained by the higher collision frequency between
particles of different particle systems.
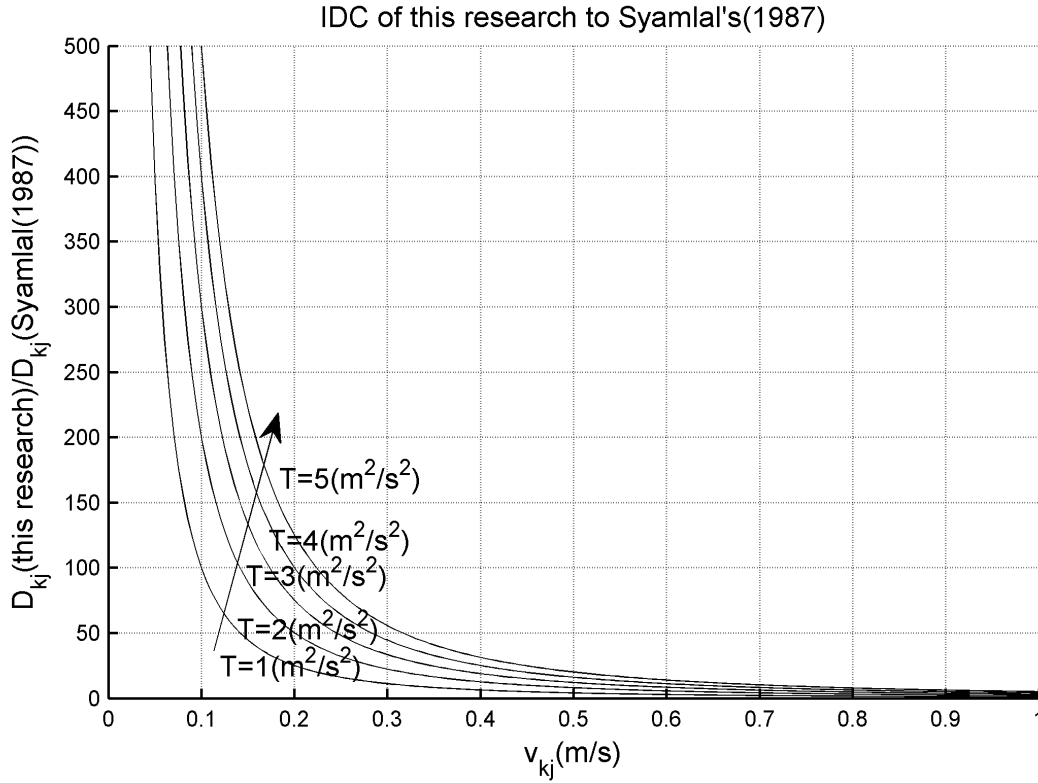
Figure 4.4: Developed drag force coefficient to the proposed by Syamlal (1987) for different fluctuating energy of particle systems by increasing v_{kj}.

Fig. 4.4 shows the general behavior of the proposed IDC for changing both variables of v_{kj} and T. As can be seen, the developed IDC results in this thesis are by far higher than that of Syamlal (1987), particularly for higher granular fluctuating energies (T).

If we consider the value of differences between the developed $\boldsymbol{I_{kj}}$ in this thesis with the Syamlal (1987)'s formula, it can be written as:

$$|(\boldsymbol{I_{kj}})_{this\ thesis} - (\boldsymbol{I_{kj}})_{Syamlal\ (1987)}| = A(T_k + T_j) \tag{4.30}$$

where

$$A = -3\alpha_k\alpha_j\rho_k\rho_j(1+e)(d_k + d_j)^2 g_{kj}(\pi/2 + \mu_N\pi^2/8)/(2\pi(\rho_k d_k^3 + \rho_j d_j^3)) \tag{4.31}$$

This means that the developed IDC includes the fluctuating energy of particles in a granular system, whereas the Syamlal (1987)'s formula is not capable of describing this important property. Coming back to Eq. 4.10, $\tilde{\boldsymbol{\tau_w}}$ is the shear stress tensor of water, which is written by use of Boussinesq (1877) approximation as:

$$\tilde{\boldsymbol{\tau_w}} = \alpha_w\mu_w(\boldsymbol{\nabla U_w} + \boldsymbol{\nabla U_w^T}) + \alpha_w(\lambda_w - \frac{2}{3}\mu_w)(\boldsymbol{\nabla.U_w})\tilde{\boldsymbol{I}} \tag{4.32}$$

where μ_w and λ_w are dynamic and bulk viscosity of water, respectively.
P_m is divided into two parts as collisional and frictional, to consider the transport of sand grains in the sand media, then:

$$P_m = P_m^c + P_m^f \tag{4.33}$$
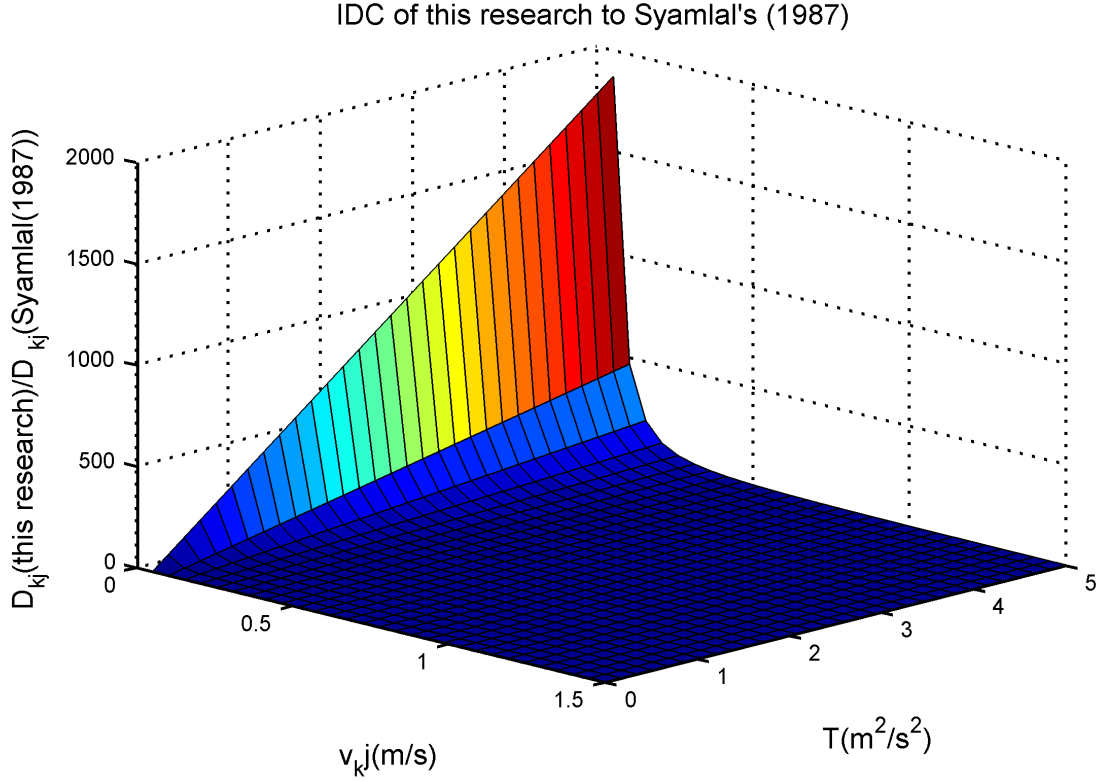
Figure 4.5: Developed drag force coefficient to the proposed by Syamlal (1987) against fluctuating energy of particle systems and v_{kj}.

In the same way the tensor of shear stress is also defined as:

$$\tilde{\boldsymbol{\tau_m}} = \tilde{\boldsymbol{\tau_m}}^{\boldsymbol{c}} + \tilde{\boldsymbol{\tau_m}}^{\boldsymbol{f}} \tag{4.34}$$

Syamlal et al. (1993) proposed Eq. A.9 for collisional pressure of mth fraction, which is required for its momentum equation (Eq. 4.10) and the frictional pressure is given by proposed equation of Johnson and Jackson (1987) as Eq. A.10. The $\tilde{\boldsymbol{\tau_m}}^{\boldsymbol{c}}$ is defined like fluid-phase, which was proposed by Gidaspow (1994) as:

$$\tilde{\boldsymbol{\tau_m}}^{\boldsymbol{c}} = \alpha_m \mu_m^c (\boldsymbol{\nabla U_m} + \boldsymbol{\nabla U_m^T}) + \alpha_m (\lambda_m^c - \frac{2}{3}\mu_m^c)(\boldsymbol{\nabla.U_m})\tilde{\boldsymbol{I}} \tag{4.35}$$

where μ_m^c is the collisional dynamic viscosity and is given by Syamlal et al. (1993) asEq. A.11. The frictional shear stresses for sand fractions is given by Cheng and Hsu (2014) like collisional as:

$$\tilde{\boldsymbol{\tau_m}}^{\boldsymbol{f}} = \alpha_m \mu_m^f (\boldsymbol{\nabla U_m} + \boldsymbol{\nabla U_m^T}) + \alpha_m (\lambda_m^f - \frac{2}{3}\mu_m^f)(\boldsymbol{\nabla.U_m})\tilde{\boldsymbol{I}} \tag{4.36}$$

where μ_m^f and λ_m^f are dynamic and bulk frictional viscosity of mth sand fraction. The bulk viscosity in frictional stresses could be neglected (in contrast to collisional bulk viscosity) and dynamic frictional viscosity is given by Cheng and Hsu (2014) as:

$$\mu_m^f = \frac{P_m^f sin\phi}{\alpha_m \sqrt{2\tilde{\boldsymbol{\chi_m}} : \tilde{\boldsymbol{\chi_m}}}} \tag{4.37}$$

where $\boldsymbol{\chi_m}$ is the deviator of the strain rate tensor for mth sand fraction, which is defined as Eq. A.13, and ϕ is the angle of repose which is given as 35° for mixed sands in this thesis compared to 28° for uniform sands by Cheng and Hsu (2014).

The transport equation of granular temperature for mth sand fraction (T_m) is written based on the Syamlal et al. (1993) approach as:

$$
\frac{3}{2}\left(\frac{\partial(\alpha_m\rho_m T_m)}{\partial t}+\boldsymbol{\nabla}.(\alpha_m\rho_m T_m\boldsymbol{U_m})\right)=(-P_m\tilde{\boldsymbol{I}}+\tilde{\boldsymbol{\tau_m}}):\boldsymbol{\nabla U_m}+\boldsymbol{\nabla}.(k_m\boldsymbol{\nabla}T_m)
$$
$$
-\gamma_m+J_{mw}+\sum_{m=1,m\neq n}^{N}J_{m,n}
$$
(4.38)

where k_m is the diffusion parameter of granular temperature for mth sand fraction and is given by Syamlal et al. (1993) as Eq. A.14 and γ_m is the dissipation rate of T_m due to the inelastic collisions and is given by Syamlal et al. (1993) as Eq. A.16.

J_{mw} represents the granular energy exchange between water and mth sand fraction, which is given by Cheng and Hsu (2014) as:

$$
J_{mw}=\alpha_m\ D_{m,w}\ (2A_m k_w-3T_m)
$$
(4.39)

where A_m accounts for the capability of mth sand fraction to follow the water-phase velocity fluctuations. Therefore, it could be presented by means of Stokes number of mth sand fraction (St_m) and is given like proposed equation by Cheng and Hsu (2014) as:

$$
A_m=exp(-B\ St_m)
$$
(4.40)

where B is an empirical coefficient and was proposed as 0.15 by Cheng and Hsu (2014). The Stokes number is defined as:

$$
St_m=\frac{t_m}{t_w}
$$
(4.41)

where t_m is the sand particle response time for the mth sand fraction and has a relation to the density of sand particles and its drag force coefficient. It is defined as:

$$
t_m=\frac{\rho_m}{D_{m,w}}
$$
(4.42)

and t_w represents the time-scale of water-phase eddies. It is given as:

$$
t_w=\frac{k_w}{(6\epsilon_w)}
$$
(4.43)

where k_w and ϵ_w are kinetic energy and its dissipation rate.

$J_{m,n}$ is the granular energy exchange between sand fractions, which will be neglected after summing in Eq. 4.38.

4.3   Turbulence Model

Following the modified $k-\epsilon$ model for sand transport by Cheng and Hsu (2014), k-equation for water-phase is written as:

$$
\frac{\partial(\rho_w k_w)}{\partial t}+\boldsymbol{\nabla}.(\rho_w k_w\boldsymbol{U_w})=\boldsymbol{\nabla}.\left((\mu_w+\frac{\mu_w^t}{\sigma_k})\boldsymbol{\nabla}k_w\right)+\tilde{\boldsymbol{R_w^t}}:\boldsymbol{\nabla U_w}-\epsilon_w
$$
$$
-\frac{2D_{m,w}(1-A_m)\alpha k_w}{\alpha_w}-\frac{1}{\alpha_w}\frac{\mu_w^t}{\sigma_c}(\boldsymbol{\nabla}\alpha).(\rho_s-\rho_w)\boldsymbol{g}
$$
(4.44)

where $\tilde{\boldsymbol{R}_{\boldsymbol{w}}^{\boldsymbol{t}}}$ accounts for the large-scale components of shear stresses (like Reynolds stresses after Reynolds averaging) in comparison with $\tilde{\boldsymbol{r}_{\boldsymbol{w}}^{\boldsymbol{v}}}$, which is the small-scale shear stresses (like viscous stresses) in the total shear stress tensor ($\tilde{\boldsymbol{\tau}_{\boldsymbol{w}}} = \tilde{\boldsymbol{R}_{\boldsymbol{w}}^{\boldsymbol{t}}} + \tilde{\boldsymbol{r}_{\boldsymbol{w}}}$).
Hsu (2002) defined the R_w^t as:

$$\boldsymbol{R}_{\boldsymbol{w}_{\boldsymbol{ij}}}^{\tilde{\boldsymbol{t}}} = \rho_w \nu_w^t \left(\frac{\partial \boldsymbol{u}_{\boldsymbol{i_w}}}{\partial x_j} + \frac{\partial \boldsymbol{u}_{\boldsymbol{j_w}}}{\partial x_i}\right) - \frac{2}{3}\rho_w \nu_w^t \left(\frac{\partial \boldsymbol{u}_{\boldsymbol{i_w}}}{\partial x_j}\right)\delta_{ij} - \frac{2}{3}\rho_w((1-\alpha)k_w)\delta_{ij} \qquad (4.45)$$

and k_w as:

$$k_w = \frac{1}{2(1-\alpha)}\overline{(1-\alpha)\Delta u_{w_i}\Delta u_{w_i}} \qquad (4.46)$$

Cheng and Hsu (2014) used the similar formulation for R_w^t and defined the $\tilde{\boldsymbol{\tau}_{\boldsymbol{w}}}$ as:

$$\tilde{\boldsymbol{\tau}_{\boldsymbol{w}}} = \boldsymbol{R}_{\boldsymbol{w}_{\boldsymbol{ij}}}^{\tilde{\boldsymbol{t}}} + \tilde{\boldsymbol{r}_{\boldsymbol{w}}} = \rho_w \nu_w^{eff}\left(\frac{\partial \boldsymbol{u}_{\boldsymbol{i_w}}}{\partial x_j} + \frac{\partial \boldsymbol{u}_{\boldsymbol{j_w}}}{\partial x_i}\right) - \frac{2}{3}\rho_w \nu_w^{eff}\left(\frac{\partial \boldsymbol{u}_{\boldsymbol{i_w}}}{\partial x_j}\right)\delta_{ij} - \frac{2}{3}\rho_w k_w \delta_{ij} \qquad (4.47)$$

where:

$$\nu_w^{eff} = \nu_w + \nu_w^t \qquad (4.48)$$

This is the Boussinesq (1877) hypothesis and is usually used like above-mentioned in literature and therefore is used in this thesis unchanged. The last two terms include the water-sediment interactions and are unchanged from the available solver sedFoam, however, because of changing the α, which represents the concentration in this thesis, the computed turbulence and its dissipations are different from the results using sedFoam. It should be noted that the α calculated in this thesis is different from the solver developed by Cheng and Hsu (2014), and therefore the reults of the developed solver in this thesis are different from the sedFoam. Trying to solve the uniform sand transport using sedFoam was not successful, because of instability of sedFoam solver.

The first three terms on the right hand side of Eq. 4.44 describe diffusion, production and dissipation rates of k, respectively. The last two terms are modification terms compared to the standard k-equation, which describe the interaction between sand fractions and waterphase. The forth term describes the drag effect on the turbulent eddies, which prevent the sand grains to follow the eddies, and therefore the Stokes dependent parameter (A_m) and drag force coefficient $D_{m,w}$ are involved. The fifth term accounts for eddy dissipation rate through density stratification caused by the sand grains settling. σ_k and σ_c are constants, which are determined by calibration (Cheng and Hsu, 2014). In a similar way, ϵ-equation could be written as:

$$\frac{\partial(\rho_w \epsilon_w)}{\partial t} + \boldsymbol{\nabla}.(\rho_w \epsilon_w \boldsymbol{U_w}) = \boldsymbol{\nabla}.\left((\mu_w + \frac{\mu_w^t}{\sigma_\epsilon})\boldsymbol{\nabla}\epsilon_w\right) + C_{1\epsilon}(\frac{\epsilon_w}{k_w})\tilde{\boldsymbol{R}_{\boldsymbol{w}}^{\boldsymbol{t}}} : \boldsymbol{\nabla}\boldsymbol{U_w} - C_{2\epsilon}(\frac{\epsilon_w}{k_w})\epsilon_w$$
$$-C_{3\epsilon}(\frac{\epsilon_w}{k_w})\frac{2D_{m,w}(1-A_m)\alpha k_w}{\alpha_w} - C_{4\epsilon}(\frac{\epsilon_w}{k_w})\frac{1}{\alpha_w}\frac{\mu_w^t}{\sigma_c}(\boldsymbol{\nabla}\alpha).(\rho_s - \rho_w)\boldsymbol{g} \qquad (4.49)$$

where σ_ϵ, $C_{1\epsilon}$, $C_{2\epsilon}$, $C_{3\epsilon}$ and $C_{4\epsilon}$ are calibration parameters and $\frac{\epsilon_w}{k_w}$ depicts the dissipation intensity.

Eddy viscosity could be defined based on dimensional analysis (Malalasekera and Versteeg, 2007) as:

$$\mu_w^t = C_\mu \rho_w \frac{k_w^2}{\epsilon_w} \qquad (4.50)$$

where C_μ is a dimensionless constant.

Aforementioned constants are not changed in the developed model in this thesis, however, the A_m parameter is increased by decreasing the B-value for mixed sands. Tab. 4.1 shows the constant parameters.

Table 4.1: Constants in $k - \epsilon$ turbulence model (Cheng and Hsu, 2014).

σ_k	σ_c	σ_ϵ	$C_{1\epsilon}$	$C_{2\epsilon}$	$C_{3\epsilon}$	$C_{4\epsilon}$	C_μ
1.0	1.0	1.30	1.44	1.92	1.20	1.0	0.09

4.4   Mixed sand transport solver (mixedSedFoam)

Discussed equations in section 4.1 were implemented by Rusche (2003) in the form of uniform condition (m=1) in OpenFOAM within the solver twoPhaseEulerFoam. Cheng et al. (2017) modified this solver by defining θ-equation (Gidaspow, 1994), and hence KTGF to model the uniform sand transport under sheet flow conditions. This solver is called twoPhaseEulersedFoam (or sedFoam) and was calibrated and validated by means of O'Donoghue and Wright (2004a)'s experimental dataset for uniform sand.

The new developed solver in this thesis is called mixedSedFoam and is developed using the twoPhaseEulersedFoam solver of Cheng and Hsu (2014). mixedSedFoam includes the implementation of the new developments of this thesis for the available mixture model approach of Manninen et al. (1996). The new developed formulation for the continuity equation in this thesis remedies the inconsistency of mixture approach for volume of fraction, as was mentioned by Niemi (2012). It should be noted that the numerical studies using a two- or multi-phase flow to study the dynamics of mixed sands under sheet-flow condition due to the complexity and the expensive computational effort are rare. To the best knowledge of the author, there is an Eulereian-Lagrangian solver by Rafati et al. (2022), which applies the sedFoam formulation of Cheng et al. (2017) for flow phase and tracks the position of particle phases using a Lagrangian approach. In contrast, in this thesis both phases are modelled in an Eulerian framework, which reduces the computational cost and therefore extends the computational domain from 6 mm of Rafati et al. (2022) to 50 cm like the test-cases of sedFoam for the streamwise (x) direction. However, the applied solver for new development is sedFoam, which does not consider the air phase and consequently neglects the effects of the free surface progressive waves.

Recently, Kim et al. (2019) applied the sedFoam and developed a new solver i.e. sedWaveFoam, which includes the third phase (i.e. air) to the phases equations and models the uniform sand transport. However, due to the computational cost, lack of a mixed sand transport, and also lack of a systematic dataset for mixed-sand transport under free surface waves, this thesis focuses on the development a new solver for mixed sand transport without considering a free surface i.e. the air phase.

mixedSedFoam in contrast to sedFoam includes the fractional sand grains interactions and consequently is capable of reproducing the velocity and concentration profiles for each sand fraction under sheet flow conditions. The model results are calibrated and validated by means of the O'Donoghue and Wright (2004a) dataset for mixed sand transport under sheet flow. Therefore, the development part of this thesis with its capabilities and limitations through comparison the model results with measurements are discussed and for uniform sands the interested reader is referred to Cheng et al. (2017).

The main focus of this thesis is on the mixed sand transport under sheet flow conditions. Interaction between grains as well as simplification and implementation of related equations are discussed. Using the new development for the phase-equations and coupling the results with the super-ordinate two-phase flow model in this thesis, the available mixture model approach proposed by Manninen et al. (1996) for multi-phase flows is developed, and its limitation to couple with the phase and transport equations of the super-ordinate

equations is solved by means of the new developed solver in this thesis (mixedSedFoam). This limitation was exemplary discussed by Niemi (2012) in ANSYS FLUENT® for fluidized bed combustion boilers, where he was not able to couple the fractional results to the super-ordinate two-phase model results. The new proposed formulation for phase equations, improves the coupling capability of the mixture approach. Moreover, the phase equation for each sand fraction is different than the available classic equations for phase equation. Furthermore, the new developed interparticle drag equation in this thesis shows a more reasonable description of the fractional velocities contribution to the interparticle drag interactions.

In mixture approach (Manninen et al., 1996), the governing equations in section 4.1 should be summed over the number of solid-phases (sand fractions) for sand fractions (continuity and momentum), which was proposed by Manninen et al. (1996) . Section A.4 summarizes the mixture approach.

Following simplifications in mixture approach make it computationally efficient in comparison with a multi-phase approach Niemi (2012). However, due to the following reasons for the behavior of sand grains in the sheet flow layer, these assumptions do not disturb its accuracy:

(i) velocity fluctuations of sand fractions is in the same order of the whole sand-phase, that it makes sense specially for high concentrations of sand fractions in the sheet flow layer. Therefore:

$$\rho_s \frac{\partial}{\partial t}(\boldsymbol{U_m} - \boldsymbol{U_s}) = 0 \tag{4.51}$$

(ii) due to the similar order of velocity differences of the second and third term on the RHS of Eq. A.91, they could be canceled.

(iii) using this assumption that the sand fractions pressure could be computed proportionally to the corresponding fractional concentration, i. e. :

$$P_m = \frac{\alpha_m}{\alpha_s} P_S \tag{4.52}$$

, the forth term on the RHS of Eq. A.91 could be neglected.

(iv) the two parts of the fifth term on the RHS of Eq. A.91 are small compared to drag term (sixth term on the RHS), and therefore their difference could be resulted in an insignificant value, which could be neglected.

Consequently, Eq. A.91 could be simplified as:

$$\boldsymbol{M_{m,w}} + \sum_{m=1,m\neq n}^{N} \boldsymbol{M_{m,n}} = (\frac{\alpha_m}{\alpha_s}) \sum_{m=1}^{N} \boldsymbol{M_{m,w}} \tag{4.53}$$

or

$$\boldsymbol{M_{m,w}} + \sum_{m=1,m\neq n}^{N} \boldsymbol{M_{m,n}} = (\frac{\alpha_m}{\alpha_s})\boldsymbol{M_{s,w}} \tag{4.54}$$

Solving nonlinear equations system of Eq. 4.54 will reproduce the velocity and volumetric concentration of sand fractions.

For example, Eq. 4.54 could be extended for a system of three nonlinear equations of a

mixed sand composed of three fractions (F : fine, M : medium and C : coarse) as:

$$
\begin{cases}
D_{F,w}(\boldsymbol{U_F} - \boldsymbol{U_w}) + D_{F,M}(\boldsymbol{U_M} - \boldsymbol{U_F}) + D_{F,C}(\boldsymbol{U_C} - \boldsymbol{U_F}) = (\frac{\alpha_F}{\alpha_s})D_{s,w}(\boldsymbol{U_s} - \boldsymbol{U_w}) \\
D_{M,w}(\boldsymbol{U_M} - \boldsymbol{U_w}) + D_{M,F}(\boldsymbol{U_F} - \boldsymbol{U_M}) + D_{M,C}(\boldsymbol{U_C} - \boldsymbol{U_M}) = (\frac{\alpha_M}{\alpha_s})D_{s,w}(\boldsymbol{U_s} - \boldsymbol{U_w}) \\
D_{C,w}(\boldsymbol{U_C} - \boldsymbol{U_w}) + D_{C,F}(\boldsymbol{U_F} - \boldsymbol{U_C}) + D_{C,M}(\boldsymbol{U_M} - \boldsymbol{U_C}) = (\frac{\alpha_C}{\alpha_s})D_{s,w}(\boldsymbol{U_s} - \boldsymbol{U_w})
\end{cases}
\tag{4.55}
$$

Corresponding continuity equations for these three sand fractions could be another equations system as:

$$
\begin{cases}
\dfrac{\partial \alpha_F}{\partial t} + \boldsymbol{\nabla}.(\alpha_F \boldsymbol{U_F}) = 0 \\
\dfrac{\partial \alpha_M}{\partial t} + \boldsymbol{\nabla}.(\alpha_M \boldsymbol{U_M}) = 0 \\
\dfrac{\partial \alpha_C}{\partial t} + \boldsymbol{\nabla}.(\alpha_C \boldsymbol{U_C}) = 0
\end{cases}
\tag{4.56}
$$

Therefore, six equations for six unknowns are produced. Solving equations systems of 4.55 and 4.56 will be resulted in the velocities and volumetric concentrations for each sand fraction.

4.5   New developed complement phase-averaged velocity

In this thesis a new formula for continuity(phase) equations is developed which increases the contribution of all available phases properties and consequently increases the coupling between fractional sand concentrations and corresponding velocities. Moreover, the total sand concentration in continuity and momentum equations is changed based on the sum of the composing fractional concentrations, therefore, at the first the coupling between two-phase model and constituting phases is guaranteed and finally the results are different than the two-phase solver for uniform sand.
To this end, a phase averaged velocity is defined as:

$$
\overline{U} = \sum_{i=1}^{n+fluid} \alpha_i \boldsymbol{U_i}
\tag{4.57}
$$

therefore, for a sand composed of three fractions Eq. 4.57 is written as:

$$
\overline{U} = \alpha_1 \boldsymbol{U_1} + \alpha_2 \boldsymbol{U_2} + \alpha_3 \boldsymbol{U_3} + \alpha_w \boldsymbol{U_w}
\tag{4.58}
$$

where:

$$
\alpha_w = 1 - \sum_{i=1}^{n} \alpha_i
\tag{4.59}
$$

now in this thesis a new formula for velocity is developed, which is called *complement phase−averaged velocity* and given as:

$$
\overline{U_i}' = \sum_{j=1}^{n+fluid} (1 - \delta_{ij})\alpha_j(\boldsymbol{U_i} - \boldsymbol{U_j})
\tag{4.60}
$$

The *complement phase − averaged velocity* for first fraction of a mixed sand composed of three sand fractions is written as:

$$
\overline{U_1}' = (\alpha_2(\boldsymbol{U_1} - \boldsymbol{U_2}) + \alpha_3(\boldsymbol{U_1} - \boldsymbol{U_3}) + \alpha_w(\boldsymbol{U_1} - \boldsymbol{U_w}))
\tag{4.61}
$$

Therefore:

$$\alpha_i \boldsymbol{U_i} = \alpha_i(\overline{\boldsymbol{U}} + \overline{\boldsymbol{U_i}}') \tag{4.62}$$

Eq. 4.62 for the first fraction of a tri-modal mixed sand is written as:

$$
\begin{aligned}
\alpha_1 \boldsymbol{U_1} = \alpha_1(\alpha_1 \boldsymbol{U_1} + \alpha_2 \boldsymbol{U_2} + \alpha_3 \boldsymbol{U_3} + \alpha_w \boldsymbol{U_w}) + \\
\alpha_1(\alpha_2(\boldsymbol{U_1} - \boldsymbol{U_2}) + \alpha_3(\boldsymbol{U_1} - \boldsymbol{U_3}) + \alpha_w(\boldsymbol{U_1} - \boldsymbol{U_w})) = \\
\alpha_1\alpha_1\boldsymbol{U_1} + \alpha_1\alpha_2\boldsymbol{U_2} + \alpha_1\alpha_3\boldsymbol{U_3} + \alpha_1\alpha_w\boldsymbol{U_w} + \\
\alpha_1\alpha_2\boldsymbol{U_1} - \alpha_1\alpha_2\boldsymbol{U_2} + \alpha_1\alpha_3\boldsymbol{U_1} - \alpha_1\alpha_3\boldsymbol{U_3} + \alpha_1\alpha_w\boldsymbol{U_1} - \\
\alpha_1\alpha_w\boldsymbol{U_w} = \alpha_1\boldsymbol{U_1}(\alpha_1 + \alpha_2 + \alpha_3 + \alpha_w)
\end{aligned}
\tag{4.63}
$$

Finally, using following principal rule of VOF in multi-phase flows:

$$\alpha_1 + \alpha_2 + \alpha_3 + \alpha_w = 1 \tag{4.64}$$

the mass conservation of all phases is guarantied and the application of the new developed complement phase-averaged velocity remedies the mixture approach problem.

To understand the newly defined velocity, complement phase-averaged velocity, an example with four phases (fine sand (with index 1), medium sand (with index 2), coarse sand (with index 3), and water (with index w)) is proposed to have the following velocities and volume fractions:

α_1=0.50, $\boldsymbol{U_1}$=(0.85,0.0,0.0) (m/s)
α_2=0.20, $\boldsymbol{U_2}$=(0.75,0.0,0.0) (m/s)
α_3=0.10, $\boldsymbol{U_3}$=(0.70,0.0,0.0) (m/s)
α_w=1.00-$(\alpha_1 + \alpha_2 + \alpha_3)$=0.20, $\boldsymbol{U_w}$=(0.90,0.0,0.0) (m/s)

The phase-averaged velocity for the following phases is written using Eq. 4.58 as:

$\overline{\boldsymbol{U}} = \alpha_1\boldsymbol{U_1} + \alpha_2\boldsymbol{U_2} + \alpha_3\boldsymbol{U_3} + \alpha_w\boldsymbol{U_w}$=0.50(0.85,0.0,0.0) + 0.20(0.75,0.0,0.0) + 0.10(0.70,0.0,0.0) + 0.20(0.90,0.0,0.0) = (0.825,0.0,0.0) (m/s)

The complement phase-averaged velocity for aforementioned phases is written using Eq. 4.60 as:

$\overline{\boldsymbol{U_1}}' = (\alpha_2(\boldsymbol{U_1} - \boldsymbol{U_2}) + \alpha_3(\boldsymbol{U_1} - \boldsymbol{U_3}) + \alpha_w(\boldsymbol{U_1} - \boldsymbol{U_w}))$=0.20((0.85,0.0,0.0)-(0.75,0.0,0.0)) + 0.10((0.85,0.0,0.0)-(0.70,0.0,0.0)) + 0.20((0.85,0.0,0.0)-(0.90,0.0,0.0)) = (0.025,0.0,0.0) (m/s)

$\overline{\boldsymbol{U_2}}' = (\alpha_1(\boldsymbol{U_2} - \boldsymbol{U_1}) + \alpha_3(\boldsymbol{U_2} - \boldsymbol{U_3}) + \alpha_w(\boldsymbol{U_2} - \boldsymbol{U_w}))$=0.50((0.75,0.0,0.0)-(0.85,0.0,0.0)) + 0.10((0.75,0.0,0.0)-(0.70,0.0,0.0)) + 0.20((0.75,0.0,0.0)-(0.90,0.0,0.0)) = (-0.075,0.0,0.0) (m/s)

$\overline{\boldsymbol{U_3}}' = (\alpha_1(\boldsymbol{U_3} - \boldsymbol{U_1}) + \alpha_2(\boldsymbol{U_3} - \boldsymbol{U_2}) + \alpha_w(\boldsymbol{U_3} - \boldsymbol{U_w}))$=0.50((0.70,0.0,0.0)-(0.85,0.0,0.0)) + 0.20((0.70,0.0,0.0)-(0.75,0.0,0.0)) + 0.20((0.70,0.0,0.0)-(0.90,0.0,0.0)) = (-0.125,0.0,0.0) (m/s)

$\overline{\boldsymbol{U_w}}' = (\alpha_1(\boldsymbol{U_w} - \boldsymbol{U_1}) + \alpha_2(\boldsymbol{U_w} - \boldsymbol{U_2}) + \alpha_3(\boldsymbol{U_w} - \boldsymbol{U_3}))$=0.50((0.90,0.0,0.0)-(0.85,0.0,0.0)) + 0.20((0.90,0.0,0.0)-(0.75,0.0,0.0)) + 0.10((0.90,0.0,0.0)-(0.70,0.0,0.0)) = (0.075,0.0,0.0)

(m/s)

As can be seen, the presented complement phase-averaged velocity represents the transport of all phases apart from itself, using the relative velocity of the absent phase to the velocities of other phases, in other words, it shows the proportion of the corresponding phase in the the transport of other phases. Now, the validity of Eq. 4.62 for aforementioned example is examined:

$$\alpha_1(\overline{\boldsymbol{U}} + \overline{\boldsymbol{U_1}}') = 0.50((0.825,0.0,0.0) + (0.025,0.0,0.0)) = 0.425 \text{ (m/s)}$$
$$\alpha_2(\overline{\boldsymbol{U}} + \overline{\boldsymbol{U_2}}') = 0.20((0.825,0.0,0.0) + (\text{-}0.075,0.0,0.0)) = 0.150 \text{ (m/s)}$$
$$\alpha_3(\overline{\boldsymbol{U}} + \overline{\boldsymbol{U_3}}') = 0.10((0.825,0.0,0.0) + (\text{-}0.125,0.0,0.0)) = 0.070 \text{ (m/s)}$$
$$\alpha_w(\overline{\boldsymbol{U}} + \overline{\boldsymbol{U_w}}') = 0.20((0.825,0.0,0.0) + (0.075,0.0,0.0)) = 0.180 \text{ (m/s)}$$

The corresponding values for Eq. 4.62 are:
$$\alpha_1(\boldsymbol{U_1}) = 0.50(0.85,0.0,0.0) = 0.425 \text{ (m/s)}$$
$$\alpha_2(\boldsymbol{U_2}) = 0.20(0.75,0.0,0.0) = 0.150 \text{ (m/s)}$$
$$\alpha_3(\boldsymbol{U_3}) = 0.10(0.70,0.0,0.0) = 0.070 \text{ (m/s)}$$
$$\alpha_w(\boldsymbol{U_w}) = 0.20(0.90,0.0,0.0) = 0.180 \text{ (m/s)}$$

As can be seen, the proposed replacement for continuity equation is valid and satisfies the fundamental equation of VOF formulation (Eq. 4.9) as well.

Another new development of this thesis in comparison with the proposed equations by Manninen et al. (1996) is the new interparticle drag force coefficient. The high differences between the new developed formula with the formula proposed by Syamlal (1987), particularly for the granular systems with high fluctuating energy, in one hand and the importance of the interparticular drag after the simplifications proposed by Manninen et al. (1996) on the other hand, enhance the worth of the new developments.

Therefore, the new development for continuity equations in the system of equations is a new feature of this thesis in Manninen et al. (1996) mixture approach. This new formulation improves the coupling between velocities as well as volume concentrations of all contributing phases and fractions. Therefore, the variation of each fractional velocity and concentration influences the other fractional concentrations and velocities, and hence the phases concentrations in the super-ordinate two-phase flow.

Therefore, the developments are fully coupled with the two-phase flow model equations and are not solely a post-processing of the super-ordinate two-phase flow model, but also the results of the two-phase flow model are modified based on the results of the equations systems of the new developments. The worth of this methodology is twofold, first the expensive computational costs of a multi-phase flow equations for each fraction are substituted using the algebraic equations systems and secondly the equations system using new formulation for phase equations and finally coupling with two phase model equations represents the simplification not as a post-processing tool, but as a coupled equations system with super-ordinate two-phase flow model. This is the main worth and success of this research, because Niemi (2012) tried to use the mixture approach in the modeling framework of FLUENT, but he could not couple the equations system with the super-ordinate two-phase flow momentum and continuity equations. Therefore,he tried to modify the calculated volume concentration of fractions in such a way to satisfy the principal rule of VOF by means of distribution the error of phase inconsistency proportional to the calculated phase volume of each fraction and continued this error distribution to reach the VOF-

consistency result with a certain value of accuracy. Therefore, the reproduced numerical results of Niemi (2012) in comparison to the measurements of a fluidized tower were more than two times for velocities overestimated, and hence the computed volume concentrations were underpredicted. Moreover, he applied the equations without the new development for interparticle drag forces as well as new formulated coupled continuity equations system in this thesis.

Fig. 4.6 shows the algorithm of the developed solver (mixedSedFoam) to solve the aforementioned non-linear equations systems for sand fractions coupled with the equations of the super-ordinate two-phase flow. The dotted frame of last steps are the new developments of this thesis in the available two phase-flow model of Cheng et al. (2017). The constants of turbulence equations of two-phase flow model are also calibrated in the mixedSedFom solver. Application of these developments, calibration and validation as well as the solving procedure of equations system are discussed and described in the following sections.

4.6 Model set-up

Discussed equations in section 4.1 for a single fraction (uniform sand) were implemented by Cheng et al. (2017) as a solver in OpenFOAM, which is called twoPhaseEulersedFoam (sedFoam). However, this solver is not capable of reproducing the transport mechanisms of mixed sands, particularly when the ripple bedforms are appeared.

The new developed solver for mixed sands transport under sheet flow conditions in this thesis, which is called mixedSedFoam, applies the governing equations for sand fractions from section 4.2-4.4 to reproduce the transport mechanisms of mixed sands under sheet flow conditions.

The model results of the developed solver in this thesis for mixed sands will be compared with the experimental measurements of O'Donoghue and Wright (2004a, 2004b) to understand the mechanisms of mixed sands transport under sheet flow. To solve the governing equations for sand fractions as well as water, the computational domain will be distinguished for sand and water through the value of α_s which represents the volumetric sediment concentration. Moreover, it is assumed that all sand fractions are such mixed, that the resulted mixed sand is a homogeneous mixture of all constituting sand fractions. To have a similar sediment concentration profile like sediment profile under sheet flow condition, the initial condition of the mixed sand concentration in two-phase flow model framework is defined as a $tanh()$ function as illustrated in Fig. 4.7 and Fig. 4.8 by means of:

$$\alpha_s = 0.5 \times 0.61(1 + tanh(6 - 80(y + s_d))) \tag{4.65}$$

where s_d is the sand depth (m) in the computational domain. Fig. shows the behavior of the $tanh()$ function, which can provide a reasonable sand concentration profile for sheet flow conditions. The depth of sediment in 4.7 and Fig. 4.8 is 75 mm ($s_d = 75\ mm$).

Because the high sand concentration under sheet flow regime is occurred inside the sheet flow layer, the analytical hyperbolic function of tangent ($tanh$) could reasonably provide the behavior of high concentration gradient from sand- to water-phase.

The initial condition for each sand fraction (α_m) is defined based on its constituting proportion. At the first, the equations are solved for a 1DV computational geometry (Fig. 4.8) to find a stable condition. Moreover, due to the smaller computational cost of 1DV-models, the model runs are efficient. However, the computational domain dimensions for both 1DV- and 2DHV-tests are the same (only the horizontal grid of 1DV is composed of a single computational cell for the corresponding vertical dimension).
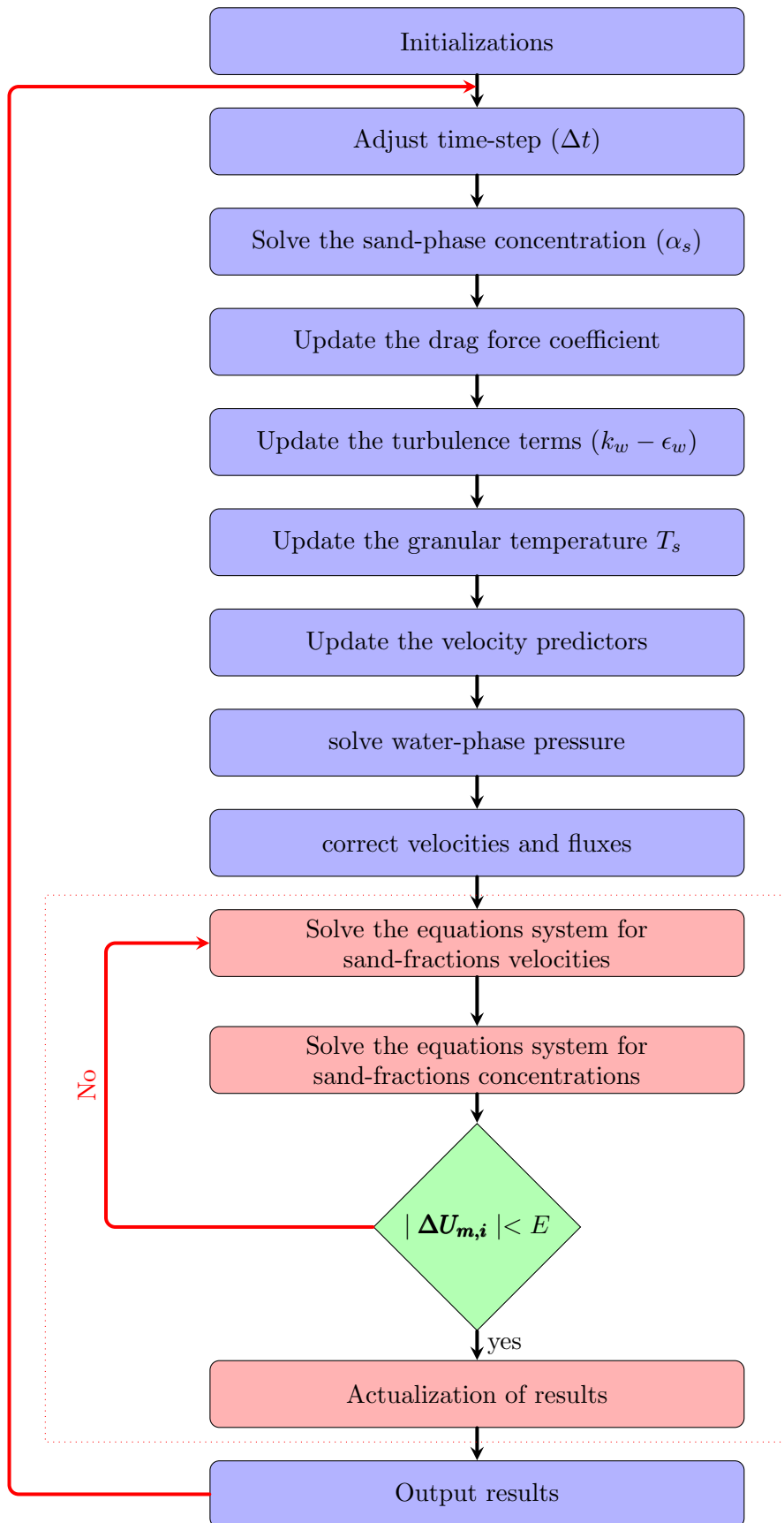
Figure 4.6: Flow chart of the mixedSedFoam solver, pink boxes are developments.
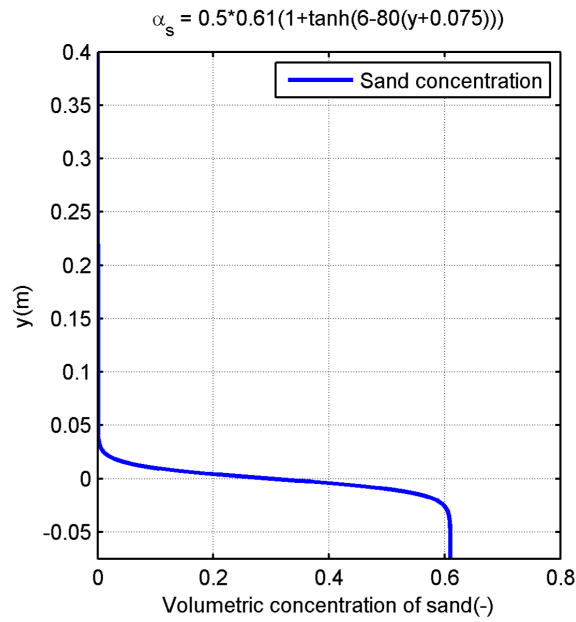
Figure 4.7: The behavior of the $tanh()$ function for initial condition of sand concentration.
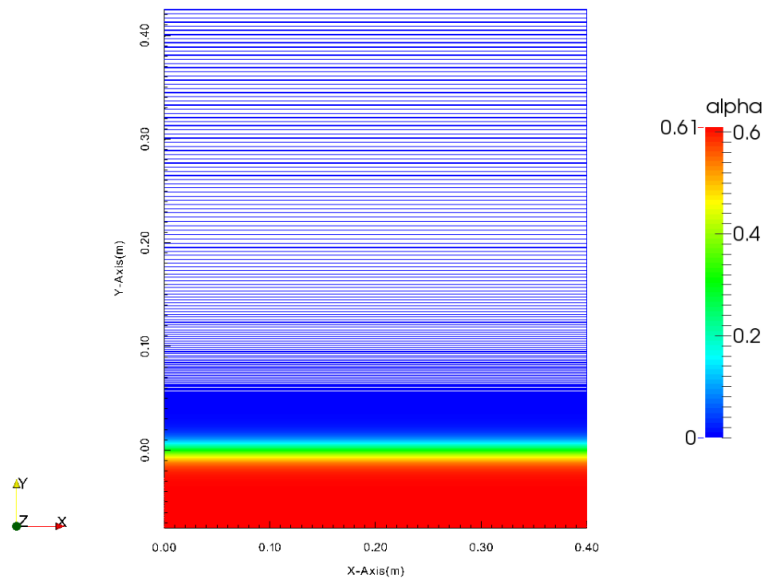
Figure 4.8: 1DV (2DV with meshing only in the y-direction) computational domain in sedFoam (Cheng et al., 2017).

This enables us to apply a consistent interpolation from 1DV- to 2DHV-computational domain in OpenFOAM.

4.7   Solving approaches in mixedSedFoam

The unknown parameters, which should be resolved using the governing equations for flow- and sand-phase are velocities and pressures. To this end, the computational domain is divided into small computational cells and the governing partial differnial equations are

resolved for each computational cell. This solving approach is called the spatial discritization. Moreover, if the unknowns change with time evolution, marching from one time to other time is performed through small time-steps. This approach is called temporal discritization. A fully developed turbulent flow regime needs the both spatial and temporal discritization.

4.7.1   Spatial discritization

For the spatial discritization, we consider two 3D-computational cell with centers of (C1, C2) and interface (f), as is illustrated in Fig. 4.9. Following the Rusche (2003) notations,
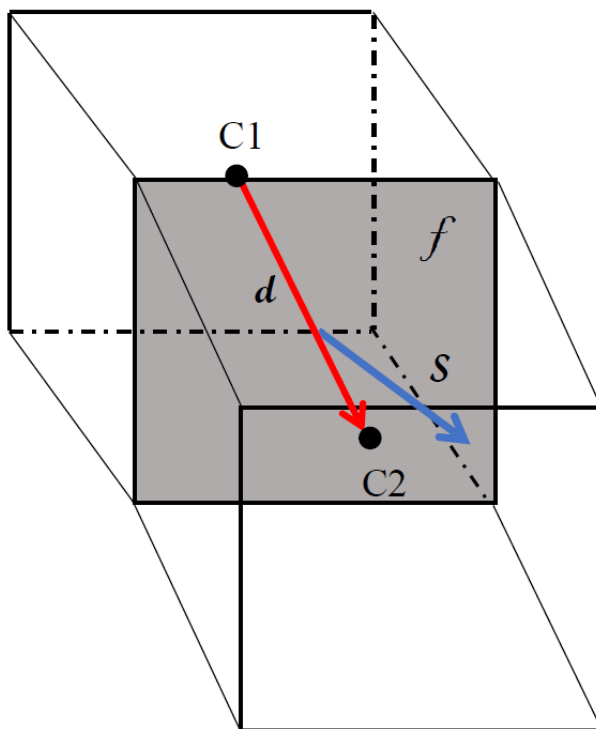
Figure 4.9: Two computational cells with interface($\mathbf{f}$), interface normal vector ($\mathbf{S}$), computational cell centers C1 and C2, and distance vector ($\mathbf{d}$).

the position of the interface normal vector is the geometrical point x_f, where the integration of all defined position vectors on this face (f), cancel each other or:

$$\int_s (\boldsymbol{x} - \boldsymbol{x_f})\boldsymbol{ds} = 0 \tag{4.66}$$

where $\boldsymbol{x}$ is the position vector of an arbitrary point on the face(s). Likewise, the position vector of the computational cell center C_i (i.e. $\boldsymbol{x_{C_i}}$) is defined as:

$$\int_{V_{C_i}} (\boldsymbol{x} - \boldsymbol{x_{C_i}})\boldsymbol{dV} = 0 \tag{4.67}$$

and $\boldsymbol{d} = \boldsymbol{x_{C_{i+1}}} - \boldsymbol{x_{C_i}}$.
Spatial discritization is used to marsh from one position to other position in a numerical

computational domain. This is performed using different approaches in CFD. Central differencing (CD) and upwind differencing (UD) are two known approaches for spatial discritization i.e. marching from one position with known parameters to another position with unknowns.

CD estimates the unknowns on a face using two points, which are located back- and forward to the face. For two computational cells in Fig. 4.9, the face value of ϕ_f (ϕ is representative of a transporting parameter in the momentum equation) is estimated as mentioned by Rusche (2003):

$$\phi_f(CD) = f_x\phi_1 + (1 - f_x)\phi_2 \tag{4.68}$$

where f_x is:

$$f_x = \frac{|x_f - x_2|}{|x_f - x_2| + |x_f - x_1|} \tag{4.69}$$

CD is a spatial discritization approach with accuracy of second order (Anderson et al., 2016).

UD estimates the unknowns from a point on to faces using the behavior of flux (F) of the transporting parameter in momentum equations i.e.

$$\phi_f(UD) = \begin{cases} \phi_1 & \text{for} \quad F \geq 0 \\ \phi_2 & \text{for} \quad F < 0 \end{cases} \tag{4.70}$$

UD is only first order accurate, and therefore the included error due to truncation cause a diffusive flux, which is termed numerical diffusion and can severely distort the solution on coarse meshes (Rusche, 2003). However, due to the boundedness of the solution, the UD is used in CFD codes, where the discritization of the problem is not massively affected by numerical diffusion of UD approach.

To have the accuracy of CD and boundedness advantage of UD, the available CFD spatial discritization approaches usually apply a combined CD and UD, which is called blended differencing (BD). BD are linear combination of CD and UD. Therefore, the BD approach is written as:

$$\phi_f(BD) = (1 - \xi)\phi_f(UD) + \xi\phi_f(CD) \tag{4.71}$$

where ξ is called blending factor and $1 \leq \xi \leq 1$.

The applied spatial discritization approaches are defined in OpenFOAM in a file, which is located in the *system* directory.

4.7.2 Temporal discritization

To find the unknowns (velocities and pressures) in an unsteady flow condition ($\frac{\partial \phi}{\partial t} \neq 0$), the application of the parameters from one time-step, which the unknowns are resolved or available from measurements (initial conditions) to another time-step is performed through two known approaches, i.e. (i) fully explicit and (ii) fully implicit methods. In a fully explicit method, all known parameters in a time-step are applied to find the these parameters in the next time-step, whereas in a fully implicit approach all of parameters from the next time-step are applied. The fully explicit method, which is called in literature as explicit Euler method, is the simplest scheme to find the parameters in the next time step.

However, the fully explicit schemes are not always lead to a convergent solution process. Therefore, application of a fully explicit scheme needs to limit the time-steps, in such a way that the variations of the parameters are reasonable from one time-step to the next

time-step. This limitation is defined using the Courant-Friedrichs-Lewy number or CFL-condition. CFL-condition is defined as:

$$CFL = \frac{\boldsymbol{u}}{\frac{\delta x}{\delta t}} \tag{4.72}$$

where $\boldsymbol{u}$ is the flow velocity passing through the computational cell, δx is the maximum dimension of computational cell, and δt is the time-step. Stability problem of explicit schemes is solved, when the CFL-number is smaller than one. Therefore, the computational cell dimensions should be enough fine or the time-step to guaranty the stability of numerical computation.

In contrast to the fully explicit schemes, the fully implicit schemes apply the values of the transporting parameters in the new time-step. The resulted equations system in the fully implicit scheme is like the explicit scheme, but because of application the unknown parameters from the new time-step, the coefficient matrix of the equations system is diagonally dominant, which guaranties the boundedness of the unknown parameters (Malalasekera and Versteeg, 2007).

Therefore, in contrast to the explicit schemes the fully implicit schemes are unconditionally stable and allows arbitrarily large time-steps. However, the shortcomings of this method are its first order accuracy in time and the resulted equations system has a coefficient matrix larger than the explicit scheme and therefore is more expensive than the fully explicit schemes. However, the advantage is the possibility of using a large time-step (Ferziger et al., 2002).

In contrast to the fully explicit and fully implicit schemes, there are mixed schemes that apply the weighted fully explicit and fully implicit schemes. In mixed schemes a part of the unknown parameters in the new time-step are calculated from the old time-step and partly from the new time-step. One of this mixed schemes is known as Crank-Nicolson scheme, which has the weighting coefficient of 0.5. It means, in the Crank-Nicolson, the parameters in the partial different equations are considered as 50 % from the old time-step and 50 % from the new time-step.

The advantage of Crank-Nicolson scheme is its second-order accuracy in time, in contrast to the fully implicit and fully explicit schemes, which have first-order accuracy in time space. Therefore, this property of Crank-Nicolson scheme suggest its application to partial differential equations when time accuracy is important. Moreover, the mixed schemes are second-order accurate, when the weight coefficient ist 0.5 and other weighting values produces mixed-schemes with first order accuracy (Ferziger et al., 2002). In the computational approaches of this thesis, the mixed scheme of Crank-Nicolson was applied to have more accuracy in the solutions. Although the Crank-Nicolson is unconditionally stable, but it can produce oscillatory solutions at large time-steps (Ferziger et al., 2002).

4.7.3   Solving the phase continuity equations

In a same methodology to Rusche (2003), continuity equation of fractions in Eq. 4.1 is written as:

$$\frac{\partial \alpha_m}{\partial t} + \boldsymbol{\nabla} . \left((\overline{\boldsymbol{U}} + \overline{\boldsymbol{U_m}}')\alpha_m \right) = 0 \tag{4.73}$$

The new developed fractions concentration program in this thesis solves Eq. 4.73 for all fractions and instead of sedFoam, which solves only a continuity equation for sediment phase, the sediment phase concentration is computed at the end of each time step as the sum of all fractional concentrations. It means that the mixture approach does not only

work as a post-processing to find the fractional concentrations from momentum equation of sediment in uniform sand, but also couples the sediment continuity equation in PIMPLE-loop of solution approach to the fractional continuity equations.

Because of 3D-model framework in OpenFOAM, the computational domain is a 3D-box with thickness of 0.001 m in z-direction, length of 0.4 m in x-direction and height of 0.5 m in y-direction (Fig. 4.10). To force the solver to solve the equations for 1DV, the computational mesh should only in the corresponding direction (y-direction) be resolved. The thickness of the sediment layer is 75 mm and the vertical resolution for this layer is 0.5 mm. The water-phase has the same resolution like sediment (0.5 mm) for a length of 25 mm from the interface, and then the resolution will be decreased along 200 mm from 0.5 mm to 4 mm, gradually and finally the resolution will be constant to 4 mm for the last 200 mm.

Initial condition for other parameters (p, T, k, ϵ, $\boldsymbol{U}_a$ and $\boldsymbol{U}_b$) is uniform value/vector of zero and boundary conditions for bottom (wall) are : $\nabla\alpha = 0$, $\nabla k = 0$, $\nabla T = 0$, p is slip ($zeroGradient$) and velocities ($\boldsymbol{U}_a, \boldsymbol{U}_b$) are no-slip ($fixedValue$-zero vectors). Top boundary condition for all parameters is $symmetryPlane$, which means the normal vector of parameters should be perfectly aligned. Inlet and outlet have a $cyclic$ boundary condition, which means the parameters should be the same in inlet and outlet. Front and back planes have the boundary condition $empty$, which means the computational domain should be considered as a slice of a 3D box with a small thickness in the third direction.

After the 1DV-model reached a quasi-steady condition (it was used for uniform sands with a runtime of five times of the wave-period), the results of the last time-step are interpolated using $mapFields$, which is a facility of OpenFOAM, on a finer mesh to provide a better initial condition. The initial condition plays a crucial role in convergence of the governing equations of fine mesh.

However, because of bedform formation and evolution from ripples to flat in mixed sands compared to the plane bed of uniform sands, the developed solver in this thesis was run for a coarse 2DHV-mesh with 4000 computational cells. The run time of this 2DHV coarse mesh was increased to ten times of the wave-period to provide a better spatially and temporally quasi-steady condition for mixed sand. Fig. 4.10 shows the coarse mesh applied for α_1 to solve the mixed sand problem for X1 experiments of O'Donoghue and Wright (2004a, 2004b).

Finally, the coarse mesh results were interpolated on a fine mesh with 72000 computational cells. Fig. 4.11 shows the final computational domain for 2DHV model. It has a resolution of 2 mm in the x-direction and the resolution in y-direction is like the 1DV-model.

The final α_s in mixedSedFoam is not the computed from PIMPEL-loop like sedFoam, but is computed as the sum of all fractional concentrations (Eq. 4.8) and the volume fraction of water as $\alpha_w = 1 - \alpha_s$.

4.7.4   Solving nonlinear equations system of fractional velocities

Nonlinear algebraic system of equations for velocities is solved using Newton-method. Newton's method in comparison to non-/quasi-Newton's methods (like Broyden's method (Broyden, 1967)) is aquatically convergent, when a good starting estimation in proximity of the solution is provided (Burden et al., 2015). Moreover, the Jacobian matrix should be non-singular. This is provided by applying small time steps (here $\Delta t_{max} = 0.0002$ (s)), and hence the initial estimation to solve the nonlinear equations could be guaranteed in the Newton's method. To tackle the singularity problem, a small value is added to the

denominators. The Newton's method is written as:

$$J(x_i)\Delta x = -f(x_i) \quad and \quad x_{i+1} = x_i + \Delta x \tag{4.74}$$

For nonlinear system of equations with velocities, the Newton's method in vectorial form could be written as:

$$J(U_i)\Delta U = -f(U_i) \quad and \quad U_{i+1} = U_i + \Delta U \tag{4.75}$$

$J(U)$ is the Jacobian matrix and for a mixed sand with three fractions is written as:

$$J(U_i) = \begin{bmatrix} \frac{\partial f_1}{\partial u_1} & \frac{\partial f_1}{\partial u_2} & \frac{\partial f_1}{\partial u_3} \\[2mm] \frac{\partial f_2}{\partial u_1} & \frac{\partial f_2}{\partial u_2} & \frac{\partial f_2}{\partial u_3} \\[2mm] \frac{\partial f_3}{\partial u_1} & \frac{\partial f_3}{\partial u_2} & \frac{\partial f_3}{\partial u_3} \end{bmatrix} \tag{4.76}$$

the components of $J(U_i)$ are scalars and the Newton's method for a mixed sand with three fractions is written as:

$$\begin{bmatrix} \frac{\partial f_1}{\partial u_1} & \frac{\partial f_1}{\partial u_2} & \frac{\partial f_1}{\partial u_3} \\[2mm] \frac{\partial f_2}{\partial u_1} & \frac{\partial f_2}{\partial u_2} & \frac{\partial f_2}{\partial u_3} \\[2mm] \frac{\partial f_3}{\partial u_1} & \frac{\partial f_3}{\partial u_2} & \frac{\partial f_3}{\partial u_3} \end{bmatrix} \begin{bmatrix} \Delta U_{1x} & \Delta U_{1y} & \Delta U_{1z} \\ \Delta U_{2x} & \Delta U_{2y} & \Delta U_{2z} \\ \Delta U_{3x} & \Delta U_{3y} & \Delta U_{3z} \end{bmatrix} = \begin{bmatrix} f_{1x} & f_{1y} & f_{1z} \\ f_{2x} & f_{2y} & f_{2z} \\ f_{3x} & f_{3y} & f_{3z} \end{bmatrix} \tag{4.77}$$

then the ΔU_i are found as:

$$\Delta(U_i) = \begin{bmatrix} \Delta U_{1x} & \Delta U_{1y} & \Delta U_{1z} \\ \Delta U_{2x} & \Delta U_{2y} & \Delta U_{2z} \\ \Delta U_{3x} & \Delta U_{3y} & \Delta U_{3z} \end{bmatrix} = \begin{bmatrix} \frac{\partial f_1}{\partial u_1} & \frac{\partial f_1}{\partial u_2} & \frac{\partial f_1}{\partial u_3} \\[2mm] \frac{\partial f_2}{\partial u_1} & \frac{\partial f_2}{\partial u_2} & \frac{\partial f_2}{\partial u_3} \\[2mm] \frac{\partial f_3}{\partial u_1} & \frac{\partial f_3}{\partial u_2} & \frac{\partial f_3}{\partial u_3} \end{bmatrix}^{-1} \begin{bmatrix} f_{1x} & f_{1y} & f_{1z} \\ f_{2x} & f_{2y} & f_{2z} \\ f_{3x} & f_{3y} & f_{3z} \end{bmatrix} \tag{4.78}$$

and new velocities in the next iteration step are written as:

$$U_{i+1} = U_i + \Delta U \tag{4.79}$$

to couple the continuity equation of fractions with the velocities equations system, the Eq. 4.73 is solved for each fraction after each iteration.
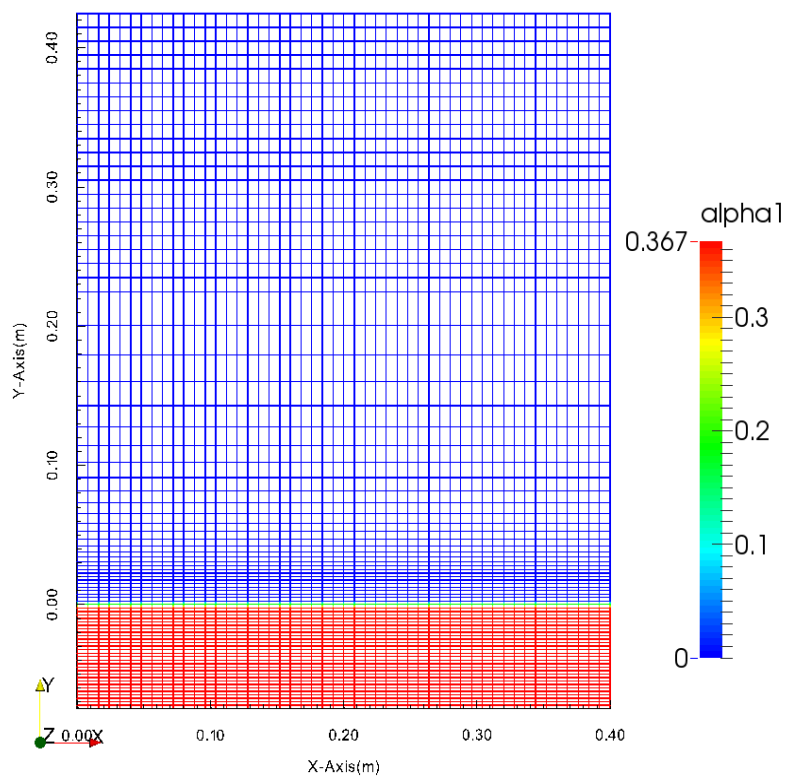
Figure 4.10: 2DHV computational coarse mesh for α_1 in mixedSedFoam.
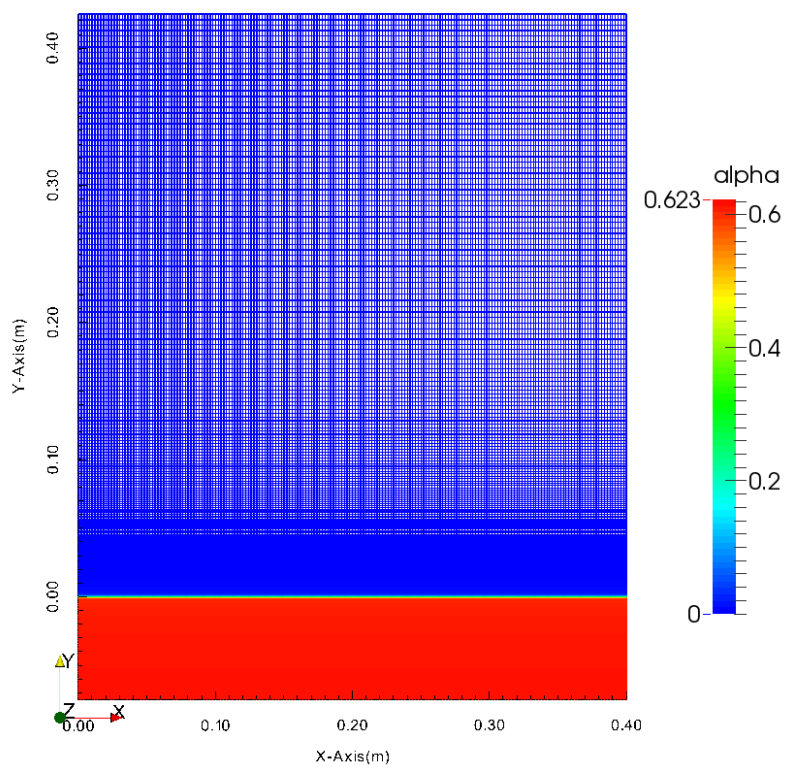
Figure 4.11: 2DHV computational fine mesh for α in mixedSedFoam.

The convergence of the Newton-loop is limited to the condition for maximum velocity of all fractions ($max|\Delta \boldsymbol{U}_m|$) smaller than one-tenth of the maximum velocity of fluid ($max|\Delta \boldsymbol{U}_m| < 0.1 \times 1.50 = 0.15$ m/s) and the maximum number of the loop-iteration is limited to three steps, however, in most of time steps the programmed loop for Newton's method is converged at the first iteration step, which in turn reduces the computational costs.

After finding the velocity fields of each fraction, the continuity equations are solved and in the next iteration, the velocities equations are solved with the new volumetric concentrations. The velocities and their corresponding volumetric concentrations are accepted, if one of the conditions of loop is satisfied. This means both of equations systems (i.e. velocities as well as concentrations equations system) are coupled and does not behave separately.

4.8   Numerical model results

As was shown in Fig. 4.6, the fully coupled equations are solved to find the fractional velocities and concentrations. To calibrate and validate the model, model results for fractional concentrations are compared with detailed performed experiments of O'Donoghue and Wright (2004a, 2004b).

These experiments were performed in AOFT and involved 7 sand beds: 3 well-sorted sands with d_{50} values of 0.15 mm, 0.28 mm, and 0.51 mm and 4 mixed sands comprising different proportions of the 3 well-sorted sands O'Donoghue and Wright (2004a, 2004b). Tab. 4.2 presents a summary of the size characteristics for the 7 sands and the corresponding percentages of the well-sorted Fine (%F), Medium (%M) and Coarse (%C). The sands

Table 4.2: Sands used in the experiments of O'Donoghue and Wright (2004a).

$Name$	$Mix(\%F - \%M - \%C)$	$d_{10}(mm)$	$d_{50}(mm)$	$d_{90}(mm)$
Fine (F)	100-0-0	0.10	0.15	0.23
Medium (M)	0-100-0	0.17	0.28	0.45
Coarse	0-0-100	0.36	0.51	0.67
Mix1 (X1)	60-30-10	0.11	0.19	0.45
Mix2 (X2)	20-60-20	0.14	0.28	0.53
Mix3 (X3)	35-60-5	0.12	0.24	0.44
Mix4 (X4)	50-0-50	0.11	0.28	0.61

Table 4.3: Flow conditions of the experiments of O'Donoghue and Wright (2004a).

$Flow\ name$	$T(s)$	$A(m)$	$R(-)$	u_{max}	u_{rms}
512	5.0	1.2	0.50	1.50	0.65
7512	7.5	1.5	0.50	1.26	0.90
A5010	5.0	1.0	0.63	1.50	0.90
A7515	7.5	1.5	0.63	1.50	0.90

were tested under 4 flows comprising 2 flow periods – 5 s and 7.5 s – and 2 flow types – sinusoidal and asymmetric. Tab. 4.3 outlines the flow conditions. Here T is the flow period, A is the flow orbital amplitude, u_{max} is the maximum velocity, u_{rms} is the root mean square velocity, and R is a measure of the flow asymmetry, which is given by Eq. 2.25. Sinusoidal flows have R=0.5. The asymmetric flows were based on Stokes 2nd order waves with R=0.63.

The numerical model is forced using the pressure gradient in x-direction. To this end, the pressure gradient is found as:

$$\rho \frac{DU}{Dt} = -\frac{\partial p}{\partial x} \tag{4.80}$$

where the applied water-phase velocity to the water column in the AOFT was a skewed velocity time series with the skewness value of 0.63, which is given as:

$$u(t) = u_1 sin(\omega t) - u_2 cos(2\omega t) \tag{4.81}$$

where:

$$u_{max} = u_1 + u_2$$
$$u_{min} = u_1 - u_2 \tag{4.82}$$

using R=0.63 and u_{max}=1.5 ms^{-1} in Eq. 2.25 and Eq. 4.82, the equation of velocity time series is given as:

$$u(t) = 1.19 sin(\omega t) - 0.31 cos(2\omega t) \tag{4.83}$$

where ω is the angular frequency of flow ($\omega = 2\pi/T$). The time series of Eq. 4.83 for a skewed velocity with period of 5 and 7.5 (s) and corresponding minimum, maximum and flow reversal points are shown in Fig. 4.12 and Fig. 4.13, respectively.

However, the time series for both periods could be shown in dimensionless form of t/T and using an especial initial phase difference, translate them in such a way that (0,0) becomes the starting point of the velocity time series. The pressure gradient from Eq. 4.80 using water-phase density of $\rho = 1000$ kgm^{-3} could be written as:

$$-\frac{\partial p}{\partial x} = 1000(1.19 \ \omega \ cos(\omega t) + 2\omega \times 0.31 \ sin(2\omega t)) \tag{4.84}$$

It should be noted that for seawater density with $\rho = 1025$ kgm^{-3} the pressure gradient will change, but because of not-seawater applied in O'Donoghue and Wright (2004a) experiments, and the calibration and validation of developed solver in this thesis with these experimental data, the water-phase density is assumed as $\rho = 1000$ kgm^{-3}.

For a skewed wave-period of T= 5 s, the pressure gradient is written as:

$$-\frac{\partial p}{\partial x} = 1495.4 \ cos(\omega t) + 779.12 \ sin(2\omega t) \tag{4.85}$$

and for T= 7.5 s as:

$$-\frac{\partial p}{\partial x} = 996.93 \ cos(\omega t) + 519.41 \ sin(2\omega t) \tag{4.86}$$

Using development of nonlinear equation system solution approach in sedFoam (Cheng et al., 2017), the equations system and hence PIMPEL-loop will not be converged. It produces unrealistic high local spurious erosions and velocities close to the time of maximum velocity in both wave periods ($T = 5$ and 7.5 s). Consequently, the erosion depth is increased and computations are broken. Following the problem, the extremely small sediment concentration coupled with PIMPLE-loop produces extremely high velocities with order of 10^8 ms^{-1} before breaking. Fig. 4.14 and Fig. 4.15 show screen-shots of the local erosion as well as corresponding local high spurious velocities in a time-step before breaking.
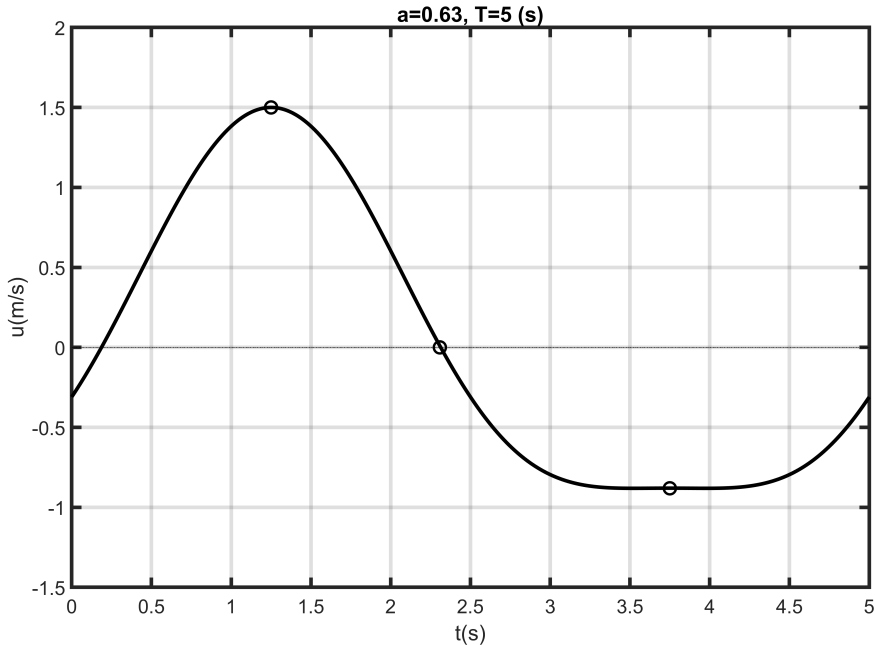
Figure 4.12: Time series of asymmetric velocity of T=5 s applied in AOFT for uniform and mixed sand experiments. max(1.25 s, 1.5 ms^{-1}), min(3.75 s, -0.881 ms^{-1}), reversal flow(2.31 s, 0.0 ms^{-1}) (in analogy to O'Donoghue and Wright (2004a, 2004b)).
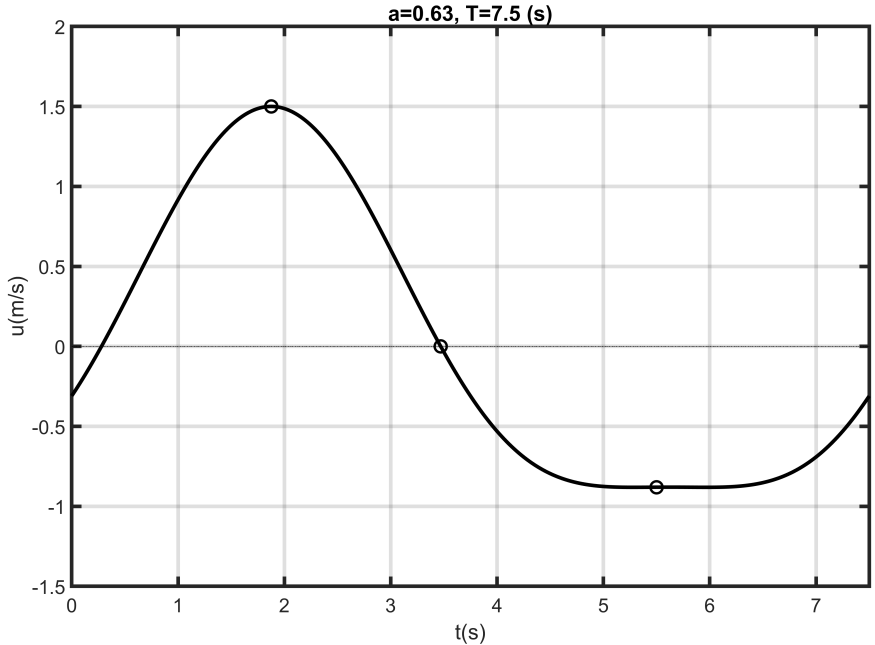
Figure 4.13: Time series of asymmetric velocity of T=7.5 s applied in AOFT for uniform and mixed sand experiments. max(1.88 s, 1.5 ms^{-1}), min(5.50 s, -0.881 ms^{-1}), reversal flow(3.47 s, 0.0 ms^{-1}) (in analogy to O'Donoghue and Wright (2004a, 2004b)).

To remedy this problem, a methodology like Johnson and Jackson (1987) for frictional pressure of sand-phase within the enduring contact layer is developed for velocity field. This

modification could be explained by means of the simplifications in the mixture approach as well as the incapability of KTGF in reproducing the mechanisms of highly concentrated sediment transport in the enduring contact regions close to the bed (see Fig 2.21). The velocity function does not interfere the velocity field of computational cells, which have a concentration from 0 to 0.57 (vol./vol.), but modifies the calculated velocities for volumetric concentrations higher than 0.57 (or 1510 kgm^{-3}). The velocity field in enduring contact layer for sediment fractions is modified as:

$$\boldsymbol{U}_m = \begin{cases} \boldsymbol{U}_m \times 1 & \text{if } \alpha_m \leq 0.93 \; \alpha_{max,m} \\ \boldsymbol{U}_m \times \eta_m (\frac{\sqrt{2gd_m}}{U_{max}}) \frac{(\alpha_{max,m} - \alpha_m)^k}{(\alpha_m - \alpha_{min,m})^l} & \text{if } \alpha_m > 0.93 \; \alpha_{max,m} \end{cases} \quad (4.87)$$

to explain the plausibility of this equation, $\sqrt{2gd_m}$ is added based on this assumption that in the enduring contact layer a steady state condition could be dominant. U_{max} is used to normalize the $\sqrt{2gd_m}$ and make the calibration parameter dimensionless. k and l are selected like applied approach for frictional pressure of the sand-phase in the enduring contact layer by Johnson and Jackson (1987) as 2 and 5, respectively. η_m is applied to calibrate the numerical results and its behavior will be discussed in following. All of these parameters are programmed in such a way that they can be tuned before running the test cases.

The developed model was run for mixed sands with sand fractional properties of O'Donoghue and Wright (2004a) experiments. Tab. 4.4 outlines the selected testcases of O'Donoghue and Wright (2004a) experiments for calibration of the developed model for mixed sands. However, the mixedSedFoam is not stable for any applied calibration factor η_m in Eq. 4.87. Tab. 4.5 shows the performed coarse mesh numerical models using mixedSedFoam for four test cases of O'Donoghue and Wright (2004a).

As can be seen, the model stability is dependent on the percentage of constitutional sand fractions in mixed sands. Therefore, the higher percentage of fine sand in a mixed sand increases the instability of model by increasing the calibration factor. Moreover, the wave period does not affect the stability of the model by coarse mesh and therefore the stability of the model with coarse mesh is independent of wave period.

Fig. 4.16 shows the intercomparison of the model results for coarse mesh of the test-case X1T50 with CCM (Conductivity Concentration Meter)-measured concentrations in AOFT by O'Donoghue and Wright (2004a). Despite the coarse resolution of the applied computational mesh (4000 cells with resolution of 8 mm in x-direction and 2.5 mm in y-direction), the results in comparison with measurements are promising. It can be seen, in contrast to fine and medium sand fractions, the coarse fraction with almost its maximum concentration is present in the sheet flow layer. The interpretation for this could be the hiding of fine fractions among the coarse fractions as well as sliding property of finer fraction for coarse ones. Therefore, as was shown in experiments, the transport rate of coarse sand in a mixture could be greater than the transport rate of that coarse sand in a uniform condition. Moreover, due to the higher resistance of coarse sands in front of the passing flow close to the bed, the total sediment transport rate could be reduced when the percentage of coarse fraction is increased.

However, the coarse mesh model results in Fig. 4.16 are over-predicted in the enduring contact layer (the closest layer to bed) for both of calibration factors of $\eta_m = 0.005$ and $\eta_m = 1$ close to the maximum velocity instant (due to the wave period of 5(s), the model was run for the duration of nine times of wave period to achieve an equilibrium condition). The over-prediction in this layer is referred to the calibration factors, which are multiplied to the computed velocity. This could be improved by running the model on a finer mesh.
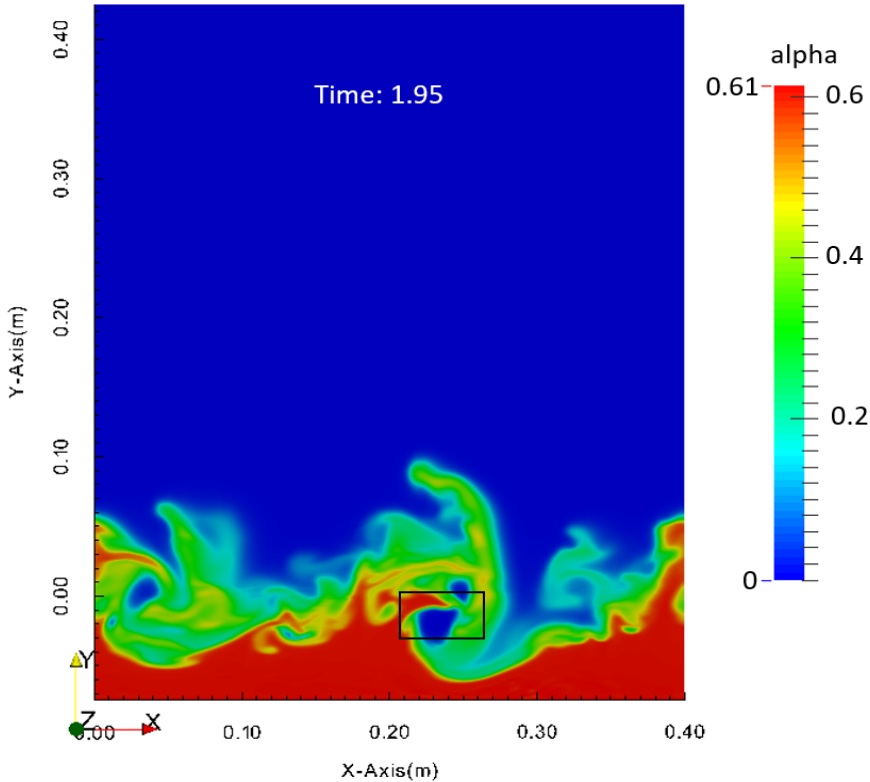
Figure 4.14: Sand-phase concentration (α_s) before breaking of computations for the test-case X1T75, the black rectangular shows the location of too high sand-phase velocity.
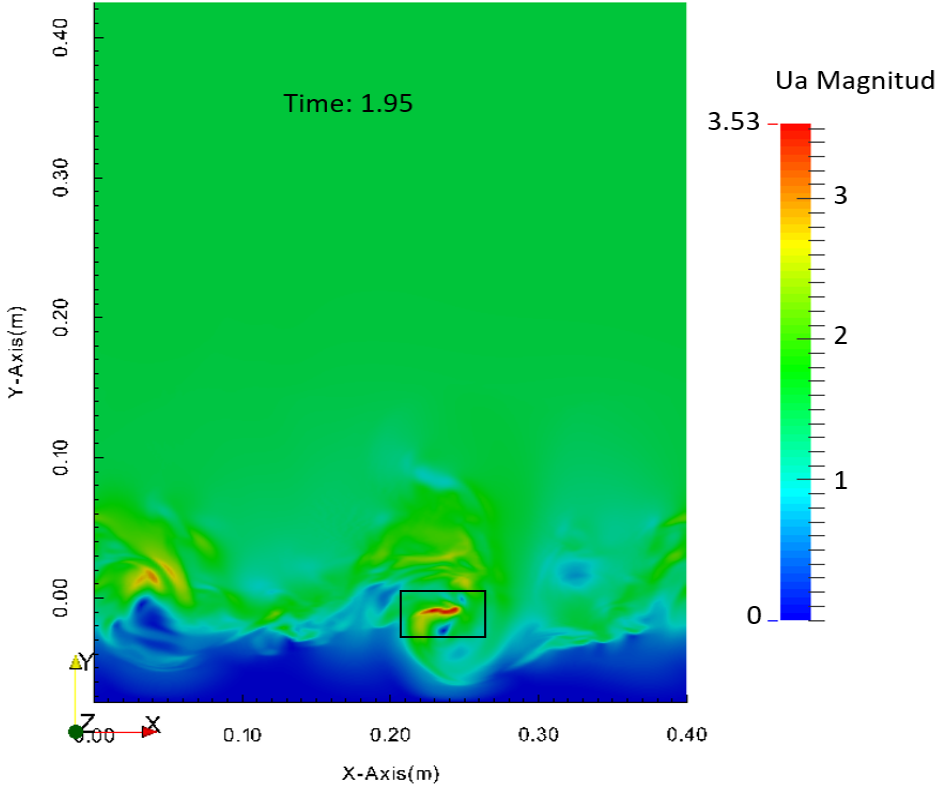
Figure 4.15: Sand-phase velocity (U_a) before breaking of computations for the test-case X1T75, the black rectangular shows the location of too high sand-phase velocity.
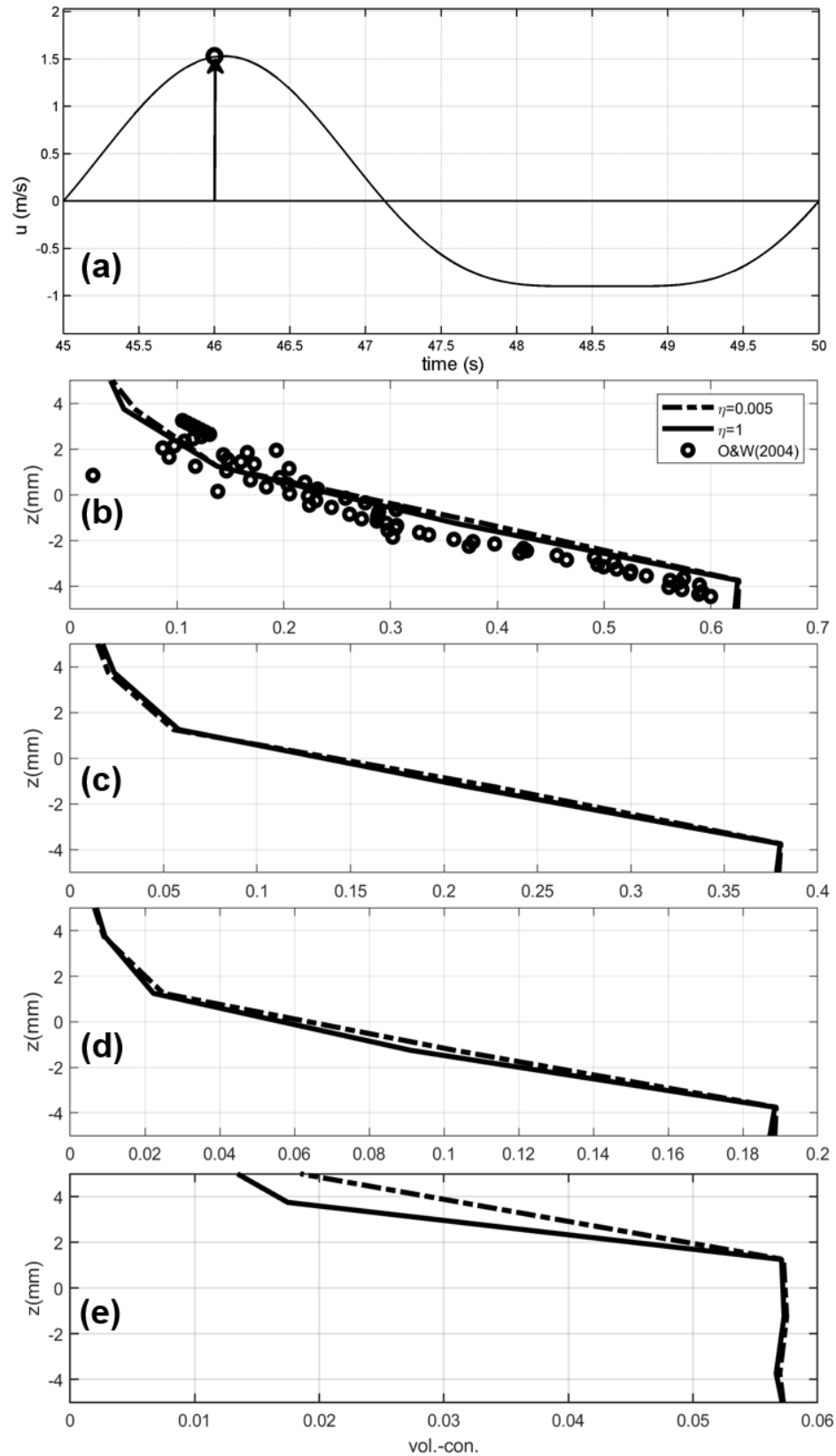
Figure 4.16: Velocity time-series (a), phase-averaged mixed sand (X1: 60%F-30%M-10%C) concentration profile (b), and fractional concentration profiles for fine (c), medium (d), and coarse sand (e) at t=46 s vs. measured data of O'Donoghue and Wright (2004a).

Table 4.4: Fractional sands percentages with their grain size characteristics (adapted from O'Donoghue and Wright (2004a)).

$Testcase$	$\%F - \%M - \%C$	$d_{10}(mm)$	$d_{50}(mm)$	$d_{90}(mm)$	$T(s)$
X1T50	60-30-10	0.11	0.19	0.45	5.0
X1T75	60-30-10	0.11	0.19	0.45	7.5
X2T50	20-60-20	0.14	0.28	0.53	5.0
X2T75	20-60-20	0.14	0.28	0.53	7.5
X4T50	50-0-50	0.11	0.28	0.61	5.0
X4T75	50-0-50	0.11	0.28	0.61	7.5

Table 4.5: Performed numerical models with a coarse mesh and η_m-range from 0.005 to 35.

η_m	$X1T50$	$X1T75$	$X2T50$	$X2T75$
0.005	Stable	Stable	Stable	Stable
0.05	Stable	Stable	Stable	Stable
0.5	Stable	Stable	Stable	Stable
1.0	Stable	Stable	Stable	Stable
5.5	Not stable	Not stable	Stable	Stable
10	Not stable	Not stable	Stable	Stable
15	Not stable	Not stable	Stable	Stable
20	Not stable	Not stable	Stable	Stable
25	Not stable	Not stable	Not stable	Not stable
35	Not stable	Not stable	Not stable	Not stable

It should be noted that the coarse mesh cases are just run to get a better approximation for initial condition of finer mesh with 72000 cells (18 times finer than the coarse mesh resolution), and hence the comparison of model results with measurements in this step of modeling cannot be generalized to the final model behavior. Fig. 4.17 shows the coarse model results close to the point of flow reversal for test case X1T50.

Again, the results of the developed model are promising. In contrast to the model results for the time of maximum flow velocity (Fig. 4.16), the smaller calibration parameter ($\eta_m = 0.005$) shows a better reproduction of sand concentration than the greater one ($\eta_m = 1.0$). Moreover, the behavior of coarse sands in flow reversal is noticeable, when we compare it with its behavior close to the time of maximum velocity. The concentration profile of the coarse fraction becomes steeper in flow reversal than the time of maximum velocity. It means that the coarse fractions are rapidly transported in the flow reversal point than the maximum flow velocity in the lower levels of sheet flow, which could be interpreted by picking-up the coarser grains in the flow reversal in comparison with the maximum flow velocity point. The higher gradient of the concentration profile of the coarse fraction in flow reversal point could represent the breaking of the enduring contact layer, which is resulted in transport of higher volume of the coarse fraction close to the bed in comparison with higher levels.

Furthermore, the enhanced differences between computed concentration profile for coarse fraction using $\eta_m = 0.005$ and $\eta_m = 1$ in comparison with other fractions show that the coarser fractions are more sensitive to the velocity calibration parameter (η_m).
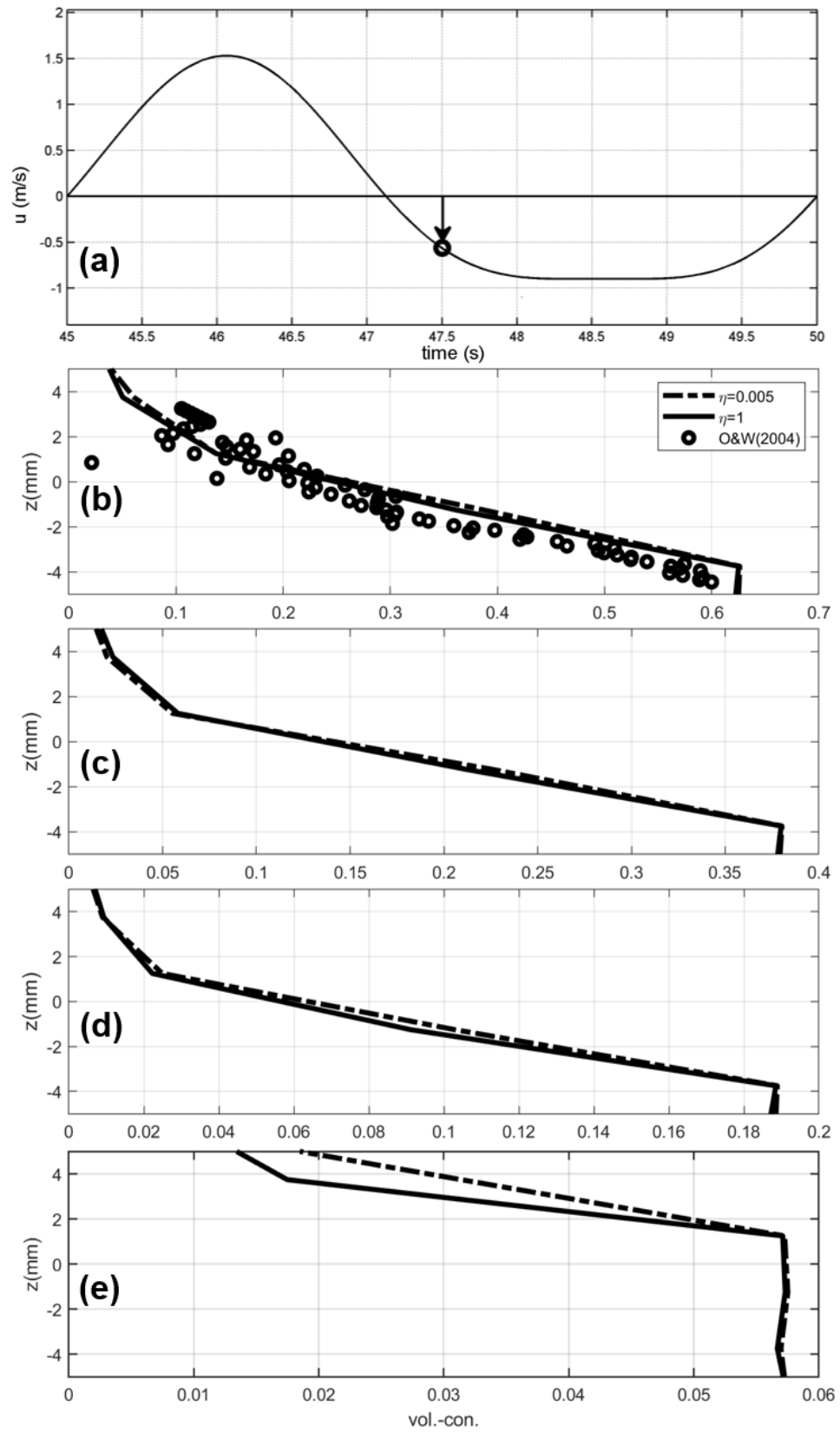
Figure 4.17: Velocity time-series (a), phase-averaged mixed sand (X1: 60%F-30%M-10%C) concentration profile (b), and fractional concentration profiles for fine (c), medium (d), and coarse sand (e) at t=47.5 s vs. measured data of O'Donoghue and Wright (2004a).

This is also a positive sign, which shows the model works properly, however, the mesh is too coarse.

Nonetheless, because of small value of participation of coarse fraction in this mixed sand (10%), the influence of its concentration on the final sand concentration profile is not significant. As can be seen, the influence of calibration factor (η_m) is reduced from the coarse fraction to the fine fraction in their concentration profile. Further, the calibration factor is more influencing in the enduring contact layer for all fractions than the outer sub-layers. Finally, the reproduced total sediment concentration profiles using smaller calibration factor (here, $\eta_m = 0.005$) is closer to the measurements than the greater one in the flow reversal point (i.e., $\eta_m = 1$). This illustrates the right behaviour of the calibration factor and the model in general, because by increasing the η_m-value, the velocity near and under the initial bed level is increased, which means higher volume of sands are transported and therefore, the corresponding concentration profile is shifted to a deeper depth in comparison with the lower η_m-values.

4.9   Mesh-refined model results

To find a better resolution of the model results as well as mesh independent predictions, the coarse mesh model results are interpolated to a finer mesh with 72000 numerical cells. Due to the successfully performed model runs for uniform sands by means of this refinement, the developed model is also run in final simulation phase for this resolution. To this end, the coarse mesh results for the largest η_m parameter are mapped on the fine mesh. The fine mesh model results are written on the same temporal resolution of the measurements (0.02 sec) to provide a high resolution of comparison with the corresponding experimental results. Then, the model with fine mesh was run for 12 wave-periods for each testcase, in accordance with the performed experiments by O'Donoghue and Wright (2004a) to provide the similar conditions for calibration of the developed model.

4.9.1   Vertical sediment concentration profiles

The calibration and validation of the model results is performed by means of the phase-averaged experimental dataset of O'Donoghue and Wright (2004b) for mixed sands under sheet flow conditions. Fig. 4.18 shows the final model results for mixed sands and the measured values of O'Donoghue and Wright (2004a) for mixed sand concentrations in corresponding phases of velocity time series. As can be seen, the mixedSedFoam can reproduce the vertical sediment concentration in a good agreement with measurements for mixed sands. The first column in Fig. 4.18 presents the vertical profile of the sediment concentration for the case of Mix1 (X1) [fine(60%), medium(30%) and coarse(10%)] in O'Donoghue and Wright (2004b) experiments at the time points of start, maximum, flow reversal and minimum flow velocity, respectively. Despite the good agreement between model results and measurements in start, maximum and minimum flow velocity phases, the model is not capable of reproducing the mixed sand concentrations at the flow reversal phase. The reason for this could be found through two aspects: the first is due to the incapability of the turbulence model, which cannot develop the produced eddies to higher levels, and therefore entrain the sediments further the bed level or the drag interparticle interactions due to the assumption of similar velocity for particles in the drag force coefficient of Syamlal (1987) are not able to provide higher interparticle interactions at reversal flow. The former could be more reasonable, because the grain size velocities at the flow reversal point are not enough high to entrain the sand grains into higher elevations after

collision. The results for the similar bed material with the flow velocity of 7.5 s-period are presented on the last three columns for similar mixed sand. As can be seen, in contrast to the 5 s-period nonlinear wave, the model reproduces the sediment concentration better for the 7.5 s-period velocity at the corresponding phase of flow reversal. This means that the reproduced sediment concentration for longer oscillatory periods could be solved more successfully compared to shorter periods. Moreover, under the generated flow velocity in shorter wave periods, higher fine sand volumes are entrained to the flow compared to longer periods. The vertical profile of sand concentration of Mix1(X1) at the phase of maximum flow velocity (X1(b)) is steeper than the start point (X1(a)), this can be interpreted by means of higher sediment concentration in the sheet flow layer at the phase of maximum flow velocity. Because at this phase the kinetic energy of the flow is higher than other phases.

The second columns under the both of flow velocity time series show the mixed sand concentration of the model results compared to measurement results of the vertical sediment concentration profile for Mix2(X2) [fine(20%), medium(60%) and coarse(20%)] under flow velocities of 5 and 7.5 s, respectively. As can be seen, the model results are capable of reproducing the measurements. Moreover, due to the lower percentage of the fine fraction in this mixed sand compared to Mix1(X1), the model results for sediment concentration at the equal elevations are lower. However, like the model results at the flow reversal phase for Mix1(X1), the measurement results for sand concentration are not well reproduced by model, but due to the lower percentage of fine sand fraction in mixed sand Mix2(X2), the agreement between model results for sediment concentration with measurements at the flow reversal phase is better than the case of Mix1(X1). The model results are over-predicted at the deeper elevations of the sheet flow layer in the case of Mix2(X2) compared to the Mix1(X1). The reason for this can be the smaller erosion depth of the model compared to the measurements. Because the erosion depth is defined from the no-flow bed level, where the concentration is equal to 0.6, and the model at this phase meets the maximum concentration more quickly than the measurements.

Comparison between the quality of the agreement between model with measurement results for the vertical profile of sediment concentration shows that like the test case of Mix1(X1), for the case of Mix2(X2) the model results at the flow reversal phase for the same bed is better reproduced for a flow velocity with wave period of 7.5 s compared to the 5 s.

It can be explained by means of the required time for settling back of sediments in the presence of fine sands. In a wave period of 7.5 s, the available time to settle of entrained fine sands is longer than a wave period of 5 s. Therefore, the incapability of model in reproducing the high concentration at higher elevations is in longer period compensated.

The model results for the sediment concentration at the phase of maximum flow velocity for Mix2(X2) show a good agreement with measurements of O'Donoghue and Wright (2004b). It is explained for flow reversal phase by the lower proportion of fine sand fraction. However, the model results in the wave period of 7.5 s at deeper elevations of the sheet flow layer are slightly over-predicted. For both wave periods (5 and 7.5 s) the model reproduces reliable concentrations for the phase of minimum flow velocity (Fig. 4.18, the second and fifth column, the lowest graphs).

Furthermore, the slope of the vertical profile of the sediment concentration for the case of Mix1(X1) is higher than Mix2(X2) (the sediment concentration profile of X1 is steeper). This is occurred due to the higher percentage of the fine sand fraction in the case of Mix1(X1) compared to Mix2(X2) and the model reproduces this difference successfully.
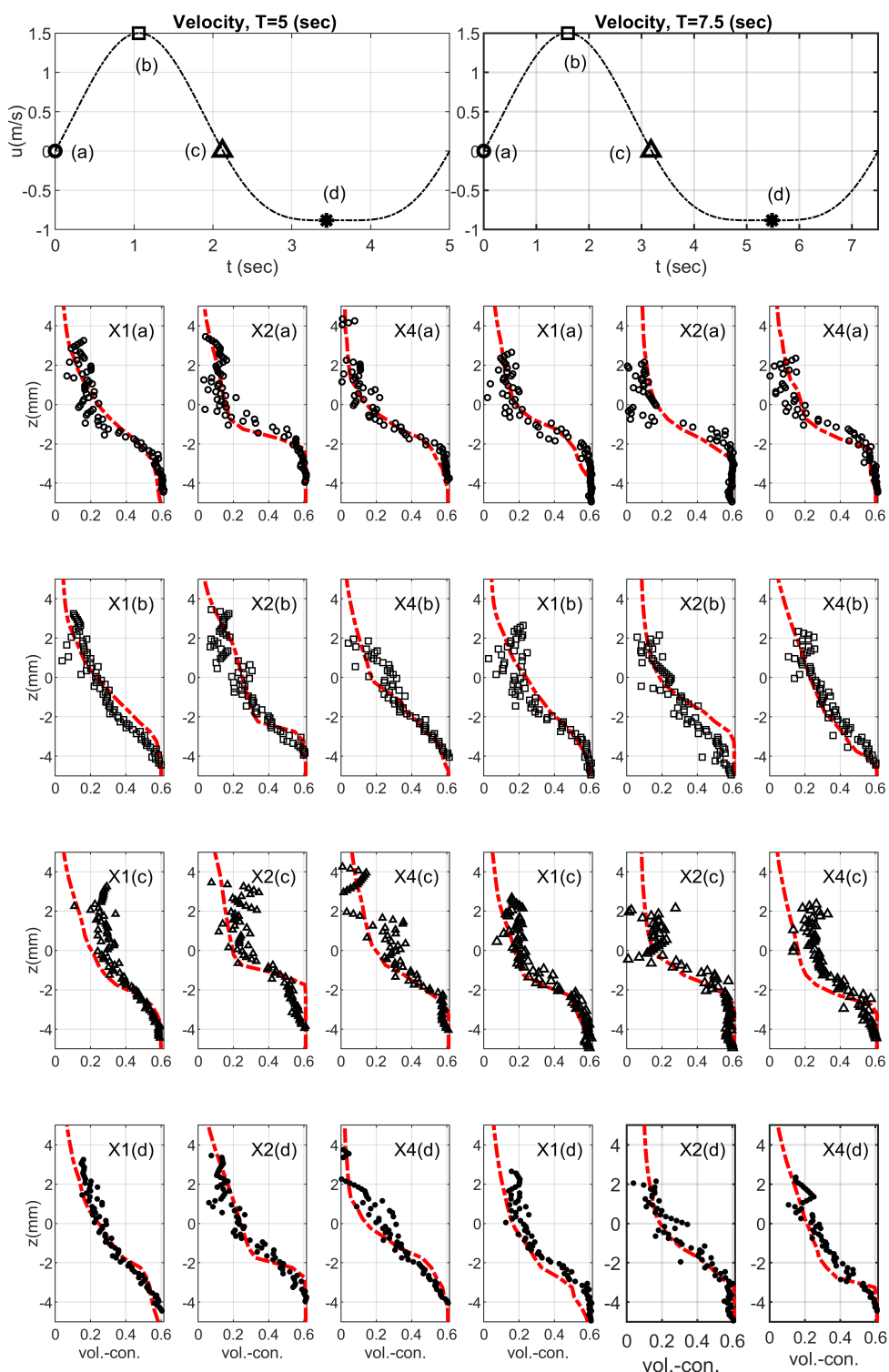
Figure 4.18: Vertical concentration profiles of mixed sands Mix1(X1), Mix2(X2) and Mix4(X4) for wave periods of T=5 and 7.5 s. Broken lines are phase-averaged model results and scatters are corresponding phase-averaged measurements of O'Donoghue and Wright (2004a) at start, maximum, flow reversal and minimum phases of flow velocities.

The third and sixth columns in Fig. 4.18 depict the vertical profiles of the sediment concentration for the case of bimodal mixed sand ([fine(50%) and coarse(50%)]) of O'Donoghue and Wright (2004b) under flow velocities with wave periods of 5 and 7 s, respectively. The model presents again good agreement with measurement results. However, the vertical profile of the mixed sand concentration at the flow reversal phase is not reproduced as well as other phases. More research is required to modify the turbulence approach to include the unsteady effect of fine sands in a mixed sand mixture at flow reversal phase. At this phase of the flow history, high volume of sands are entrained to the higher elevations of flow, while the resolved turbulence in $k - \epsilon$ model cannot reproduce these eddies.

Fig. 4.19 shows the selective vertical concentration profile for the fine fraction of the mixed sands at the corresponding phases of the mixed sands concentrations in Fig. 4.18. As can be seen, the fine fraction concentration profile for the mixed sands with higher proportion of the fine fraction (cases X1 and X4) is steeper than that of with smaller percentages of the fine fraction (X2). Therefore, the sand concentration gradient within the flow layer is smaller for the fine fraction of the cases with higher percentages of fine sands. This concept is reproduced well by means of the developed model. Further, this can also express the reason of the higher SFLT for mixed sands with greater proportion of fine fractions.

Moreover, the fine fraction concentration profile for all mixed sands shows a higher gradient at the flow reversal phase. However, in the measurements for the mixed sand concentration there is a high entrained volume of fine sands at this phase. Nonetheless, there is to date yet no selective concentration measurement within the sheet flow layer to compare with these model results, but it can be concluded that the model results at the flow reversal phase are slightly under-predicted, and hence a higher concentration gradient is shown in this phase for fine fraction concentrations.

The gradient of the fine sand concentration profile is higher for the cases under longer wave period (T=7.5 s), and hence the concentration is more rapidly decreased in higher elevation for the cases with longer period compared to the concentration profiles at the corresponding phases within the shorter. As a result, waves with shorter periods are capable of entraining the fine sands to higher elevations compared to waves with longer periods, which can be also resulted in a larger SFLT under shorter wave periods compared to longer. This can be explained by means of the higher available time for resettling in both onshore and offshore half-cycles of a longer wave period compared to the shorter, which can also lead to the enhanced unsteadiness of fine fractions under shorter wave periods. For the case with lower fine fraction (X2), a smaller erosion depth and consequently more stable condition is shown. As a result, lower offshore transport rate of the fine fraction compared to the cases with lower percentages of the coarse fraction (X1 and X4) is reproduced. However, this is not for the wave period of 7.5 s as significant as wave period of 5 s. In conclusion, the fine fractions are less entrained under shorter periods in a mixture with higher coarse fraction compared to the longer. Therefore, the empirical concept for hiding-exposure effect for interpretation of the selective transport rates is reproduced by means of the developed model. As a result, the SFLT for the mixed sands with larger proportion of the coarse fraction (X2) is smaller than that with greater fraction of the fine sand (X1 and X4).

Fig. 4.20 shows the vertical concentration profiles of the medium fraction in the corresponding phases of the mixed sands concentration profiles presented in Fig. 4.18. Due to the bimodal mixture of the X4 case (composed only of fine and coarse fractions), the medium fraction concentration is also reproduced by model as zero (columns three and six). As can be seen, the vertical concentration profile for the medium fraction is steeper in the case of X1 with higher fraction of fine sands (60 %) compared to X2 (20%).

Figure 4.19: Phase-averaged vertical concentration profiles of the fine fraction (see Tab. 4.4) corresponding to the mixed sands Mix1(X1), Mix2(X2) and Mix4(X4) for the wave periods of T=5 and 7.5 s at the start, maximum, flow reversal and minimum phases of flow velocities.

In consequence, in a case with higher proportion of the fine fraction, the medium fraction is entrained to higher elevations compared to the case with smaller percentage of fine fraction (X2). In contrast to the case X2, the medium fraction is present in the greater thickness of the transport in the case of X1, whether the percentage of the medium fraction in the case of X2 is two times of X1 (60% in X2 compared to 30% in the case of X1). Therefore, the coarser fractions compared to fine fractions are more transported in the mixtures with greater proportion of fine fraction. This concept is true for the cases under both wave periods. Therefore, apart from the wave period, it could be concluded that the coarser fractions are more transported within a mixture with higher fraction of fine sands, as was also observed at the LOWT by Hassan and Ribberink (2005) as well as at the AOFT by O'Donoghue and Wright (2004a).

The steepness of the concentration profiles for the medium fraction is enhanced under phases of the maximum and minimum flow velocity. However, the steepness is greater at the phase of the maximum velocity. Interestingly, at the phase of the maximum velocity for the case of X1 under the flow velocity with period of 7.5 s the concentration profile is slightly higher than that of 5 s. This can be explained with longer half period at the accelerating part of the flow velocity, which is shown for other test case as well. However, due to the higher percentage of the fine fraction in the case of X1, this steepness is more obvious. This leads in turn to a deeper erosion depth for the medium fraction within the longer wave period at the maximum and minimum flow velocity phases.

At the flow reversal phase, the case of X1 shows the maximum of its selective concentration at the higher elevation for the flow velocity with the period of 5 s compared to 7.5 s and this is more enhanced for the case of X2, where the maximum concentration is encountered at the roughly 3 mm higher elevation for the period of 5 s compared to 7.5 s. This can be explained by more erosion at the phases before than the flow reversal under the period of 7.5 s, in which the duration of the onshore half-cycle is greater than the 5 s. Furthermore, as was already mentioned, the entrainment length under a flow velocity with shorter period is higher than a longer, which can be resulted in higher concentration under shorter wave periods in corresponding phases of the longer.

Fig. 4.21 depicts the vertical concentration profile of the coarse fraction for the corresponding phases of the already presented vertical concentration profiles of the mixed sands in Fig. 4.18. As can be seen, the coarse fraction in the case of X1 (mixed sand with 60% of fine fraction and 10% of coarse fraction) is present as suspended in all elevations with a slightly gradient. It means that in a mixed sand with high percentage of fine sand, the coarser are suspended to higher elevations, which confirms this fundamental concept for the coarse fraction, that the coarser fractions are more exposed to the flow within a mixed sand, and hence they receive higher flow energy compared to other fractions and consequently entrained with a roughly uniform concentration at higher elevations. The developed model is capable of reproducing this concept for the coarse fraction. Nonetheless, to the knowledge of the author, a selective concentration measurement for the fractions of mixed sands in the sheet flow layer is yet not possible to compare these with the model results.

This behavior of coarse fraction in a mixed sand with high proportion of fine fraction is independent of the velocity wave period as the same for the case of X1 under velocity with period of 7.5 s was reproduced. For the case of X2 with higher percentage of the coarse fraction compared to the X1 (20% in X2 compared to 10% in X1), the relative presence of the coarse fraction is not as pronounced as X1. The reason for this is inherent in the higher percentage of the fine fraction in the X1 case (60%) compared to the case of X2(20%).
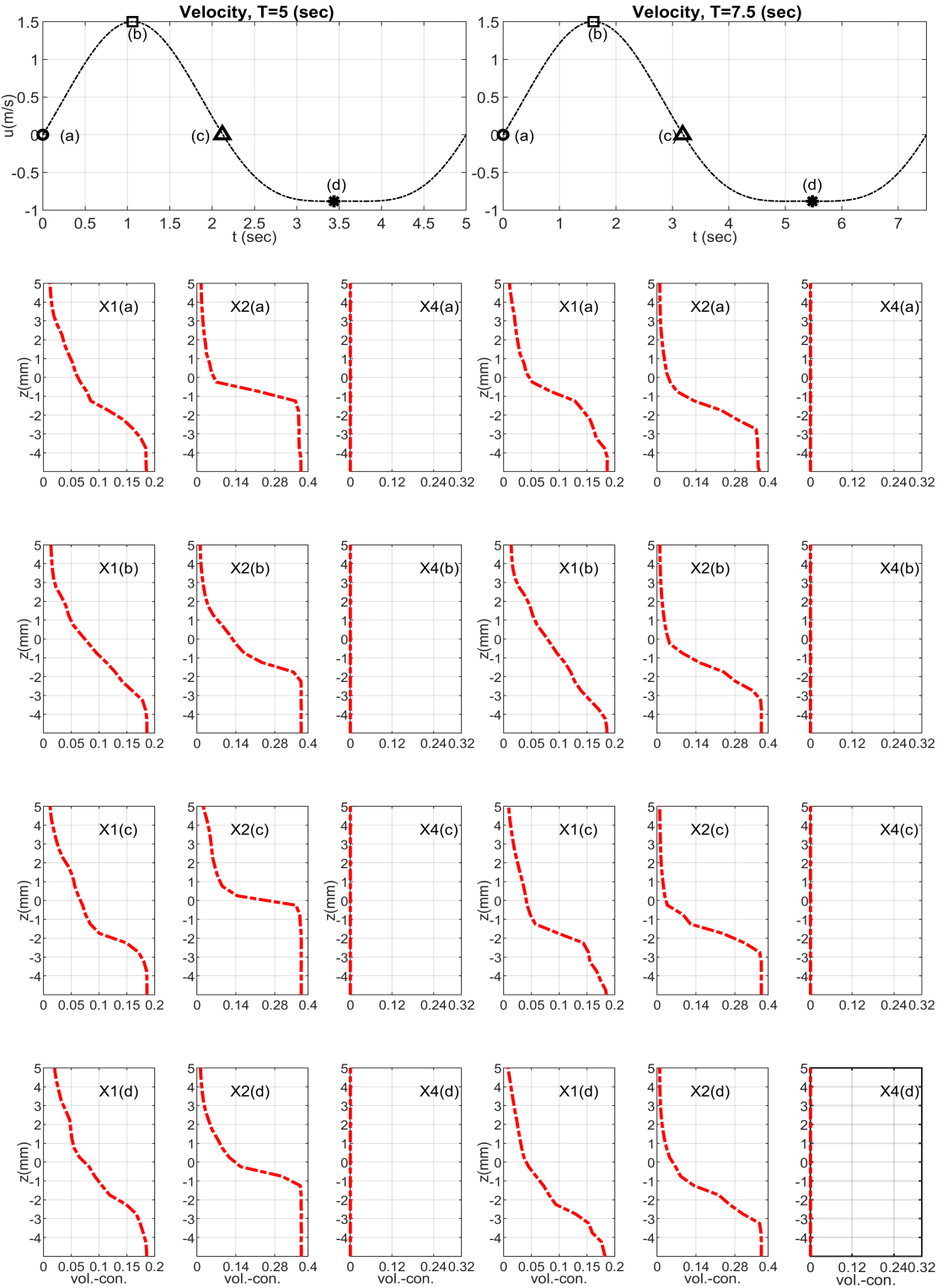
Figure 4.20: Phase-averaged vertical concentration profiles of the medium fraction (see Tab. 4.4) corresponding to the mixed sands Mix1(X1), Mix2(X2) and Mix4(X4) for the wave periods of T=5 s and 7.5 s at the start, maximum, flow reversal and minimum phases of flow velocities.

In the case of X2 at the flow reversal phase this discrepancy of the vertical concentration of the coarse fraction for higher (X1) and lower (X2) proportion of the coarse fraction is more clear, where the vertical concentration profile of the coarse fraction in the case of X2 reaches its maximum roughly close to the undisturbed bed, while at this phase in the case of X1, the coarse fraction with around half of its maximum concentration ($(\alpha_3)_{max}$ =0.061 (m^3/m^3)) is present. The maximum concentration for the case of X2 under the flow velocity with the period of 7.5 s at the phase of flow reversal appears in slightly lower elevation, which confirms the deeper erosion depth under longer wave period. Moreover, in the case of X2, the concentration of the coarse fraction at elevations above the undisturbed bed ($z > 0$) under longer wave period is greater than the shorter.

The X4 case with bimodal mixture shows a behavior between X1 and X2, due to the equal proportion of coarse and fine sands. In this case the vertical concentration profile of coarse fraction is neither qusi-uniform like X1 nor with high gradient near the maximum concentration like the case of X2. The vertical concentration profile for the case of X4 has a gentle behavior where the concaveness of the profile changes (X4(a) and X4(d)). However, at the phases of the maximum flow velocity and flow reversal, the concentration profile has no deflection point. In contrast, the case of X4 under velocity with period of 7.5 s shows no deflection point with exception of the flow reversal phase, where the concentration gradient is higher compared to other phases.

The concaveness of the vertical concentration profile for the case of X4 at the phase of maximum flow velocity under the flow velocity with the period of 5 s is different than 7.5 s, where the concentration profile is concave up. This means under the flow velocity with shorter wave period the concentration is higher than the longer. Moreover, the concentration gradient is higher at this phase for the flow velocity with the period of 7.5 s.

The vertical concentration profile at the phase of the minimum flow velocity for the case of X4 under flow velocity with the period of 7.5 s is considerably different than the concentration profile under the velocity with the period of 5 s. This can be explained with the enhancement of the fine fraction entrainment under shorter wave periods as well as the higher level of entrainment at the phase of flow reversal, which produces higher sand concentration under shorter wave periods compered to the longer. Therefore, the offshore transport of this suspended sands leads to a higher sand concentration at the minimum velocity phase for the shorter wave period compared to longer.

Fig. 4.22 shows the vertical concentration profile for fine, medium, and coarse fractions using the applied approach for mixed sand. For mixed sand X1 with high percentage of fine sand, the coarse fraction is with its maximum fractional concentration available at all elevations compared with medium and coarse fractions. However, the fine fraction has in all elevations due to its maximum percentage (60% compared to 30%-medium and 10%-coarse) the highest concentration. Interestingly, for the mixed sand X2 with the same percentage of fine and coarse sand fractions (20%-fine and 20%-coarse), available concentrations are almost similar at different elevations. It can be interpreted by means of the grading index of X2 (GI=3.79 < 4.0), which classifies X2 as a poorly graded mixed sand. Therefore, higher percentage of coarse sand is entrained compared with a mixed sand with higher grading index like X4 (GI=5.55 > 4.0). However, the vertical concentration profile of coarse sand is not as uniform as mixed sand X1. The reason is the lower percentage of fine fraction in X2 (20%-fine) compared to X1 (60%-fine).
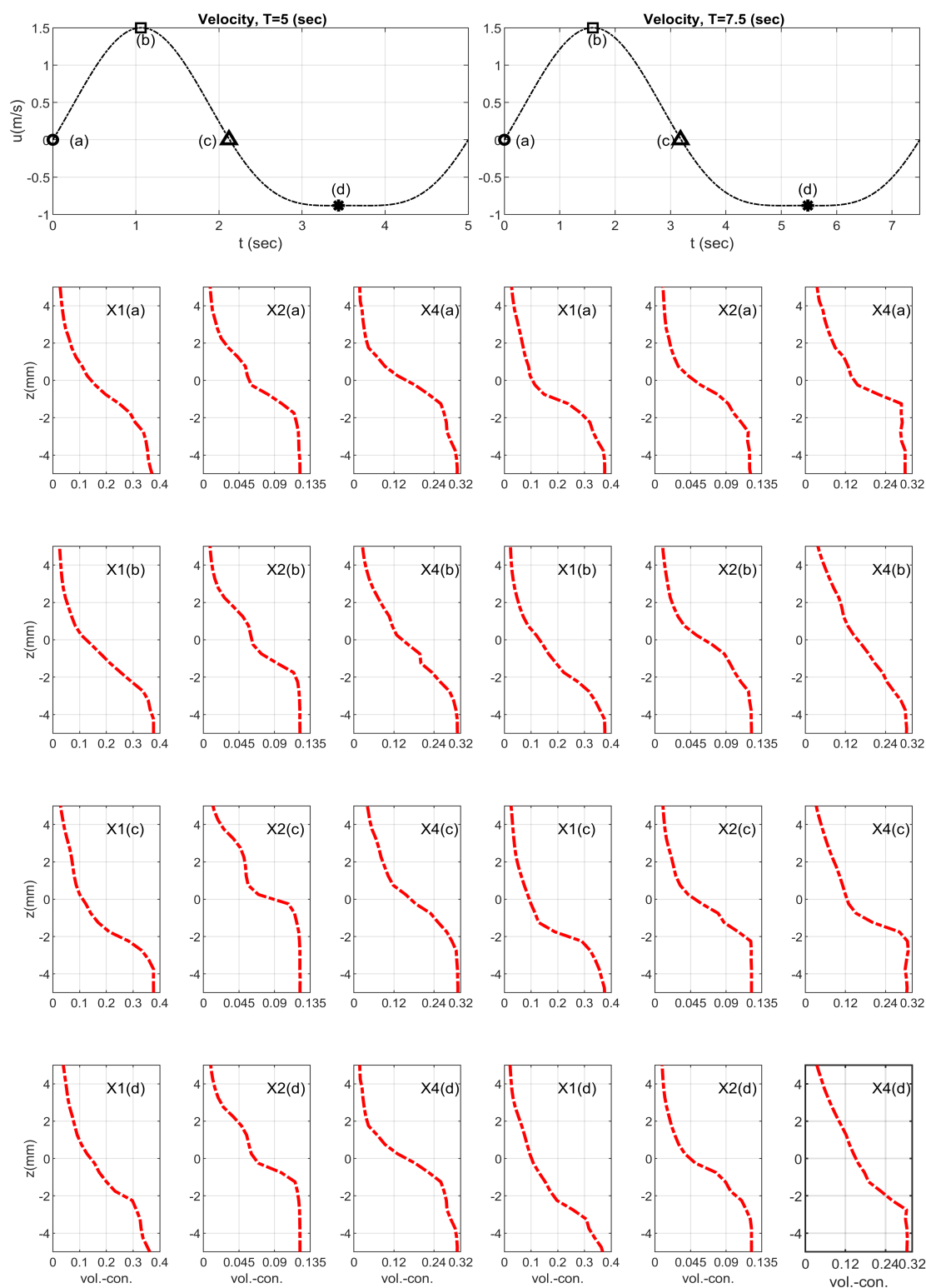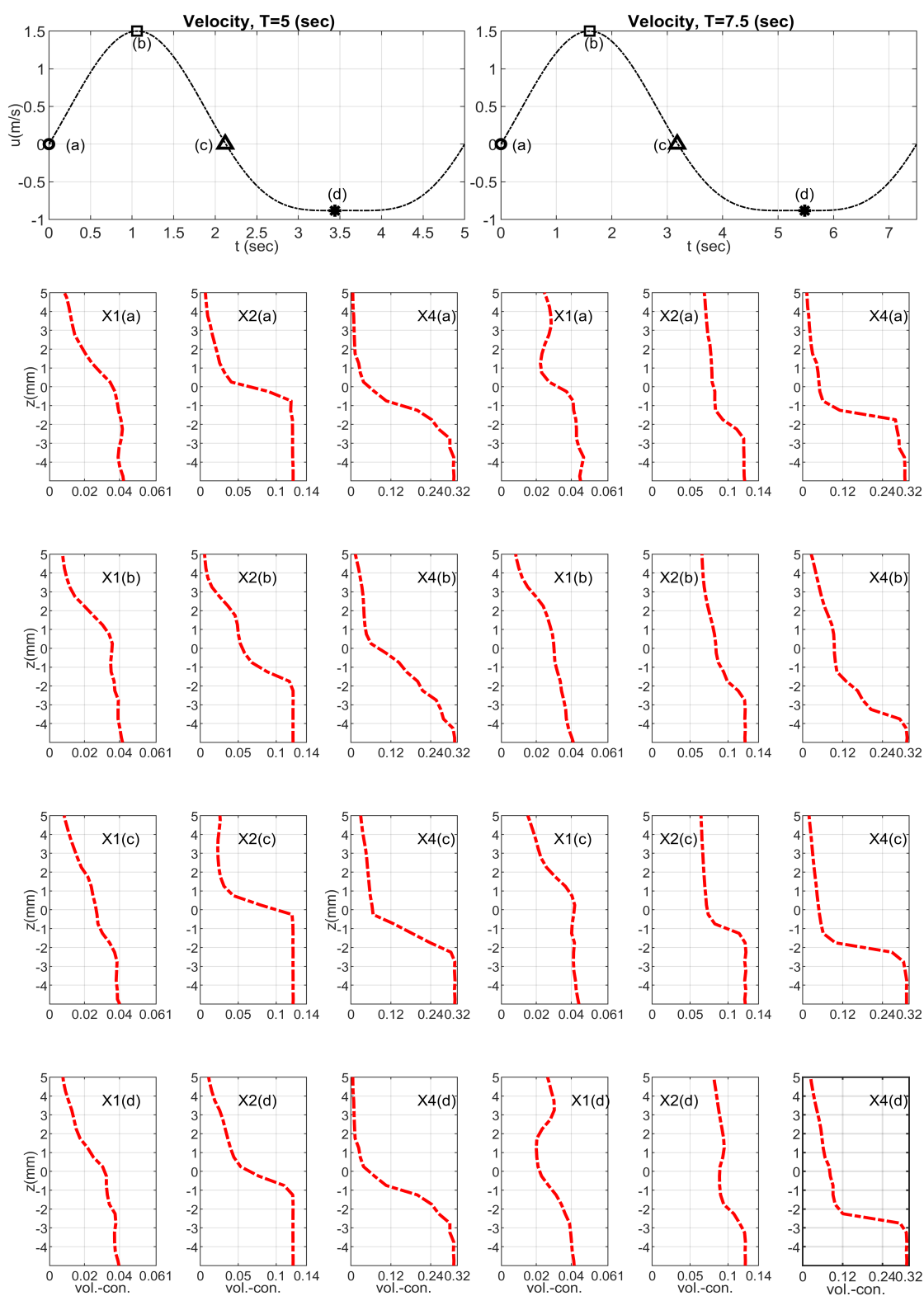
Figure 4.21: Phase-averaged vertical concentration profiles of the coarse fraction (see Tab. 4.4) corresponding to the mixed sands Mix1(X1), Mix2(X2) and Mix4(X4) for the wave periods of T=5 and 7.5 s at the start, maximum, flow reversal and minimum phases of flow velocities.
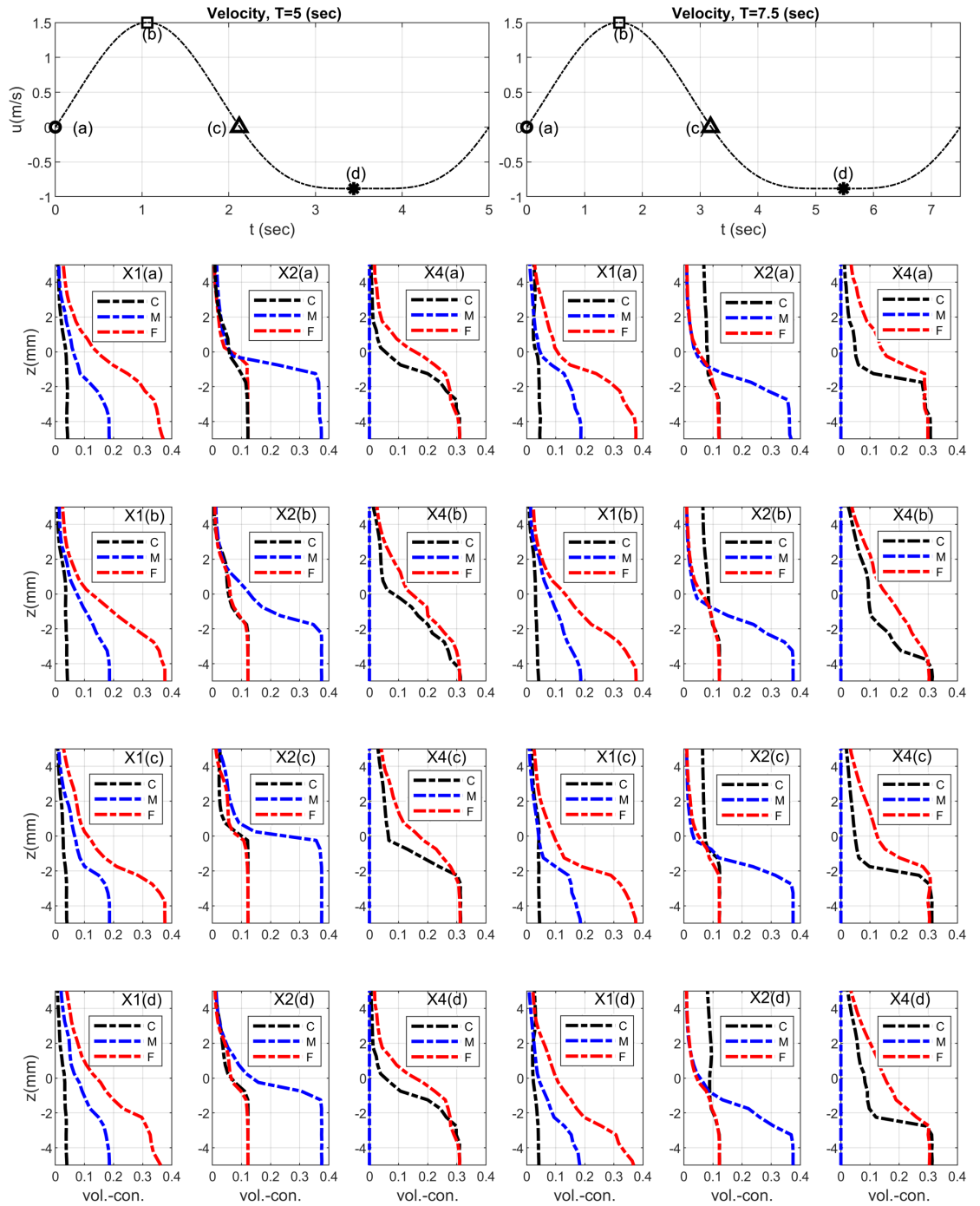
Figure 4.22: Phase-averaged vertical concentration profiles of the coarse (C), medium (M), and fine (F) fractions corresponding to the mixed sands Mix1(X1), Mix2(X2) and Mix4(X4) for the wave periods of T=5 and 7.5 s at the start, maximum, flow reversal and minimum phases of flow velocities.

4.9.2   Sheet flow layer thickness (SFLT)

SFLT is determined by means of the definition of Dohmen-Janssen (1999) for the SFLT, which defines the SFLT as the thickness of the region from the no-flow bed level to an upper elevation, where the sediment concentration is equal to the volumetric concentration of 8% (212 kgm^{-3})(see Fig. 2.21). At this concentration the interparticle interactions of sand grains (grain-grain interactions) are negligible. The importance of the SFLT is, apart from the main transport of sediments in this layer, the dependency of empirical/semi-empirical net sediment transport predictive formulas to the SFLT (like the SANTOSS (2013) formula). Therefore, a good prediction of the SFLT will improve the accuracy of the predicted net transport by means of empirical formulas. Fig. 4.23 shows the reproduced SFLT by mixedSedFoam in comparison with measurements of O'Donoghue and Wright (2004b). The lowest border of the shaded region is the phase-averaged erosion depth and the top-border depicts the elevation of the volumetric concentration of 8%.

Despite the good agreement of the model results for the case of Mix1(X1) with the measurements, the model results for other cases are relatively 2-4 mm under-predicted. The reason for this is the weakness of the turbulence model to reproduce the higher sediment concentration at higher elevations, particularly at the phase of flow reversal, which was discussed at section 4.9.1. However, the simulated SFLT by mixedSedFoam is only 2-4 mm smaller than the measurement. The predicted SFLT for the case of Mix1(X1) at the wave period of 5 s is slightly higher than the SFLT at the 7.5 s. It could be explained that in the shorter wave periods, due to the stronger unsteady effects compared to the longer wave periods, the entrained sediments are transported to higher elevations and have not the settling back time as long as longer wave periods.

Moreover, due to the time-averaged properties of RANS-equations, the predicted SFLT has not the time-dependent fluctuations compared to measurements. Therefore, the model results for SFLT should be considered as the results which are not capable of perfectly simulate the time-dependent SFLT variations. However, it can be a first effort for SFLT estimation, which can improve the prediction of SFLT by means of empirical formulas.

To examine the performance of the developed model, Fig. 4.24 compares the predicted SFLT from the developed model with the modified SANTOSS (2013) formula in section 3.3.7 for empirical formula of Dohmen-Janssen (1999) in the cases of O'Donoghue and Wright (2004a, 2004b). As can be seen, the proposed formulation for mixed sands predicts a greater SFLT for the cases with higher percentage of fine fractions. Comparing the proposed modification with the mixedSedFoam results, it can be concluded that the proposed formula can reasonably predict the SFLT, particularly for mixed sands with high proportion of fine fraction ($> 50\%$), like the proposed SFLT for the case of X1T50 as well as X1T75. However, the predicted SFLT by means of the proposed formula is for shorter wave periods under-predicted, particularly for the trough part.

Fig. 4.25 compares the predicted net transport rates for the cases of O'Donoghue and Wright (2004a, 2004b) by means of the original and modified SANTOSS (Van der A et al., 2013) formulas. As can be seen, the modified SFLT of the SANTOSS (Van der A et al., 2013) formula can predict the net transport rate of the all cases within the limits of factor two of differences. The reason for this improvement is, as discussed in chapter 3 (see section 3.3.7), the better prediction of the SFLT for the mixed sands with high proportions of fine sands using developed modification. Due to the multiplication of the SANTOSS (2013) formulation into the factor of $(1 + PF)^{e_1}$ for the SFLT in the new formulation (Eq. 3.43), where e_1 a positive number for well-graded mixed sand ($GI \geq 4$) is, the SFLT in the new formulation is increased. This increment provides higher unsteadiness through the

higher phase-lag number in the SANTOSS (2013) formula (Eq. 3.41) that leads to higher crest and trough interchange values (Eq. 3.36 to Eq. 3.39). The Pearson correlation factor between measurements and predicted results by means of the SANTOSS (Van der A et al., 2013) formula for the mixed sand cases of O'Donoghue and Wright (2004a, 2004b) is 44.53%, whilst this for the developed modification improves to 80.22%.
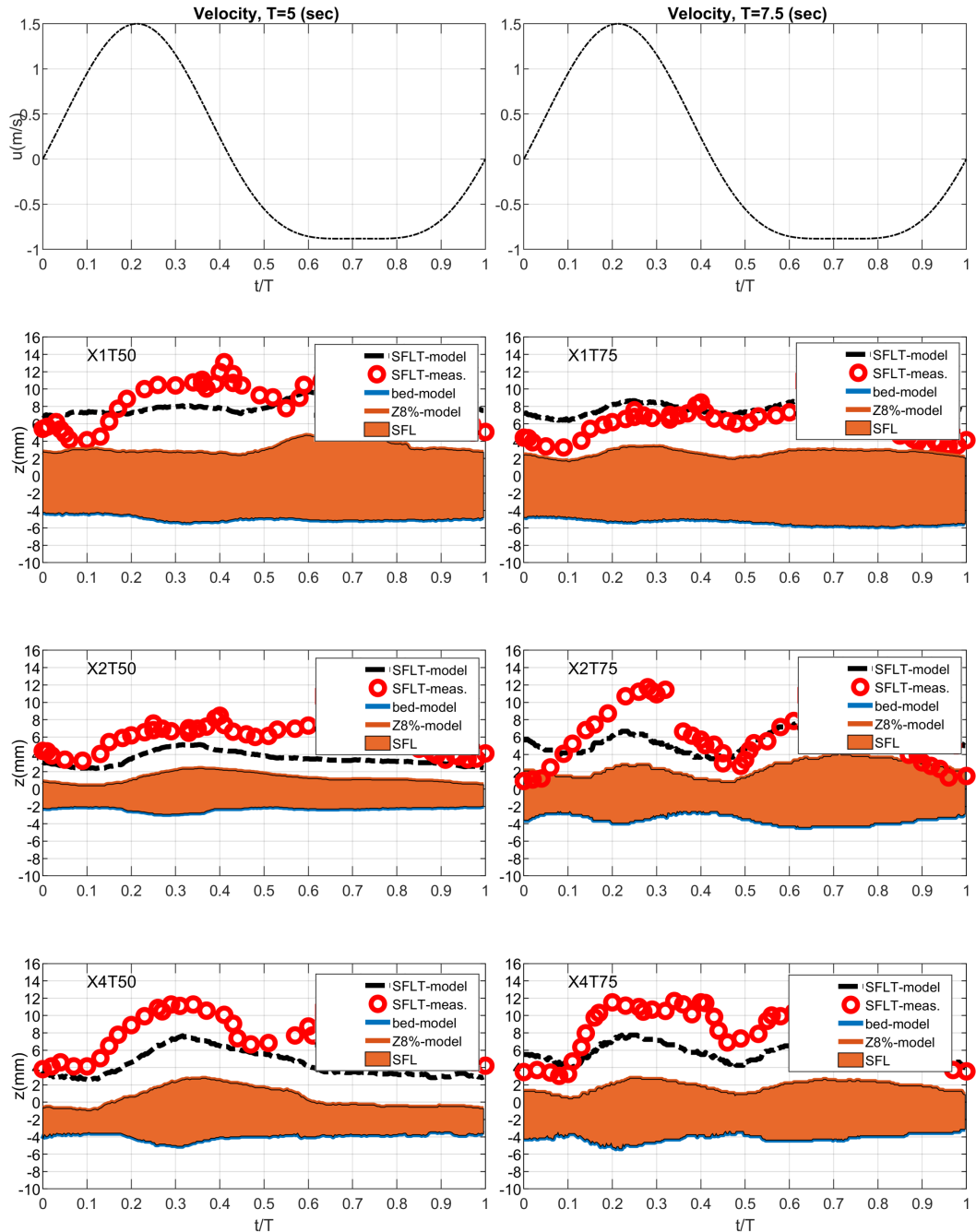
Figure 4.23: SFLT of mixed sands Mix1(X1), Mix2(X2) and Mix4(X4) for wave periods of T=5 and 7.5 s. Broken lines are phase-averaged model results and scatters are corresponding phase-averaged measurements of O'Donoghue and Wright (2004a).
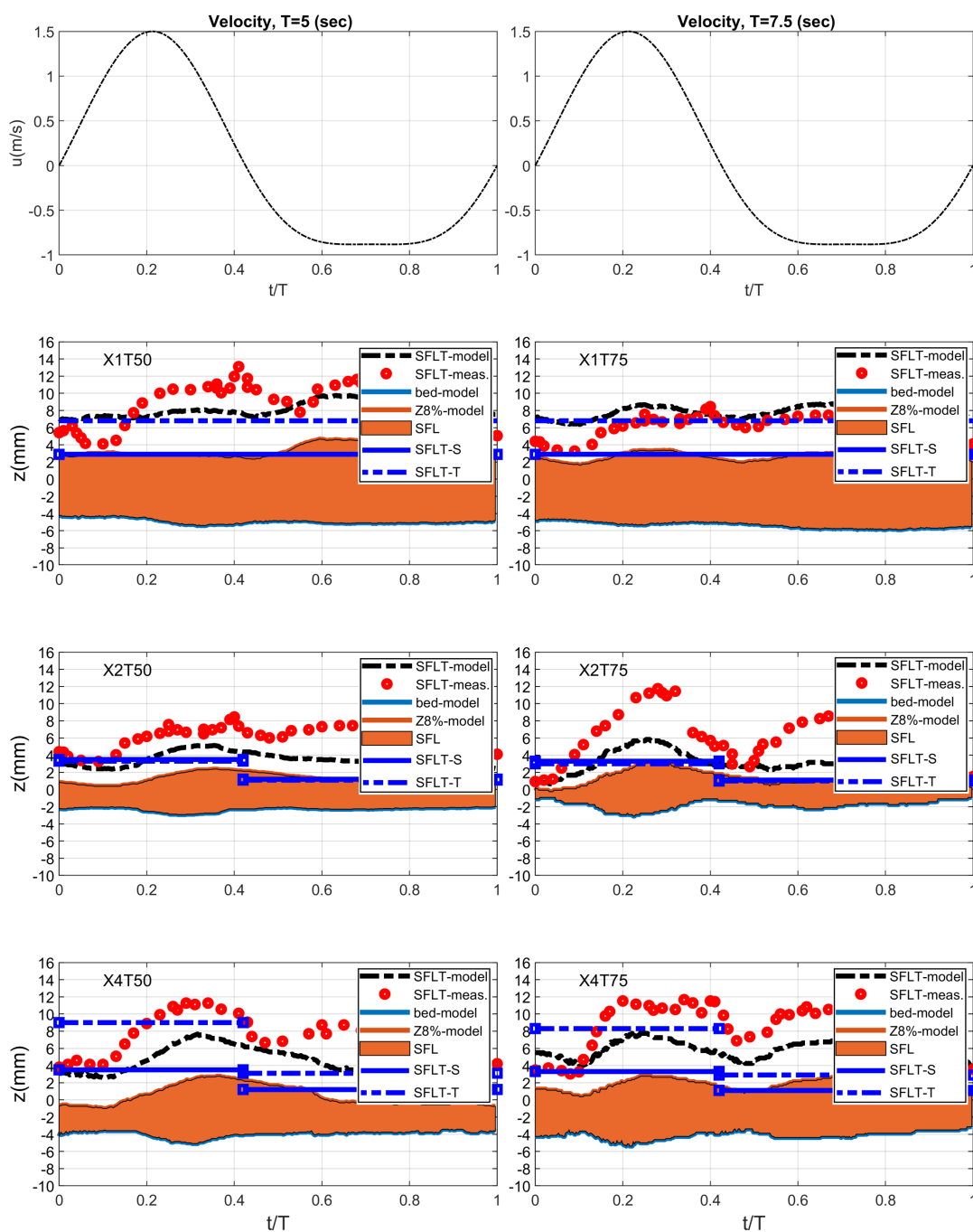
Figure 4.24: SFLT of mixed sands Mix1(X1), Mix2(X2) and Mix4(X4) for wave periods of T=5 and 7.5 s of the developed model (broken black) in comparison with Dohmen-Janssen (1999) (SFLT-S, solid blue) and proposed formula in section 3.3.7 (SFLT-T, broken blue). The breaking of the SFLT-line at the flow reversal point is due to the different formulations for crest and trough (see Eq. 3.42 and Eq. 3.43).
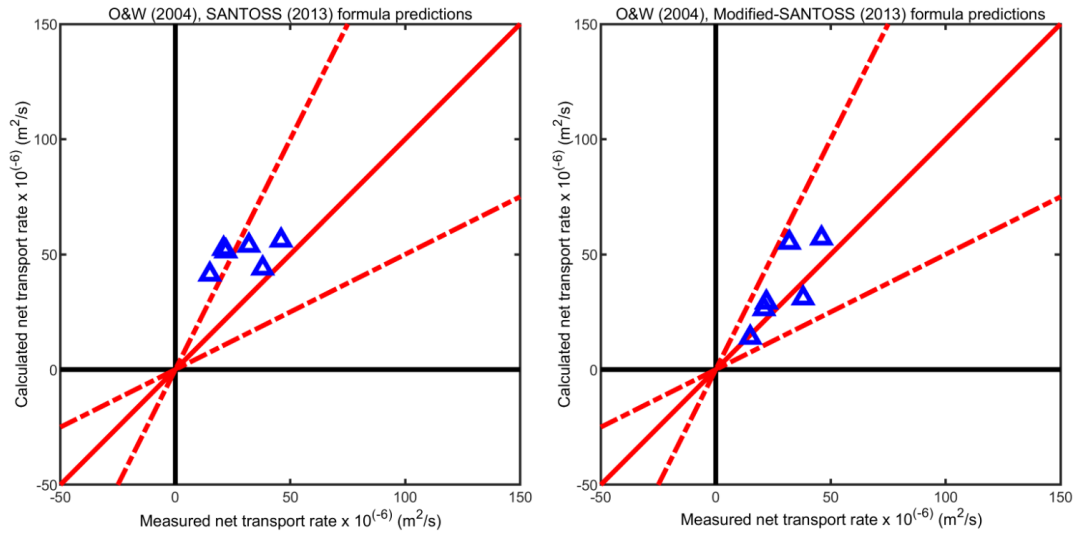
Figure 4.25: Predicted net transport rates for the cases of O'Donoghue and Wright (2004a) by means of the SANTOSS (Van der A et al., 2013) formula (left) and the proposed SFLT-modification in this thesis (right).

Moreover, the developed modification predicts a higher SFLT for the crest half-cycle than the trough half-cycle, where the SFLT differs in crest and trough. For the cases of X1T50 (Mix1(X1) under the flow velocity with the period of 5 s), X1T75 (Mix1(X1) under the flow velocity with the period of 7.5 s), because of the D_{50} of the mixed sands (0.19 mm), it is classified into the second formulas part for the SFLT (Eq. 3.43 second term), where the SFLT in this range of mixed grain size is independent of the crest-/trough-dependent Shields parameter.

Using a higher SFLT, the unsteadiness is increased, and hence the sediment interchange between half wave cycles is enhanced. Consequently, the predicted net transport rate is decreased. This is more pronounced for the case of X1T50 (with 60% of fine sand), where the measurements for the mixed sands by O'Donoghue and Wright (2004b) is 15×10^{-6} m^2/s and using the proposed formula for uniform sands by Dohmen-Janssen (1999) and developed in SANTOSS (2013) formula is predicted as 41.3×10^{-6} m^2/s and using developed formula in this thesis is predicted as 13.9×10^{-6} m^2/s.

Tab. 4.6 outlines the sediment transport parameters for the developed model results compared to the measurements of O'Donoghue and Wright (2004a). As is evident, all model cases were in the sheet flow condition at the maximum flow velocity phase ($\theta_m > 1$). Furthermore, there is a good agreement between model results and measurements of O'Donoghue and Wright (2004a) for the maximum Shields parameter. However, the model results, except of the case X1T75, are slightly over-predicted for the maximum velocity value but the root mean square velocity (u_{rms}) of the model results has a good agreement with the measurements. The mobility number is always greater than 300 ($\psi > 300$), which approves the dominant regime of the transport mode as the sheet flow in all test cases.

The maximum erosion depths are for the cases of X1 (X1T50 and X1T75) slightly over-predicted. The reason for this is the over-prediction for the flow velocity, which leads to the higher erosion depth, and hence the lower SFLT for this test cases. However, the maximum erosion depth is only 0.8 mm over-predicted in the case of X1T75. For the case of X2T75, the model results for the maximum velocity is under-predicted. Therefore, this over-prediction is evident in other transport parameters.

Table 4.6: Predicted by the developed model in this thesis (upper values) and measured (lower values) orbital excursion amplitude(A), maximum velocity (u_{max}), root mean square velocity (u_{rms}), maximum Shields parameter (θ_m), maximum mobility number (ψ_m), maximum erosion depth (δ_{em}), maximum SFLT (δ_{sm}) and net transport rate (q_N) of O'Donoghue and Wright (2004b).

Test case	D_{50} (mm)	W_s (m/s)	A (m)	u_{max} (m/s)	u_{rms} (m/s)	θ_m	ψ_m	δ_{em} (mm)	δ_{sm} (mm)	$q_N.10^{-6}$ ($m^2 s^{-1}$)
X1T50	0.15	0.017	1.0	1.59	0.89	4.19	1042.3	5.42	9.75	13.89
			1.0	1.53	0.89	3.90	946.14	4.40	12.4	15
X1T75	0.15	0.017	1.78	1.18	1.06	2.05	574.32	5.88	8.8	26.3
			1.0	1.53	0.89	3.90	964.14	3.70	8.0	21
X2T50	0.27	0.040	1.0	1.58	0.88	2.65	574.66	2.78	5.13	56.98
			1.0	1.53	0.89	2.40	535.63	3.90	10.4	46
X2T75	0.27	0.040	1.47	1.49	0.87	2.15	510.75	3.08	5.83	55.14
			1.0	1.53	0.89	2.20	535.63	4.8	11.6	32
X4T50	0.26	0.038	1.0	1.64	0.89	2.93	642.72	4.96	7.67	30.98
			1.0	1.53	0.89	2.40	556.23	4.2	11.0	38
X4T75	0.26	0.038	1.24	1.60	0.74	2.64	609.24	5.38	7.75	29.17
			1.0	1.53	0.89	2.20	556.23	4.4	11.4	22

The measured values for the maximum SFLT are higher than the model results. The main reason for this can be the $k-\epsilon$ turbulence approach of the developed model, which dissipate the eddies in higher elevations and hence is incapable of reproducing the transport of sands to higher elevations above the bed, particularly at the phase of flow reversal. Moreover, hindered settling effect or presence of other natural components like biological factors or elector-chemical repulsion, which are not included in transport equations could lead to this discrepancy. Further researches are necessary to improve the turbulence approach terms to reproduce the suspended sand concentration, particularly fine fraction, at higher elevations.

The net transport rates in Tab. 4.6 were calculated by means of the developed modification in the SANTOSS (2013) formula. As can be seen, the predicted net transport rates for the case of X1 with 60% of fine fraction have a good agreement with measurements. However, the net transport rate for the case of X2T75 is over-predicted more than other test cases. The reason for this over-prediction is as depicted in the Fig. 4.24 the under-prediction of the SFLT, particularly at the onshore half-cycle. This under-prediction reduces the rate of sand exchange between half-cycles, which in turn increases the predicted net transport rate. Likewise, the predicted net transport rate for the case of X4T75 is over-predicted, which points out to the under-predicted SFLT.

In contrast, the predicted net transport rates for the cases of X4T50 and X1T50 are under-predicted, which can be explained by slightly over-predicted SFLT for these cases at the onshore half-cycle. This over-prediction of the SFLT at the onshore half-cycles, represents a higher sand volume at this half-cycle in higher elevations above the eroded bed and

consequently their offshore transport at the successive offshore half-cycle.

4.9.3 Vertical profiles of flow velocity

Fig. 4.26 compares the simulated phase-averaged flow velocity profiles by mixedSedFoam with the experimental measurements of O'Donoghue and Wright (2004b) at four important time points. As can be seen, the model has a good agreement with measurements under the no-disturbed bed elevation($z < 0$), however, the model results in higher elevations are over-predicted. The over-prediction is increased in longer flow velocity period ($T = 7.5\ s$) and at the flow reversal point of the flow velocity with period of 7.5 s the model results for flow velocity are highly over-predicted, while for the wave period of 5 s it reproduces better results compared to measurement. The reason for the over-prediction could be explained in the highly concentrated sediment layers in measurements and weaknesses of the turbulence equations to dissipate the flow kinetic energy due to the stratification and water-sand interaction (last two terms in the k-equation 4.49). More research is required to increase the dissipation rate of the carrier flow in mixed sand compared to uniform sand at flow reversal point.

In these thesis is the dissipation of flow energy using enhancement of the water-sand interaction improved. At some points like flow reversal, this calibration cannot solve the turbulence dissipation. The over-prediction in flow velocity leads to the under-estimation of temporal sediment concentration. Nonetheless, the flow velocity at the other time points apart from the flow reversal are representative compared to measurements of O'Donoghue and Wright (2004a). It can successfully represent the flow direction as well as the vertical gradient of flow velocity. The overshoot velocity is also captured successfully by the developed model, particularly for the flow velocity with the period of 5 s (the case X1T50). This slightly over-prediction due to the applied turbulence model for uniform sand in sedFoam was also noted by Cheng (2016). The sedFoam results for velocity profiles over uniform sand in Cheng (2016) (Fig. 5.6 of Cheng (2016)) for MA7515 (medium uniform sand of O'Donoghue and Wright (2004a) with period of 7.5 s) show over-prediction at the crest half-cycle but good agreement at the trough half-cycle. The performance of mixedSedFoam is, however, different than the sedFoam. Apart from the good prediction for the maximum velocity point at the crest and minimum velocity point at the trough (points (b) and (d) at the r.h.s of Fig. 4.26), the developed model provides over-predicted velocity at the flow reversal point. Due to the coupling the fractional velocities of sand fractions to the carrier flow (Eq. 4.55 and Eq. 4.56), the fractional velocities affect the velocity of carrier flow. Therefore, the momentum of a mixture requires more dissipation terms in turbulence energy equations than the available equations for kinetic energy and dissipation rate in sedFoam.

4.9.4 Vertical profiles of sand fluxes

To understand the general form of sand fluxes in different wave periods for different grain size mixtures, the time-averaged sand fluxes were reproduced and analyzed (Fig. 4.27). The model can successfully predict the general transport direction of mixed sands within the sheet flow layer. The model results predict the mixed sands transport for fine sands in offshore direction, as was measured, but the model results are slightly over-predicted. This over-prediction can be explained due to the over-prediction of flow velocities. The model predicts the sand transport for the case of X1T50 totally offshore, however, the measurements show a slightly onshore transport in proximity of the no-flow bed elevation.

This was captured by model for the cases of X2T50, X2T75 as well as X4T75.
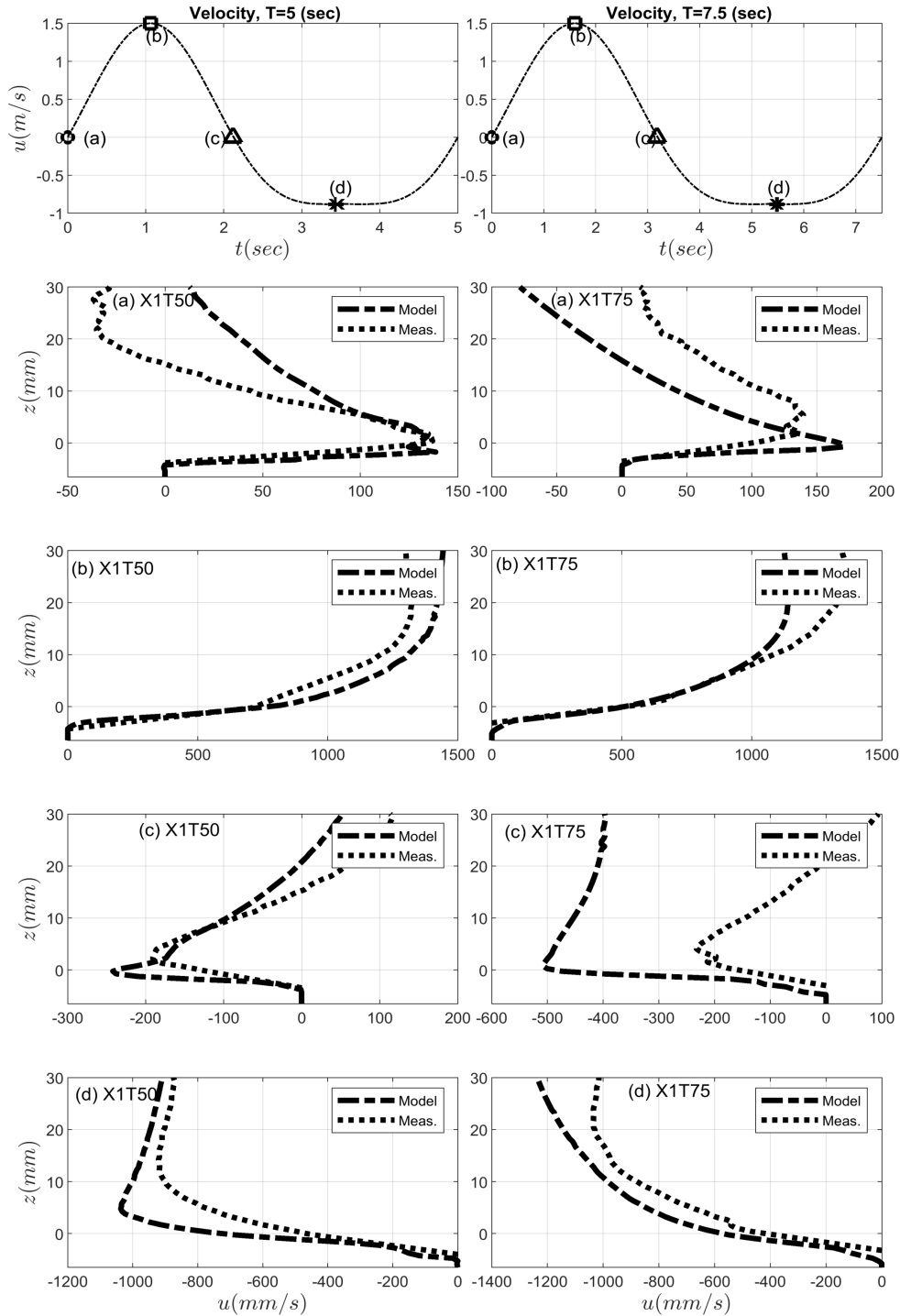
Figure 4.26: Vertical profiles of the measured flow velocity (dotted lines) in comparison with model results (broken lines).
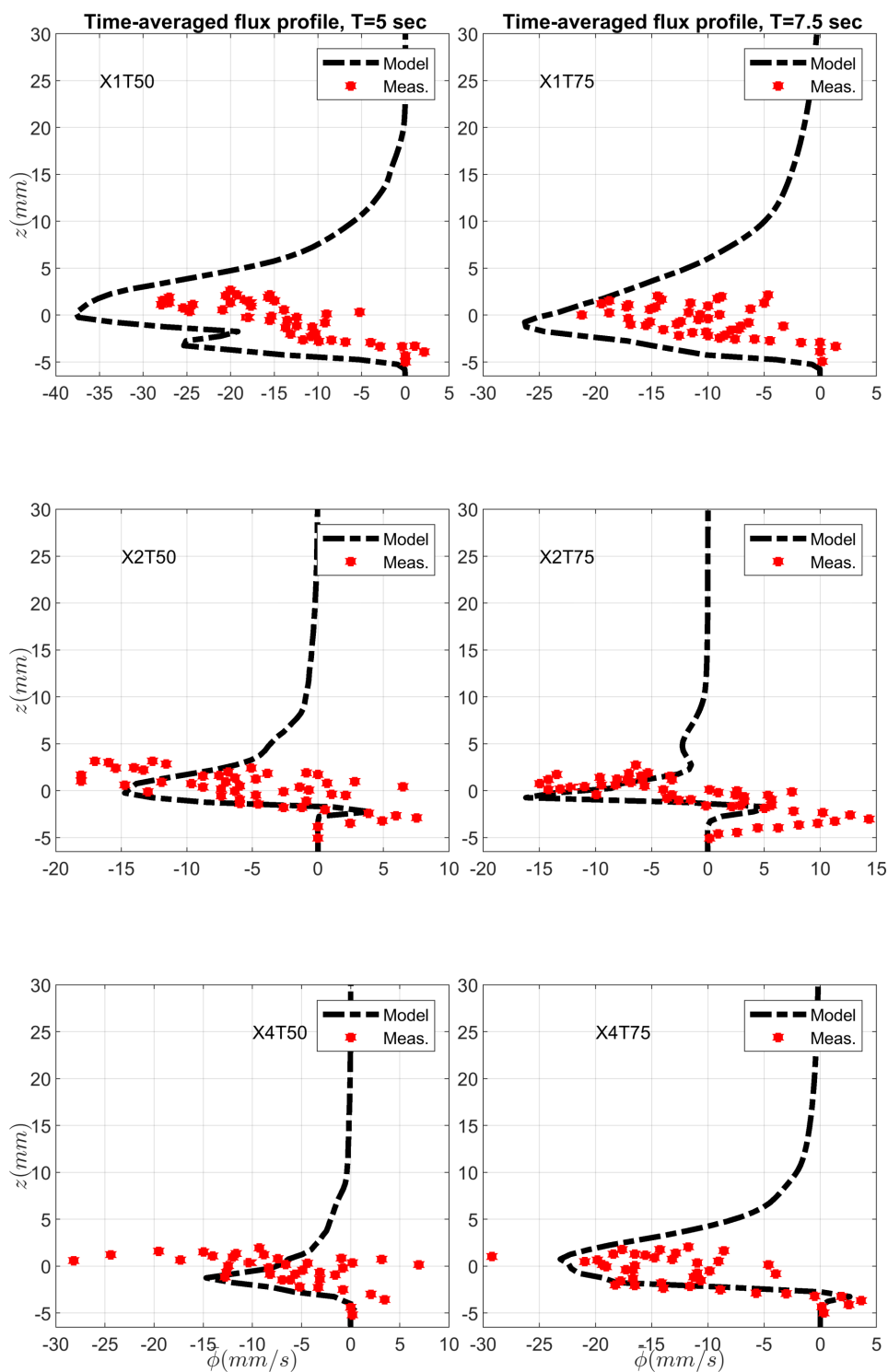
Figure 4.27: Vertical profiles of the time-averaged measured fluxes (red points) in comparison with model results (broken lines).

Moreover, the transport rate for all cases is offshore dominant as was measured. This offshore transport is enhanced for the cases under lower flow velocity periods with higher percentages of fine sand fraction. It can be concluded that in lower wave periods for the same mixed sand higher offshore transport is simulated as was observed in the xeperiments of O'Donoghue and Wright (2004a), and therefore more erosion occurs.

Further, the onshore transport rate is increased by increasing the proportion of the fine sand fraction. The cases of X2T50/X2T75 have the same D_{50} like X4T50/X4T75 ($D_{50} =$ 0.28 mm), but the offshore sand flux in X4 cases is more than the X2 cases. The reason for this is the 50% of the fine fraction in X4 cases compared to 20% in X2. Therefore, two mixed-sands with the same D_{50} can behave according to their fine proportion significantly different.

In contrast, the onshore sand flux is increased by increasing the coarser fractions. For the same D_{50}, X2 cases show more onshore transport compared to the cases of X4, concluding that the unsteady effect of fine sands in a mixed sand increases the offshore transport and applying coarser fractions retards the unsteadiness, and hence a higher crest velocity in nonlinear waves leads to lower erosion under sheet flow prevailed transport mode, like storms surges. This can show the importance of the understanding the mixed sands behavior in (re)nourishment beach protection practices.

The sand fluxes out of the bed boundary layer is predicted close to zero. However, the measurements show the onshore dominant sand fluxes for all cases with flow velocity period of 5 s. This can be reproduced by an initial condition of sand fractions above the bed boundary layer. Even though, the sheet flow layer is studied in this thesis, and hence the suspension layer is not discussed here. Moreover, the sand concentration within the suspension layer are significantly lower compared to the sheet flow layer, and therefore the influence of the suspension layer on the sheet flow layer transport mechanism could be neglected.

4.9.5   Mixed sands concentration time series

The phase-averaged time series of concentration for the cases of O'Donoghue and Wright (2004a) were simulated using the developed model at different elevations; in pick-up layer (z=-2.25 mm) as well as immediately close to the undisturbed bed level (z=-0.25 mm) and above the bed level (z=+0.75 mm). Fig. 4.28 shows the time series of mixed sand concentrations in the pick-up layer for the cases of Mix1, Mix2 and Mix4 at the flow velocity periods of 5 s (left) and 7.5 s (right), respectively. It is clear that the developed model can capture the concentration at the time of maximum velocity. Moreover, as was shown by measurements, the developed model also predicts the phase lead of sands compared to the flow velocity.

For the case of X1T50 (Mix1), the model results at the crest- as well as trough-half-cycles are slightly over-predicted. However, the model can well reproduce the time series of sediment concentration for the case of Mix2 under flow velocity period of 5 s, where at the flow reversal point the model results are slightly over-predicted. The good agreement between measurement results and model for the case of Mix2 could be explained by the smaller proportion of the fine sand fraction in the mixed sand Mix2 (20%) compared to the case of Mix1 (60%).

Despite the slightly over-prediction of the model results for the mixed sands at the trough half-cycle, the predicted results for the cases of Mix1 and Mix4 under the flow velocity with the period of 7.5 s are slightly under-predicted. Nonetheless, the model results for the case of Mix2 in this wave period (T=7.5 s) at the trough half-cycle are over-predicted.
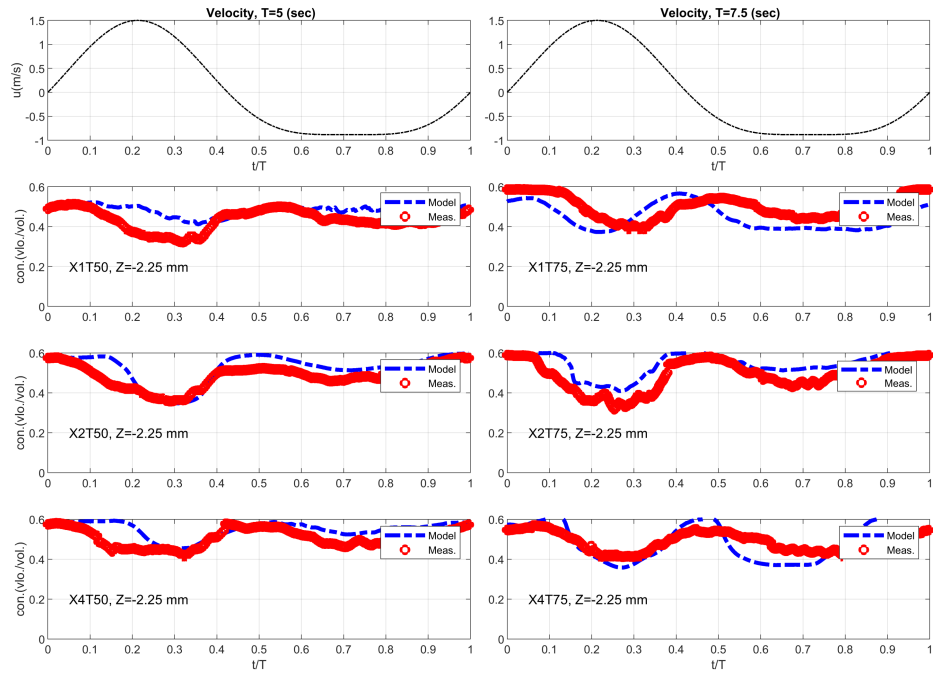
Figure 4.28: Phase-averaged concentration time series of measurements (red points) in comparison with model results (broken lines) for pick-up layer at the bed level of -2.25 mm.
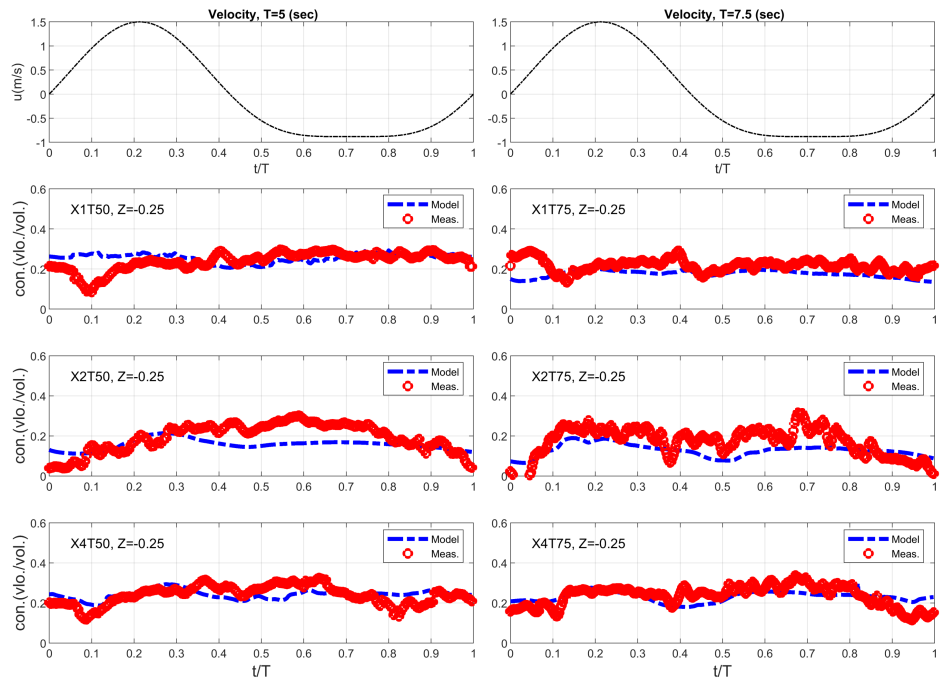
Figure 4.29: Phase-averaged concentration time series of measurements (red points) in comparison with model results (broken lines) close to the undisturbed bed level at z=-0.25 mm.
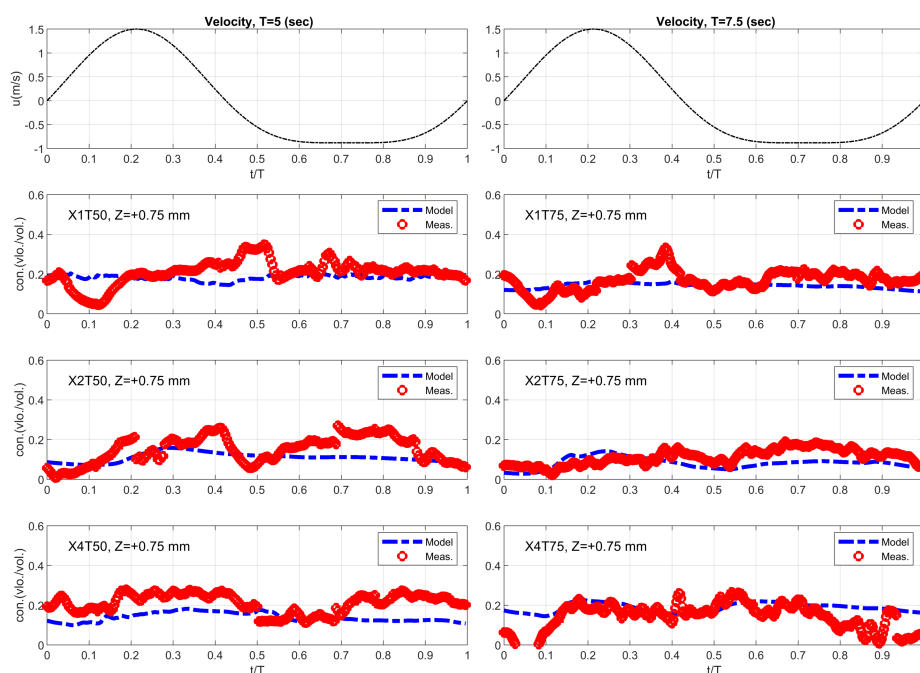
Figure 4.30: Phase-averaged concentration time series of measurements (red points) in comparison with model results (broken lines) above the undisturbed bed level at z=+0.75 mm.

This can be explained by the high percentages of the fine sand in the cases of Mix1 (60%) and Mix4 (50%) compared to the Mix2 (20%).

The reduction of the concentration corresponding to the maximum flow velocity illustrates the entrainment of sediments to higher levels, which is happened within the accelerated flow velocity from 0 to $t/T < 0.3$. During the deceleration time window $(0.3 \leq t/T < 0.6)$ the concentration is increased to the situation before erosion. This mechanism is repeated at the trough-half-cycle with smaller gradient. The model can capture this concentration reduction and increment for both of flow velocity periods.

It should be noted that single phase models are not able neither for uniform sands nor for mixed sands predict the sediment concentration below the initial bed level and to estimate the concentration close to the bed, they apply the empirical formulas, which is denoted as c_0 (e.g. formula of Engelund and Fredsoe, 1976 (Fredsøe, Deigaard, et al., 1992)).

Fig. 4.29 compares the time series of mixed sand concentration for different cases from O'Donoghue and Wright (2004a) with measurements close to the undisturbed bed elevation. As can be seen, the model results can reproduce the measurements, however, the predicted concentration for the case of X2 with lower fine sand fraction compared to other mixed sands is slightly under-predicted, particularly close to the flow reversal time step.

The reason for this is conducted to the constant reduction value (B) which was applied for calibration of the developed model. The B=0.09 produces good agreement for the other cases, but for the case of Mix2 leads to under-predicted results. Moreover, the strong concentration reduction at the beginning of the concentration time series of the measurements for the case of Mix1 is not reproduced with the model.

One reason for this behavior is the stronger unsteadiness effect of the case Mix1 with the higher fine sand fraction (60%) during the measurements, which is not reproduced by the model. In general, the model can reproduce the order of the sediment concentration for

the mixed sands, even though, the time dependent fluctuations are not well reproduced. Fig. 4.30 presents the model results for the mixed sands of the O'Donoghue and Wright (2004a) cases at the elevation of 0.75 mm above the undisturbed bed level. The model predicts the averaged concentrations reasonably, however, the extreme changes of the sand concentrations close to the flow reversal time step are not captured.

The strong reduction of the concentration at the acceleration time window of the case Mix1 can be explained through the higher SFLT in measurements compared to the model, where the high concentrated sand layer over the undisturbed bed leads to a behavior like the pick-up layer for the concentration time series. This can be clearly observed in Fig. 4.24, where the predicted results for SFLT at this time window are over-predicted.

Conclusion

- A new solver, mixedSedFoam, was developed which can successfully model the transport of mixed sands. To the best knowledge of the author, there is not yet a two-phase model, which can simulate the transport of mixed sands under sheet flow conditions. The developed model was calibrated and validated using the measurements of O'Donoghue and Wright (2004a) for mixed sands.
- A new interparticle drag force coefficient was developed which can better than the available formula of Syamlal (1987) represent the particle-particle drag force under sheet flow condition. However, the application of this new drag formula and comparison the model results in two conditions (i.e. with the Syamlal (1987) formula and with the new developed formula in this thesis) is beyond of this thesis and is recommended for future investigations on mixed sands.
- The new formulation for the phase equation of each fraction is another new developed part of this thesis which extends the proposed approach of Manninen et al. (1996) for solving the equation system of velocities and phases of sand fractions. Moreover, the final total sediment concentration is calculated by means of the summation of solved sand fractions concentrations, which distinguishes the solution of the developed solver with the former sedFoam of Cheng and Hsu (2014).
- The model results for the sand fractions concentrations in mixed sand transport are helpful tools to understand the behavior of different sand fractions, when they are in a mixture compared to a uniform condition. Therefore, the new development to include the grain-grain interactions in this thesis provides a numerically efficient approach compared to a computationally expensive multi-phase approach to reproduce the fractional sand transport concentrations.
- The main limitation of the developed model is the underestimation of the sand concentration in flow reversal, which caused due to the deficiencies of the turbulence model. This leads to the higher flow velocities in the numerical results in comparison to the measurements and finally smaller SFLT than the measurements, deeper erosion depth and finally lower concentration of sands at the flow reversal point of the time series of flow velocity.
- The time-step of the run examples are smaller than 0.0002 s and this cause to almost expensive computations. Parallel computation of test cases using open-mpi property of OpenFOAM is possible, however, based on the recommendation of Dr. Cheng, the results of the parallel computations were not comparable with measurements, and therefore, the developed solver in this thesis is also possible

to run using multi processors, but what are presented here are the results run using a single task computation.

- The developed equation to calculate the SFLT (Eq. 3.45) based on the gathered data in chapter 3, can represent the model results well in comparison with the formula of Dohmen-Janssen (1999). Therefore, the application of the developed formula for SFLT is recommended for computations the sand transport rate in large scale models. The performed comparison of the SANTOSS (Van der A et al., 2013) formula in Delft3D-FLOW with the GWK experiment results for bi-modal mixed sands by Van der Werf et al. (2019) revealed the incapability of the SANTOSS(Van der A et al., 2013) formula for mixed sand transport rate prediction under sheet flow conditions. Application of the new developed formula in this thesis in Delft3D-FLOW or XBeach and comparison the model results with the measurements can be performed in future investigations for the mixed sands.

5   Systematic parameter study

To understand the behavior of mixed sands by changing the constitutive fractions a systematic parameter study is performed. To this end, a bimodal mixed sand composed of different proportions of uniform fine and coarse sands is introduced to the developed model and the results are discussed. The hydrodynamic forcing is a skewed velocity water wave with the period of 5 s, which was already applied by O'Donoghue and Wright (2004b) at AOFT and used in the previous chapter to calibrate and validate the developed model.

The following numerical experiments for a bimodal mixed sand can reveal the mixed sand transport rate under sheet flow condition when the constituting fractions percentages change, and hence show the applicability of the developed model to find an optimum mixture of sand fractions to minimize the erosion of mixed sand under sheet flow inducing conditions such as storm surges. A typical example in coastal engineering for a bimodal mixed sand is the mixture of the native and nourished sand in a (re)nourishment practice. Therefore, this chapter can show how the model provides numerical information for a bimodal mixed sand under sheet flow conditions.

5.1   Studied mixed sands

Tab. 5.1 outlines the studied mixed sands grain size properties composed of the uniform fine and coarse sand fractions applied by O'Donoghue and Wright (2004b). The grain sizes in Tab. 5.1 are the interpolated grain sizes from the applied uniform and mixed sands by O'Donoghue and Wright (2004b). Due to the relationship between GI of mixed sands with the constituting fine fraction percentage, it was followed an predictive equation. Fig. 5.1 shows the relationship between GI and fine fraction. As can be seen, based on the generated mixed sands, the GI has not a uniform relationship with fine fraction proportion, but has a conditional. This condition in Fig. 5.1 is fine fraction of 50%, which divides the mixed sands into two groups. The first group with the fine fractions smaller than 50% has a parabolic relationship with a minimum, whereas that of greater than 50 % a parabolic with a maximum. Moreover, it can be seen that a parabolic equation could well represent the GI for these mixed sands with a mixture of two fractions.

Further, based on these mixed sands, the mixtures with the fine fractions between 40% and 75% show a greater GI than the proposed value 4 ($GI > 4$), and hence could be classified as well-graded sands, whereas the mixed sands composed of other proportions could behave like uniform/poorly-graded sands.

The main idea behind the parameter study is to understand, how the fine fraction percentage changes the mixed sand transport and corresponding vertical concentration profiles as well as SFLT. To this end, the calibrated and validated numerical tool developed in this thesis is run with proposed fractions in Tab. 5.1 and the detailed concentrations within sheet flow layer are discussed.

However, this parameter study is a numerical data comparison and for further validation requires the experiments with these proposed sand compositions.

Table 5.1: Fractional sands percentages with their grain size characteristics.

$Testcase$	$\%F - \%C$	$d_{10}(mm)$	$d_{50}(mm)$	$d_{90}(mm)$
2080	20-80	0.26	0.42	0.64
3070	30-70	0.21	0.37	0.63
4060	40-60	0.16	0.33	0.62
5050	50-50	0.11	0.28	0.61
6040	60-40	0.11	0.25	0.53
7030	70-30	0.11	0.23	0.46
8020	80-20	0.10	0.20	0.38
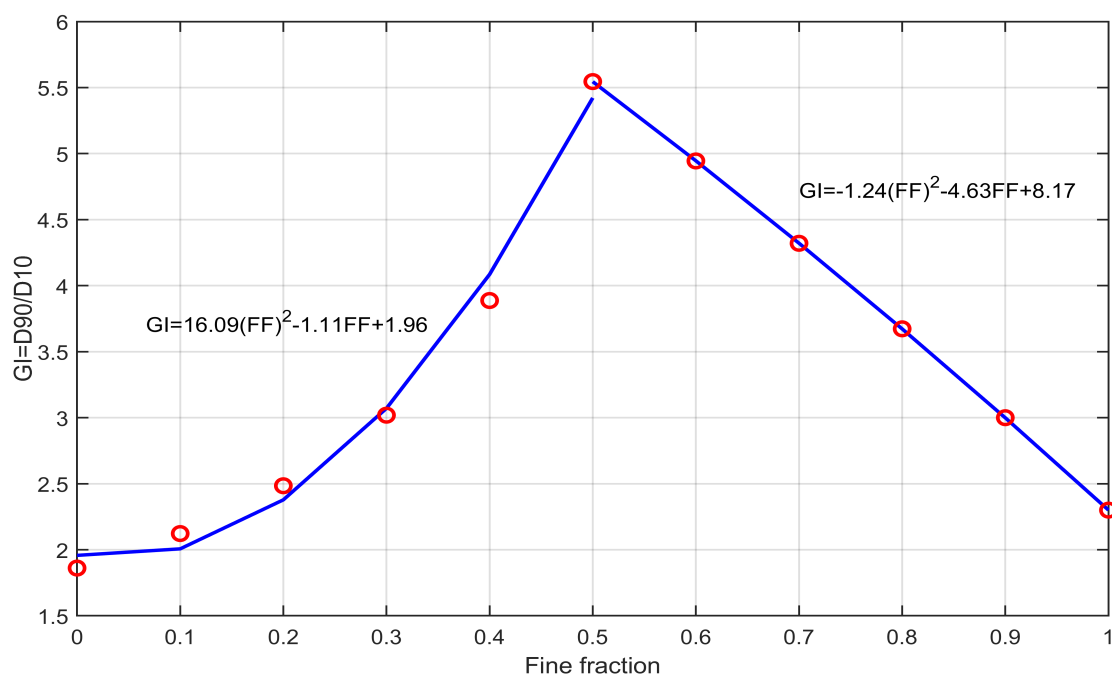
Figure 5.1: GI(D_{90}/D_{10}) and the fine fraction percentage for studied mixed sands in parameter study.

5.2 Vertical concentration profiles

Fig. 5.2 shows the vertical concentration profile for the proposed mixed sands in Tab. 5.1 at the corresponding phases shown at the velocity time series. As is evident, there is a fundamental difference between the vertical concentration profiles of the mixed sand with 50% fine and 50 % coarse fraction with other mixed sands. The vertical concentration profile of the mixed sands with higher percentage of the coarse fraction shows a deeper elevation for the same concentration compared to all mixed sands. It can be explained through this hypothesis that in a mixed sand with dominant proportion of coarse fraction (e.g. in 2080 that the coarse fraction proportion is four times of fine fraction), the heterogeneity is so high, that the fine fractions are not able to be hidden among the coarse fraction and therefore they are transported easier than the coarse fraction, which leads to the subsidence of the coarse fraction after erosion of fine fraction.
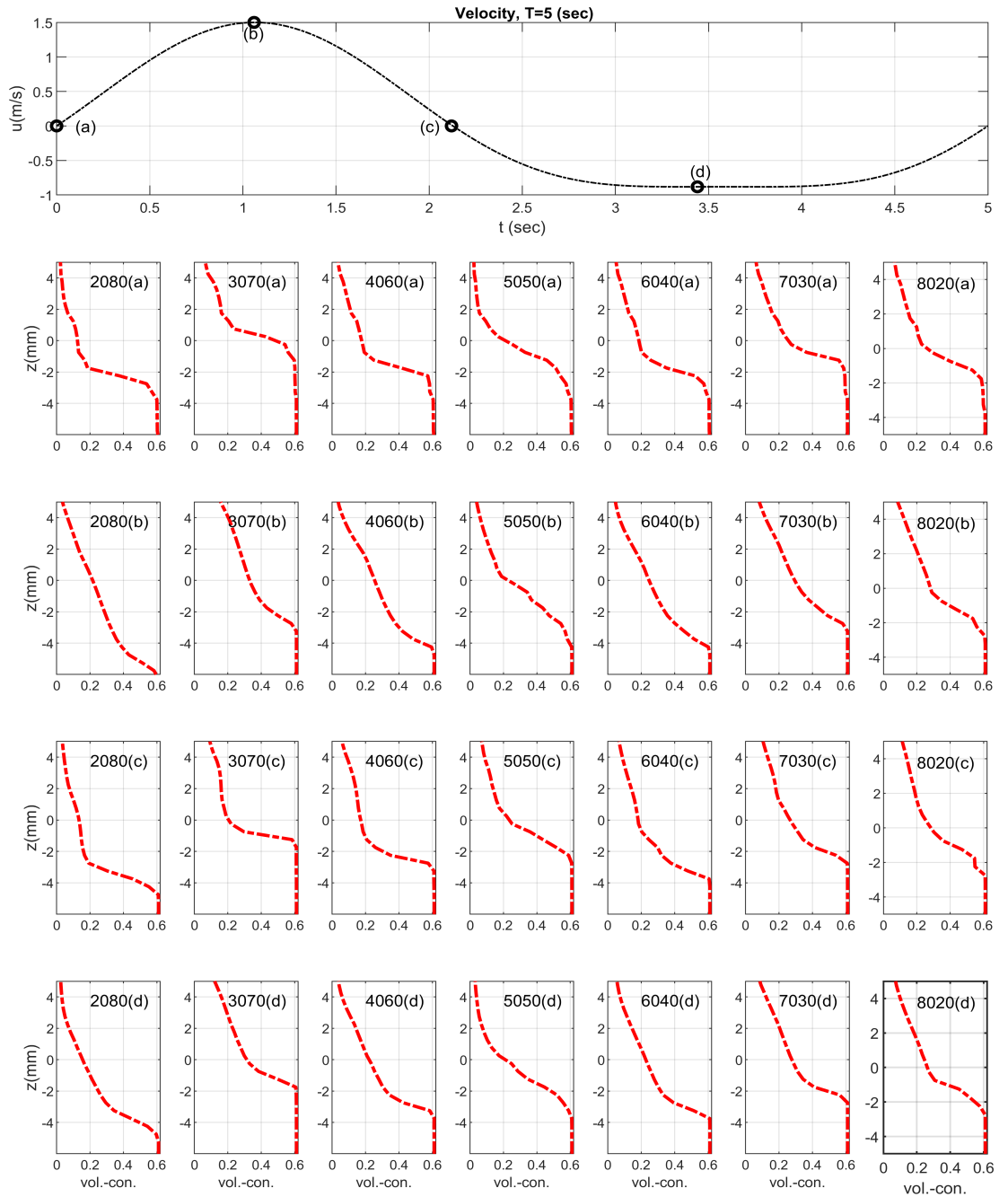
Figure 5.2: Vertical concentration profiles at the corresponding phases of the velocity time series for the studied mixed sands in Tab. 5.1 (first two digits on the top of each figure depict the percentage of the fine sand fraction and the latter the coarse).

This hypothesis is consistent with the fractional vertical concentration profiles for the fine and coarse fractions in Fig. 4.19 and Fig. 4.21, respectively. Therefore, it can be concluded that using always the large volume of the coarse fraction compared to the fine fraction cannot progress a better sustainable and stable sand beach after (re)nourishment of eroded sandy beaches under storm conditions. However, as was mentioned, these numerical results are from the numerical experiments and further physical experimental studies are required

to approve/improve this hypothesis.

This falling elevation of the vertical concentration profile is more enhanced at the maximum velocity phase for all mixed sands studied in this thesis. The concentration at different elevations of the sheet flow layer are greater at the phase of maximum velocity for the case of 2080 compared to other phases. This is more enhanced for the fine fraction, where the concentration within $1\ mm < z < -3\ mm$ is uniform (Fig. 5.3), whereas for the coarse fraction it is not uniform along the vertical elevation within this part of the sheet flow layer. Therefore, it can be concluded that the fine fraction of the case of 2080 are present with their maximum concentration along a longer height, in contrast to the coarse fraction, for which the concentration decreases towards the outer part of the sheet flow layer (Fig. 5.4). This fractional concentration is reduced in corresponding elevations for the coarse fraction of the case 2080, whereas the reduction for fine fraction is considerably low. This is consistent with this explanation that the fine fraction due to its light weight in a mixed sand with dominant coarse fraction is most likely entrained to higher elevations and due to the dominance of coarse fraction, they cannot hide among coarse fractions. Finally, based on this parameter study, the fine fraction is more entrained and transported within a mixed sand with dominant percentage of the coarse fraction.

At the phase of flow reversal, the vertical concentration profile of the coarse and fine fractions in Fig. 5.3 and Fig. 5.4 show that the concentrations reach their maximum at the elevation of around $z = -4\ mm$. However, just above of this elevation the fine fraction is present for a longer height with a greater proportion of its maximum concentration compared to the coarse fraction concentration at corresponding elevations.

This enhanced entrainment of the fine fraction in the case of 2080 does not change significantly at the phase of minimum velocity compared to the maximum and flow reversal phases. This points out that in the case of 2080, the fine fraction participates with its maximum proportion in this mixed sand transport. In contrast, the coarse fraction concentration varies considerably within maximum, flow reversal and minimum phases of the flow velocity. These show that in this case, the hiding/exposure is not strongly influencing the fine fraction and the general behavior of the constituting fractions is similar to the case of uniform sands. This behavior is generally acceptable and reasonable, because of the small value of GI (GI=2.5) for the case of 2080, as is evident in Fig. 5.1.

The second column in Fig. 5.2 shows the vertical concentration profile at the corresponding phases of the velocity time series for the mixed sand of 3070 (30% fine and 70 % coarse fraction). It is shown that the sediment concentration reduces with ongoing time, but this is not as considerable as the case of 2080. The concentration reaches its maximum at the elevation of around $z = -3\ mm$ in 2080 compared to the $z = -1\ mm$ in 3070 at initial phase. Considering the fractional concentration of fine and coarse fractions in Fig. 5.3 and 5.4 this elevation is the same for both fractions, however, the fine fraction is present with higher percentage of its maximum fractional concentration at elevations just above the bed. Moreover, the sediment concentration gradient is higher than in the case of 2080 at the phase of maximum velocity. This can be explained through the reduction of the coarse fraction contribution in this case, which in turn, improves the hiding property for the fine fraction. Consequently, the elevation of the maximum concentration is higher than in the case of 2080.

The concentration of the coarse fraction is increased in the case of 3070 compared to the case of 2080 at the corresponding elevations above the point of maximum concentration, whereas the percentage of the constituting coarse fraction in the case of 3070 is lower than the case of 2080. This increasing in the concentration of the coarse fraction and hence

decreasing in the concentration of the fine fraction, is the consequence of hiding/exposure effect, which is pronounced by increasing the grading ($GI = 3$) in the case of 3070 compared to the ($GI = 2.5$) in the case of 2080.
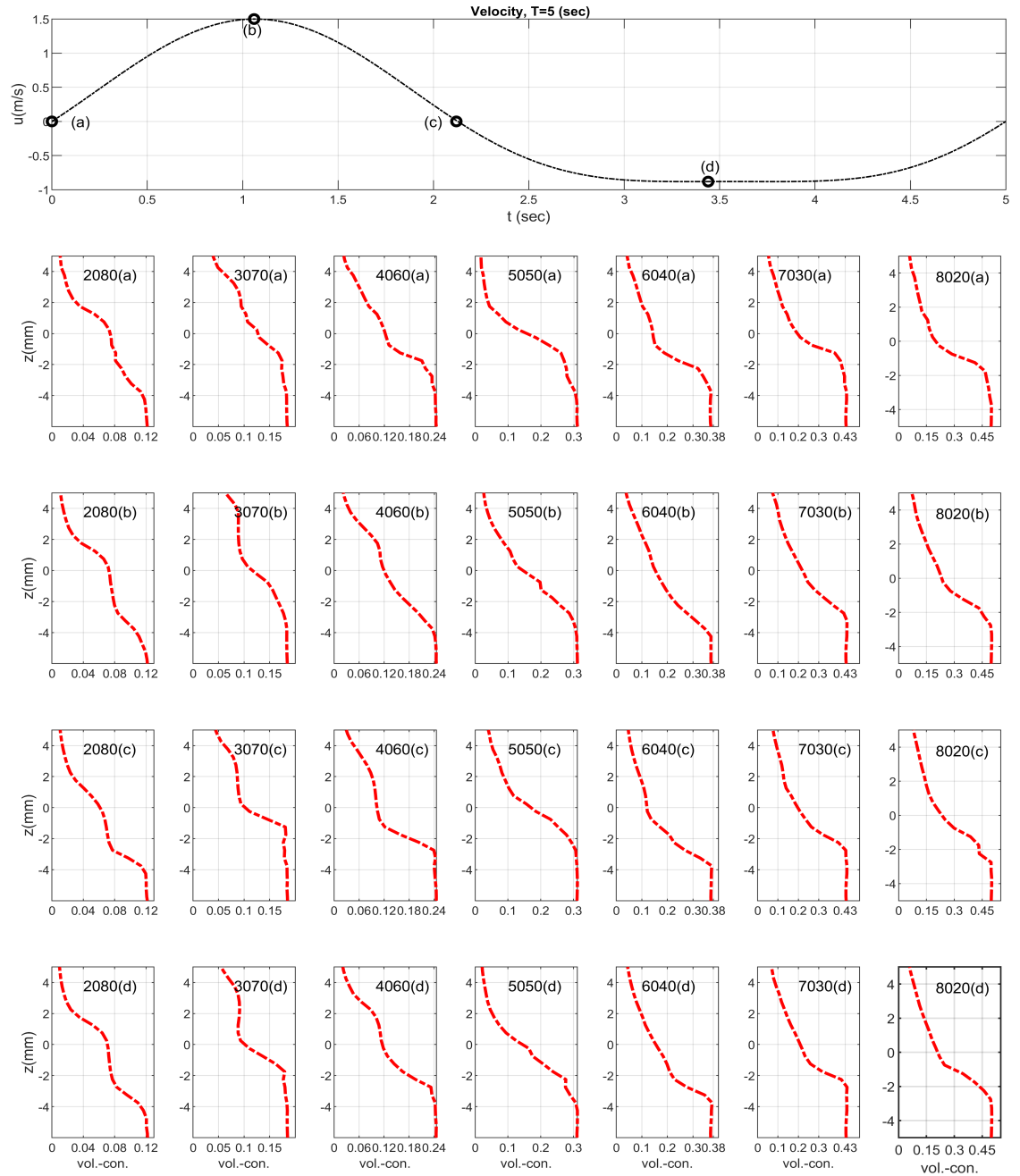
Figure 5.3: Vertical concentration profiles at the corresponding phases of the velocity time series for the fine fraction of the studied mixed sands.

Moreover, at the phase of flow reversal both of the constituting fractions of 3070 and hence the mixed sand are located in a higher elevation for the maximum concentration compared to the case of 2080. This can point out to the fact that in a mixed sand with higher grading

and not a higher percentage of the coarse fraction, the mixture can better resist against the transport under sheet flow condition. Therefore, in a beach (re)nourishment the degree of the grading is the most important parameter to preserve the beach under a hydrodynamic condition with the dominant sheet flow transport rate in comparison with the increasing the percentage of the coarse fraction. On the other hand, a coarse beach compared to a smooth and pleasant fine sand can decrease the interest of the tourists to visit the beach, but this is not the matter of this thesis and required further research.

At the flow reversal phase, the case of 3070 produces smaller concentrations at the elevations above the erosion depth compared to the phase of the maximum flow velocity. This behavior is like the case of 2080, however, the concentration gradient is greater than the case of 2080, which denotes that the presence of sands in this case at the higher levels above the erosion depth are lower than the case of 2080. Moreover, in both cases the concentration gradient is higher for the coarse fraction, which means the fine fraction is with higher percentage of its maximum concentration present at the elevations above the erosion depth compared to the coarse fraction.

At the phase of minimum velocity in the case of 3070 both fine and coarse fractions show a higher concentration at the corresponding elevations compared to the flow reversal phase but the growth rate of concentration is higher for the coarse fraction than fine. That can be explained by the settling back of the coarse fraction at the phase of the flow reversal compared to the entrainment at the minimum flow velocity phase, whereas due to the light weight of the fine fraction this is not as pronounced as coarse fraction. The level of the maximum sand concentration at the phase of minimum flow velocity is slightly higher than that at the maximum velocity phase. This can be explained by the higher velocity of the skewed waves at the crest compared to the trough, which leads to higher erosion rate at the maximum velocity phase.

The third column in Fig. 5.2 shows the vertical profile of the concentration profile for the case of 4060. The concentration at the corresponding elevations at the phase of maximum velocity are smaller than the case of 3070. However, the vertical concentration profile at the starting phase (4060(a)) has a lower elevation for the maximum concentration. This phase of the case of 4060 is similar to the case 2080, however, the erosion at the phase of maximum velocity is lower than the case of 2080 at the corresponding elevations, where the elevation of the maximum concentration positioned at $z = -4\ mm$ for the case of 4060. Considering the fractional vertical concentration profile of the constituting fractions for the case of 4060, the fine fraction concentration profile has a higher gradient than the cases of 2080(b) and 3070(b). This is consistent with the smaller entrainment of the fine fraction when the grading and consequently hiding/exposure effect is pronounced. The grading in the case of 4060 is around 4 (Fig. 5.1), which classifies this mixed sand as roughly well graded sand.

The fourth column in Fig. 5.2 shows the vertical concentration profile for the case of equal proportions of fine and coarse fractions. As is evident, the concentration profile evolves gently than other mixed sands in all phases. The concentration profile has a deflection point compared to other vertical concentration profiles and the mixed sand shows a stable condition in terms of the elevation of the maximum concentration. This could be inherent in the GI of the case 5050 in Fig. 5.1, which has the maximum GI among other mixed sands with $GI = 5.5$ and therefore is classified as a well-graded sand.
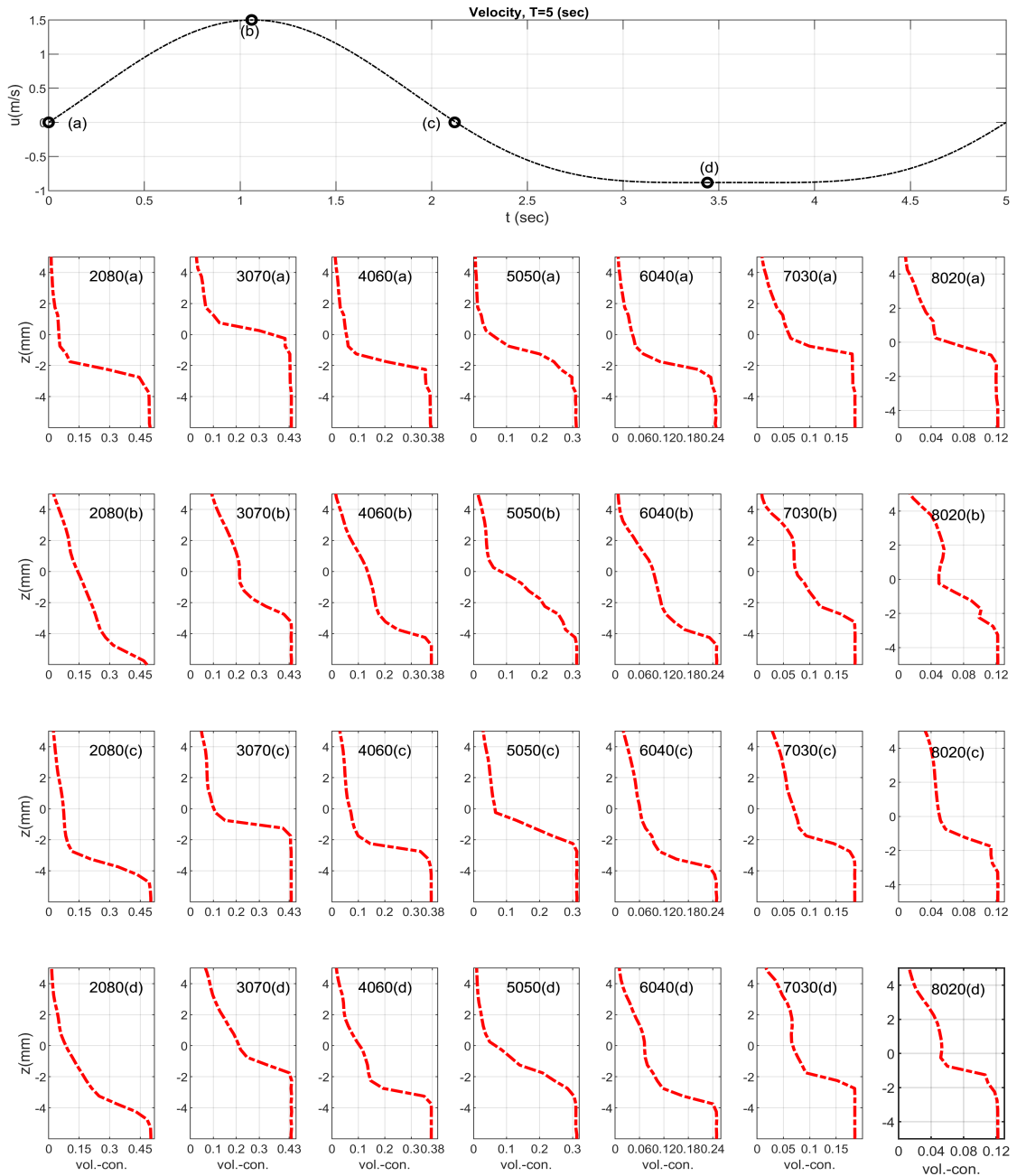
Figure 5.4: Vertical concentration profiles at the corresponding phases of the velocity time series for the coarse fraction of the studied mixed sands.

By increasing the fine fraction proportion in other mixed sands after the case of 5050, the coarse fraction shows a vertical concentration profile with higher concentration compared to its maximum concentration at the elevations above of the maximum concentration elevation, which is consistent with the hiding of the fine fraction and pronounced exposure of the coarse fraction. This was also observed in the case of X1 with the 60% of fine sand and 10% of the coarse sand. The vertical concentration profile of the coarse fraction in the case of 8020 at the phase of maximum velocity shows clearly the pronounced entrainment of the coarse fraction, where a high concentration of the coarse fraction is present in a

greater length of the sheet flow layer compared to other cases of mixed sands.

5.3   Sheet flow layer thickness (SFLT)

Fig. 5.5 shows the model results for the SFLT and erosion depth of the mixed sands composed of different fine and coarse fractions proportions compared to the predictions of the SANTOSS (2013) formula and the proposed modification in this thesis. As can be seen, the SFLT by increasing the fine fraction from 20% to 30% is slightly increased, whereas the 20% fine sand case experiences higher erosion depth. The maximum SFLT of the latter is 9.33 mm in Tab. 5.2 and that for the case of 30% fine material is 10 mm. However, the maximum erosion depth for the case of 20% fine sand is 7.17 mm, which is about two times greater than the case with 30% fine material. This can be explained by means of the lower GI of the case with 20% fine sand compared to the case of 30% fine sand. Moreover, in all mixed sands the maximum erosion depth is occurred with a phase-delay after the phase of the maximum velocity. As is also evident in Tab. 5.2, the maximum SFLT is increased from the case of 2080 to the case of 3070 but after that decreased, when the fine fraction proportion increased. This points out that not only the fine fraction proportion, but also the degree of grading (GI) is determining the SFLT.

Furthermore, the case of 5050 has the minimum SFLT compared to all cases. This is consistent with the grading index of the case of 5050, which is the maximum among other mixed sands. The SFLT involves a thicker and more uniform form by increasing the fine fraction proportion. As can be seen in Fig. 5.5, the SFLT in the cases of 8020, 7030, and 6040 shows a more uniform and thicker layer at all times, whereas for smaller fractions of the fine fraction in the mixture (cases of 2080 to 5050) the SFLT close to the phase of the maximum velocity is thicker than other phases. This can be explained through higher entrainment rate of the fine fractions compared to the coarse fraction at this phase.

In addition, the mobility number for the cases with larger fractions of the coarse fraction in Tab. 5.2 is smaller than the cases with higher percentages of the fine fraction. Therefore, the sheet flow transport regime can be more present for the cases with higher percentage of the fine fraction. This is consistent with the maximum Shields parameter, which is increasing by enlargement the proportion of fine fraction.

The predicted SFLT by means of the SANTOSS (2013) formula as well as the proposed formula in this thesis are also illustrated in Fig. 5.5. As can be seen, the proposed formulation predicts the higher SFLT for the cases with $GI \geq 4$ as well as higher percentages of fine fraction (in these mixed sands for fine fractions $\geq 50\%$). However, for the cases with lower proportion of the fine fraction as well as smaller GI, the predicted SFLT for both crest and troughs are similar to the predictions of the SANTOSS (2013) formula. Besides, the predicted SFLT by the proposed formulation for the well-graded cases as well as the cases with high percentages of fine sands is more pronounced at the crest half-cycle than trough. The explanation for this is the higher crest velocity than trough for the applied skewed velocity.
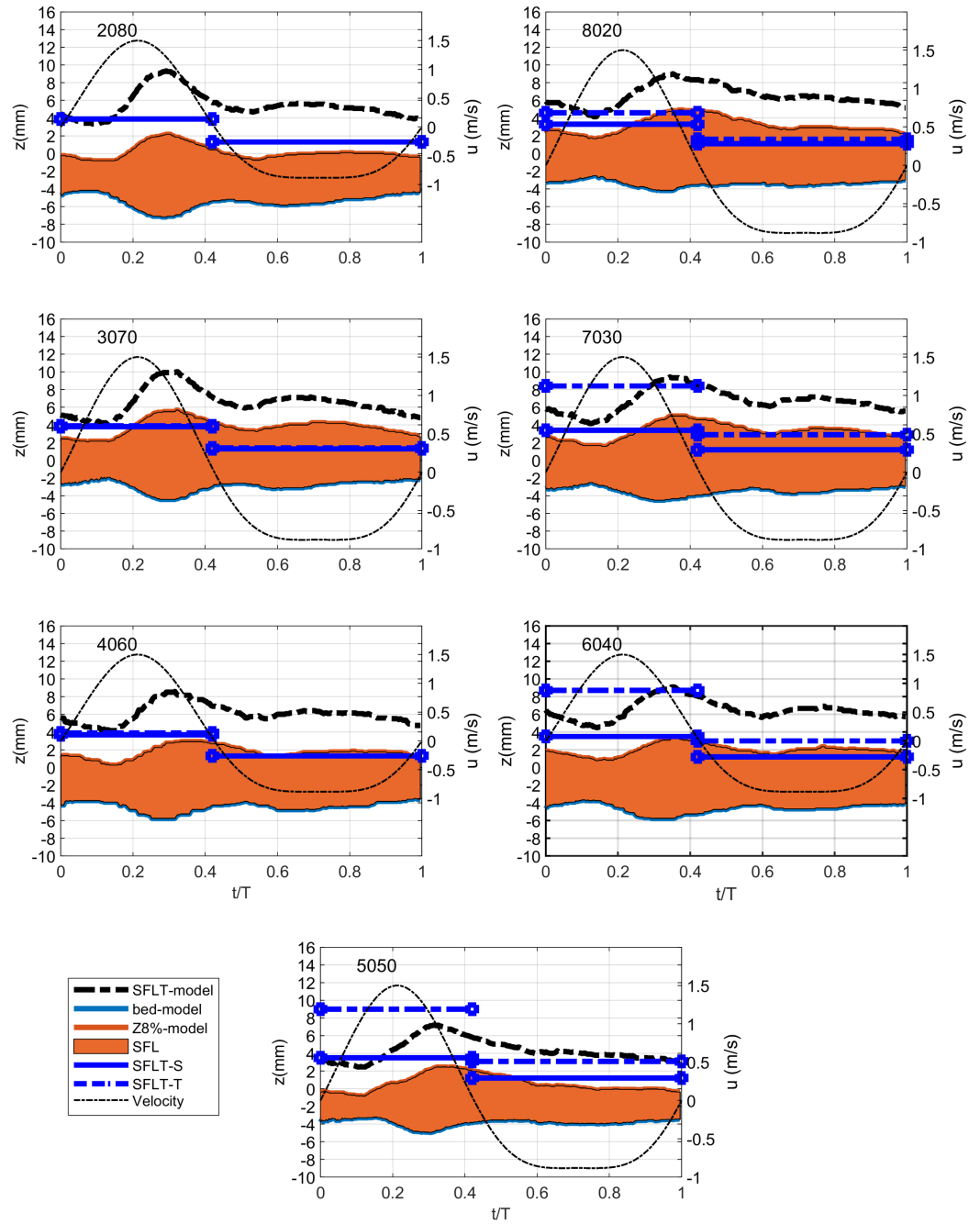
Figure 5.5: Time series of the model results for the SFLT (broken black), erosion depth (the lowest line), the predicted SFLT by means of the SANTOSS (2013) formula (solid blue) and the proposed modification in this thesis (broken blue).

Table 5.2: Predicted orbital excursion amplitude (A), maximum velocity (u_{max}), root mean square velocity (u_{rms}), maximum Shields parameter (θ_m), maximum mobility number (ψ_m), maximum erosion depth (δ_{em}), maximum SFLT (δ_{sm}) and net transport rate (q_N).

Test case	D_{50} (mm)	W_s (m/s)	A (m)	u_m (m/s)	u_{rms} (m/s)	θ_m	ψ_m	δ_{em} (mm)	δ_{sm} (mm)	$q_N.10^{-6}$ (m^2s^{-1})
2080	0.418	0.063	1.0	1.59	0.89	1.93	373.74	7.17	9.33	60.52
3070	0.372	0.056	1.03	1.57	0.91	2.04	410.26	4.42	10.0	54.58
4060	0.326	0.049	1.0	1.57	0.90	2.27	469.83	5.75	8.58	48.39
5050	0.260	0.038	1.0	1.64	0.89	2.93	642.72	4.96	7.67	30.98
6040	0.254	0.037	1.0	1.63	0.89	2.93	646.43	5.75	9.08	19.56
7030	0.228	0.032	1.01	1.62	0.90	3.15	712.86	4.50	9.42	7.14
8020	0.202	0.027	1.0	1.61	0.90	3.42	795.77	4.17	9.0	6.35

5.4 Net mixed sand transport rate prediction

Fig. 5.6 shows the predicted net transport rate by means of the SANTOSS (2013) formula as well as the proposed formulation in this thesis (Eq. 3.45). As can be seen, for the cases with lower proportions of the fine fraction as well as poorly graded mixed sands the proposed formulations does not change the predicted values of the SANTOSS (2013) formula, whereas by increasing the fine fraction percentage from 40% the predicted net transport rates by the proposed formulation are smaller than the predicted net transport rate of the SANTOSS (2013) formula. These can be explained by means of the enhancement of the unsteadiness behavior of the fine fractions in the mixed sands, which improves the interchange of the entrained fine sands between crest and trough half-cycles.

Moreover, both of formulations predict a negative net transport rate for the cases with fine fractions larger than 90% and the net transport rate tends to offshore by increasing the fine fraction percentage. The net transport rate for the cases with 70% and 80% fine sand is roughly the same, which can define the 70% of the fine fraction as the lower limit for the mixed sand transport, where the net transport rate is just 7.14×10^{-6} (m^2s^{-1}) for the case of 70% fine sand and 6.35×10^{-6} (m^2s^{-1}) for the case of 80% fine sand. The case of 5050 could be termed as the optimized mixed sand compared to other cases, where the SFLT is reduced and after that by increasing the fine proportions is increased. However, the cases of 7030 to 9010 produce a net transport rate close to the balanced condition between erosion and sedimentation. Therefore, for a beach (re)nourishment with a final sand grain size distribution like the case of 7030, under the hydrodynamic condition with the dominant skewed wave of experimental measurements of O'Donoghue and Wright (2004a), the cases with $70\% < FP < 90\%$ could be resulted in a sustainable beach with a small sedimentation ($q_s < 7.14 \times 10^{-6}$ (m^2s^{-1})) and no erosion problem. As a practical example for a bimodal mixed sand in nature, the final mixed sand composed of the original sand of beach before (re)nourishment and the transported sand from borrow could be representative to understand the importance of mixed sand transport mechanisms. It shows that the developed model in this thesis is capable of simulating the detailed contributing transport parameters as was described in Tab. 5.2, and hence could be applied as a practical tool in beach nourishment practices to evaluate the transport behavior of final mixed sand after (re)nourishment under future storms. To know the proportion of the fine
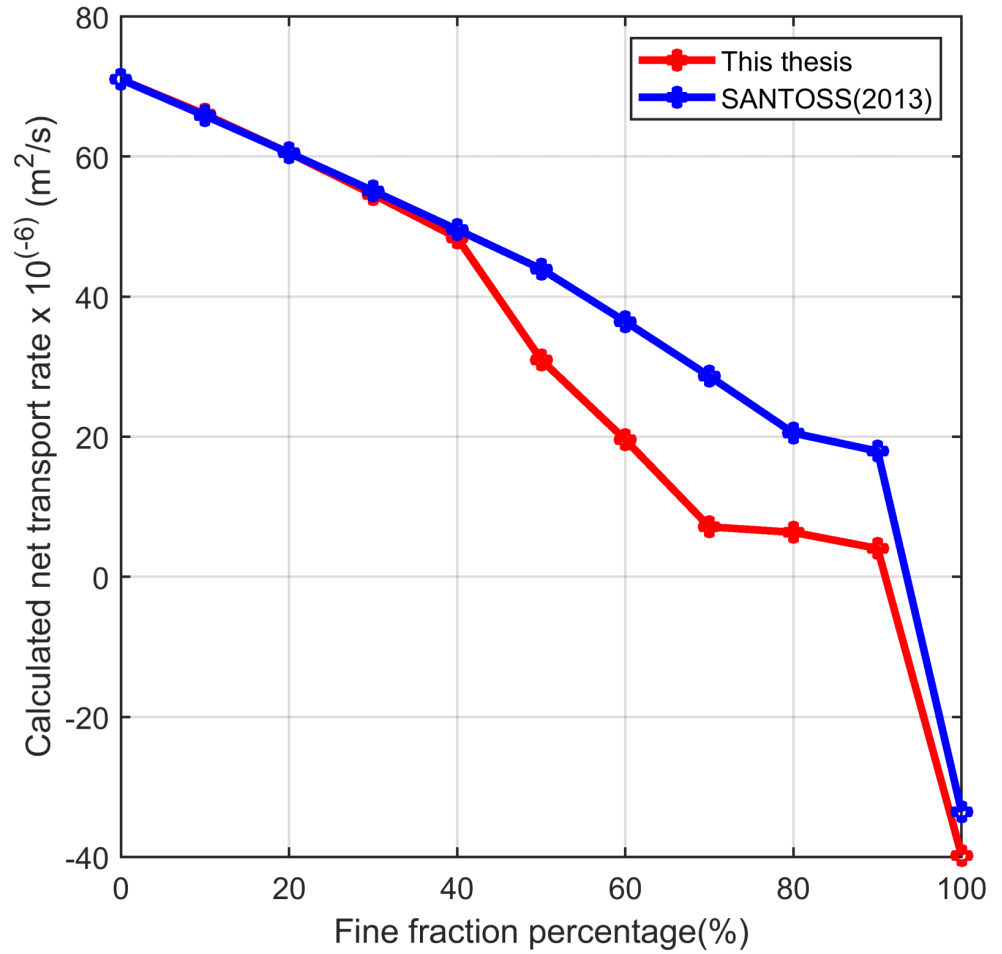
Figure 5.6: Predicted net transport rates for the mixed sands by means of the SANTOSS (2013) formula (solid blue) and the proposed formulation for SFLT in this thesis(solid red) for different fine fractions in a bimodal mixed sand.

and coarse fractions in the net transport of the mixed sands, Fig. 5.7 and Fig. 5.8 show the net transport rate for the fine and coarse fractions, respectively. As is evident in Fig. 5.7, both formulations predict an offshore transport of fine fraction. However, the proposed formulation enhances the offshore transport of fine fractions for the cases with fine fraction proportion greater than 40 % . This could be explained through the higher SFLT applied in the developed net transport equation (Eq. 3.45), and therefore higher exchange rate between half-cycles compared to the original SANTOSS (2013) formula. However, this offshore transport rate gradient is decreased for the cases with fine fractions greater than 70%. This can also be explained by means of the GI, where cases with the fine percentages greater than 70% are not well-graded sands (Fig. 5.1).

Fig. 5.8 shows the same prediction net transport rates for the coarse fraction by means of the SANTOSS (2013) as well as the proposed formulation in this thesis. Therefore, the proposed formulation changes the net transport rate of the fine fraction by enhancement the interchange of entrained fine sands within both crest and trough half-cycles. This enhancement is increased by increasing the grading index ($GI = D_{90}/D_{10}$) and decreased by values < 4. However, the presented and discussed results in this parameter study are

only numerical experiments and to prove their validity, performing the physical experiments under discussed hydrodynamic as well as mixed sand conditions are required.   As can be
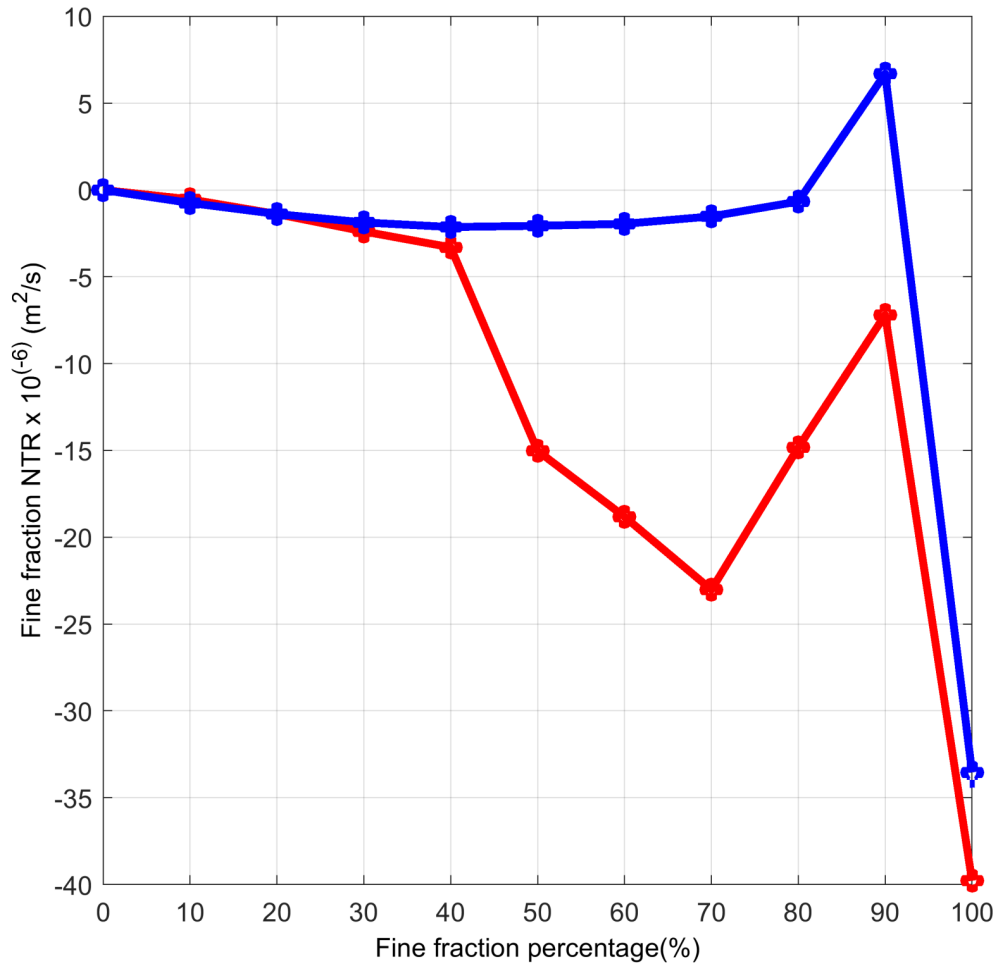
Figure 5.7: Predicted net transport rate of the fine fraction for the studied mixed sands by means of the SANTOSS (2013) formula (solid blue) as well as proposed formulation in this thesis (solid red).

seen in Fig. 5.8, the net transport rate of the coarse fraction tends to offshore by increasing the fine fraction proportion, which is consistent with the enhanced offshore transport of the coarse fraction by increasing the fine fraction in a mixed sand compared to a uniform coarse sand. It should be noted, that the transport rate is the net transport rate, which means the sum of the transport rates within both half-cycles as well as the interchanged sands, as was formulated in the SANTOSS (2013) formula. Therefore, the net transport rate of the coarse fraction to offshore is increased by increasing the fine fraction proportion.
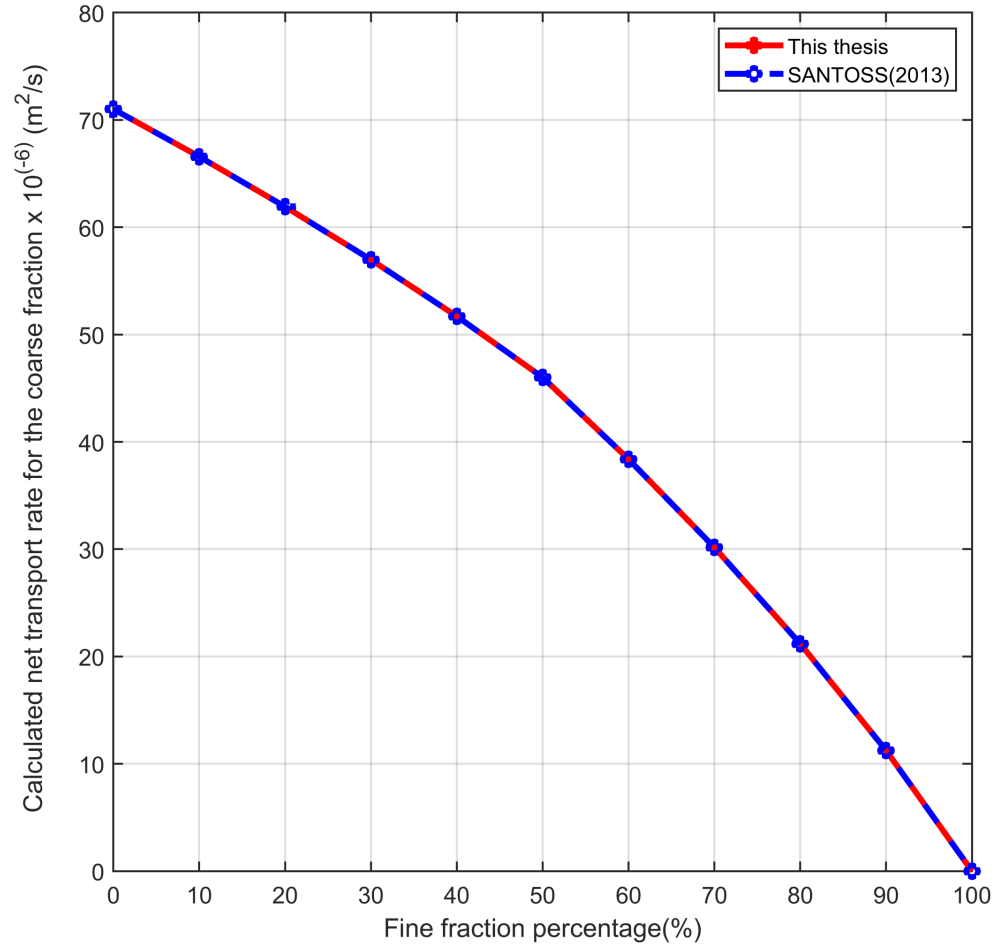
Figure 5.8: Predicted net transport rate of the coarse fraction for the studied mixed sands by means of the SANTOSS (2013) formula (solid blue) as well as proposed formulation in this thesis (solid red is hidden under blue).

Conclusion

- The developed and validated model for mixed sand transport in the previous chapter was applied to understand the mixed sand transport mechanisms by increasing the fine fraction contribution under sheet flow in different bimodal mixtures. The model produces reasonable results based on the explanations achieved for the mixed sands behavior within validation cases. However, without physical experiments and comparison the numerical results presented in this chapter with them, it is far to conclude the model results as simulating the natural/physical processes. Therefore, performance/analysis of the test cases with the similar proportions of sand fractions as well as hydrodynamic forcing are required for future studies.
- Based on the numerical experiments in this chapter, the behavior of SFLT for bimodal mixed sands shows that the increasing of the coarse fraction proportion

in a mixed sand does not always lead to a lower total net transport rate. For the test case of 2080 (i.e. 20% fine and 80% coarse sand fractions) the results show deeper erosion depth and presence of fine fraction with its proportion close to its maximum concentration at all levels. Therefore, increasing the coarse fraction in a beach modification within (re)nourishment dose not mean improvement of and retrofitting of beach against next storm, in contrast, it could be resulted in enhancement of the fine fraction erosion and coarse fraction retention.Moreover, using a large volume of coarse uniform sand for (re)nourishment could be resulted in coarsening of the beach as well as higher costs to compensate this fraction and provide a pleasant beach.

- This numerical study shows that the grading index ($GI = D_{90}/D_{10}$) is an important parameter in improvement of a mixed sand stability against the erosion under sheet flow conditions. By increasing the GI of a mixed sand, it means we have a beach with a wide range of sand grain size distribution with a gentle s-curve, the transport rate is decreased as was depicted in this chapter by smaller erosion depth and gentle concentration profiles for both fine and coarse fractions. Because the proportion of coarse fraction in a mixed sand is not as high as uniform coarse sand, and hence in a mixed sand there is enough porosity between coarse fraction grains, where finer fractions could be hidden and reduce the erosion depth. However, the porosity parameter is not defined within the transport equations explicitly and using the maximum volume concentration of 0.635 the porosity of around 0.4 is guaranteed for all studied mixed sand in this research.

- The test case 5050 (i.e. a bimodal mixed sand composed of 50% fine and 50% coarse fractions) behave as the most distinguished test case in terms of the SFLT and concentration profile compared to other test cases. The main reason for this difference is the GI-value of this test case. Because the GI-value is increased for the studied bimodal mixed sand by increasing the coarse fraction proportion to the case 5050 and after that is decreased, in other words, GI of the case 5050 posses the maximum GI, and therefore in contrast to other cases, its concentration profile is a gentle profile and its maximum erosion depth is the minimum among other studied cases.

- Comparison the selective net transport rate for studied cases by means of SAN-TOSS (2013) with the new formula in this thesis, shows that the development in the SFLT formula enhances the unsteadiness of fine sand transport and their offshore transport. However, due to the lack of physical experiments for the studied test cases, it cannot be concluded that the development in this thesis is more promising than the SANTOSS (2013) predictions.

- Increasing the fine fraction percentage in a mixed sand means increasing the erosion rate, which was illustrated by both SANTOSS (2013) and the new developed modification in this thesis. However, the development in this thesis shows a roughly constant transport rate by increasing the fine fraction percentage from 70% to 90%. This means in a bimodal mixed sand by reducing the fine sand fraction from 90% to 70%, the mixed sand mixture does not improve significantly under the same erosion conditions within sheet flow.

6 Conclusions and recommendations

The main objective of this thesis was to improve the understanding of cross-shore mixed sand transport mechanisms under sheet flow conditions. To this end, the available experiments on the mixed sands under sheet flow conditions were gathered and the performance of the developed empirical formulas for the prediction of the net transport rate were studied. Then, the best predictive transport formula was selected for the further research and development. The SANTOSS (2013) formula has performed a better prediction among other formulas, but it was not able to predict the transport rate of the mixed sands with high proportions of fine fraction accurately. The reason for this was found in the applied empirical formula of Dohmen-Janssen (1999) for the prediction of the sheet flow layer thickness (SFLT), which applies the same formula for uniform as well as well-graded mixed sands. Therefore, the development of a new formulation for the SFLT based on the fine fraction as well as the degree of the grading was defined as the main development in this thesis.

Moreover, the empirical formulas are not capable of representing the detailed transport mechanisms of the nonuniform grain-grain interactions from different sand fractions of a mixed sands as well as their mutual interactions with carrier flow. To elucidate these transport mechanisms in detail, development of a high resolution numerical tool within an open source CFD-toolbox OpenFOAM framework was also proposed and performed in this thesis, which is termed as *mixedSedFoam*. The developed model was calibrated and validated by means of the detailed experimental results on the mixed sand under sheet flow condition performed by O'Donoghue and Wright (2004a). The detailed new numerical information about the fractional concentration profiles show the contribution of the grading effect on reducing the net transport rate, which can be applied in practical coastal engineering by (re)nourishment, to optimize the grading of the nourished beach.

Within the development of the new solver, a new formulation for interparticle drag force coefficient was developed. Due to the high attention to the interparticle drag force in KTGF as the dominant force in particle-particle interactions, the development of this new formulation could improve the understanding of particle-particle (grain-grain) interactions within sheet flow layer. The velocity distribution function in the new developed formulation is the well-known Maxwell (1860)-Boltzmann (1872) equation for dense gases. The application of this velocity distribution function for sand grains requires more research. Comparison of the measured sand grains velocity distribution function under skewed/asymmetric waves with the Delta dirac function of Syamlal (1987) or Maxwell (1860)-Boltzmann (1872) in this thesis is an urgent research need, where could change the fundamental equations of KTGF for studying mixed as well as uniform sand transport under sheet flow conditions. This is the most important part of KTGF equations due to the presence of the fluctuation energy of particle system in all (semi-) empirical equations of KTGF.

The new developed phase equation for sand fractions in the mixture approach makes a better coupling of the fractional volume concentrations and velocities with each other as well as with the whole sand phase, which is a new development in this approach, however the simplifying assumptions in the mixture approach to transform the nonlinear differential equation system of momentum transport to an algebraic equation system by neglecting the nonlinear terms is still a challenge to solve.

6.1   Recommendations for future works

The future studies can investigate the role of the applied simplifications in the mixture approach to find their contribution to the final concentrations solution. Moreover, in the momentum equation of sand phase as well as in the fundamental equations of KTGF for momentum exchange in collision between particles, only the linear momentum exchange is considered. The angular momentum equation could also be involved to include the rotation of sand particles, and hence the exchanged angular momentum. This future work can contribute to solve the under-prediction of the developed model for mixed sand concentration at the flow reversal point.

The applied turbulence model in this thesis is k-ϵ and the under-prediction of the model results at the flow reversal point could be originate from the poor performance of this turbulence model in resolving the produced eddies in flow reversal point. Therefore, applying different turbulence approaches, which do a better performance in development of the turbulent eddies to higher elevations is recommended for future works.

The developed model in this thesis can distinguish between the size and density of contributing fractions in a mixture. Therefore, the application of this model for investigation of contamination transport within sand fractions as a mixture composed of sand-contaminates is recommended to study the contaminants distribution and transport in sand layer(e.g. the mixture of microplastic from different polymers of various densities with sand).

Application of the developed solver for mixed sand transport under sheet flow induced by acceleration-asymmetric waves in the swash zone (after breaking waves) is another next practical suggestion for future studies. This importance can be more pronounced because of the significant shallow waters in this region and presence of the sheet flow as the dominant transport mode in swash zone. Moreover, using a wave spectrum instead of the different modes of wave non-linearity (skewness and asymmetry) in the developed model can improve the understanding of the role of an irregular water wave over mixed sands. However, to the knowledge of the author, there is no experimental measurement for mixed sands composed of systematically provided uniform sands under sheet flow induced by irregular waves. Consequently, running the irregular waves in both small and large scale over mixed sands is proposed as an urgent investigation to improve the predicting formulas for sand transport rate. Moreover, performing this investigation could improve the understanding of the role of mixed sands in improvement the sustainability of beach nourishment practices.

The recently published results for the first experiments on mixed sands at the GWK by Van der Werf et al. (2019) show the weak performance of the SANTOSS (2013) formula for prediction the net transport rate of mixed sands under progressive surface waves, in contrast to its good performance to predict the net transport rate for OFT experiments. Application of the new developed formula in this thesis, which improves the prediction accuracy of the SANTOSS (2013) formula for sheet flow conditions, could improve the mixed sand transport rate predictions under progressive surface waves. Therefore, application of the new formula of this thesis and compare the new predicted results with the GWK measurements is highly recommended for future works.

To date, to the knowledge of the author, all detailed two-phase numerical tools for investigating the transport mechanisms of uniform sand use the detailed experimental dataset of O'Donoghue and Wright (2004a) at the AOFT. For the mixed sands, a dataset like that for the conditions with progressive surface waves is considerably required. The performed experiments within Hydralab+(COMPLEX) as well as STENCIL at the GWK are a good start to this end. Moreover, the performed experiments at the GWK were not conducted

with the same detailed experiments of the AOFT. Therefore, the new experiments with the same conditions of the detailed experiments of the AOFT, can help to understand the main differences and quantify the absent but important components of the large wave flumes by transport of the mixed sands such as streaming. The structure and guidelines of the AOFT dataset can also be applied to generate a such detailed dataset from the recently performed experiments at the GWK. This dataset will help to improve the SAN-TOSS (2013) formula with the developed modification in this thesis and understand the transport mechanisms of mixed sands under storm induced sheet flow conditions in large scale flumes. The importance of this development can be understood through the extreme accelerated climate change and induced storms, which in turn cause the high costs of the periodically beach (re)nourishments.

The developed approach in this thesis within the available solver sedFoam, which resulted in the new solver mixedSedFoam, can be applied in the recently published solver sedWave-Foam (Kim et al., 2019) to model the transport rate of mixed sand under progressive surface waves induced sheet flow conditions. Therefore, the application of the new developed approaches for numerical modeling of mixed sand transport in this thesis, in sedWaveFoam and calibrate as well as validate with the recently performed experiments of the GWK is recommended for future works to extend the range of experimental dataset of the GWK for mixed sands transport under progressive surface waves.

Based on the numerical results of this thesis, among the bimodal mixed sands, the case of 5050 (50% fine fraction and 50% coarse fraction) shows the optimum mixture for a mixed sand under sheet flow conditions in terms of the low erosion rate. However, the developed numerical tool was calibrated and validated by means of an OFT dataset. Due to the high costs of the large scale experiments for mixed sand on one hand, and the importance of the experiments at large wave flumes to reproduce the absent determining components on the other hand, it is highly recommended to perform different hydro-morphodynamic test cases by means of this mixture to understand the role of the deciding mechanisms in the GWK for mixed sand transport, which are absent in OFTs. Moreover, a bimodal mixture could represents the two different grain size distributions of original sand in beach compared to the borrow sand, which are different from original sand.

Bibliography

Abreu, T., Silva, P. A., Sancho, F., and Temperville, A. (2010). Analytical approximate wave form for asymmetric waves. *Coastal Engineering*, *57*(7), 656–667. doi: https://doi.org/10.1016/j.coastaleng.2010.02.005 (cit. on pp. 23 and 24).

Ahilan, R., and Sleath, J. F. (1987). Sediment transport in oscillatory flow over flat beds. *Journal of Hydraulic Engineering*, *113*(3), 308–321. doi: https://doi.org/10.1061/(ASCE)0733-9429(1987)113:3(308) (cit. on pp. 39 and 40).

Ahmadi, G., and Shahinpoor, M. (1983). A note on collision operators in rapid granular flows of rough inelastic particles. *Powder Technology*, *35*(1), 119–122. doi: https://doi.org/10.1016/0032-5910(83)85035-9 (cit. on p. 164).

Ahmari, A. (2012). *Suspended sediment transport above rippled and plane sea bed induced by non breaking and near breaking waves: a large scale laboratory study* (PhD Thesis). Technische Universität Carolo-Wilhelmina zu Braunschweig, Germany. (cit. on pp. iv, v, 18, 19, 20, 21, and 22).

Ahmed, A. S., and Sato, S. (2003). A sheetflow transport model for asymmetric oscillatory flows: Part ii: Mixed grain size sediments. *Coastal engineering journal*, *45*(03), 339–361. doi: https://doi.org/10.1142/S0578563403000798 (cit. on pp. vii, 24, 26, 49, 54, 55, 57, 58, 59, 63, 66, 158, and 159).

Amoudry, L., Hsu, T.-J., and Liu, P.-F. (2005). Schmidt number and near-bed boundary condition effects on a two-phase dilute sediment transport model. *Journal of Geophysical Research: Oceans*, *110*(C9). doi: https://doi.org/10.1029/2004JC002798 (cit. on p. 39).

Amoudry, L., Hsu, T.-J., and Liu, P.-F. (2008). Two-phase model for sand transport in sheet flow regime. *Journal of Geophysical Research: Oceans*, *113*(C3). doi: https://doi.org/10.1029/2007JC004179 (cit. on pp. v, 28, 30, and 39).

Anderson, D., Tannehill, J. C., and Pletcher, R. H. (2016). *Computational fluid mechanics and heat transfer*. Taylor & Francis. (cit. on p. 92).

Asano, T. (1990). Two-phase flow model on oscillatory sheet-flow. *Coastal Engineering Proceedings*, *1*(22). doi: https://doi.org/10.1061/9780872627765.181 (cit. on pp. 32 and 39).

Bagnold, R. A. (1946). Motion of waves in shallow water. interaction between waves and sand bottoms. *Proceedings of the Royal Society of London. Series A. Mathematical and Physical Sciences*, *187*(1008), 1–18. doi: https://doi.org/10.1098/rspa.1946.0062 (cit. on p. 16).

Bailard, J. A. (1981). An energetics total load sediment transport model for a plane sloping beach. *Journal of Geophysical Research: Oceans*, *86*(C11), 10938–10954. doi: https://doi.org/10.1029/JC086iC11p10938 (cit. on pp. vi, vii, xii, 43, 44, 45, 46, 48, 52, 53, and 54).

Bakhtyar, R., Barry, D. A., Yeganeh-Bakhtiary, A., Li, L., Parlange, J.-Y., and Sander, G. (2010). Numerical simulation of two-phase flow for sediment transport in the inner-surf and swash zones. *Advances in water resources*, *33*(3), 277–290. doi: https://doi.org/10.1016/j.advwatres.2009.12.004 (cit. on p. 39).

Bakhtyar, R., Yeganeh-Bakhtiary, A., Barry, D. A., and Ghaheri, A. (2009). Two-phase hydrodynamic and sediment transport modeling of wave-generated sheet flow. *Advances in Water Resources*, *32*(8), 1267–1283. doi: https://doi.org/10.1016/j.advwatres.2009.05.002 (cit. on p. 39).

Bakker, W., Van Kesteren, W., and Yu, Z. (1988). Grain-grain interaction in oscillating sheetflow. *Coastal Engineering Proceedings*, *1*(21). doi: https://doi.org/10.1061/

`9780872626874.054` (cit. on pp. v, 26, and 27).

Bijker, E. W. (1971). Longshore transport computations. *Journal of the Waterways, Harbors and Coastal Engineering Division*, *97*(4), 687–701. doi: `https://doi.org/10.1061/AWHCAR.0000122` (cit. on p. 43).

Boltzmann, L. (1872). *Weitere studien über das wärmegleichgewicht unter gasmolekülen*. Aus der kk Hot-und Staatsdruckerei. (cit. on pp. viii, 74, 75, 76, 77, 142, and 165).

Boscia, D., van der A, D. A., and O'Donoghue, T. (2019). Dynamics and transport of sand mixtures in oscillatory flows. In *15th uk young coastal scientists and engineers conference (ycsec)* (p. 24). Retrieved from `https://ycsec2019.files.wordpress.com/2019/05/ycsec2019_conferenceprogrammeabstracts.pdf` (cit. on p. 66).

Boussinesq, J. (1877). Theorie de l'ecoulement tourbillant. *Mem. Acad. Sci.*, *23*, 46. (cit. on pp. 79 and 82).

Broyden, C. G. (1967). Quasi-newton methods and their application to function minimisation. *Mathematics of Computation*, *21*(99), 368–381. (cit. on p. 94).

Burden, R. L., Faires, J. D., and Burden, A. M. (2015). *Numerical analysis*. Cengage learning. (cit. on p. 94).

Camenen, B., and Larroudé, P. (2003). Comparison of sediment transport formulae for the coastal environment. *Coastal Engineering*, *48*(2), 111–132. doi: `https://doi.org/10.1016/S0378-3839(03)00002-4` (cit. on p. 46).

Camenen, B., and Larson, M. (2006). Phase-lag effects in sheet flow transport. *Coastal Engineering*, *53*(5-6), 531–542. doi: `https://doi.org/10.1016/j.coastaleng.2005.12.003` (cit. on p. 19).

Carnahan, N. F., and Starling, K. E. (1969). Equation of state for nonattracting rigid spheres. *The Journal of chemical physics*, *51*(2), 635–636. doi: `https://doi.org/10.1063/1.1672048` (cit. on p. 162).

Carrillo-Serrano, V., and Pacheco-Tobar, E. (2018). Application of openfoam solver settlingfoam to bedload sediment transport analysis. *Dyna*, *85*(206), 121–127. doi: `https://doi.org/10.15446/dyna.v85n206.66804` (cit. on p. 37).

Chapman, S., Cowling, T. G., and Burnett, D. (1970). *The mathematical theory of nonuniform gases: an account of the kinetic theory of viscosity, thermal conduction and diffusion in gases*. Cambridge university press. (cit. on p. 165).

Chauchat, J., Cheng, Z., Nagel, T., Bonamy, C., and Hsu, T.-J. (2017). Sedfoam-2.0: a 3-d two-phase flow numerical model for sediment transport. *Geoscientific Model Development*, *10*(12). doi: `https://doi.org/10.5194/gmd-10-4367-2017` (cit. on p. 36).

Chen, X., Li, Y., Niu, X., Chen, D., and Yu, X. (2011). A two-phase approach to wave-induced sediment transport under sheet flow conditions. *Coastal Engineering*, *58*(11), 1072–1088. doi: `https://doi.org/10.1016/j.coastaleng.2011.06.003` (cit. on p. 40).

Cheng, Z. (2016). *A multi-dimensional two-phase flow modeling framework for sediment transport applications* (PhD Thesis, University of Delaware). Retrieved from `http://udspace.udel.edu/handle/19716/19988` (cit. on p. 120).

Cheng, Z., and Hsu, T.-J. (2014). A multi-dimensional two-phase eulerian model for sediment transport—twophaseeulersedfoam (version 1.0). In *Tech. rep cacr-14-08*. University of Delaware. (cit. on pp. xii, 80, 81, 82, 83, 126, and 162).

Cheng, Z., Hsu, T.-J., and Calantoni, J. (2017). Sedfoam: A multi-dimensional eulerian two-phase model for sediment transport and its application to momentary bed failure. *Coastal Engineering*, *119*, 32–50. doi: `https://doi.org/10.1016/j.coastaleng`

.2016.08.007 (cit. on pp. viii, 2, 5, 36, 37, 38, 40, 73, 83, 88, 90, and 98).

Cloin, B. (1998). *Gradation effects on sediment transport in oscillatory sheet flow* (Report-H2305, Technical university Delft, Delft, The Netherlands). Retrieved from http://resolver.tudelft.nl/uuid:501d41c6-08eb-4bb2-8f20-5e2f348ce91f (cit. on pp. 24 and 42).

Cundall, P., Jenkins, J., and Ishibashi, I. (1989). Micromechanical modeling of granular materials with the assistance of experiments and numerical simulations. *Powders and Grains, Balkema, Rotterdam*, 319–322. (cit. on p. 34).

Da Silva, P. A., Temperville, A., and Santos, F. S. (2006). Sand transport under combined current and wave conditions: A semi-unsteady, practical model. *Coastal Engineering*, *53*(11), 897–913. doi: https://doi.org/10.1016/j.coastaleng.2006.06.010 (cit. on pp. 51 and 59).

Davies, A., and Li, Z. (1997). Modelling sediment transport beneath regular symmetrical and asymmetrical waves above a plane bed. *Continental Shelf Research*, *17*(5), 555–582. doi: https://doi.org/10.1016/S0278-4343(96)00048-9 (cit. on pp. 30 and 31).

Davies, A., Van Rijn, L., Damgaard, J., Van de Graaff, J., and Ribberink, J. (2002). Intercomparison of research and practical sand transport models. *Coastal Engineering*, *46*(1), 1–23. (cit. on p. 38).

Day, T. J. (1980). A study of the transport of graded sediments. *Hydraulics Research Station, Report IT 190, Wallingford*. Retrieved from http://eprints.hrwallingford.com/id/eprint/33 (cit. on pp. 2, 41, 42, 43, 46, 47, 54, and 59).

Dibajnia, M., and Watanabe, A. (1992). Sheet flow under nonlinear waves and currents. *Coastal Engineering Proceedings*, *1*(23). doi: https://doi.org/10.1029/2001JC001045 (cit. on pp. 23, 28, 43, 48, 50, and 59).

Dibajnia, M., and Watanabe, A. (1996). A transport rate formula for mixed-size sands. *Coastal Engineering Proceedings*, *1*(25). doi: https://doi.org/10.1061/9780784402429.293 (cit. on pp. vii, 48, 49, 54, 55, 56, 57, 58, and 59).

Dibajnia, M., and Watanabe, A. (2000). Moving layer thickness and transport rate of graded sand. In *Proceedings of the 27th international conference on coastal engineering* (p. 2752–2765). doi: https://doi.org/10.1061/40549(276)215 (cit. on p. 57).

Ding, J., and Gidaspow, D. (1990). A bubbling fluidization model using kinetic theory of granular flow. *AIChE journal*, *36*(4), 523–538. doi: https://doi.org/10.1002/aic.690360404 (cit. on pp. 73, 161, and 165).

Dohmen-Janssen, C. M. (1999). *Grain size influence on sediment transport oscillatory sheet flow* (PhD Thesis, Delft University of Technology, Delft, The Netherlands). Retrieved from http://resolver.tudelft.nl/uuid:b448c04e-914c-484c-94cb-bcf046f6609f (cit. on pp. x, 9, 19, 52, 115, 117, 118, 127, and 142).

Dohmen-Janssen, C. M., and Hanes, D. M. (2002). Sheet flow dynamics under monochromatic nonbreaking waves. *Journal of geophysical research: Oceans*, *107*(C10). doi: https://doi.org/10.1029/2001JC001045 (cit. on pp. 8, 9, 20, and 28).

Dohmen-Janssen, C. M., Hassan, W. N., and Ribberink, J. S. (2001). Mobile-bed effects in oscillatory sheet flow. *Journal of geophysical research: Oceans*, *106*(C11), 27103–27115. doi: https://doi.org/10.1029/2000JC000513 (cit. on p. 3).

Dohmen-Janssen, C. M., Kroekenstoel, D. F., Hassan, W. N., and Ribberink, J. S. (2002). Phase lags in oscillatory sheet flow: experiments and bed load modelling. *Coastal Engineering*, *46*(1), 61–87. doi: https://doi.org/10.1016/S0378-3839(02)00056

`-X` (cit. on pp. 3 and 43).

Dong, Sato, S., and Liu, H. (2013). A sheetflow sediment transport model for skewed-asymmetric waves combined with strong opposite currents. *Coastal Engineering*, *71*, 87-101. doi: `https://doi.org/10.1016/j.coastaleng.2012.08.004` (cit. on p. 24).

Dong, and Zhang, K. (1999). Two-phase flow modelling of sediment motions in oscillatory sheet flow. *Coastal Engineering*, *36*(2), 87–109. doi: `https://doi.org/10.1016/S0378-3839(98)00052-0` (cit. on pp. 32 and 39).

Dong, and Zhang, K. (2002). Intense near-bed sediment motions in waves and currents. *Coastal Engineering*, *45*(2), 75–87. doi: `https://doi.org/10.1016/S0378-3839(02)00040-6` (cit. on p. 39).

Egiazaroff, I. V. (1965). Calculation of nonuniform sediment concentrations. *Journal of the Hydraulics Division*, *91*(4), 225–247. doi: `https://doi.org/10.1061/JYCEAJ.0001277` (cit. on pp. 2, 41, 42, and 43).

Einstein, H. A. (1950). *The bed-load function for sediment transportation in open channel flows*. Technical Bulletins 156389, United States Department of Agriculture, Economic Research Service. doi: `10.22004/ag.econ.156389` (cit. on pp. v, 31, and 32).

Engelund, F., and Fredsøe, J. (1976). A sediment transport model for straight alluvial channels. *Hydrology Research*, *7*(5), 293–306. doi: `https://doi.org/10.2166/nh.1976.0019` (cit. on pp. v, vi, 30, 31, 32, 33, 34, 35, and 36).

Ferziger, J. H., Perić, M., and Street, R. L. (2002). *Computational methods for fluid dynamics* (Vol. 3). Springer. (cit. on p. 93).

Foerster, S. F., Louge, M. Y., Chang, H., and Allia, K. (1994). Measurements of the collision properties of small spheres. *Physics of Fluids*, *6*(3), 1108–1115. doi: `https://doi.org/10.1063/1.868282` (cit. on p. 161).

Fredsøe, J., and Deigaard, R. (1992). *Mechanics of coastal sediment transport, advanced series on ocean engineering, vol. 3.* World Scientific Publishing Co. Pte. Ltd. (cit. on pp. iv, 10, and 14).

Fredsøe, J., Deigaard, R., et al. (1992). *Mechanics of coastal sediment transport* (Vol. 3). World Scientific Publishing Co. Pte. Ltd. (cit. on p. 125).

Fromant, G., Hurther, D., van Der Zanden, J., Van Der A, D., Cáceres, I., O'Donoghue, T., and Ribberink, J. (2019). Wave boundary layer hydrodynamics and sheet flow properties under large-scale plunging-type breaking waves. *Journal of geophysical research: Oceans*, *124*(1), 75–98. (cit. on p. 3).

Fuhrman, D. R., Schløer, S., and Sterner, J. (2013). Rans-based simulation of turbulent wave boundary layer and sheet-flow sediment transport processes. *Coastal engineering*, *73*, 151–166. doi: `https://doi.org/10.1016/j.coastaleng.2012.11.001` (cit. on pp. 30 and 31).

Gidaspow, D. (1994). *Multiphase flow and fluidization: continuum and kinetic theory descriptions.* Academic press. (cit. on pp. 80 and 83).

Gonzalez-Rodriguez, D. (2009). *Wave boundary layer hydrodynamics and cross-shore sediment transport in the surf zone* (PhD Thesis, Massachusetts Institute of Technology). Retrieved from `http://dspace.mit.edu/handle/1721.1/7582` (cit. on p. 23).

Gonzalez-Rodriguez, D., and Madsen, O. S. (2007). Seabed shear stress and bedload transport due to asymmetric and skewed waves. *Coastal Engineering*, *54*(12), 914–929. doi: `https://doi.org/10.1016/j.coastaleng.2007.06.004` (cit. on pp. 23 and 24).

Bibliography

Hamm, L., Katopodi, I., Dohmen-Janssen, C., Ribberink, J. S., Samothrakis, P., Cloin, B., Savioli, J., Chatelus, Y., Bosboom, J., and Hein, R. (1998). Grain size and gradation effects on sediment transport processes in oscillatory flow conditions, part1: Gradation effects (series k). *Data report Z2153, WL Delft Hydraulics. 2435–2448.*. (cit. on pp. 24, 26, 52, 53, 57, 58, 59, 157, and 158).

Hansen, J. B., and Svendsen, I. (1985). A theoretical and experimental study of undertow. In *Coastal engineering 1984* (pp. 2246–2262). doi: https://doi.org/10.1061/9780872624382.152 (cit. on p. 9).

Hassan, W. N. (2003). *Transport of size-graded and uniform sediment under oscillatory sheet-flow conditions* (PhD Thesis). University of Technology Delf, The Netherlands. (cit. on pp. iv, 4, and 9).

Hassan, W. N., Kroekenstoel, D., and Ribberink, J. S. (2001). Size-gradation effect on sand transport rates under oscillatory sheet-flows. In *Proc. coastal dynamics* (Vol. 1, pp. 928–937). doi: https://doi.org/10.1061/40566(260)95 (cit. on pp. 43 and 57).

Hassan, W. N., and Ribberink, J. S. (2005). Transport processes of uniform and mixed sands in oscillatory sheet flow. *Coastal Engineering*, *52*(9), 745–770. doi: https://doi.org/10.1016/j.coastaleng.2005.06.002 (cit. on pp. iv, 2, 3, 5, 24, 26, 41, 59, 66, 110, 159, and 160).

Hassan, W. N., and Ribberink, J. S. (2010). Modelling of sand transport under wave-generated sheet flows with a rans diffusion model. *Coastal Engineering*, *57*(1), 19–29. doi: https://doi.org/10.1016/j.coastaleng.2009.08.009 (cit. on p. 30).

Higuera, P., Lara, J. L., and Losada, I. J. (2013). Realistic wave generation and active wave absorption for navier–stokes models: Application to openfoam®. *Coastal Engineering*, *71*, 102–118. doi: https://doi.org/10.1016/j.coastaleng.2012.07.002 (cit. on p. 36).

Hsu, T.-J. (2002). *A two-phase flow approach for sediment transport* (PhD Thesis). (cit. on p. 82).

Hsu, T.-J., Jenkins, J. T., and Liu, P. L.-F. (2003). On two-phase sediment transport: Dilute flow. *Journal of Geophysical Research: Oceans*, *108*(C3). doi: https://doi.org/10.1029/2001JC001276 (cit. on pp. 33 and 39).

Hsu, T.-J., Jenkins, J. T., and Liu, P. L.-F. (2004). On two-phase sediment transport: sheet flow of massive particles. *Proceedings of the Royal Society of London. Series A: Mathematical, Physical and Engineering Sciences*, *460*(2048), 2223–2250. doi: https://doi.org/10.1098/rspa.2003.1273 (cit. on pp. 28, 33, and 39).

Inui, T., Dibajnia, M., Isobe, M., and Watanabe, A. (1995). A transport rate formula for mixed-size sands and its application. In *42th Japanese Annual Conference on Coastal Engineering. JSCE, (in Japanese)* (pp. 356–360). Retrieved from "https://ci.nii.ac.jp/naid/10021137039/en/" (cit. on pp. 24, 59, 63, and 157).

Jackson, L. A., Tomlinson, R., et al. (2017). 50 years of seawall and nourishment strategy evolution on the gold coast. *Australasian Coasts & Ports 2017: Working with Nature*, 640. (cit. on p. 1).

Jacobsen, N. G., Fuhrman, D. R., and Fredsøe, J. (2012). A wave generation toolbox for the open-source cfd library: Openfoam®. *International Journal for numerical methods in fluids*, *70*(9), 1073–1088. doi: https://doi.org/10.1002/fld.2726 (cit. on p. 36).

Jenkins, J. T., and Hanes, D. M. (1998). Collisional sheet flows of sediment driven by a turbulent fluid. *Journal of Fluid Mechanics*, *370*, 29–52. doi: https://doi.org/10.1017/S0022112098001840 (cit. on pp. 28 and 36).

Jenkins, J. T., and Savage, S. B. (1983). A theory for the rapid flow of identical, smooth, nearly elastic, spherical particles. *Journal of fluid mechanics*, *130*, 187–202. (cit. on pp. 33 and 34).

Johnson, P. C., and Jackson, R. (1987). Frictional–collisional constitutive relations for granular materials, with application to plane shearing. *Journal of fluid Mechanics*, *176*, 67–93. doi: https://doi.org/10.1017/S0022112087000570 (cit. on pp. 80, 99, and 100).

Jonsson, I. G. (1967). Wave boundary layers and friction factors. In *Coastal engineering 1966* (pp. 127–148). doi: https://doi.org/10.1061/9780872620087.010 (cit. on pp. 15 and 28).

Karambas, T. V. (2003). Nonlinear wave modeling and sediment transport in the surf and swash zone. In *Elsevier oceanography series* (Vol. 67, pp. 267–298). doi: https://doi.org/10.1016/S0422-9894(03)80127-7 (cit. on p. 3).

Kim, Y., Mieras, R. S., Cheng, Z., Anderson, D., Hsu, T.-J., Puleo, J. A., and Cox, D. (2019). A numerical study of sheet flow driven by velocity and acceleration skewed near-breaking waves on a sandbar using sedwavefoam. *Coastal Engineering*, *152*, 103526. doi: https://doi.org/10.1016/j.coastaleng.2019.103526 (cit. on pp. 37, 40, 83, and 144).

Kranenburg, W. M., Ribberink, J. S., Schretlen, J. J., and Uittenbogaard, R. E. (2013). Sand transport beneath waves: The role of progressive wave streaming and other free surface effects. *Journal of Geophysical Research: Earth Surface*, *118*(1), 122–139. doi: https://doi.org/10.1029/2012JF002427 (cit. on pp. 2, 3, 8, and 40).

Lanckriet, T., Puleo, J. A., Masselink, G., Turner, I. L., Conley, D., Blenkinsopp, C., and Russell, P. (2013). Comprehensive field study of swash-zone processes. ii: Sheet flow sediment concentrations during quasi-steady backwash. *Journal of Waterway, Port, Coastal, and Ocean Engineering*, *140*(1), 29–42. doi: https://doi.org/10.1061/(ASCE)WW.1943-5460.0000209 (cit. on pp. 26 and 27).

Li, M., Pan, S., and O'Connor, B. A. (2008). A two-phase numerical model for sediment transport prediction under oscillatory sheet flows. *Coastal Engineering*, *55*(12), 1159–1173. doi: https://doi.org/10.1016/j.coastaleng.2008.05.003 (cit. on p. 39).

Liu, H., and Sato, S. (2006). A two-phase flow model for asymmetric sheetflow conditions. *Coastal Engineering*, *53*(10), 825–843. doi: https://doi.org/10.1016/j.coastaleng.2006.04.002 (cit. on p. 39).

Malalasekera, W., and Versteeg, H. (2007). An introduction to computational fluid dynamics. *The finite volume method, Harlow: Prentice Hall*, 1995. (cit. on pp. 82 and 93).

Manninen, M., Taivassalo, V., Kallio, S., et al. (1996). *On the mixture model for multiphase flow*. Retrieved from http://www.vtt.fi/inf/pdf/publications/1996/P288.pdf (cit. on pp. 5, 83, 84, 87, and 126).

Maxwell, J. C. (1860). V. illustrations of the dynamical theory of gases.—part i. on the motions and collisions of perfectly elastic spheres. *The London, Edinburgh, and Dublin Philosophical Magazine and Journal of Science*, *19*(124), 19–32. (cit. on pp. viii, 74, 75, 76, 77, 142, and 165).

McTigue, D. F. (1981). Mixture theory for suspended sediment transport. *Journal of the Hydraulics Division*, *107*(6), 659–673. doi: https://doi.org/10.1061/JYCEAJ.0005678 (cit. on p. 74).

Muis, S., Verlaan, M., Winsemius, H. C., Aerts, J. C., and Ward, P. J. (2016). A global reanalysis of storm surges and extreme sea levels. *Nature communications*, *7*, 11969.

doi: https://doi.org/10.1038/ncomms11969 (cit. on p. 1).

Naqshband, S. (2009). *Wave boundary layer streaming* (M.Sc. Thesis). University of Twente, Enschede, The Netherlands. (cit. on pp. 8 and 9).

Nielsen, P. (1992). *Coastal bottom boundary layers and sediment transport* (Vol. 4). World Scientific Publishing Co. Pte. Ltd. (cit. on pp. 17 and 18).

Niemi, T. (2012). *Particle size distribution in cfd simulation of gas-particle flows* (Master Thesis, Aalto university, Finland). Retrieved from http://urn.fi/URN:NBN:fi:aalto-201209213159 (cit. on pp. 83, 84, 87, and 88).

Nikuradse, J. (1933). Gesetzmäßigkeiten der turbulenten strömung in glatten rohren (nachtrag). *Forschung im Ingenieurwesen*, *4*(1), 44–44. (cit. on p. 13).

O'Donoghue, T., and Clubb, G. S. (2001). Sand ripples generated by regular oscillatory flow. *Coastal Engineering*, *44*(2), 101–115. doi: https://doi.org/10.1016/S0378-3839(01)00025-4 (cit. on p. 17).

O'Donoghue, T., Doucette, J., Van der Werf, J. J., and Ribberink, J. S. (2006). The dimensions of sand ripples in full-scale oscillatory flows. *Coastal Engineering*, *53*(12), 997–1012. doi: https://doi.org/10.1016/j.coastaleng.2006.06.008 (cit. on pp. v, 17, 18, and 19).

O'Donoghue, T., and Wright, S. (2004a). Concentrations in oscillatory sheet flow for well sorted and graded sands. *Coastal Engineering*, *50*(3), 117–138. doi: https://doi.org/10.1016/j.coastaleng.2003.09.004 (cit. on pp. vi, vii, ix, x, xii, 2, 6, 24, 32, 33, 34, 35, 36, 37, 45, 46, 47, 53, 54, 57, 59, 83, 88, 94, 97, 98, 99, 100, 102, 103, 104, 105, 107, 110, 115, 116, 118, 120, 123, 125, 126, 137, 142, 143, and 159).

O'Donoghue, T., and Wright, S. (2004b). Flow tunnel measurements of velocities and sand flux in oscillatory sheet flow for well-sorted and graded sands. *Coastal Engineering*, *51*(11-12), 1163–1184. doi: https://doi.org/10.1016/j.coastaleng.2004.08.001 (cit. on pp. ix, xii, 66, 72, 88, 94, 97, 99, 105, 106, 108, 115, 116, 118, 119, 120, and 128).

Peters, K. U. F. (2003). *Morphodynamik in der brandungszone sandiger küsten - konzentrationsverteilung suspendierter sedimente* - (PhD Thesis). Technische Universität Carolo-Wilhelmina zu Braunschweig, Germany. (cit. on pp. iv and 4).

Pörtner, H.-O., Roberts, D. C., Masson-Delmotte, V., Zhai, P., Tignor, M., Poloczanska, E., and Weyer, N. (2019). The ocean and cryosphere in a changing climate. *IPCC Special Report on the Ocean and Cryosphere in a Changing Climate*. (cit. on p. 1).

Rafati, Y., Hsu, T.-J., Calantoni, J., and Puleo, J. (2022). Entrainment and transport of well-sorted and mixed sediment under wave motion. *Journal of Geophysical Research: Oceans*, *127*(8), e2022JC018686. (cit. on pp. 36, 40, and 83).

Ramsdell, R. C., and Miedema, S. A. (2011). Hydraulic transport of sand/shell mixtures. In *Asme 2011 30th international conference on ocean, offshore and arctic engineering* (pp. 533–547). doi: https://doi.org/10.1115/OMAE2011-49695 (cit. on pp. iv and 17).

Revil-Baudard, T., and Chauchat, J. (2013). A two-phase model for sheet flow regime based on dense granular flow rheology. *Journal of Geophysical Research: Oceans*, *118*(2), 619–634. doi: https://doi.org/10.1029/2012JC008306 (cit. on pp. 36 and 40).

Ribberink, J. S. (1998). Bed-load transport for steady flows and unsteady oscillatory flows. *Coastal Engineering*, *34*(1-2), 59–82. doi: https://doi.org/10.1016/S0378-3839(98)00013-1 (cit. on pp. vii, xii, 13, 43, 46, 47, 48, 50, 51, 54, 55, and 59).

Ribberink, J. S., Dohmen-Janssen, C. M., Hanes, D. M., McLean, S. R., and Vincent,

C. (2001). Near-bed sand transport mechanisms under waves—a large-scale flume experiment (sistex99). In *27th international conference on coastal engineering (icce)* (p. 3263-3276). doi: https://doi.org/10.1061/40549(276)254 (cit. on pp. 9, 10, and 20).

Roelvink, D., Van Dongeren, A., McCall, R., Hoonhout, B., van Rooijen, A., and van Geer, K. N. E. Q., Lodewijk de Vet. (2015). Xbeach technical reference: Kingsday release. model description and reference guide to functionalities. *Delft-The Netherlands*. (cit. on p. 4).

Rusche, H. (2003). *Computational fluid dynamics of dispersed two-phase flows at high phase fractions* (PhD Thesis, Imperial College London (University of London)). Retrieved from http://hdl.handle.net/10044/1/8110 (cit. on pp. 36, 83, 91, 92, and 93).

Savage, S. B., and McKeown, S. (1983). Shear stresses developed during rapid shear of concentrated suspensions of large spherical particles between concentric cylinders. *Journal of Fluid Mechanics*, *127*, 453–472. doi: https://doi.org/10.1017/S0022112083002827 (cit. on pp. 32, 33, and 39).

Schendel, A. (2018). *Wave-current-induced scouring processes and protection by widely graded material* (PhD Thesis, Hannover: Institutionelles Repositorium der Leibniz Universität Hannover). doi: https://doi.org/10.15488/4453 (cit. on p. 9).

Schiller, L., and Naumann, A. (1935). A drag coefficient correlation. *Zeitschrift des Vereins Deutscher Ingenieure*, *77*, 318–320. (cit. on p. 161).

Schretlen, J. L. M. (2012). *Sand transport under full-scale progressive surface waves* (PhD Thesis, University of Twente, Enschede, The Netherlands). Retrieved from https://research.utwente.nl/en/publications/sand-transport-under-full-scale-progressive-surface-waves (cit. on pp. iv, v, 2, 3, 8, 10, 14, 16, 18, 20, and 22).

Shields, A. (1936). Anwendung der aehnlichkeitsmechanik und der turbulenzforschung auf die geschiebebewegung. *PhD Thesis Technical University Berlin*. (cit. on pp. iv, 11, and 12).

Shiravani, G., Vousdoukas, M., Schimmels, S., and Stagonas, D. (2014). A methodology for measuring the velocity and thickness of wave-induced up-rushing jets on vertical seawalls and superstructure. *Coastal Engineering Proceedings, 1(34), waves.48*. doi: https://doi.org/10.9753/icce.v34.waves.48 (cit. on p. 1).

Sistermans, P. G. J. (2002). *Graded sediment transport by non-breaking waves and a current* (PhD Thesis, Delft University of Technology, Delft, The Netherlands). Retrieved from http://resolver.tudelft.nl/uuid:a61234fe-a3d8-433e-9196-96a851324bf6 (cit. on p. 23).

Sleath, J. (1987). Turbulent oscillatory flow over rough beds. *Journal of Fluid Mechanics*, *182*, 369–409. doi: https://doi.org/10.1017/S0022112087002374 (cit. on pp. iv and 14).

Soulsby, R. (1997). *Dynamics of marine sands: a manual for practical applications*. Thomas Telford Ltd. Retrieved from https://www.icevirtuallibrary.com/doi/abs/10.1680/doms.25844.fm (cit. on p. 44).

Staudt, F., Gijsman, R., Ganal, C., Mielck, F., Wolbring, J., Hass, H. C., Goseberg, N., Schüttrumpf, H., Schlurmann, T., and Schimmels, S. (2021). The sustainability of beach nourishments: a review of nourishment and environmental monitoring practice. *Journal of Coastal Conservation*, *25*(2), 1–24. (cit. on p. 2).

Swart, D. H. (1974). Offshore sediment transport and equilibrium beach profiles. *Delft Hydraulics Lab Publ No. 131*. (cit. on pp. 14, 15, 44, and 51).

Syamlal, M. (1987). *The particle-particle drag term in a multiparticle model of fluidization* (Tech. Rep.). EG and G Washington Analytical Services Center, Inc., Morgantown, WV (USA). Retrieved from https://www.osti.gov/biblio/6355923 (cit. on pp. viii, xii, 6, 74, 75, 77, 78, 79, 80, 87, 105, 126, 142, 161, 163, 164, and 165).

Syamlal, M., Rogers, W., and O'Brien, T. J. (1993). *Mfix documentation theory guide* (Tech. Rep.). USDOE Morgantown Energy Technology Center, WV (United States). doi: https://doi.org/10.2172/10145548 (cit. on pp. 74, 80, 81, and 162).

Tanaka, M. (2000). *Study on sediment transport rate and beach deformation for mixed-grain size beds* (Unpublished doctoral dissertation). The University of Tokyo. (cit. on pp. vii, 49, 54, 56, 57, and 58).

Thorne, P. D., Davies, A. G., and Williams, J. J. (2003). Measurements of near-bed intra-wave sediment entrainment above vortex ripples. *Geophysical Research Letters*, *30*(20). doi: https://doi.org/10.1029/2003GL018427 (cit. on pp. iv and 18).

Van der A, D. A., O'Donoghue, T., and Ribberink, J. S. (2010). Measurements of sheet flow transport in acceleration-skewed oscillatory flow and comparison with practical formulations. *Coastal Engineering*, *57*(3), 331–342. doi: https://doi.org/10.1016/j.coastaleng.2009.11.006 (cit. on pp. 24 and 52).

Van der A, D. A., Ribberink, J. S., Van der Werf, J. J., O'Donoghue, T., Buijsrogge, R. H., Kranenburg, W. M., et al. (2013). Practical sand transport formula for non-breaking waves and currents. *Coastal engineering*, *76*, 26–42. doi: https://doi.org/10.1016/j.coastaleng.2013.01.007 (cit. on pp. vii, x, 24, 43, 50, 60, 63, 65, 115, 116, 118, and 127).

Van der Werf, J., Schretlen, J. J., Ribberink, J. S., and O'Donoghue, T. (2009). Database of full-scale laboratory experiments on wave-driven sand transport processes. *Coastal Engineering*, *56*(7), 726–732. doi: https://doi.org/10.1016/j.coastaleng.2009.01.008 (cit. on pp. 8, 9, 23, and 59).

Van der Werf, J., Staudt, F., Posanski, D., Van De Wardt, W., Van der Zanden, J., Vermeulen, B., Ribberink, J. S., and Schimmels, S. (2019). Understanding and modeling wave-driven mixed sand transport. doi: https://doi.org/10.1142/9789811204487_0070 (cit. on pp. 2, 4, 66, 127, and 143).

Van Rijn, L. C. (1984). Sediment pick-up functions. *Journal of Hydraulic engineering*, *110*(10), 1494–1502. doi: https://doi.org/10.1061/(ASCE)0733-9429(1984)110:10(1494) (cit. on pp. v, vi, 30, 31, 32, 35, and 36).

Van Rijn, L. C. (1993). *Principles of sediment transport in rivers, estuaries and coastal seas* (Vol. 1006). Aqua publications Amsterdam. (cit. on pp. iv, 8, 11, 12, 13, and 42).

Van Rijn, L. C. (2007). Unified view of sediment transport by currents and waves. III: Graded beds. *Journal of Hydraulic Engineering*, *133*(7), 761–775. doi: https://doi.org/10.1061/(ASCE)0733-9429(2007)133:7(761) (cit. on pp. 2, 43, 59, and 62).

Van Rijn, L. C., Walstra, D., Grasmeijer, B., Sutherland, J., Pan, S., and Sierra, J. (2003). The predictability of cross-shore bed evolution of sandy beaches at the time scale of storms and seasons using process-based profile models. *Coastal Engineering*, *47*(3), 295–327. doi: https://doi.org/10.1016/S0378-3839(02)00120-5 (cit. on pp. 52 and 54).

Wilson, K. (1989). Friction of wave-induced sheet flow. *Coastal Engineering*, *12*(4), 371–379. doi: https://doi.org/10.1016/0378-3839(89)90013-6 (cit. on p. 19).

Wong, W. H. (2010). *A comparison of wave-dominated cross-shore sand transport models* (M.Sc. Thesis, Technical university Delft, Delft, The Netherlands). Retrieved from

http://purl.utwente.nl/essays/59669 (cit. on pp. 4 and 8).

Wright, S. (2002). *Well-sorted and graded sands in oscillatory sheet-flow* (PhD Thesis, University of Aberdeen). Retrieved from ttps://ethos.bl.uk/OrderDetails.do?uin=uk.bl.ethos.252155 (Not cited.)

Wu, W., and Wang, S. S. (2006). Formulas for sediment porosity and settling velocity. *Journal of Hydraulic Engineering*, *132*(8), 858–862. doi: https://doi.org/10.1061/(ASCE)0733-9429(2006)132:8(858) (cit. on p. 16).

Yeh, H., and Wenwen, L. (2008). Tsunami scour and sedimentation. In *Proceedings 4th international conference on scour and erosion (icse-4). november 5-7, 2008, tokyo, japan* (pp. 95–106). (cit. on p. 3).

Yu, X., Hsu, T.-J., and Hanes, D. M. (2010). Sediment transport under wave groups: Relative importance between nonlinear waveshape and nonlinear boundary layer streaming. *Journal of Geophysical Research: Oceans*, *115*(C2). doi: https://doi.org/10.1029/2009JC005348 (cit. on p. 39).

Yu, X., Hsu, T.-J., Jenkins, J. T., and Liu, P. L.-F. (2012). Predictions of vertical sediment flux in oscillatory flows using a two-phase, sheet-flow model. *Advances in water resources*, *48*, 2–17. doi: https://doi.org/10.1016/j.advwatres.2012.05.012 (cit. on pp. vi, 35, 36, 38, and 40).

Zhou, Y., Xu, B. H., Yu, A.-B., and Zulli, P. (2002). An experimental and numerical study of the angle of repose of coarse spheres. *Powder technology*, *125*(1), 45–54. doi: https://doi.org/10.1016/S0032-5910(01)00520-4 (cit. on p. 161).

Zyserman, J. A., and Fredsøe, J. (1994). Data analysis of bed concentration of suspended sediment. *Journal of Hydraulic Engineering*, *120*(9), 1021–1042. doi: https://doi.org/10.1061/(ASCE)0733-9429(1994)120:9(1021) (cit. on pp. v, vi, 30, 31, 32, 33, and 34).

Appendices

A   Appendices

A.1 Dataset

Table A1: Available experiments with graded sands under sheet flow conditions.

Nr.	Test name	OFT-name	Fractions D_{50} (mm)	Fractions %	D_{10} (mm)	D_{50} (mm)	GI (D_{90}/D_{10})	R	β	T (s)	U_c (m/s)	$T_c(s)$	Net transport rate $\times 10^{-6}(m^2/s)$
1	Inui et al. (1995)- P02501	TUOFT	[0.2, 0.87]	[50, 50]	Not avai.	0.54	Not avai.	0.6516	0.5	3	0.6344	1.12	-4.20
2	Inui et al. (1995)- P02502	TUOFT	[0.2, 0.87]	[50, 50]	Not avai.	0.54	Not avai.	0.6509	0.5	3	0.7294	1.12	0.80
3	Inui et al. (1995)- P02503	TUOFT	[0.2, 0.87]	[50, 50]	Not avai.	0.54	Not avai.	0.7022	0.5	5	0.6006	1.80	2.40
4	Inui et al. (1995)- P02504	TUOFT	[0.2, 0.87]	[50, 50]	Not avai.	0.54	Not avai.	0.6849	0.5	5	0.7206	1.92	4.00
5	Inui et al. (1995)- P02505	TUOFT	[0.2, 0.87]	[50, 50]	Not avai.	0.54	Not avai.	0.6808	0.5	5	0.8987	1.92	14.80
6	Inui et al. (1995)- P02759	TUOFT	[0.2, 0.87]	[75, 25]	Not avai.	0.37	Not avai.	0.6516	0.5	3	0.6344	1.12	7.40
7	Inui et al. (1995)- P027510	TUOFT	[0.2, 0.87]	[75, 25]	Not avai.	0.37	Not avai.	0.6509	0.5	3	0.7294	1.12	13.80
8	Inui et al. (1995)- P027512	TUOFT	[0.2, 0.87]	[75, 25]	Not avai.	0.37	Not avai.	0.6457	0.5	3	0.8255	1.12	20.50
9	Inui et al. (1995)- P027513	TUOFT	[0.2, 0.87]	[75, 25]	Not avai.	0.37	Not avai.	0.6480	0.5	3	0.9925	1.18	-6.00
10	Inui et al. (1995)- P022516	TUOFT	[0.2, 0.87]	[25, 75]	Not avai.	0.70	Not avai.	0.6480	0.5	3	0.9925	1.18	47
11	Hamm et al. (1998)- K1-T1	LOWT	[0.128, 0.317]	[50, 50]	0.097	0.19	4.19	0.6639	0.5	6.5	1.584	2.6640	54.80
12	Hamm et al. (1998)- K1-T2	LOWT	[0.128, 0.317]	[50, 50]	0.097	0.19	4.19	0.6661	0.5	6.5	1.580	2.6610	46.40
13	Hamm et al. (1998)- K1-T5	LOWT	[0.128, 0.317]	[50, 50]	0.097	0.19	4.19	0.6651	0.5	6.5	1.5390	2.6620	29.40
14	Hamm et al. (1998)- K1-T6	LOWT	[0.128, 0.317]	[50, 50]	0.097	0.19	4.19	0.6638	0.5	6.5	1.524	2.6640	28.70
15	Hamm et al. (1998)- K1-T7	LOWT	[0.128, 0.317]	[50, 50]	0.097	0.19	4.19	0.6646	0.5	6.5	1.5320	2.6630	31.20
16	Hamm et al. (1998)- K1-T8	LOWT	[0.128, 0.317]	[50, 50]	0.097	0.19	4.19	0.6613	0.5	6.5	1.5070	2.6670	34.80
17	Hamm et al. (1998)- K1-T8	LOWT	[0.128, 0.317]	[50, 50]	0.097	0.19	4.19	0.6639	0.5	6.5	1.5110	2.6640	38.30

Continuation of Table A1

Nr.	Test name	OFT-name	Fractions D_{50} (mm)	Fractions %	D_{10} (mm)	D_{50} (mm)	GI (D_{90}/D_{10})	R	β	T (s)	U_c (m/s)	$T_c(s)$	Net transport rate $\times10^{-6}(m^2/s)$
18	Hamm et al. (1998)- K2-T1	LOWT	[0.128, 0.317]	[50, 50]	0.097	0.19	4.19	0.6651	0.5	6.5	1.0980	2.6620	17.10
19	Hamm et al. (1998)- K2-T2	LOWT	[0.128, 0.317]	[50, 50]	0.097	0.19	4.19	0.6524	0.5	6.5	1.1150	2.6790	17.20
20	Hamm et al. (1998)- K2-T3	LOWT	[0.128, 0.317]	[50, 50]	0.097	0.19	4.19	0.6656	0.5	6.5	1.0830	2.6610	16.80
21	Hamm et al. (1998)- K3-T1	LOWT	[0.128, 0.317]	[50, 50]	0.097	0.19	4.19	0.5292	0.67	6.4	1.143	3.194	16.75
22	Hamm et al. (1998)- K3-T2	LOWT	[0.128, 0.317]	[50, 50]	0.097	0.19	4.19	0.5329	0.67	6.4	1.175	3.194	16.70
23	Hamm et al. (1998)- K3-T3	LOWT	[0.128, 0.317]	[50, 50]	0.097	0.19	4.19	0.5248	0.67	6.4	1.155	3.194	20.70
24	Ahmed and Sato (2003)- A-M1	TUOFT	[0.21, 0.49, 0.74]	[70, 20, 10]	0.17	0.23	3.1176	0.60	0.5	3	1.40	1.30	36
25	Ahmed and Sato (2003)- A-M6	TUOFT	[0.21, 0.49, 0.74]	[70, 20, 10]	0.17	0.23	3.1176	0.60	0.5	3	1.60	1.30	36.40
26	Ahmed and Sato (2003)- A-M11	TUOFT	[0.21, 0.49, 0.74]	[70, 20, 10]	0.17	0.23	3.1176	0.60	0.5	3	1.80	1.30	36.70
27	Ahmed and Sato (2003)- B-M2	TUOFT	[0.21, 0.49, 0.74]	[50, 30, 20]	0.18	0.34	3.6111	0.60	0.5	3	1.40	1.30	45.70
28	Ahmed and Sato (2003)- B-M7	TUOFT	[0.21, 0.49, 0.74]	[50, 30, 20]	0.18	0.34	3.6111	0.60	0.5	3	1.60	1.30	67.30
29	Ahmed and Sato (2003)- B-M12	TUOFT	[0.21, 0.49, 0.74]	[50, 30, 20]	0.18	0.34	3.6111	0.60	0.5	3	1.80	1.30	77.40
30	Ahmed and Sato (2003)- C-M8	TUOFT	[0.21, 0.49, 0.74]	[30, 40, 30]	0.19	0.48	3.8421	0.60	0.5	3	1.60	1.30	88.80
31	Ahmed and Sato (2003)- C-M13	TUOFT	[0.21, 0.49, 0.74]	[30, 40, 30]	0.19	0.48	3.8421	0.60	0.5	3	1.80	1.30	113.10
32	Ahmed and Sato (2003)- D-M9	TUOFT	[0.21, 0.49, 0.74]	[20, 40, 40]	0.22	0.54	3.50	0.60	0.5	3	1.60	1.30	91.50
33	Ahmed and Sato (2003)- D-M14	TUOFT	[0.21, 0.49, 0.74]	[20, 40, 40]	0.22	0.54	3.50	0.60	0.5	3	1.80	1.30	113.60
34	Ahmed and Sato (2003)- M16	TUOFT	[0.21, 0.74]	[50, 50]	0.17	0.354	4.8235	0.60	0.5	3	1.58	1.30	45.90
35	Ahmed and Sato (2003)- M17	TUOFT	[0.21, 0.74]	[70, 30]	Not avail.	0.2280	Not avail.	0.60	0.5	3	1.58	1.30	65.30
36	Ahmed and Sato (2003)- M18	TUOFT	[0.21, 1.02]	[70, 30]	Not avail.	0.4530	Not avail.	0.60	0.5	3	1.80	1.30	8.50

Continuation of Table A1

Nr.	Test name	OFT-name	Fractions D_{50} (mm)	Fractions %	D_{10} (mm)	D_{50} (mm)	GI (D_{90}/D_{10})	R	β	T (s)	U_c (m/s)	$T_c(s)$	Net transport rate $\times 10^{-6} (m^2/s)$
37	Ahmed and Sato (2003)- M19	TUOFT	[0.21, 1.02]	[70, 30]	Not avail.	0.4530	Not avail.	0.60	0.5	3	2.00	1.30	-7.00
38	O'Donoghue and Wright (2004a)- X1T50	AOFT	[0.15, 0.28,0.51]	[60, 30, 10]	0.11	0.19	4.0909	0.6301	0.5	5	1.53	2.126	15.00
39	O'Donoghue and Wright (2004a)- X1T75	AOFT	[0.15, 0.28,0.51]	[60, 30, 10]	0.11	0.19	4.0909	0.6301	0.5	7.5	1.53	3.18	21.00
40	O'Donoghue and Wright (2004a)- X2T50	AOFT	[0.15, 0.28,0.51]	[20, 60, 20]	0.14	0.28	3.7857	0.6301	0.5	5	1.53	2.126	46.00
41	O'Donoghue and Wright (2004a)- X2T75	AOFT	[0.15, 0.28,0.51]	[20, 60, 20]	0.14	0.28	3.7857	0.6301	0.5	7.5	1.53	3.18	32.00
42	O'Donoghue and Wright (2004a)- X4T50	AOFT	[0.15, 0.51]	[50, 50]	0.11	0.28	5.5455	0.6301	0.5	5	1.53	2.126	38.00
43	O'Donoghue and Wright (2004a)- X4T75	AOFT	[0.15, 0.51]	[50, 50]	0.11	0.28	5.5455	0.6301	0.5	7.5	1.53	3.18	22.00
44	(Hassan and Ribberink, 2005)- P1	LOWT	[0.21, 0.97]	[70, 30]	0.16	0.24	6.1875	0.6545	0.5	6.5	1.08	2.676	19.50
45	(Hassan and Ribberink, 2005)- P2	LOWT	[0.21, 0.97]	[70, 30]	0.16	0.24	6.1875	0.6545	0.5	6.5	1.23	2.6720	30.50
46	(Hassan and Ribberink, 2005)- P3	LOWT	[0.21, 0.97]	[70, 30]	0.16	0.24	6.1875	0.6545	0.5	6.5	1.59	2.6810	64.30
47	(Hassan and Ribberink, 2005)- S1	LOWT	[0.13, 0.34, 0.97]	[60, 20, 20]	0.11	0.15	9.8182	0.6591	0.5	6.5	0.87	2.67	10.40
48	(Hassan and Ribberink, 2005)- S2	LOWT	[0.13, 0.34, 0.97]	[60, 20, 20]	0.11	0.15	9.8182	0.6667	0.5	6.5	1.14	2.66	19.00
49	(Hassan and Ribberink, 2005)- S3	LOWT	[0.13, 0.34, 0.97]	[60, 20, 20]	0.11	0.15	9.8182	0.6667	0.5	6.5	1.30	2.66	22.40

Continuation of Table A1

Nr.	Test name	OFT-name	Fractions D_{50} (mm)	Fractions %	D_{10} (mm)	D_{50} (mm)	GI (D_{90}/D_{10})	R	β	T (s)	U_c (m/s)	T_c (s)	Net transport rate $\times 10^{-6} (m^2/s)$
50	(Hassan and Ribberink, 2005)-S4	LOWT	[0.13, 0.34, 0.97]	[60, 20, 20]	0.11	0.15	9.8182	0.6667	0.5	6.5	1.63	2.6620	15.40
51	(Hassan and Ribberink, 2005)-K1	LOWT	[0.13, 0.34]	[50, 50]	0.097	0.194	4.1856	0.6638	0.5	6.5	1.54	2.6640	35.20
52	(Hassan and Ribberink, 2005)-K2	LOWT	[0.13, 0.34]	[50, 50]	0.097	0.194	4.1856	0.6667	0.5	6.5	1.10	2.6600	17.40

A.2 Mathematical equations

Drag force coefficient of Ding and Gidaspow (1990):

$$D_{m,w} = \begin{cases} \frac{150\alpha_m \nu \rho_w}{\alpha_w d_m^2} + \frac{1.75\rho_w |\boldsymbol{U_w} - \boldsymbol{U_m}|}{d_m} & \text{if} \quad \alpha_m \geq 0.2 \\ \frac{0.75 C_D \rho_w |\boldsymbol{U_w} - \boldsymbol{U_m}| \alpha_w^{-1.65}}{d_m} & \text{if} \quad \alpha_m < 0.2 \end{cases} \quad \text{(A.1)}$$

where ν is the kinematic viscosity of water ($1.0023 \times 10^{-6} m^2 s^{-1}$ at $20°C$) and C_D is the drag coefficient and defined using Schiller and Naumann (1935)'s formula as:

$$C_D = \begin{cases} \frac{24(1+0.5 Re_m^{0.687})}{Re_m} & \text{if} \quad Re_m \leq 1000 \\ 0.44 & \text{if} \quad Re_m > 1000 \end{cases} \quad \text{(A.2)}$$

where Re_m is the sand fraction Reynolds number, which is given as:

$$Re_m = \alpha_w \frac{|\boldsymbol{U_w} - \boldsymbol{U_m}| d_m}{\nu} \quad \text{(A.3)}$$

$$\boldsymbol{\Delta_t} = -\frac{\nu^t}{\sigma_c} \boldsymbol{\nabla} \alpha_m \quad \text{(A.4)}$$

where σ_c is the Schmidt number and considered as one and ν^t is the turbulent viscosity. The Syamlal (1987) drag force coefficient between sand fractions:

$$D_{m,n} = \frac{3(1 + e_{(m,n)})(\frac{\pi}{2} + C_{f,(m,n)}\frac{\pi^2}{8})(\alpha_m \alpha_n)(\rho_m \rho_n)(d_m + d_n)^2 g_{0,(m,n)}}{2\pi(\rho_m d_m^3 + \rho_n d_n^3)} |\boldsymbol{U_m} - \boldsymbol{U_n}| \quad \text{(A.5)}$$

In Eq.A.5, $e_{(m,n)}$ is the coefficient of restitution (COR) after collision of mth sand fraction with n^{th}, and is defined as the ratio of relative velocity of grains after collision to before collision. Therefore, for an elastic collision COR is one, but because of energy reformation to heat or deformation, it has usually a positive value smaller than one. It is given as:

$$e_{(m,n)} = \frac{|\boldsymbol{U_{m,a}} - \boldsymbol{U_{n,a}}|}{|\boldsymbol{U_{m,b}} - \boldsymbol{U_{n,b}}|} \quad \text{(A.6)}$$

For two identical spherical grains from soda lime glass with diameter of 3.18 mm and $\rho_g = 2500 \ kgm^{-3}$, Foerster et al. (1994) measured $e = 0.97$ and for cellulose acetate with size of 6 mm as $e = 0.87$. However, for two sand grains with identical sizes or different diameters there is no literature recommended/measured value.

$C_{f,(m,n)}$ is the friction coefficient between sand grains from different fractions. Zhou et al. (2002) performed a series of experimental and numerical studies to find the internal friction factor for mono-sized glass beads with $\rho = 2500 \ kgm^{-3}$. Based on these results, $C_{f,(m,n)}$ for an angle of repose equal to $35°$ is considered as 0.5 in this thesis. However, it needs more research to understand the role of $C_{f,(m,n)}$ for different sizes of sand fractions. The developed solver in this thesis takes the coefficients independently from the source code, and hence it can be changed for a particular test case after compiling the solver too.

$g_{0,(m,n)}$ is the radial distribution function, which estimates the probability of collisions among sand fractions and therefore is defined as a function of volumetric concentration of sand fractions in a numerical cell. For uniform sands usually the probability function of

Carnahan and Starling (1969) is used as was also applied in sedFoam (Cheng and Hsu, 2014). It is defined as:

$$g_{0,ss} = \frac{2 - \alpha}{2(1 - \alpha)^3} \tag{A.7}$$

The probability of collisions among sand grains from different fractions is defined based on the proposed relationship by Syamlal et al. (1993), which is defined as:

$$g_{0,(m,n)} = \frac{1}{(1 - \alpha)} + \frac{3(\sum_{m=1}^{N} \frac{\alpha_m}{d_m})}{(1 - \alpha)^2(d_m + d_n)} d_m d_n \tag{A.8}$$

$$P_m^c = 2\rho_m T_m g_{0,(m,m)} \alpha_m^2 (1 + e_{(m,m)}) \tag{A.9}$$

$$P_m^f = \begin{cases} 0 & \text{if} \quad \alpha < \alpha_c \\ k_{(m,m)} \frac{(\alpha_m - \alpha_{m,c})^{l(m,m)}}{(\alpha_{m,max} - \alpha_m)^{h(m,m)}} & \text{if} \quad \alpha \geq \alpha_c \end{cases} \tag{A.10}$$

$$\mu_m^c = 0.5\rho_m \ d_m \sqrt{T_m} \left(\frac{\sqrt{\pi}}{3(3 - e_{(m,m)})}(1 + 0.4(1 + e_{(m,m)})(3e_{(m,m)} - 1)\alpha_m g_{0,(m,m)} + \right.$$
$$\left. \frac{8\alpha_m \ g_{0,(m,m)(1+e_{m,m})}}{5\sqrt{\pi}}) \right) \tag{A.11}$$

and λ_m^c is the bulk viscosity of mth fraction in collisional part of transport, which is given by Syamlal et al. (1993) as:

$$\lambda_m^c = \alpha_m \sqrt{T_m} \ g_{0,(m,m)} \left(\frac{0.75\rho_m d_m(1 + e_{(m,m)})}{\sqrt{\pi}} \right) \tag{A.12}$$

$$\tilde{\boldsymbol{\chi_m}} = \frac{1}{2}(\boldsymbol{\nabla U_m} + \boldsymbol{\nabla U_m^T}) - \frac{1}{3}(\boldsymbol{\nabla . U_m})\tilde{\boldsymbol{I}} \tag{A.13}$$

$$k_m = \frac{15d_m\rho_m\alpha_m\sqrt{\pi T_m}}{4(41 - 33\eta_m)} \left(1 + \frac{12}{5}\eta_m^2(4\eta_m - 3)\alpha_m \ g_{0,(m,m)} \right.$$
$$\left. + \frac{16}{15\pi}(41 - 33\eta_m)\eta_m\alpha_m \ g_{0,(m,m)} \right) \tag{A.14}$$

where

$$\eta_m = \frac{1}{2}(1 + e_{(m,m)}) \tag{A.15}$$

$$\gamma_m = k_{\gamma_m}\alpha_m^2 T_m^{(3/2)} \tag{A.16}$$

where k_{γ_m} is given as:

$$k_{\gamma_m} = \frac{12\rho_m \ g_{0,(m,m)}(1 - e_{(m,m)}^2)}{d_m \ \sqrt{\pi}} \tag{A.17}$$

A.3   Particles collision and interparticle drag force coefficient

The Kinetic Theory of Granular Flow (KTGF) is based on the developed equations for two particles collision. Fig. A.1 shows the collision of two particles, which is the basis of available researches in such two-phase flow model in literature. In this figure, the vector $\boldsymbol{b}$ is the unit vector in the direction of the connecting line between centers of the pair particles. Particle j is located in position $\boldsymbol{r}$ and therefore the position vector of the particle k is $\boldsymbol{r} - \sigma\boldsymbol{b}$. The vectors $\boldsymbol{c_k}$ and $\boldsymbol{c_j}$ represent the velocity vectors of k and j particles, respectively. σ is the length of the connecting line between centers of particles, therefore: $\sigma = (d_k + d_j)/2$. The rate of collisional momentum transfer per unit volume was calculated by Syamlal (1987) as:

$$I_{kj} = \int_{c_{kj}.b>0} \sigma f_k \sigma f_j g_{kj} \Delta m (c_{kj}.b) \; db \; dc_k \; dc_j \tag{A.18}$$

where $\boldsymbol{c_{kj}} = \boldsymbol{c_k} - \boldsymbol{c_j}$ and the condition of $\boldsymbol{c_{kj}}.\boldsymbol{b} > 0$ provides the collision between particle
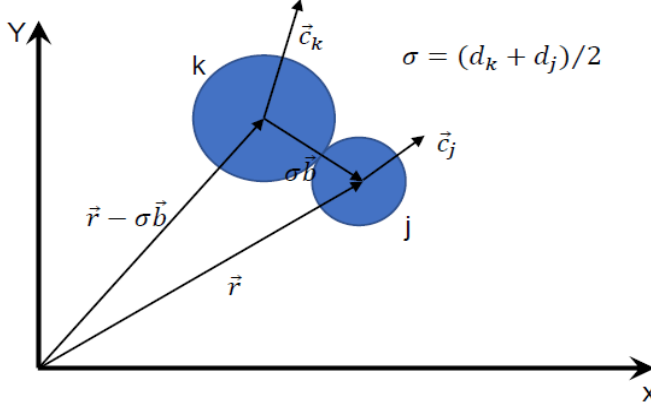

Figure A.1: Collision between two particles (after Syamlal (1987)-a principal sketch).

k and j. f_k and f_j are the probability velocity distribution functions of particles and $\boldsymbol{\Delta m}$ is the transferred momentum between particles. Syamlal (1987) assumed that all particles of each fractions have the same velocity and therefore proposed the velocity distribution function using Dirac delta function as:

$$f_k = 6 \; \alpha_k \; \delta_f (\boldsymbol{c_k} - \boldsymbol{v_k})/(\pi \; d_k{}^3) \tag{A.19}$$

where $6\alpha_k/(\pi \; d_k{}^3)$ in Eq. A.19 is due to the prerequisite of a velocity distribution function to satisfy the following condition:

$$\iiint_{c_k} f_k \, \boldsymbol{dc_k} = n_k \tag{A.20}$$

where n_k is the number density function of k-system of particles and is defined as:

$$m_k n_k = \rho_k \; \alpha_k \tag{A.21}$$

then:

$$n_k = \rho_k \alpha_k / m_k \;\; and \;\; m_k = \rho_k v_k \tag{A.22}$$

163

therefore:

$$n_k = \alpha_k / v_k \tag{A.23}$$

using the particle form assumption as spheres:

$$n_k = 6\alpha_k / (\pi d_k{}^3) \tag{A.24}$$

To calculate the interchanged momentum between two particles in Eq. A.18, it is assumed that the collision between particles is inelastic and therefore for a schematic collision between particles as illustrated in Fig. A.1, the interchanged momentum ($\boldsymbol{J}$) could be calculated as:

$$\begin{cases} m_k \boldsymbol{c_k} = m_k \boldsymbol{c'_k} + \boldsymbol{J} \\ m_j \boldsymbol{c_j} = m_j \boldsymbol{c'_j} - \boldsymbol{J} \end{cases} \tag{A.25}$$

where $\boldsymbol{c'_k}$ and $\boldsymbol{c'_j}$ are the velocities after collision for particles k and j, respectively. From equation system A.25 the $\boldsymbol{c_k}$ and $\boldsymbol{c_j}$ are written as:

$$\begin{cases} \boldsymbol{c_k} = \boldsymbol{c'_k} + \boldsymbol{J}/m_k \\ \boldsymbol{c_j} = \boldsymbol{c'_j} - \boldsymbol{J}/m_j \end{cases} \tag{A.26}$$

and by subtracting the equations in the equation system A.26, a new equation is derived as:

$$\boldsymbol{c_{kj}} = \boldsymbol{c'_{kj}} + \boldsymbol{J}(1/m_k + 1/m_j) \tag{A.27}$$

or

$$\boldsymbol{c_{kj}} = \boldsymbol{c'_{kj}} + \boldsymbol{J}((m_k + m_j)/m_k m_j) \tag{A.28}$$

using the definition for the restitution coefficient:

$$e = -(\boldsymbol{c'_j} - \boldsymbol{c'_k})/(\boldsymbol{c_j} - \boldsymbol{c_k}) = -\boldsymbol{c'_{kj}}/\boldsymbol{c_{kj}} \tag{A.29}$$

Eq. A.28 is written as:

$$\boldsymbol{c_{kj}}(1 + e) = \boldsymbol{J}((m_k + m_j)/m_k m_j) \tag{A.30}$$

or

$$\boldsymbol{J} = \boldsymbol{c_{kj}}(1 + e)(m_k m_j / (m_k + m_j)) \tag{A.31}$$

and in the same direction of collision ($\boldsymbol{b}$), it is written as:

$$\boldsymbol{J.b} = \boldsymbol{c_{kj}.b}(1 + e)(m_k m_j / (m_k + m_j)) \tag{A.32}$$

for the tangent direction at the collision point (perpendicular to the collision direction ($\boldsymbol{b}$)), using the friction coefficient between two particles (μ_N), the interchanged momentum $\boldsymbol{J_t}$ could be written as:

$$\boldsymbol{J_t} = \mu_N(\boldsymbol{J.b}) \tag{A.33}$$

and finally:

$$\boldsymbol{J} = (\boldsymbol{J.b})\boldsymbol{b} + (\boldsymbol{J_t})\boldsymbol{t_n} \tag{A.34}$$

where $\boldsymbol{b}$ and $\boldsymbol{t_n}$ are the unit vectors in the collision and tangent direction, respectively. To find the direction of $\boldsymbol{t_n}$, Syamlal (1987) used the method of Ahmadi and Shahinpoor (1983) as:

$$\boldsymbol{t_n} = \boldsymbol{b} \times (\boldsymbol{c_{kj}} \times \boldsymbol{b})/|\boldsymbol{b} \times (\boldsymbol{c_{kj}} \times \boldsymbol{b})| \tag{A.35}$$

therefore the exchanged momentum is written as:

$$\Delta \boldsymbol{m} = m_k(\boldsymbol{c_k\prime} - \boldsymbol{c_k}) = -\boldsymbol{J} = -\boldsymbol{c_{kj}.b}(1+e)(m_k m_j/(m_k + m_j))\, \boldsymbol{b} -$$
$$\mu_N \boldsymbol{c_{kj}.b}(1+e)(m_k m_j/(m_k + m_j))\, \boldsymbol{t_n} \tag{A.36}$$

or

$$\Delta \boldsymbol{m} = -\boldsymbol{c_{kj}.b}(1+e)(m_k m_j/(m_k + m_j))\, (\boldsymbol{b} +$$
$$\mu_N\, \boldsymbol{b} \times (\boldsymbol{c_{kj}} \times \boldsymbol{b})/|\boldsymbol{b} \times (\boldsymbol{c_{kj}} \times \boldsymbol{b})|\, \boldsymbol{t_n}) \tag{A.37}$$

using the vector rules of production, the Eq. A.35 could be written as:

$$\boldsymbol{t_n} = (\boldsymbol{c_{kj}} - (\boldsymbol{c_{kj}.b})\boldsymbol{b})/|(\boldsymbol{c_{kj}} - (\boldsymbol{c_{kj}.b})\boldsymbol{b})| \tag{A.38}$$

then the Eq. A.37 using Eq. A.38 is written as:

$$\Delta \boldsymbol{m} = -\boldsymbol{c_{kj}.b}(1+e)(m_k m_j/(m_k + m_j))\, (\boldsymbol{b} +$$
$$\mu_N\, (\boldsymbol{c_{kj}} - (\boldsymbol{c_{kj}.b})\boldsymbol{b})/|(\boldsymbol{c_{kj}} - (\boldsymbol{c_{kj}.b})\boldsymbol{b})|) \tag{A.39}$$

Substituting Eq. A.39 in Eq. A.18 :

$$\boldsymbol{I_{kj}} = -36/(\pi^2 d_k^3 d_j^3(m_k + m_j))(\sigma^2)(1+e)(m_k m_j \alpha_k \alpha_j\, g_{kj})$$
$$\int_{\boldsymbol{c_{kj}.b}>0} (\boldsymbol{c_{kj}.b})^2(\boldsymbol{b} + \mu_N \boldsymbol{t_n})\delta_f(\boldsymbol{c_k} - \boldsymbol{v_k})\delta_f(\boldsymbol{c_j} - \boldsymbol{v_j})\, \boldsymbol{db}\, \boldsymbol{dc_k}\, \boldsymbol{dc_j} \tag{A.40}$$

which is the Eq. 19 in Syamlal (1987). Syamlal (1987) solved the integral of Eq. A.40 and proposed $\boldsymbol{I_{kj}}$ as:

$$\boldsymbol{I_{kj}} = -36/(\pi^2 d_k^3 d_j^3(m_k + m_j))(\sigma^2)(1+e)(\pi/2 + \mu_N \pi^2/8)(m_k m_j \alpha_k \alpha_j\, g_{kj})|\boldsymbol{v_{kj}}|\, \boldsymbol{v_{kj}} \tag{A.41}$$

and then because of $\boldsymbol{I_{kj}} = -C_D \boldsymbol{v_{kj}}$, therefore the interparticle drag force coefficient based on the Syamlal (1987) research is:

$$C_D = 3(1+e)\rho_k \rho_j \alpha_k \alpha_j g_{kj}(\pi/2 + \mu_N \pi^2/8)|\boldsymbol{v_{kj}}|(d_k + d_j)^2/(2\pi(\rho_k d_k^3 + \rho_j d_j^3)) \tag{A.42}$$

Based on Ding and Gidaspow (1990), the 3D-VDF of Maxwell (1860)-Boltzmann (1872) is written as:

$$f_k = n/(2\pi T_k)^{(3/2)}\, exp(-(\boldsymbol{c_k} - \boldsymbol{v_k})^2/(2T_k)) \tag{A.43}$$

Chapman et al. (1970) defined the unit vector $\mathbf{b}$ and its differential as:

$$\boldsymbol{b} = \boldsymbol{h}cos\theta + \boldsymbol{i}sin\theta\, cos\phi + \boldsymbol{j}sin\theta\, sin\phi$$
$$,$$
$$\boldsymbol{db} = sin\theta\, d\theta\, d\phi \tag{A.44}$$

A.3.1 Solving the first integral in Eq. 4.21:

$$\int_{c_{kj}.b>0} ((C_{kj} + v_{kj})cos\theta)^2 (hcos\theta + isin\theta\ cos\phi + jsin\theta\ sin\phi)$$

$$exp(-((C_k)^2/(2T_k) + (C_j)^2/(2T_j)))\ dC_k\ dC_j\ sin\theta\ d\theta\ d\phi =$$

$$\int_{c_{kj}.b>0} ((C_{kj} + v_{kj}))^2 (cos\theta)^2\ sin\theta\ (hcos\theta + isin\theta\ cos\phi + jsin\theta\ sin\phi)$$

$$exp(-((C_k)^2/(2T_k) + (C_j)^2/(2T_j)))\ dC_k\ dC_j\ d\theta\ d\phi = \tag{A.45}$$

$$\int_{c_{kj}.b>0} (C_{kj}{}^2 + v_{kj}{}^2 + 2C_{kj}v_{kj})(cos\theta)^2\ sin\theta\ (hcos\theta + isin\theta\ cos\phi + jsin\theta\ sin\phi)$$

$$exp(-((C_k)^2/(2T_k) + (C_j)^2/(2T_j)))\ dC_k\ dC_j\ d\theta\ d\phi$$

and

$$C_{kj}{}^2 = (C_k - C_j)^2 = C_k{}^2 + C_j{}^2 - 2C_kC_j \tag{A.46}$$

therefore the first part of the integral in Eq. A.45 is written as:

$$\int_{c_{kj}.b>0} (C_k{}^2 + C_j{}^2 - 2C_kC_j)(cos\theta)^2\ sin\theta\ (hcos\theta + isin\theta\ cos\phi + jsin\theta\ sin\phi)$$

$$exp(-((C_k)^2/(2T_k) + (C_j)^2/(2T_j)))\ dC_k\ dC_j\ d\theta\ d\phi \tag{A.47}$$

using:

$$\int_{-\infty}^{+\infty} exp(-\lambda x^2)\ dx = \sqrt{\pi/\lambda} \tag{A.48}$$

,

$$\int_{-\infty}^{+\infty} x^2\ exp(-\lambda x^2)\ dx = (1/(2\lambda))\sqrt{\pi/\lambda} \tag{A.49}$$

and

$$\int_{-\infty}^{+\infty} x\ exp(-\lambda x^2)\ dx = 0 \tag{A.50}$$

then

$$\int_{-\infty}^{+\infty} C_k{}^2\ exp(-C_k{}^2/(2T_k))\ dC_k = T_k\sqrt{2\pi T_k} \tag{A.51}$$

and for the second term in Eq. A.47:

$$\int_{-\infty}^{+\infty} exp(-C_k{}^2/(2T_k))\ dC_k = \sqrt{2\pi T_k} \tag{A.52}$$

and for the third term:

$$\int_{-\infty}^{+\infty} C_k exp(-C_k{}^2/(2T_k))\ dC_k = 0 \tag{A.53}$$

then:

$$\int_{-\infty}^{+\infty}\int_{-\infty}^{+\infty} (C_k{}^2 + C_j{}^2 - 2C_kC_j)\ exp(-((C_k)^2/(2T_k)+$$

$$(C_j)^2/(2T_j)))\ dC_k\ dC_j =$$

$$T_k\sqrt{2\pi T_k}\int_{-\infty}^{+\infty} exp(-C_j{}^2/(2T_j))dC_j + \sqrt{2\pi T_k}\int_{-\infty}^{+\infty} C_j{}^2\ exp(-C_j{}^2/(2T_j)dC_j \tag{A.54}$$

$$-2(0) = T_k\sqrt{2\pi T_k}\ \sqrt{2\pi T_j} + \sqrt{2\pi T_k}\ T_j\ \sqrt{2\pi T_j} = 2\pi T_k\sqrt{T_kT_j} + 2\pi T_j\sqrt{T_kTj}$$

$$= 2\pi\ \sqrt{T_kT_j}(T_k + T_j)$$

Integration of the second term in Eq. A.45 :

$$\boldsymbol{v_{kj}}^2 \int_{-\infty}^{+\infty} \int_{-\infty}^{+\infty} exp(-((\boldsymbol{C_k})^2/(2T_k) + (\boldsymbol{C_j})^2/(2T_j))) \, d\boldsymbol{C_k} \, d\boldsymbol{C_j} =$$

$$\boldsymbol{v_{kj}}^2 \sqrt{2\pi T_k} \sqrt{2\pi T_j} = 2\boldsymbol{v_{kj}}^2 \pi \sqrt{T_k T_j} \tag{A.55}$$

Integration of the third term in Eq. A.45:

$$\int_{-\infty}^{+\infty} \int_{-\infty}^{+\infty} 2 \, \boldsymbol{v_{kj}} \boldsymbol{C_{kj}} \, exp(-((\boldsymbol{C_k})^2/(2T_k) + (\boldsymbol{C_j})^2/(2T_j))) \, d\boldsymbol{C_k} \, d\boldsymbol{C_j} =$$

$$\int_{-\infty}^{+\infty} \int_{-\infty}^{+\infty} 2 \, \boldsymbol{v_{kj}}(\boldsymbol{C_k} - \boldsymbol{C_j}) \, exp(-((\boldsymbol{C_k})^2/(2T_k) + (\boldsymbol{C_j})^2/(2T_j)))$$

$$d\boldsymbol{C_k} \, d\boldsymbol{C_j} = 2 \, \boldsymbol{v_{kj}} \int_{-\infty}^{+\infty} \int_{-\infty}^{+\infty} \boldsymbol{C_k} \, exp(-((\boldsymbol{C_k})^2/(2T_k) + (\boldsymbol{C_j})^2/(2T_j))) d\boldsymbol{C_k} \, d\boldsymbol{C_j}$$

$$-2 \, \boldsymbol{v_{kj}} \int_{-\infty}^{+\infty} \int_{-\infty}^{+\infty} \boldsymbol{C_j} \, exp(-((\boldsymbol{C_k})^2/(2T_k) + (\boldsymbol{C_j})^2/(2T_j))) \, d\boldsymbol{C_k} \, d\boldsymbol{C_j} = 0 \tag{A.56}$$

Then the C-dependent terms in Eq. A.47 is written as:

$$\int_{-\infty}^{+\infty} \int_{-\infty}^{+\infty} (\boldsymbol{C_k}^2 + \boldsymbol{C_j}^2 - 2\boldsymbol{C_k}\boldsymbol{C_j}) \, exp(-((\boldsymbol{C_k})^2/(2T_k) + (\boldsymbol{C_j})^2/(2T_j)))$$

$$d\boldsymbol{C_k} \, d\boldsymbol{C_j} = 2\pi \, \sqrt{T_k T_j}(T_k + T_j) + 2\boldsymbol{v_{kj}}^2 \pi \sqrt{T_k T_j} = 2\pi \sqrt{T_k T_j}(T_k + T_j + \boldsymbol{v_{kj}}^2) \tag{A.57}$$

Now, it is tried to solve the $\theta-$ and $\phi-$ dependent terms in the integral of Eq. A.47. To satisfy the condition of $\boldsymbol{c_{kj}}.\boldsymbol{b} > 0$, θ should be $0 \leq \theta \leq \pi/2$ and $0 \leq \phi \leq 2\pi$. Therefore, the angular part of Eq. A.47 is written as:

$$\int_0^{2\pi} \int_0^{\pi/2} (cos\theta)^2 \, sin\theta \, (\boldsymbol{h}cos\theta + \boldsymbol{i}sin\theta \, cos\phi + \boldsymbol{j}sin\theta \, sin\phi) \, d\theta \, d\phi \tag{A.58}$$

because of :

$$\int_0^{2\pi} cos\phi \, d\phi = 0 \ , \ \int_0^{2\pi} sin\phi \, d\phi = 0 \tag{A.59}$$

the integral in Eq. A.58 is simplified as:

$$\int_0^{2\pi} \int_0^{\pi/2} (cos\theta)^2 \, sin\theta \, (\boldsymbol{h}cos\theta) \, d\theta \, d\phi = \int_0^{2\pi} \int_0^{\pi/2} \boldsymbol{h}(cos\theta)^3 \, sin\theta \, d\theta \, d\phi$$

$$= \int_0^{2\pi} \boldsymbol{h}(-(cos\theta)^4/4)\Big|_0^{\pi/2} \, d\phi = \boldsymbol{h}(1/4)(2\pi) = (\pi/2)\boldsymbol{h} \tag{A.60}$$

where $\boldsymbol{h}$ is the unit vector in the direction of $\boldsymbol{C_{kj}}$.

A.3.2 Solving the second integral in Eq. 4.21:

Now it is tried to solve the second part of the integration in Eq. 4.21:

$$\int_0^{2\pi} \int_0^{\pi/2} (cos\theta)^2 sin\theta \, (\mu_N \boldsymbol{t}) \, d\theta \, d\phi = \int_0^{2\pi} \int_0^{\pi/2} (cos\theta)^2 sin\theta \, (\mu_N \, ((\boldsymbol{C_{kj}} + \boldsymbol{v_{kj}})$$
$$-|\boldsymbol{C_{kj}} + \boldsymbol{v_{kj}}|cos\theta \, (\boldsymbol{h}cos\theta + \boldsymbol{i}sin\theta cos\phi + \boldsymbol{j}sin\theta \, sin\phi)/|((\boldsymbol{C_{kj}} + \boldsymbol{v_{kj}})$$
$$-|\boldsymbol{C_{kj}} + \boldsymbol{v_{kj}}|cos\theta \, (\boldsymbol{h}cos\theta + \boldsymbol{i}sin\theta cos\phi + \boldsymbol{j}sin\theta \, sin\phi)|)d\theta \, d\phi =$$
$$\int_0^{2\pi} \int_0^{\pi/2} \mu_N \, (cos\theta)^2 sin\theta \, (\, (|(\boldsymbol{C_{kj}} + \boldsymbol{v_{kj}})|\boldsymbol{h}$$
$$-|\boldsymbol{C_{kj}} + \boldsymbol{v_{kj}}|cos\theta \, (\boldsymbol{h}cos\theta + \boldsymbol{i}sin\theta cos\phi + \boldsymbol{j}sin\theta \, sin\phi)/$$
$$(||(\boldsymbol{C_{kj}} + \boldsymbol{v_{kj}})|\boldsymbol{h} - |\boldsymbol{C_{kj}} + \boldsymbol{v_{kj}}|cos\theta \, (\boldsymbol{h}cos\theta + \boldsymbol{i}sin\theta cos\phi + \boldsymbol{j}sin\theta \, sin\phi)|)d\theta \, d\phi$$
$$= \int_0^{2\pi} \int_0^{\pi/2} \mu_N(\boldsymbol{h} - \boldsymbol{h}(cos\theta)^2 - \boldsymbol{i}sin\theta cos\theta cos\phi - \boldsymbol{j}sin\theta cos\theta sin\phi)$$
$$/(|\boldsymbol{h} - \boldsymbol{h}(cos\theta)^2 - \boldsymbol{i}sin\theta cos\theta cos\phi - \boldsymbol{j}sin\theta cos\theta sin\phi|)(cos\theta)^2 sin\theta \, d\theta d\phi \quad (A.61)$$

and we know:

$$|\boldsymbol{h} - \boldsymbol{h}(cos\theta)^2 - \boldsymbol{i}sin\theta cos\theta cos\phi - \boldsymbol{j}sin\theta cos\theta sin\phi|=$$
$$\sqrt{(1 - (cos\theta)^2)^2 + (-sin\theta cos\theta cos\phi)^2 + (-sin\theta cos\theta sin\phi)^2} =$$
$$\sqrt{(sin\theta)^4 + (1/4)(sin2\theta)^2(cos\phi)^2 + (1/4)(sin2\theta)^2(sin\phi)^2} = \quad (A.62)$$
$$\sqrt{(sin\theta)^4 + (1/4)(sin2\theta)^2((cos\phi)^2 + (sin\phi)^2)} =$$
$$\sqrt{(sin\theta)^4 + (1/4)(sin2\theta)^2}$$

using Eq. A.59 and Eq. A.62, the simplification of the integral in Eq. A.61 is followed as:

$$\int_0^{2\pi} \int_0^{\pi/2} \mu_N\boldsymbol{h}(1 - (cos\theta)^2)(cos\theta)^2 sin\theta/(\sqrt{((sin\theta)^4 + (1/4)(sin2\theta)^2)})d\theta d\phi =$$
$$\int_0^{2\pi} \int_0^{\pi/2} \mu_N\boldsymbol{h}((sin\theta)^2(cos\theta)^2)(sin\theta)/(\sqrt{((sin\theta)^4 + (1/4)(sin2\theta)^2)})d\theta d\phi =$$
$$\int_0^{2\pi} \int_0^{\pi/2} \mu_N\boldsymbol{h}((sin\theta cos\theta)^2)sin\theta/(\sqrt{((sin\theta)^4 + (1/4)(sin2\theta)^2)})d\theta d\phi = \quad (A.63)$$
$$\int_0^{2\pi} \int_0^{\pi/2} \mu_N\boldsymbol{h}((1/4)(sin2\theta)^2)sin\theta/(\sqrt{((sin\theta)^4 + (1/4)(sin2\theta)^2)})d\theta d\phi$$

extending the denominator in the final result of Eq. A.63:

$$\sqrt{(sin\theta)^4 + (1/4)(sin2\theta)^2} = \sqrt{(1 - (cos\theta)^2)^2 + (1/4)(sin2\theta)^2} =$$
$$\sqrt{(1 - (1 + cos2\theta)/2)^2 + (1/4)(sin2\theta)^2} = \sqrt{((2 - 1 - cos2\theta)/2)^2 + (1/4)(sin2\theta)^2} =$$
$$\sqrt{((1 - cos2\theta)/2)^2 + (1/4)(sin2\theta)^2} = \sqrt{(1/4)(1 - cos2\theta)^2 + (1/4)(sin2\theta)^2} =$$
$$(1/2)\sqrt{1 + (cos2\theta)^2 - 2cos2\theta + (sin2\theta)^2} = (1/2)\sqrt{2 - 2cos2\theta} = (1/\sqrt{2})\sqrt{(1 - cos2\theta)}$$
$$(A.64)$$

Then the Eq. A.63 using the result of the Eq. A.64 is written as:

$$\int_0^{2\pi} \int_0^{\pi/2} \mu_N\boldsymbol{h}((1/4)(sin2\theta)^2)sin\theta/((1/\sqrt{2})\sqrt{1 - cos2\theta})d\theta d\phi \quad (A.65)$$

168

Using the following trigonometric rules:

$$sin\theta = \sqrt{1-(cos\theta)^2}$$

$$cos2\theta = (cos\theta)^2 - (sin\theta)^2 = (cos\theta)^2 - 1 + (cos\theta)^2 = 2(cos\theta)^2 - 1 \tag{A.66}$$

and

$$(cos\theta)^2 = (1 + cos2\theta)/2 \tag{A.67}$$

then

$$1 - (cos\theta)^2 = 1 - (1 + cos2\theta)/2 = (1 - cos2\theta)/2 \tag{A.68}$$

therefore:

$$sin\theta = \sqrt{1-(cos\theta)^2} = \sqrt{(1-cos2\theta)/2} = (1/\sqrt{2})\sqrt{1-cos2\theta} \tag{A.69}$$

and Eq.A.65 is written as:

$$\int_0^{2\pi} \int_0^{\pi/2} \mu_N \boldsymbol{h}((1/4)(sin2\theta)^2)(1/\sqrt{2})\sqrt{1-cos2\theta}/((1/\sqrt{2})\sqrt{1-cos2\theta})d\theta d\phi =$$
$$\int_0^{2\pi} \int_0^{\pi/2} \mu_N \boldsymbol{h}((1/4)(sin2\theta)^2)d\theta d\phi = \int_0^{2\pi} \int_0^{\pi/2} \mu_N \boldsymbol{h}(1/4)(1-cos4\theta)/2d\theta d\phi =$$
$$\mu_N \boldsymbol{h}((1/4)\int_0^{2\pi} (\theta/2 - (1/8)sin4\theta)\Big|_0^{\pi/2} d\phi) = \mu_N \boldsymbol{h}(1/4)(\pi/4)(2\pi) = (\mu_N\pi^2/8)\boldsymbol{h} \tag{A.70}$$

A.4 Mixture approach

$$\sum_{m=1}^N \frac{\partial\alpha_m}{\partial t} + \sum_{m=1}^N \boldsymbol{\nabla}.(\alpha_m\boldsymbol{U_m}) = 0 \tag{A.71}$$

and

$$\sum_{m=1}^N \frac{\partial(\alpha_m\rho_m\boldsymbol{U_m})}{\partial t} + \sum_{m=1}^N \boldsymbol{\nabla}.(\alpha_m\rho_m\boldsymbol{U_m}\boldsymbol{U_m}) = -\sum_{m=1}^N \alpha_m\boldsymbol{\nabla}P_w - \sum_{m=1}^N \boldsymbol{\nabla}P_m +$$
$$\sum_{m=1}^N \boldsymbol{\nabla}.\tilde{\boldsymbol{\tau_m}} + \sum_{m=1}^N \boldsymbol{M_{m,w}} + \sum_{m=1}^N \boldsymbol{M_{m,n}} + \sum_{m=1}^N \alpha_m\rho_m\boldsymbol{g} \tag{A.72}$$

because of $\sum_{m=1}^N \alpha_m = \alpha_s$, Eq. A.71 could be simplified as:

$$\frac{\partial\alpha_s}{\partial t} + \boldsymbol{\nabla}.(\alpha_s\boldsymbol{U_s}) = 0 \tag{A.73}$$

where:

$$(\alpha_s\boldsymbol{U_s}) = \sum_{m=1}^N (\alpha_m\boldsymbol{U_m}) \tag{A.74}$$

The second term on LHS of Eq. A.72 could be simplified using relative velocity of sand fractions (U_{ms}) as:

$$U_{ms} = U_m - U_s \tag{A.75}$$

then:

$$\alpha_m U_{ms} = \alpha_m U_m - \alpha_m U_s \tag{A.76}$$

now by summation over Eq. A.76, it could be simplified as:

$$\sum_{m=1}^{N} \alpha_m U_{ms} = \sum_{m=1}^{N} \alpha_m U_m - \sum_{m=1}^{N} \alpha_m U_s \tag{A.77}$$

and using Eq. A.74, Eq. A.77 is simplified as:

$$\sum_{m=1}^{N} \alpha_m U_{ms} = \alpha_s U_s - \alpha_s U_s = 0 \tag{A.78}$$

then:

$$\sum_{m=1}^{N} \alpha_m U_{ms} = 0 \tag{A.79}$$

now the second part of the LHS could be rewritten as:

$$(\alpha_m \rho_m U_m U_m) = (\alpha_m \rho_m (U_{ms} + U_s)(U_{ms} + U_s)) \tag{A.80}$$

and:

$$\begin{aligned}(\alpha_m \rho_m U_m U_m) = \alpha_m \rho_m U_{ms} U_{ms} + \alpha_m \rho_m U_{ms} U_s \\ + \alpha_m \rho_m U_s U_{ms} + \alpha_m \rho_m U_s U_s\end{aligned} \tag{A.81}$$

now by summation over Eq. A.81 and using Eq. A.79 the second part of LHS in Eq. A.72 could be rewritten as:

$$\sum_{m=1}^{N} \nabla.(\alpha_m \rho_m U_m U_m) = \sum_{m=1}^{N} \nabla.(\alpha_m \rho_m U_{ms} U_{ms}) + \nabla.(\alpha_s \rho_s U_s U_s) \tag{A.82}$$

U_{sm} could represent the difference between the overall sand-phase velocity and the velocity of m th sand fraction, therefore it is called diffusive velocity. The first term on the RHS of Eq. A.82 could represent the diffusive shear stress for sand-phase (like Reynolds shear stresses), then:

$$\tilde{\tau_{Ds}} = -\sum_{m=1}^{N} (\alpha_m \rho_m U_{sm} U_{sm}) \tag{A.83}$$

The usual sand-phase shear-stress could be defined as:

$$\tilde{\tau_s} = \sum_{m=1}^{N} \tilde{\tau_m} \tag{A.84}$$

Likewise, the pressure of sand-phase could also be defined as:

$$P_s = \sum_{m=1}^{N} P_m \tag{A.85}$$

Therefore, the Eq. A.72 could be simplified as:

$$\frac{\partial(\alpha_s\rho_s\boldsymbol{U_s})}{\partial t} + \boldsymbol{\nabla}.(\alpha_s\rho_s\boldsymbol{U_s}\boldsymbol{U_s}) = -\alpha_s\boldsymbol{\nabla}P_w - \boldsymbol{\nabla}P_s$$
$$+\boldsymbol{\nabla}.(\tilde{\boldsymbol{\tau_s}} + \boldsymbol{\tau\tilde{_{Ds}}}) + \alpha_s\rho_s\boldsymbol{g} + \sum_{m=1}^{N} M_{m,w} \tag{A.86}$$

The LHS of Eq. A.86 could be written as:

$$\frac{\partial(\alpha_s\rho_s\boldsymbol{U_s})}{\partial t} + \boldsymbol{\nabla}.(\alpha_s\rho_s\boldsymbol{U_s}\boldsymbol{U_s}) = \alpha_s\rho_s\frac{\partial}{\partial t}(\boldsymbol{U_s}) + \alpha_s\rho_s(\boldsymbol{\nabla}.\boldsymbol{U_s})\boldsymbol{U_s} \tag{A.87}$$

and the pressure gradient for water-phase from Eq. A.86 and Eq. A.87 could be written as:

$$\boldsymbol{\nabla}P_w = (\frac{1}{\alpha_s}) \left(-\alpha_s\rho_s\frac{\partial}{\partial t}(\boldsymbol{U_s}) - \alpha_s\rho_s(\boldsymbol{\nabla}.\boldsymbol{U_s})\boldsymbol{U_s} \right.$$
$$\left. -\boldsymbol{\nabla}P_s + \boldsymbol{\nabla}.(\tilde{\boldsymbol{\tau_s}} + \boldsymbol{\tau\tilde{_{Ds}}}) + \alpha_s\rho_s\boldsymbol{g} + \sum_{m=1}^{N} \boldsymbol{M_{m,w}} \right) \tag{A.88}$$

Moreover, Eq. 4.10 could be written as:

$$\alpha_m\rho_m\frac{\partial}{\partial t}(\boldsymbol{U_m}) + \alpha_m\rho_m(\boldsymbol{\nabla}.\boldsymbol{U_m})\boldsymbol{U_m} = -\alpha_m\boldsymbol{\nabla}P_w - \boldsymbol{\nabla}P_m + \boldsymbol{\nabla}.\tilde{\boldsymbol{\tau_m}} + \alpha_m\rho_m\boldsymbol{g}+$$
$$\boldsymbol{M_{m,w}} + \sum_{m=1,m\neq n}^{N} \boldsymbol{M_{m,n}} \tag{A.89}$$

by replacing the pressure gradient from Eq. A.88 in Eq. A.89, it could be written as:

$$\alpha_m\rho_m\frac{\partial}{\partial t}(\boldsymbol{U_m}) + \alpha_m\rho_m(\boldsymbol{\nabla}.\boldsymbol{U_m})\boldsymbol{U_m} = -(\frac{\alpha_m}{\alpha_s}) \left(-\alpha_s\rho_s\frac{\partial}{\partial t}(\boldsymbol{U_s}) - \alpha_s\rho_s(\boldsymbol{\nabla}.\boldsymbol{U_s})\boldsymbol{U_s} \right.$$
$$\left. -\boldsymbol{\nabla}P_s + \boldsymbol{\nabla}.(\tilde{\boldsymbol{\tau_s}} + \boldsymbol{\tau\tilde{_{Ds}}}) + \alpha_s\rho_s\boldsymbol{g} + \sum_{m=1}^{N} \boldsymbol{M_{m,w}} \right) - \boldsymbol{\nabla}P_m + \boldsymbol{\nabla}.\tilde{\boldsymbol{\tau_m}} \tag{A.90}$$
$$+\alpha_m\rho_m\boldsymbol{g} + \boldsymbol{M_{m,w}} + \sum_{m=1,m\neq n}^{N} \boldsymbol{M_{m,n}}$$

then:

$$\boldsymbol{M_{m,w}} + \sum_{m=1,m\neq n}^{N} \boldsymbol{M_{m,n}} = \alpha_m \left(\rho_s\frac{\partial}{\partial t}(\boldsymbol{U_m} - \boldsymbol{U_s}) + \rho_s(\boldsymbol{\nabla}.\boldsymbol{U_m})\boldsymbol{U_m} - \rho_s(\boldsymbol{\nabla}.\boldsymbol{U_s})\boldsymbol{Us}+ \right.$$
$$\left. \boldsymbol{\nabla}(\frac{P_m}{\alpha_m} - \frac{P_s}{\alpha_s}) + \boldsymbol{\nabla}.(\frac{\tilde{\boldsymbol{\tau_s}} + \boldsymbol{\tau\tilde{_{Ds}}}}{\alpha_s} - \frac{\tilde{\boldsymbol{\tau_m}}}{\alpha_m}) + \frac{1}{\alpha_s}\sum_{m=1}^{N} \boldsymbol{M_{m,w}} \right) \tag{A.91}$$

A.5 Optimization code

```matlab
function   [qiSnm,qtSnm,SFLTCmdm,SFLTTmdm,Pcjmo,Ptjmo,Qcjmo,Qtjmo,...
      Qccjmo,Qctjmo,Qttjmo,Qtcjmo,rimo,t1,u11,Tcc,Ttc,alphaBeta]=...
         Santoss_modi(VS,Sin,Fr,PF,D50FmC,D10M,D50M,D90M,nt,Un,T,Tcm,
            Uc,Ut,t1,m2)

   %%%%%%%%%%%%%%%%%%%%%%%%%%%%%%%%%%%%%%%%%%%%%%%%%%%%%%%%%%%%%%%%%

nu=1.3*10^(-6);g=9.81;de=2.65-1;
pr=Fr;
%%%%%%%%%%%%%%%%%%%%%%%%%%%%%%%%%%%Fractional calculations
dm=D50M*10^(-3);
   alph1=-1:0.1:1;
      alph2=-1:0.1:1;

 alph1l=length(alph1);
 alph2l=length(alph2);

for  jj=1:length(Fr)

     eTaeff=((D50FmC(jj)*10^(-3))/(dm))^0.25;
     eTaefSan(jj)=eTaeff;
     Di=D50FmC(jj)*10^(-3);
     Dst50frsn=Di*(de*g*nu^(-2))^(1/3);
     Dst50frj(jj)=Dst50frsn;
     wssn=(nu./Di)*((10.36^2+1.049*Dst50frsn^3)^0.5-10.36);
     wsss(jj)=wssn;
     Dst50fr08=(0.8*Di)*(de*g*nu^(-2))^(1/3);
     Dst50fr08sn(jj)=Dst50fr08;
     ws=(nu./Di)*((10.36^2+1.049*Dst50fr08^3)^0.5-10.36);
     ws08Fr50(jj)=ws;
     Mk=de*g*Di;
%%%%%%%%%%%%%%%%%%%%%%%%%%%%%Teta calculation
teTcr=0.3/(1+1.2*Dst50frsn)+0.055*(1-exp(-0.02*Dst50frsn));
teCrcr(jj)=teTcr;
%%
%%%%%%%%%%%%%%%%%%%%%%%%%%%%%%%%%%%%%%Sediment Dynamics calculations
for  i=1:Un
Tcl(i)=Tcm(i);
w(i)=2*pi./T(i);
u1(i)=0.5*(Uc(i)+Ut(i));
u2(i)=0.5*(Uc(i)-Ut(i));
if (VS==1 && Sin==1 && T(1)~=7.5)
u11=u1(i)*sin(w(i).*t1)-u2(i)*cos(2*w(i).*t1);
ref=zeros(1,length(t1));
in=(find(u11<0,1));%,'last'));
```

```matlab
45    elseif(VS==1 && Sin==1)
46        u11=u1(i)*sin(w(i).*t1)-u2(i)*cos(2*w(i).*t1);
47            ref=zeros(1,length(t1));
48            in=find(u11<0,1);
49    elseif(VS==1 && Sin==0)
50    u11=u1(i)*cos(w(i).*t1)+u2(i)*cos(2*w(i).*t1);
51    ref=zeros(1,length(t1));
52    in=find(u11<0,1);
53    elseif(VS==0 && Sin==0)
54
55    u11=u1(i)*cos(w(i)*t1)-u2(i)*sin(2*w(i).*t1);
56    ref=zeros(1,length(t1));
57    in=find(u11<0,1);
58    elseif(VS==2 && Sin==0)
59            if nt==1150
60            m2=m2;
61            else
62            m2=0.8158;
63            end
64
65        u11=cn2(t1,T(i),m2,Uc(i),Ut(i));
66        ref=zeros(1,length(t1));
67        in=find(u11<0,1);
68    end
69
70    if Tcl(i)==0
71    tcf(i)=in;
72    Tc(i)=(t1(tcf(i)-1))-t1(1);
73    Tt(i)=t1(end)-t1(tcf(i)-1);
74    Tcc(i)=Tc(i);
75    Ttc(i)=T(i)-Tcc(i);
76    else
77        Tc(i)=Tcl(i);
78        Tt(i)=T(i)-Tc(i);
79        tn2=5.17+bbp:0.001:Tc(i)+bbp+5.17;
80        tcf(i)=length(tn2);
81        Tcc(i)=Tc(i);
82        Ttc(i)=T(i)-Tcc(i);
83    end
84    urms(i)=sqrt(0.5*((u1(i))^2+(u2(i))^2));
85    %%%%%%%%%%%%%%%%%%%%%%%%%%%%%%%%%%%%%%%%%%%%%%%%%%%%%%%%%%%%%%%%%%%
86     u112=u11.*u11;
87     uh(i)=sqrt((2/T(i))*(trapz(0:0.001:T(i),u112)));%%
88     ah(i)=uh(i).*T(i)/(2*pi);
89     utc(i)=0.5*sqrt(2)*Uc(i);
90     utt(i)=0.5*sqrt(2)*Ut(i);
91    %%%%%%%%%%%%%%%%%deSfCr
92    kw1=dm;
```

```matlab
co11=(utc(i))^2;
fwm=0.00251*exp(5.21*(ah(i)./kw1)^-0.19);
if (ah(i)/kw1)<=1.587
    fwm=0.3;
end
fwdm(i)=fwm;
%%%%%%%%%%%%%%%%%%%%%%%%%%%%%%%%%%%%%%%%%%%%%%
teprcm=((0.5*fwm*co11/(de*g*dm)));
ErDecdm(i)=3.7*dm*teprcm;
SLNcdm(i)=(utc(i)).*w(i)/(g*de);%Sleath number
teprcdm(i)=teprcm;
ficdm(i)=co11/(de*g*dm);
SSPCdm(jj,i)=ws08Fr50(jj)*(fwm)^-0.5*(co11)^-1;
%%%%%%%%%%%%%%%%%%%%%%%%%%%%%%%%%%%%%%%%%%%%%teprt
kw1=dm;
co12=(utt(i))^2;%t is tilda and not trough!
fwtdm=0.00251*exp(5.21*(ah(i)./kw1)^-0.19);
if (ah(i)/kw1)<=1.587
    fwtdm=0.3;
end
teprt=((0.5*fwtdm*co12/(de*g*dm)));%%%%%
ErDetdm(i)=3.7*dm*teprt;
SLNtdm(i)=(utt(i)).*w(i)/(g*de);
teprtdm(i)=teprt;
fitdm(i)=co12/(de*g*dm);
SSPTdm(jj,i)=ws08Fr50(jj)*(fwtdm^-0.5)*(co12)^-1;
%%
%%%%%%%%%%%%%%%%%%%%%%%SFLT of crest%%%%%%%%%%%%%%%%
    for Rep1=1:length(alph1)
            alpha1=alph1(Rep1);

        for Rep2=1:length(alph2)
            alpha2=alph2(Rep2);

%%%%%%%%%%%%%%%%%%%%%%%%%%%%%%%
          
if (isnan(D90M ) && isnan(D10M))
    af1(Rep1,Rep2)=1;
    af2(Rep1,Rep2)=1;
    af3(Rep1,Rep2)=1;
elseif (D90M/D10M)>4.0%%%%%%%%%%%
af1(Rep1,Rep2)=(D90M/D10M)^(alph1)*(1+PF)^(alph2);
af2(Rep1,Rep2)=(D90M/D10M)^(alph1)*(1+PF)^(alph2);
af3(Rep1,Rep2)=(D90M/D10M)^(alph1)*(1+PF)^(alph2);

else
    af1(Rep1,Rep2)=(D90M/D10M)^(alph1)*(1+PF)^(alph2);
    af2(Rep1,Rep2)=(D90M/D10M)^(alph1)*(1+PF)^(alph2);
```

```matlab
141        af3(Rep1,Rep2)=(D90M/D10M)^(alph1)*(1+PF)^(alph2);
142
143  end
144    if dm<=0.15*10^(-3)
145        deCR(Rep1,Rep2)=af1(Rep1,Rep2)*25*teprcm*dm;
146    elseif (dm<0.2*(10^-3) && dm>0.15*10^-3)
147        deCR(Rep1,Rep2)=af2(Rep1,Rep2)*(25-12*(dm*10^3-0.15)
                /(0.2-0.15))*dm;
148    else
149        deCR(Rep1,Rep2)=af3(Rep1,Rep2)*13*teprcm*dm;
150    end
151  SFLTCmdm{jj,i}(Rep1,Rep2)=deCR(Rep1,Rep2);
152  alphaBeta{jj,i}(Rep1,Rep2)={[alpha1 alpha2]};
153
154  %%%%%%%%%%%%%%%%%%%%%%%%%%%%%%%%%%%%%%%%%%%%%%%%%%%%%%%%%%%%%%%%%%
155    if dm<=0.15*10^(-3)
156        deTR(Rep1,Rep2)=af1(Rep1,Rep2)*25*teprt*dm;
157    elseif (dm<0.2*(10^-3) && dm>0.15*10^-3)
158        deTR(Rep1,Rep2)=af2(Rep1,Rep2)*(25-12*(dm*10^3-0.15)
                /(0.2-0.15))*dm;
159    else
160        deTR(Rep1,Rep2)=af3(Rep1,Rep2)*13*teprt*dm;
161    end
162  SFLTTmdm{jj,i}(Rep1,Rep2)=deTR(Rep1,Rep2);
163
164  %%%%%%%%%%%%%%%%%%%%%%%%%Pc and Pt%%%%%%%%%%%%%%%%%%%
165  Pc(jj,i)=8.2*deCR(Rep1,Rep2)/(Tc(i)*ws);%
166  Pt(jj,i)=8.2*deTR(Rep1,Rep2)/(Tt(i)*ws);%
167  Pcjmo{jj,i}(Rep1,Rep2)=Pc(jj,i);
168  Ptjmo{jj,i}(Rep1,Rep2)=Pt(jj,i);
169  %%
170  %%%%%%%%%%%%%%%teCR jth jth fraction
171  kw1j=Di;
172  co13=(utc(i))^2;
173
174  fwjc=0.00251*exp(5.21*(ah(i)./kw1j)^-0.19);
175  if (ah(i)/kw1j)<=1.587
176        fwjc=0.3;
177  end
178  fwj(jj,i)=fwjc;
179  teEffj=((eTaeff*co13*0.5*fwjc)/(de*g*Di));
180  teprcEffj(jj,i)=teEffj;
181  %%%%%%%%%%%%%%%%%teTR jth fraction
182  kw1tj=Di;
183  co1t=(utt(i))^2;
184  fwtj=0.00251*exp(5.21*(ah(i)./kw1tj)^-0.19);
185  if (ah(i)/kw1tj)<=1.587
186        fwtj=0.3;
```

```matlab
187  end
188
189  teEfftj =((eTaeff*co1t*0.5*(fwtj))/(de*g*Di));
190  teprtEffj(jj,i)=teEfftj;
191  %%
192  %%%%%%%%%%%%%%%%%Qij%%%%%%%%%%%%%%
193  if abs(teEffj)<=teTcr
194      Qc=0;
195  else
196      Qc=11*(abs(teEffj)-teTcr).^1.2;
197  end
198  Qcjmo{jj,i}(Rep1,Rep2)=Qc;
199  %%%%%%%%%%%%%%%%%%%%%%Qt%%%%%%%%%%%%%%%%%%%%%%%%
200  if abs(teEfftj)<=teTcr
201      Qt=0;
202  else
203      Qt=11*(abs(teEfftj)-teTcr).^1.2;
204  end
205  Qtjmo{jj,i}(Rep1,Rep2)=Qt;
206  %%%%%%%%%%%%%%%%%%%Qcc%%%%%%%%%%%%%%%%%%%%%%%%%%%
207   if (Pc(jj,i)<=1)
208      Qcc=Qc;
209   elseif (Pc(jj,i)>1)
210      Qcc=(1/Pc(jj,i))*Qc;
211   end
212    Qccjmo{jj,i}(Rep1,Rep2)=Qcc;
213    %%%%%%%%%%%%%%%%%%%%%%%Qct%%%%%%%%%%%%%%%%%%%%%%%%
214    if (Pc(jj,i)<=1)
215      Qct=0;
216   elseif (Pc(jj,i)>1)
217      Qct=(1-1/Pc(jj,i))*Qc;
218    end
219    Qctjmo{jj,i}(Rep1,Rep2)=Qct;
220    %%%%%%%%%%%%%%%%%%%%%%Qtt%%%%%%%%%%%%%%%%%%%%%%
221    if (Pt(jj,i)<=1)
222      Qtt=Qt;
223   elseif (Pt(jj,i)>1)
224      Qtt=(1/Pt(jj,i))*Qt;
225    end
226    Qttjmo{jj,i}(Rep1,Rep2)=Qtt;
227     %%%%%%%%%%%%%%%%%%%%%Qtc%%%%%%%%%%%%%%%%%%%%%%%%
228    if (Pt(jj,i)<=1)
229      Qtc=0;
230   elseif (Pt(jj,i)>1)
231      Qtc=(1-1/Pt(jj,i))*Qt;
232    end
233
234      Qtcjmo{jj,i}(Rep1,Rep2)=Qtc;
```

```matlab
235      %%%%%%%%%%%%%%%%%%%%%%%%%%%%%%%%%%%%%%%%%%%%%%%%
236      %%%%%%%%%%%%%%%%%%%%%%%%%%%%%%%%%%%%%%%%%%%%%%%%
237      %%%%%%%%%%%%%%%%%%%%%%%%%%%%%%%%%%%%%%%%%%%%%%%%
238      rimo(jj,i)=((Tc(i)*sqrt(abs(teEffj))*(Qcc+Qtc)-Tt(i)*sqrt(abs(
             teEfftj))*(Qtt+Qct))/T(i));
239   qiSnmm(jj,i)=10^6*Fr(jj)*sqrt(Di^3*g*de)*rimo(jj,i);
240   qiSnm{jj,i}(Rep1,Rep2)=qiSnmm(jj,i);
241    end
242
243  end
244  end
245  end
246  %%%%%%%%%%%%%%%%%%%%%%%%%%%%%%%%%%%%%%%%%%%%%%%%%%%%%%%%%
247          qtSnm=cell(1,Un);
248
249       for zt=1:Un
250            qtSnm{1,zt}=zeros(alph1l,alph2l);
251       end
252  %%%%%%%%%%%%%%%%%%%%%%%%%%%%%%%%%%%%%%%%%%%%%%%%%%%%
253
254
255  for pds=1:jj
256
257      for pdz=1:Un
258   qtSnm{1,pdz}=qtSnm{1,pdz}+qiSnm{pds,pdz};
259
260      end
261  end
262  end
```

Curriculum Vitae

Personal Details

Name	Gholamreza Shiravani
Date/place of birth	August 20, 1982 in Darab (Fars Province-Iran)
Personal status	single

Work Experience

Feb. 2018 – current	Resaerch Associate at Lower Saxony Water Management, Coastal Defence and Nature Conservation Agency (NLWKN)-Coastal Research Station (FSK) (full time)
Sep. 2015 – Feb. 2018	Research Associate at Leibniz University Hannover-Coastal Research Center (FZK) (50% time)
Apr. 2015 – Sep. 2015	Research Assistant at Leibniz University Hannover-Coastal Research Center (FZK) (35 hours per month)
Apr. 2015 – Sep. 2015	Research Assistant at Leibniz University Hannover-Hannover Centre for Production Technology (PZH)-Institute of Assembly Technology (match) (30 hours per month)
Apr. 2014 – Apr. 2015	Research Assistant at Leibniz University Hannover-Coastal Research Center (FZK) (35 hours per month)
Jan. 2014 – Apr. 2014	Research Assistant at Leibniz University Hannover-Coastal Research Center (FZK) (28 hours per month)
Dec. 2012 – Jan. 2014	Research Assistant at Leibniz University Hannover-Coastal Research Center (FZK) (86 hours per month)
Oct. 2010 – May. 2011	Research Associate at Iranian Port and Maritime Organization (PMO)-Tehran (120 hours per month)

Community Service

Sep. 2009 – August. 2010	Project Engineer at Omran Abshar Spadana-Isfahan (full time)

Education

Sep. 2006 – Mar. 2009	M. Sc. in Civil Engineering – Marine Structures Engineering at the faculty of Technology and Engineering in University of Hormozgan (Master Thesis: Diffraction of Water Waves with Arrays of Vertical Cylinders)
Sep. 2001 – Feb. 2006	B. Sc. in Civil Engineering – Water and Wastewater at Power and Water University of Technology (PWUT)

School Education

Sep. 1999 – May. 2000	Pre-University with major in Mathematics and Physics at Kharazmi Pre-University Center
Sep. 1996 – May. 1999	High School Diploma with major in Mathematics and Physics at Shahid Beheshti High School (II)

Norderney, 11$^{\text{th}}$ May 2021
Gholamreza Shiravani

Kurzfassung

Küstennaher Sedimenttransport in Richtung des Strandes könnte bei z.B. Sturmfluten zu erheblichen morphologischen Veränderungen und massiver Küstenerosion mit drastischen, teils irreversiblen Folgen führen. Um Strände vor sturmbedingten Erosionen zu schützen, werden Küstenschutzmaßnahmen in harte/graue oder weiche/umweltfreundliche Ingenieurmaßnahmen klassifiziert. Schäden an harten Schutzmaßnahmen (z. B. Ufermauern) haben meist sowohl hohe Reparaturkosten zur Folge, als auch Einschränkungen des Zugangs und folglich eine Verringerung der touristischen Attraktivität. Um diese Probleme zu umgehen, werden häufig weiche Unterhaltungsmaßnahmen, wie z.B. die Strandaufspülung, angewendet. Diese können den Strand ebenfalls vor möglichen schweren Sturmschäden schützen. Die Produktivität sowie die Beliebtheit der weichen Maßnahmen, sowohl für die Natur als auch für den Menschen, führen dazu, dass diese in der Literatur als Bauen mit der Natur bezeichnet werden, im Gegensatz zu grauen Strukturen, die als Bauen gegen die Natur bekannt sind.

Die große Menge an Stranderosionen aufgrund von Sturmereignissen und den damit verbundenen hohen Unterhaltungskosten der Strandaufspülungen sind eines der Hauptfragestellungen in der Strandunterhaltung. Um das Erosionsverhalten von sandigen Stränden und Sturmflutbedingungen zu verstehen, wird hauptsächlich die Erosions-Methode im „Sheet Flow" verwendet. Beim „Sheet Flow" wird die Sohlschubgeschwindigkeit so groß, dass Sand hauptsächlich in sogenannten hochkonzentrierten Schichten nahe der Sohle transportiert wird. Die Sohlenformen werden dadurch wegtransportiert, sodass die Sohle flach bleibt.

Die praktischen Erfahrungen bei der Strandaufspülung zeigen, dass das neu aufgebrachte Material in der Regel andere Eigenschaften, insbesondere in der Korngrößenverteilung, aufweist als der ursprüngliche Sand. Darüber hinaus spielt diese Diskrepanz zwischen der Korngrößenverteilung von eingelagertem und bereits vorhandenem Sand eine wichtige Rolle bei der Erhöhung/Verringerung der Erosionsrate bei zukünftigen Sturmereignissen. Um die Erosionsmechanismen von aufgespülten Stränden zu verstehen, ist es entscheidend, die Transportmechanismen von gemischtem Sand im Gegensatz zu homogen verteiltem Sand zu untersuchen. Durchgeführte Experimente mit gemischtem Sand mit der gleichen mittleren Korngröße wie bei homogenem Sand zeigten in speziellen Untersuchungen, dass die Erosionsrate von gemischtem Sand etwa zehnmal kleiner ist verglichen zum homogenen Sandgemisch. Diese Erkenntnis bestätigt die praktischen Erfahrungen, bei denen die Kornzusammensetzung nach der Strandaufspülung ein entscheidender Parameter ist, um die Erosionsrate bei zukünftigen Stürmen zu steuern bzw. zu reduzieren.

Aufgrund der natürlichen ungleichförmigen Zusammensetzung von Sedimenten wurde in Küsteningenieurwesen versucht, die effektive Schubspannung oder kritische Schubspannung von Sandkörnern mit empirischen Faktoren zu modifizieren, die im Sedimenttransport als Hiding/Exposure-Formeln bekannt sind. Diese empirischen Faktoren sind jedoch nicht in der Lage, die im Detail vorkommenden Prozesse des gemischten Sedimenttransports in Transportformeln miteinzubeziehen und daher ergeben sich je nach verwendeter Gleichung unterschiedliche Transportraten. Somit ist die Genauigkeit von Transportformeln abhängig von den angewendeten Modifikationsfaktoren. Darüber hinaus können die Hiding/Exposure-Faktoren keine detaillierten Informationen über den Konzentrationsfluss der einzelnen Fraktionen in einem gemischten Sand liefern. Daher ist es von großer Wichtigkeit, diese Prozesse zu verstehen und die Strandaufspülungen umwelttechnisch und -schonend zu verbessern, um auch langfristig für eine nachhaltige umweltfreundliche

Sicherung der Küstenlinie zu sorgen.

In der vorliegenden Studie werden die vorhandenen Experimente zum gemischten Sedimenttransport unter „Sheet Flow"-Bedingungen systematisch verglichen und die Leistungsfähigkeit der entsprechenden Gleichungen aus dem Küsteningenieurwesen in Kombination mit verfügbaren empirischen Gleichungen für Hiding/Exposure-Formeln bewertet. Aufgrund der Bedeutung von gemischtem Sand, zur Reduzierung der Erosionsrate nach einer Sandaufspülung bei Sturmfluten, wird hier ein detaillierter RANS (Reynolds Averaged Navier Stokes) eulerscher zweiphasiger numerischer Löser (solver), mixedSedFoam, innerhalb des Open-Source-CFD-Toolbox-Frameworks OpenFOAM entwickelt. Der hier entwickelte Ansatz ist anhand von verfügbaren experimentellen Daten aus der Literatur kalibriert und validiert worden. Dies ist der erste Ansatz seiner Art, bei der die Sandkonzentration und die Transportgeschwindigkeit der konstituierenden Fraktionen, sowie ihre entsprechenden Geschwindigkeiten zusammen berechnet werden. Aufgrund der Bedeutung von interpartikulären Wechselwirkungen innerhalb des „Sheet Flow"-Zustands wurde in dieser Arbeit außerdem ein neuer interkristalliner Widerstandsbeiwert basierend auf der Kollision von Partikeln (hier Sandkörnern) und der kinetischen Energie des granularen Systems entwickelt. Der entwickelte neue Widerstandsbeiwert kann die Dynamik verschiedener granularer Systeme wesentlich besser beschreiben als die bisherigen Beiwerte. Eine neue Formel zur Vorhersage der Schichtdicke der Schichtströmung wird vorgestellt, die in der Lage ist, die Genauigkeit der verfügbaren (semi-) empirischen Transportformeln für die Vorhersage des gemischten Sandtransports zu verbessern.

Der hier entwickelte Modellansatz verbessert das Verständnis der Transportmechanismen von gemischten Sandfraktionen unter Schichtströmungsbedingungen und ist in der Lage zukünftig bei der Entscheidung über die Korngrößenverteilung von Sandaufspülungen zu unterstützen. Ebenfalls kann dieser Ansatz verwendet werden, um das neue aufzubringende Material hinsichtlich der Stabilitätskriterien zu untersuchen, um so den zukünftigen Unterhaltungsaufwand zu reduzieren bzw. zu optimieren.

Schlüsselwörter: gemischter Sedimenttransport, „Sheet Flow", numerischer Modellversuch, (semi-) empirische Sedimenttransportformeln

Abstract

Cross-shore sediment transport during extreme climate events (e.g. storm surges) may lead to significant morphological evolution and shoreline recession with drastic irreversible consequences. To protect sandy beaches against storm induced erosion issues, coastal engineering practices could be classified into hard/gray protecting coastal structures versus soft or environmentally friendly engineering measurements. Hard structures (e.g. seawalls) have usually been posed many problems during storm surges, which can be summarized as expensive reparation costs of structures after storm and damages of protected infrastructures as well as restriction of human access to beach for leisure activities, and consequently reduction the tourist attraction. In contrast, the soft measurements for beach protection like beach nourishment can protect the sandy beaches against storms and preserves the beautiful beach scenes for tourists, and therefore provide financial support for people living along the coastline. The productivity as well as favorability of soft measurements for both nature and human parties lead to calling these activities in literature as building with nature in contrast to hard structures, which are known as building against nature.

The high rate of beach erosion during storms and corresponding high costs for beach (re)nourishment to compensate the lost sand is one of the major issues in coastal zone management. To understand the erosion of sandy beaches under storm conditions, the associated erosion mode in literature is known as sheet flow, where the near bed current velocity is such great that sands are basically transported within highly concentrated sheets near the bed and therefore the bed forms are disappeared.

The practical experiences on beach nourishment show that the new applied material (borrow material) have usually different properties, particularly grain size distribution, than the native sand. Moreover, this discrepancy between the grain size distribution of incorporated and native sand has an important role in increment/reduction of the erosion rate of (re)nourished beaches under future storms. To understand the erosion mechanisms of (re)nourished beaches, coastal engineers were interested to study the transport mechanisms of mixed sand versus uniform sand. Performed experiments on a mixed sand (well graded sand) with the same median grain size to a uniform sand (well sorted sand) in small scale experiments under storm induced transport mode (i.e. sheet flow) revealed that the erosion rate of the mixed sand is around ten times smaller than the uniform. This importance can approve the practical experiences, where the final sand mixture grain size distribution after (re)nourishment is a deciding parameter to reduce the erosion rate at future storms.

Due to the natural heterogeneity of sand grains, coastal engineers tried to modify the effective shear stress or critical shear stress on grains using empirical/theoretical modification factors to include this in prediction formulas. These modification approaches are known in sediment transport as hiding/exposure factors. However, these are not able to include the detailed mechanisms of mixed sand transport in prediction formulas, and therefore depending on the applied formula for predicting the transport rate. The accuracy of transport formulas generally differs with respect to the applied modification factor. Moreover, the hiding/exposure factors are not able to provide detailed information about the concentration flux of constituting fractions in a mixed sand. Therefore, with regard to the positive economical property of mixed sand based on the performed experiments, detailed investigations like this thesis could be worthful to improve the protection performance of beach (re)nourishment as a sustainable environmentally friendly measurement in coastal engineering.

In this study, the available experiments on mixed sand transport under sheet flow con-

ditions are systematically compared. Then the capability of available (semi-) empirical formulas in coastal engineering for sheet flow induced sand transport in combination with available empirical equations for hiding/exposure coefficients are evaluated. Moreover, due to the importance of non-uniformity of mixed sand in reduction of the erosion rate after (re)nourishment under storm condition, a detailed RANS (Reynolds Averaged Navier Stokes) Eulerian two-phase numerical solver, mixedSedFoam, within the open-source CFD-toolbox framework OpenFOAM is developed, and with available experimental data calibrated and validated. This is the first time that accompanied with the sand concentration and velocity, the concentration of constituting fractions as well as their corresponding velocities are computed. This importance could improve the understanding of the transport mechanisms of mixed sand under sheet flow conditions and be implemented in the practice of coastal engineering, by deciding on the available borrow material with different grain size distribution for beach (re)nourishment.

Moreover, due to the importance of inter-particle interactions within the sheet flow layer, in this thesis a new intergranular drag force coefficient based on the collision of particles (here sand grains) and the kinetic energy of granular system is developed. The developed new drag force coefficient can better than the previous describe the dynamics of different granular systems. Finally, a new formula for prediction of sheet flow layer thickness is presented, which improves the accuracy of available (semi-) empirical transport formula for mixed sand transport prediction.

Keywords: Mixed sand transport, sheet flow, numerical modeling, (semi-) empirical sand transport formulas

Eidesstattliche Versicherung

gem. §5 Abs. 4 der Promotionsordnung vom 04.06.2020

<div align="right">

Gholamreza Shiravani
An der Mühle 4A
26548 Norderney
Matr.-Nr. 3199100

</div>

Ich, Gholamreza Shiravani, versichere an Eides Statt durch meine Unterschrift, dass ich

(a) die Regeln der geltenden Promotionsordnung zu kennen und eingehalten zu haben und mit einer Prüfung nach den Bestimmungen der Promotionsordnung einverstanden zu sein,

(b) die Dissertation selbst verfasst zu haben (Selbständigkeitserklärung), keine Textabschnitte von Dritten oder eigener Prüfungsarbeiten ohne Kennzeichnung übernommen und alle von ihr oder ihm benutzten Hilfsmittel und Quellen in seiner Arbeit angegeben zu haben,

(c) Dritten weder unmittelbar noch mittelbar geldwerte Leistungen für Vermittlungstätigkeiten oder für die inhaltliche Ausarbeitung der Dissertation erbracht zu haben (d.h. die wissenschaftliche Arbeit darf weder in Teilen noch in Gänze von Dritten gegen Entgelt oder sonstige Gegenleistung erworben oder vermittelt worden sein),

(d) die Dissertation noch nicht als Prüfungsarbeit für eine staatliche oder andere wissenschaftliche Prüfung eingereicht zu haben,

(e) ob sie bzw. er die gleiche oder eine in wesentlichen Teilen ähnliche Arbeit bei einer anderen Hochschule als Dissertation eingereicht hat und gegebenenfalls mit welchem Ergebnis; zugleich ist mitzuteilen, ob eine andere Abhandlung als Dissertation eingereicht wurde und gegebenenfalls mit welchem Ergebnis.

Norderney, den 15. Juni 2021, —————————————————————

<div align="center">

Gholamreza Shiravani

</div>